SUPERSYMMETRY WITH HEAVY SCALARS AT THE LHC

A THESIS SUBMITTED TO
THE GRADUATE SCHOOL OF NATURAL AND APPLIED SCIENCES
OF
MIDDLE EAST TECHNICAL UNIVERSITY

BY

SEZEN SEKMEN

IN PARTIAL FULFILLMENT OF THE REQUIREMENTS
FOR
THE DEGREE OF DOCTOR OF PHILOSOPHY
IN
PHYSICS

DECEMBER 2008

Approval of the thesis:

SUPERSYMMETRY WITH HEAVY SCALARS AT THE LHC

submitted by **SEZEN SEKMEN** in partial fulfillment of the requirements for the degree of **Doctor of Philosophy in Physics Department, Middle East Technical University** by,

Prof. Dr. Canan Özgen
Dean, Graduate School of **Natural and Applied Sciences** _____

Prof. Dr. Sinan Bilikmen
Head of Department, **Physics** _____

Prof. Dr. Mehmet T. Zeyrek
Supervisor, **Physics Department** _____

Examining Committee Members:

Prof. Dr. Ali Ulvi Yılmazer
Physics Department, Ankara University _____

Prof. Dr. Mehmet T. Zeyrek
Physics Department, METU _____

Prof. Dr. Maria Spiropulu
Physics Department, CERN (Switzerland), CALTECH (USA) _____

Prof. Dr. Erhan Onur İltan
Physics Department, METU _____

Assoc. Prof. Dr. Altuğ Özpineci
Physics Department, METU _____

Date: _____

I hereby declare that I have obtained and presented all information in this document in accordance with academic rules and ethical conduct. I also declare that, as required by these rules and conduct, I have fully cited and referenced all material and results that are not original to this work.

Name, Last Name: SEZEN SEKMEN

Signature :

ABSTRACT

SUPERSYMMETRY WITH HEAVY SCALARS AT THE LHC

Sekmen, Sezen
Ph.D., Department of Physics
Supervisor : Prof. Dr. Mehmet T. Zeyrek

December 2008, 172 pages

We consider three distinct categories of supersymmetric scenarios with heavy scalars and light gauginos. First, we investigate the SO(10) SUSY GUTs, and locate MSSM parameter space regions that satisfy GUT scale Yukawa unification, which is a distinct feature of these models. Then taking example SO(10) cases, we perform a Monte Carlo study with toy detector simulation at 14 TeV at the LHC on the no $\not\!\!E_T$ leptonic channels 2,3 leptons + ≥4 jets and show that discovery is possible with ∼1 fb^{-1} of integrated luminosity. We also demonstrate the feasibility of invariant mass endpoint measurements for ∼100 fb^{-1}. Furthermore, in a cosmological context, we propose that SO(10) scenarios with excess neutralino relic abundance can be made WMAP-compatble by assuming neutralino decays to axinos, and show that there are various axino/axion cold and warm dark matter admixtures which can be consistent with non-thermal leptogenesis requirements for the thermal re-heat temperature.

Afterwards we complement the SO(10)s with the string-inspired G_2-MSSM and focus point mSUGRA scenarios and perform a full simulation search of these at $\sqrt{s}$ = 14 TeV at the LHC with the CMS detector where the main production mechanism is through gluino pair production and the final states are cheracterized by all-hadronic topologies (including *b*s and *t*s). Through the design of six prototype all-hadronic selection paths and using the CMS High Lever Trigger paths with highest significance (including the *b*-enriched ones), we find that all but one model benchmarks are accessible with 100 pb^{-1} integrated luminosity. We present

the results as a function of the gluino mass considering the major detector systematic effects.

Keywords: Supersymmetry, Dark Matter, CMS, Jet-MET

ÖZ

LHC'DE AĞIR SKALARLI SÜPERSİMETRİ

Sekmen, Sezen
Doktora, Fizik Bölümü
Tez Yöneticisi : Prof. Dr. Mehmet T. Zeyrek

Aralik 2008, 172 sayfa

Bu tezde ağır skalar ve hafif gaugino kütlelerine sahip olan üç ayrı süpersimetri senaryosu ele alınmıştır. Başta SO(10) SUSY BBTler incelenerek MSSM parametre uzayında bu modellerin ayırdedici özelliği olan BBT olçeğinde Yukawa birleşimini sağlayan bolgeler saptanmıstır. Sonra örnek SO(10) noktaları uzerinde genel basit detektör simulasyonu ile $\sqrt{s}$ = 14 TeV'de LHC için kayıp enerjisiz lepton kanalları 2,3 lepton + ≥4 jet ile bir Monte Carlo çalışması yapılarak ∼1 fb^{-1} toplam ışınlıkta keşif olasılıgı gösterilmiştir. Ek olarak ∼100 fb^{-1} için değişmez kütle dağılımı uç noktalarının ölçülebilirliği vurgulanmıştır. Ayrıca evrebilim kapsamında yapılan bir çalışmada aşırı neutralino kalıntı yoğunluğuna sahip senaryoların neutralinoların axinolara bozundukları durumlarda WMAP ölçümlerine uyumlu hale gelecekleri önerilmiş ve ısıl olmayan leptogenesisin gerektirdigi tekrar ısınma sıcaklıgı koşullarını saglayan bazı axino/axion soğuk ve ılık karanlık madde karışımların olasılıgı belirlenmiştir.

Sonrasında SO(10)'lara sicim kaynaklı G_2-MSSM ve odak noktası mSUGRA senaryoları da eklenerek $\sqrt{s}$ = 14 TeV'de LHC için CMS detektörü ile tam simulasyon araştırmasi gerçekleştirilmiştir. Burada ana üretim mekanizması çift gluino üretimidir ve sonuç olarak çoğunlukla *b* ve *t* açısından zengin tam-hadronik durumlar ortaya çıkmaktadır. Altı örnek tam-hadronik seçim yolunun tasarımı ve güvenilirliği en yüksek CMS HLT'lerinin (ayrıca b HLT'lerinin) kullanımı ile bir tanesi hariç tüm model noktalarının 100 pb^{-1} toplam ışınlık ile erişilir olduğu belirlenmiştir. Sonuçlar detektör temelli sistematik etkiler de gözönüne

alınarak gluino kütlesine karşı gösterilmiştir.

Anahtar Kelimeler: Süpersimetri, Karanlık Madde, CMS, Jet-Kayıp Enerji

ACKNOWLEDGMENTS

I shall not spare words when it is the time to thank.

I greatly thank my supervisor Mehmet T. Zeyrek for the always supporting, encouraging and cheerful mentor he has been on this long, hard way we have walked. He constantly gave opportunuties, and most of all, generously offered me the gift of CERN on a golden plate of freedom.

I was blessed with the supervision of Maria Spir(it)opulu at CERN. She guided me through all challenging details of CMS work with such care and attention, and dedicated vast efforts to the planning and creation of this thesis. Her sincerity and example devotion to physics has been a most inspiring spring of motivation and the perfect shield against a sea of troubles. Ευχαριστώ για όλα...

I am truly grateful to Sabine Kraml for finally officially admitting me to the ”sdark side” (by which I was long ago seduced, thanks to John Ellis). I was honored to be apprenticed to a master of such wisdom, clarity and kindness throughout a greatly enriching collaboration.

I had the best guide in the SUSY parameter space and have actually worked with the very encyclopedia of SUSY himself! Many thanks to Howie Baer whose great insight and creativity contributed so much to this work. Also thanks to Heaya Summy and Markus Haider for their valuable part in our SO10 studies.

I thank Gordon Kane and Bobby Acharya for adding a bit of ”fine stringy flavor” to the whole thing, and to Jing Shao for his help during implemention of the G2s for CMS analysis. Many thanks to Luc Pape for all his advice and the complementary idea to include the focus points. I am indebted to Maurizio Pierini, Massimiliano Chiorboli, Chris Rogan and Thiago Tomei for the great help they readily offered during my CMS analysis, and further thank Joe Lykken for comments on the results. I acknowledge as well all the other CMS colleagues from whom I received help in diverse physics and computing issues. I also thank Maggie Mühlleitner and Sasha Pukhov for their patient support with SUSYHIT and micrOMEGAs.

Heartfelt thanks to my eternally young friend and protector Daniel Denegri for his kindness, concern and humor...and for all that tango.

Further thanks to Albert (P.W.B.) de Roeck, my good old ally against the black holes, for

our joyful work and discussions. I also thank the CMS SUSY conveners Oliver Buchmüller and Jeff Richman for supporting my studies and allowing me to contribute actively to the CMS SUSY group, and acknowledge the hadronic SUSY subgroup for useful comments. Many thanks to Gigi Rolandi and Paris Sphicas for guidance for thesis protocol in CMS. I as well thank Harrison Prosper for adding a considerable amount of comfort to my mood during the final stages of this work.

I had the full support of METU High Energy Physics Group. I am indebted to Meltem Serin for her kind support and for the restless work she did to settle our official and financial matters.

I thank ”my cousin” Efe Yazgan whose unique views have constantly stimulated my intuition and started my scientific maturing (well, sort of opened my eyes) - and to Yasemin Uzunefe Yazgan for her ever warm presence (may the horse be with us). Their friendship is invaluable.

I thank Halil ”Ağa” Gamsızkan for his honesty, support and help in every sense, specially for significant contributions while getting my IT Brunette Certificate.

I thank the many good friends whose company enhanced the joy of staying at CERN, particularly to Ellie Lockner, Jason St. John, Sharon and Vasken Hagopian, Neslihan and Max Schmidt, Cüseppe Suratti, Richard Brauer, Michael Tytgat and Monica Vazquez Acosta..

I also thank Barış Malcıoğlu and Emre Taşçı, the generous Lords of the Geekland, oh, but great friends, too! Special thanks to Hafize Bakırcı for her sincere encouragement and all the fun we had in insane moments. Also thanks to Nihal Samsun and Cem Tüzüner for their constant friendship and merry presence in my adventures throughout the years and for their hospitality in Ankara.

Most of all, I am deeply grateful to my dear parents and brother for understanding and supporting my uncurable passion for physics, and for all they have sacrificed and done for me to pursue it at best.

...

CERN visits during the work included in this thesis were financially supported by The Scientific and Technological Research Council of Turkey (TUBİTAK) grant 106T457 (TBAG-HD 190) and The Turkish Atomic Energy Authority (TAEK) CERN Project.

TABLE OF CONTENTS

ABSTRACT iv

ÖZ vi

ACKNOWLEDGMENTS viii

TABLE OF CONTENTS x

LIST OF TABLES xiv

LIST OF FIGURES xvii

CHAPTERS

1 INTRODUCTION: QUEST FOR A NEW THEORY 1

2 SUPERSYMMETRY 6

2.1 Introducing supersymmetry 6

2.2 Superfields 9

2.3 Supersymmetry Lagrangian 11

2.3.1 Lagrangian for the chiral superfield 12

2.3.2 Lagrangian for the vector superfield 13

2.3.3 Interaction Lagrangian 13

2.3.4 Soft SUSY breaking Lagrngian 14

2.4 Supersymmetry breaking 15

2.4.1 Gravity-mediated SUSY breaking (SUGRA) 16

2.4.2 Gauge-mediated SUSY breaking (GMSB) 17

2.5 Electroweak symmetry breaking 18

2.6 Sparticle mixing and masses 20

2.6.1 Squarks and sleptons 20

2.6.2 The gluino 21

2.6.3 Neutralinos 22

2.6.4 Charginos . . . 23
2.7 Experimental bounds on sparticle masses . . . 24
2.8 Reasons to favor SUSY . . . 24
2.9 R parity and supersymmetric dark matter . . . 25
2.10 Spectrum and relic density comparisons . . . 27
3 PHENOMENOLOGY OF THE G_2-MSSM . . . 32
3.1 Introducing strings . . . 32
3.2 The G_2-MSSM . . . 33
4 PHENOMENOLOGY OF THE SIMPLE SO(10) SUPERSYMMETRIC GUTs 36
4.1 Introduction and motivation . . . 36
4.2 Search for DM-allowed scenarios for Yukawa-unified SO(10) SUSY GUTs . . . 38
4.2.1 The Markov Chain Monte Carlo method . . . 41
4.2.2 The GSH solutions . . . 42
4.2.3 The WSH solutions . . . 45
4.2.4 Adjusting the DM relic density . . . 48
4.2.4.1 $\tilde{\chi}_1^0$ may not be the LSP... . . . 48
4.2.4.2 Solution via non-universal gaugino masses . . . 49
4.2.4.3 Solution via non-universal scalar masses . . . 49
4.2.5 LHC scenarios for SO(10) . . . 49
4.3 Search for SO(10) scenarios using the lepton channels at $\sqrt{s} = 14$ TeV at the CERN LHC . . . 53
4.3.1 The $\tilde{g} \to b\bar{b}\tilde{\chi}_2^0 \to b\bar{b}(l\bar{l}/b\bar{b})\tilde{\chi}_1^0$ chain . . . 54
4.3.2 A note on trileptons signal from $\tilde{\chi}_2^{\pm}\tilde{\chi}_1^0$ production . . . 61
4.4 Sensitivity of Yukawa unification to small variances in input parameters 62
4.5 Cosmological consequences of SO(10) models with mixed axion/axino cold and warm dark matter . . . 63
4.5.1 Introducing axions and axinos . . . 66
4.5.2 Axions and axinos as dark matter . . . 66
4.5.2.1 Cosmological bounds on T_R . . . 67
4.5.3 Mixed axion/axino cold and warm dark matter scenarios for SO(10) . . . 68

5 PHENOMENOLOGY OF THE FOCUS POINT mSUGRA 71
5.1 Introducing focus point mSUGRA 71
5.2 Focus point scenarios for the LHC 72
6 CERN LARGE HADRON COLLIDER AND THE COMPACT MUON SOLENOID EXPERIMENT 78
6.1 The Large Hadron Collider 78
6.2 The Compact Muon Solenoid Experiment 82
6.2.1 Tracker 83
6.2.1.1 The Pixel Detector 83
6.2.1.2 The Silicon Strip Detector 84
6.2.2 The Electromagnetic Calorimeter 85
6.2.3 The Hadron Calorimeter 86
6.2.4 Superconducting Magnet Coil 88
6.2.5 Muon System 89
6.2.6 Trigger 92
7 SEARCH FOR THE G_2-MSSM, SO(10) AND FOCUS POINT SUSY SCENARIOS IN CMS USING THE INCLUSIVE MISSING E_T+JETS SIGNATURE AT $\sqrt{s}$ = 14 TeV AT THE CERN LHC 95
7.1 Introduction 95
7.2 Selected benchmarks and signal generation 96
7.3 Backgrounds and background samples 101
7.3.1 Objects and reconstruction 102
7.4 Trigger studies 108
7.5 Offline event selection 114
7.5.1 Defining the paths 114
7.5.2 Cleaning the lepton-rich backgrounds 118
7.5.2.1 Leading track isolation 118
7.5.2.2 Jet and event electromagnetic fraction 119
7.5.3 Cleaning the QCD background 122
7.5.3.1 Missing hadronic transverse energy 122
7.5.3.2 $d\phi(jet - \not{E}_T)$ cuts 123

7.5.4 Cleaning further 126
7.5.4.1 1st jet η 126
7.5.4.2 Event shape variables 128
7.6 Selection results 128
7.7 Making use of the *b* triggers 133
7.8 Background estimation from data 134
7.9 Effects of uncertainties 144
8 CONCLUSIONS 150
REFERENCES 154
APPENDICES
A PDJetMET TRIGGERS 160
B APLANARITY 163
C *b* TRIGGERS 167

LIST OF TABLES

TABLES

Table 2.1 Field content of the MSSM 11

Table 3.1 Microscopic parameters (first 5 columns) as explained in the text, some EW scale parameters (columns 6-10) and $\Omega_{\tilde{\chi}_1^0}h^2$ for benchmark Points 1 and 4 from Table 1 of [53] which are renamed as G21 and G24 respectively. $P - Q = 3$ and $P_{eff} = 83$. Here Z_{eff} is the effective Higgs bilinear coefficient, which is a complex values function of all hidden sector chiral fields in general and is used in determination of the pases μ and $B\mu$. $\Omega_{\tilde{\chi}_1^0}h^2$ is computed using micrOMEGAs 2.0.7. 35

Table 4.1 Masses and parameters in GeV units for five benchmark Yukawa unified points using Isajet 7.75 and $m_t = 171.0$ GeV. The upper entry for the $\Omega_{\tilde{\chi}_1^0}h^2$ etc. come from IsaReD/Isatools, while the lower entry comes from micrOMEGAs; $\sigma(\tilde{\chi}_1^0 p)$ is computed with Isatools. 51

Table 4.2 Events generated and cross sections (in fb) for various signal and SM background processes before and after cuts. C1' and C1' + $\not{E}_T$ cuts are specified in the text. $W + n$ jets and $Z + n$ jets backgrounds have been computed within the restriction $p_T(W, Z) > 100$ GeV. 55

Table 4.3 Clean trilepton signal after cuts listed in the text. 62

Table 5.1 GUT scale input parameters, μ, higgsino component, $m_{\tilde{g}}$, $m_{\tilde{\chi}_1^0}$ and $\Omega_{\tilde{\chi}_1^0}h^2$ for the two selected FP benchmarks FP1 and FP2. $m_t = 172.5$. Spectra are calculated using SOFTSUSY 2.0.14 and $\Omega_{\tilde{\chi}_1^0}h^2$s are computed using micrOMEGAs 2.0.7. . . 74

Table 6.1 Important LHC parameters 81

Table 7.1 Spectra for selected G2, SO10 and FP benchmark points 98

Table 7.2 LO (NLO) cross sections for G2, SO10 and FP points computed using PROSPINO 2.0 99

Table 7.3 BRs computed with SUSYHIT for G2, SO10 and FP benchmarks 100

Table 7.4 Important mass differences for G2, SO10 and FP benchmark points 101

Table 7.5 Generated signal samples. The event weights are calculated according to PROSPINO LO cross sections 101

Table 7.6 CSA07 background samples used in the analysis 103

Table 7.7 First 10 unprescaled HLT paths with highest efficiency for each signal point 108

Table 7.8 PDJetMET HLT path selection efficiencies for all signals and backgrounds . 111

Table 7.9 Number of signal and total background events passing PDJetMET HLT paths along with HLT selection significances. 112

Table 7.10 Offline prototype selection paths characterized by $\not\!\!E_T$, jet multiplicity and $\not\!\!E_T/H_T$ requirements proposed as alternatives to be used during signal excess searches 117

Table 7.11 Selection results for all paths for signal and backgrounds after the offline selection. The numbers of events represent 100 pb^{-1} of integrated luminosity. . . 131

Table 7.12 Analysis flow for path 6 corresponding to $\mathcal{L}$ = 100 pb^{-1} for signals and backgrounds. Number of RAW events for backgrounds are estimated from cross sections (since no AllEvents datasets for the backgrounds are available). 132

Table 7.13 Selection results including the *b* trggers requirement for all paths for signal and backgrounds after the offline selection. The numbers of events represent 100 pb^{-1} of integrated luminosity. 135

Table 7.14 Background estimation results for different selection paths including *b* trigger requirement for $\mathcal{L}$ = 100 pb^{-1} using variables that optimize the estimation for all signals. 137

Table 7.15 Background estimation results using alternative variables for different selection paths given for $\mathcal{L}$ = 100 pb^{-1}. 140

Table 7.16 Statistical (first) and systematic (second) errors on signal and background events after cuts (including *b* triggers) for the six paths. Systematics consist of %5 JES uncertainty and %5 event averaged $\not\!\!E_T$ tail uncertainty. 147

Table A.1 Information on triggers that define PDJetMET - 1 161

Table A.2 Information on triggers that define PDJetMET - 2 162

Table B.1 Selection results for all paths for signal and backgrounds after the offline selection plus $A > 0.01$. The numbers of events represent 100 pb^{-1} of integrated luminosity. 164

Table B.2 Selection results including the b triggers requirement for all paths for signal and backgrounds after the offline selection plus $A > 0.01$. The numbers of events represent 100 pb^{-1} of integrated luminosity. 165

Table C.1 Information on lifetime *b* triggers 167

Table C.2 Information on soft muon *b* triggers 167

Table C.3 Information on L1 seeds for *b* triggers 167

LIST OF FIGURES

FIGURES

Figure 2.1 Upper bound from the relic denisty, $\Omega_{\tilde{\chi}_1^0}h^2 = 0.136$, on the $m_{1/2}$–m_0 plane for $\tan\beta = 10$, $A_0 = 0$, $\mu > 0$ and $m_t = 175$ GeV. The black, red, green and blue lines are for ISAJET, SOFTSUSY, SPHENO and SUSPECT respectively. Also shown is the corresponding $\delta\Omega_{\tilde{\chi}_1^0}h^2$. The yellow regions are excluded by LEP measurements or because of a stau LSP. 28

Figure 2.2 Higgs mass parameter μ (left) and top Yukawa coupling $y_t(M_{\rm SUSY})$ (right) as functions of m_0; the black, red, green and blue lines are for ISAJET, SOFTSUSY, SPHENO and SUSPECT respectively. 28

Figure 2.3 Pseudoscalar Higgs mass m_A (left) and bottom Yukawa coupling $y_b(M_{\rm SUSY})$ (right) as functions of $\tan\beta$ for $m_0 = 500$ GeV, $m_{1/2} = 300$ GeV, $A_0 = 0$, $\mu > 0$ and $m_t = 175$ GeV; the black, red, green and blue lines are for ISAJET, SOFTSUSY, SPHENO and SUSPECT respectively. 29

Figure 2.4 Upper bound from the relic denisty, $\Omega_{\tilde{\chi}_1^0}h^2 = 0.136$, on the $m_{1/2}$–m_0 plane for $\tan\beta = 50$ and $A_0 = 0$ (left) and $A_0 = -m_{1/2}$ (right). The black, red, green and blue lines are for ISAJET, SOFTSUSY, SPHENO and SUSPECT respectively. Also shown is the corresponding $\delta\Omega_{\tilde{\chi}_1^0}h^2$ in grey. The triangular yellow regions are excluded by stau LSP. 30

Figure 2.5 Light stop mass $m_{\tilde{t}_1}$ as a function of A_0 for $m_0 = 500$ GeV, $m_{1/2} = 300$ GeV, $\tan\beta = 10$, $\mu > 0$ and $m_t = 175$ GeV (left) and upper bound from the relic denisty, $\Omega_{\tilde{\chi}_1^0}h^2 = 0.136$, in the $m_{1/2}$–m_0 plane for $\tan\beta = 10$, $A_0 = -4m_{1/2}$, $\mu > 0$ and $m_t = 175$ GeV (right). The black, red, green and blue lines are for ISAJET, SOFTSUSY, SPHENO and SUSPECT respectively. Also shown are the corresponding $\delta\Omega_{\tilde{\chi}_1^0}h^2$ for SOFTSUSY, SPHENO and SUSPECT. The yellow regions are excluded because of a stau or stop LSP for the above 3 codes. The yellow line gives the $m_{\tilde{t}_1} = m_{\tilde{\chi}_1^0}$ boundary for ISAJET. 30

Figure 4.1 Yukawa-unified GSH points found by MCMC on the m_{10} vs. m_{16} (top left), A_0/m_{10} vs. m_{16} (top right), $m_{1/2}$ vs m_{16} (bottom left) and $m_{H_{u,d}}$ vs. m_{16} (bottom right) planes; the light-blue (dark-blue) points have $R < 1.1$ (1.05), while the orange (red) points have $R < 1.1$ (1.05) plus $\Omega_{\tilde{\chi}_1^0}h^2 < 0.136$. 43

Figure 4.2 Plot of MCMC scan points on the $m_A - 2m_{\tilde{\chi}_1^0}$ vs. $m_h - 2m_{\tilde{\chi}_1^0}$ plane with $R < 1.1$ (1.05) for dark-blue (light-blue) dots. We also show points with both $\Omega_{\tilde{\chi}_1^0}h^2 < 0.136$ and $R < 1.1$ (1.05) as orange (red) dots. 45

Figure 4.3 Plot of MCMC results for the GSH scenario on the $m_{\tilde{t}_1}$ vs. $m_{\tilde{g}}$ plane (left) and the m_h vs. $m_{\tilde{\chi}_2^0} - m_{\tilde{\chi}_1^0}$ plane (right); the light-blue (dark-blue) points have $R <$ 1.1 (1.05), while the orange (red) points have $R < 1.1$ (1.05) plus $\Omega_{\tilde{\chi}_1^0}h^2 < 0.136$. 46

Figure 4.4 Plot of MCMC scan points using WSH boundary conditions on the A_0/m_{16} vs. m_{16} plane (left) and $m_{1/2}$ vs. m_{16} plane (right) with $R < 1.1$ (1.05) for dark-blue (light-blue) dots. We also show points with both $\Omega_{\tilde{\chi}_1^0}h^2 < 0.136$ and $R < 1.1$ (1.05) as orange (red) dots. 46

Figure 4.5 Plot of MCMC scan points using WSH boundary conditions on the μ vs. m_A (top left), $m_A - 2m_{\tilde{\chi}_2^0}$ vs. $m_h - 2m_{\tilde{\chi}_2^0}$ plane (top right), $m_A - 2m_{\tilde{\chi}_2^0}$ vs. m_A (bottom left) and $BD(B_s - \mu\mu)$ (botttom right) planes with $R < 1.1$ (1.05) for dark-blue (light-blue) dots. We also show points with both $\Omega_{\tilde{\chi}_1^0}h^2 < 0.136$ and $R < 1.1$ (1.05) as orange (red) dots. 47

Figure 4.6 $\sigma(pp \to \tilde{g}\tilde{g})$ at $\sqrt{s} = 14$ TeV versus $m_{\tilde{g}}$ for $m_{\tilde{g}} = 350 - 500$ GeV using PROSPINO with scale $Q = m_{\tilde{g}}$. Solid (dashed) lines show LO (NLO) values. Red (lower) lines have 10 TeV squarks (SO10A-like) and blue (upper) lines have 3 TeV squarks (SO10D-like). 52

Figure 4.7 Various $\sigma(pp \to \tilde{\chi}\tilde{\chi})$ at $\sqrt{s} = 14$ TeV versus $m_{\tilde{\chi}_1^\pm}$ for $m_{\tilde{q}} = 3$ TeV and $\mu = m_{\tilde{g}}$ with $\tan\beta = 49$ and $\mu > 0$ (Plot by H. Summy). 53

Figure 4.8 Dilepton invariant mass distribution for SFOS leptons after cuts C1' for SO10A (red, solid) and SO10D (blue, dashed) (Plot by H. Summy). 56

Figure 4.9 Parton level $m(bb)$ distributions with PYTHIA for SO10A using bb pairs coming from $\tilde{g} \to bb\tilde{\chi}$ (shaded), $\tilde{g} \to bb\tilde{\chi}_1^0$ (black), $\tilde{g} \to bb\tilde{\chi}_2^0$ (red) and $\tilde{g} \to bb\tilde{\chi}_2^0 \to bbll\tilde{\chi}_1^0$ (blue) decay modes. 57

Figure 4.10 Combinations of all $X_1(bb)-X_2(bb)$s. Selection variables for right $X_1(b\bar{b})-X_2(b\bar{b})$ (red), wrong $X_1(b\bar{b})-X_2(b\bar{b})$ (green) and wrong $X_1(bb)-X_2(\overline{bb})$ (blue). . 58

Figure 4.11 $m(bb)$s for both pairs in the X_1-X_2 combination determined according to different selections. Black curves respectively for: $\Delta\phi(X_1-X_2)^{max}$, $\Delta R(X_1-X_2)^{max}$, $\Delta p_T(X_1-X_2)^{min}$, avg $(p_T(X_1)-p_T(X_2))^{max}$, $\Delta m(X_1-X_2)^{min}$, avg $(m(X_1-m(X_2))^{min}$. The different color fills under the black curves show the components from right and wrong distributions for the selected pair: light red/brown component from right $b\bar{b}$, green component from wrong $b\bar{b}$ and blue-gray component from wrong $bb/\overline{bb}$. The red curve shows the total right $b\bar{b}$ distribution, green curve shows the total wrong $b\bar{b}$ distribution and the blue curve shows the wrong $bb/\overline{bb}$ distribution. The yellow curve shows the case of inverse selection: $\Delta\phi(X_1-X_2)^{min}$, $\Delta R(X_1-X_2)^{min}$, $\Delta p_T(X_1-X_2)^{max}$, avg $(p_T(X_1)-p_T(X_2))^{min}$, $\Delta m(X_1-X_2)^{max}$, avg $(m(X_1-m(X_2))^{max}$. This shows that even when one selects a wrong combination with a certain requirement, that wrong combination does not generally have an invariant mass which spoils the distribution. The combinations with spoiler masses are generally those combinations made by inverse selections. 59

Figure 4.12 Plot of $m(X_{1,2}\ell^+\ell^-)_{min}$ from SO10A (red, solid) and SO10D (blue, dashed), minimizing $\Delta m(X_1-X_2)$ as explained in the text, along with SM backgrounds (Plot by H. Summy). 60

Figure 4.13 Plot of $m(X_{1,2}\ell^+\ell^-)_{min}$ from SO10A (red, solid) and SO10D (blue, dashed), minimizing $\Delta m(X_1-X_2)$ as explained in the text, along with SM backgrounds (Plot by H. Summy). 60

Figure 4.14 Plot of y_t, y_b and y_τ evolution from the weak scale to the GUT scale for SO10A (red, solid) and SO10D (blue, dashed). The large jumps around 3 TeV correspond to the MSSM threshold corrections. 63

Figure 4.15 Efficiency of finding RGE solutions as explained in the text (left) and R values (right) on input GUT scale parameter planes, obtained by varying the input parameters of SO10A randomly in a uniform distribution of %10 around the central values. R ranges shown are $1 \leq R \leq 1.01$ (red), $1.01 < R \leq 1.05$ (yellow), $1.05 < R \leq 1.1$ (green), $1.1 < R \leq 1.15$ (light blue), $1.15 < R \leq 1.20$ (blue) and $1.20 < R$ (purple). Black dot marks the position of SO10A. 64

Figure 4.16 Efficiency of finding RGE solutions as explained in the text (left) and R values (right) on input GUT scale parameter planes, obtained by varying the input parameters of SO10D randomly in a uniform distribution of %10 around the central values. R ranges shown are $1 \leq R \leq 1.01$ (red), $1.01 < R \leq 1.05$ (yellow), $1.05 < R \leq 1.1$ (green), $1.1 < R \leq 1.15$ (light blue), $1.15 < R \leq 1.20$ (blue) and $1.20 < R$ (purple). Black dot marks the position of SO10D. 65

Figure 4.17 Plot of locus in the T_R vs. $m_{\tilde{a}}$ plane of four Yukawa-unified cases of mixed axion/axino dark matter, along with four different m_{16} values. Purple (small), dark blue (medium), blue (large) and light blue (very large) dots show solutions with $m_{16} = 5, 8, 10, 15$ TeV. The thermally produced axino relic density calculation is only valid for $T_R \gtrsim 10^4$ GeV. Non-thermal leptogenesis prefers the region with $T_R \gtrsim 10^6$ GeV. The black, vertical lines intersecting C1 and C2 show the axino mass limit $m_{\tilde{a}} = 10^{-4}$ GeV below which axinos constitute warm dark matter. . . . 70

Figure 5.1 Focus point solutions found by MCMC scans using SOFTSUSY 2.0.14 + micrOMEGAs 2.0.7 on the $m_{1/2}$ vs. m_0 (top left), A_0 vs. m_0 (top right), $\tan\beta$ vs. m_0 (bottom left) and $m_{\tilde{\chi}_1^0}$ vs. m_0 (bottom right) planes. Different colors represent diferent gluino masses: $m_{\tilde{g}} \leq 500$ (red), $500 < m_{\tilde{g}} \leq 550$ (orange), $550 < m_{\tilde{g}} \leq 600$ (yellow), $600 < m_{\tilde{g}} \leq 650$ (green), $650 < m_{\tilde{g}} \leq 700$ (light blue), $700 < m_{\tilde{g}} \leq 750$ (blue) and $750 m_{\tilde{g}} \leq 800$ (purple). 73

Figure 5.2 Focus point solutions found by MCMC scans using SOFTSUSY 2.0.14 + micrOMEGAs 2.0.7 on the μ vs. m_0 (left) and higgsino content vs. μ (right) planes. Different colors represent diferent gluino masses: $m_{\tilde{g}} \leq 500$ (red), $500 < m_{\tilde{g}} \leq 550$ (orange), $550 < m_{\tilde{g}} \leq 600$ (yellow), $600 < m_{\tilde{g}} \leq 650$ (green), $650 < m_{\tilde{g}} \leq 700$ (light blue), $700 < m_{\tilde{g}} \leq 750$ (blue) and $750 m_{\tilde{g}} \leq 800$ (purple). 74

Figure 5.3 Efficiency of finding RGE solutions (left) and values of $\Omega_{\tilde{\chi}_1^0} h^2$ (right) on input GUT scale parameter planes, obtained by varying the input parameters of FP1 randomly in a uniform distribution of %10 around the central values. Different relic density ranges shown are: $\Omega_{\chi^1} h^2 \leq 0.001$ (red), $0.001 < \Omega_{\chi^1} h^2 \leq 0.094$ (yellow), $0.094 < \Omega_{\chi^1} h^2 \leq 0.136$: WMAP range (green), $0.136 < \Omega_{\chi^1} h^2 \leq 1$ (blue), $1 < \Omega_{\chi^1} h^2 \leq 10$ (purple) and $10 < \Omega_{\chi^1} h^2 \leq 100$ (pink). The black dot marks the position of FP1. 76

Figure 5.4 Efficiency of finding RGE solutions (left) and values of $\Omega_{\tilde{\chi}_1^0}h^2$ (right) on input GUT scale parameter planes, obtained by varying the input parameters of FP2 randomly in a uniform distribution of %10 around the central values. Different relic density ranges shown are: $\Omega_{\chi^1}h^2 \leq 0.001$ (red), $0.001 < \Omega_{\chi^1}h^2 \leq 0.094$ (yellow), $0.094 < \Omega_{\chi^1}h^2 \leq 0.136$: WMAP range (green), $0.136 < \Omega_{\chi^1}h^2 \leq 1$ (blue) and $1 < \Omega_{\chi^1}h^2 \leq 10$ (purple). The black dot marks the position of FP2. . . 77

Figure 6.1 Large Hadron Collider and its experiments. Figure shows the cooldown status on 12 November 2008 [91] 80

Figure 6.2 Schematic view of the Compact Muon Solenoid detector. 83

Figure 6.3 Layout of the pixel detector. 84

Figure 6.4 Schematic description of CMS muon system. 91

Figure 6.5 Production cross sections for various processes at hadron colliders (pp and $p\bar{p}$) as a function of c.o.m. energy. Discontinuities in some curves are due to transition from $p\bar{p}$ to pp collisions [98]. 93

Figure 7.1 The leading order processes contributing to $pp \to \tilde{g}\tilde{g}$ production. a) gluon-gluon initial states, b) quark-antiquark initial states 96

Figure 7.2 Reconstruction efficiency (# of matched GEN jets / total # of GEN jets) distribution in p_T and η for the signals. Comparison between iterative cone $R = 0.5$ and SIScone $R = 0.5$ algorithms are also shown 104

Figure 7.3 Purity (# of matched reconstructed jets / total # of reconstructed jets) distribution in p_T and η for the signals. Comparison between iterative cone $R = 0.5$ and SIScone $R = 0.5$ algorithms are also shown. 105

Figure 7.4 1st jet p_T (left) and jet multiplicity (right) for jets having $p_T > 30$ GeV and $|\eta| < 3$. Comparison of iterative cone $\Delta R = 0.5$ and SIScone $\Delta R = 0.5$ calojets. . 106

Figure 7.5 IC5 jet p_T^{REC}/p_T^{GEN} distribution versus p_T^{GEN} (top left), IC5 jet resolution versus p_T^{GEN} (top right) and η^{GEN} (bottom left) for the signals G24, SO10A and FP1. Also shown is the comparison of jet resolution curves versus p_T^{GEN} among jets having $|\eta| \leq 1.4$ and $1.4 < |\eta| < 3$ (bottom right). 107

Figure 7.6 $\not\!\!E_T^{REC}/\not\!\!E_T^{GEN}$ distribution (left) and $\not\!\!E_T$ resolution (right) versus $\not\!\!E_T^{GEN}$ for the signals G24, SO10A and FP1. 107

Figure 7.7 HLT efficiency curves for SO10A for $p_T(j_1)$ and $p_T(j_2)$ (top left), $\not\!\!E_T$ (top right), $d\phi(j_1 - j_2)$ (bottom left) and $d\phi(j_1 - \not\!\!E_T)$ (bottom right) after applying the acoplanarity trio requirement. 113

Figure 7.8 $\not\!\!E_T$ (left) and jet multiplicity (right) distributions after HLT selection (1st row) for signals and backgrounds. Also shown are the S/B ratio (2nd row) and Punzi significance (3rd row) calculated assuming that a cut was put at the value seen on the x-axis. 115

Figure 7.9 Jet multiplicity distributions after the $\not\!\!E_T$ cut (step 1). Shown for path 1: $\not\!\!E_T > 200$ (left) and paths 4 and 5: $\not\!\!E_T > 100$ (right). 116

Figure 7.10 1st (left) and 2nd (right) jet p_T distributions after the jet multiplicity cut (step 2). Shown for path 5: $\not\!\!E_T > 100$, $n_{jets} \geq 5$. 117

Figure 7.11 $\not\!\!E_T$/HT distributions after the jet multiplicity cut (step 2). Shown for path 3: $\not\!\!E_T > 0$, $n_{jets} \geq 5$ (left) and path 5: $\not\!\!E_T > 100$, $n_{jets} \geq 5$ (right). 118

Figure 7.12 P_{trkIso} distributions after the $\not\!\!E_T/H_T$ cut (step 3). Shown for path 6. 120

Figure 7.13 2nd jet EMF vs 1st jet EMF after the leading track isolation cut (step 4). Shown for path 5 for SO10A (top left), QCD (top right), $W + n$ jets (bottom left) and $t\bar{t} + n$ jets (bottom right). Solid lines show the strict cuts while dashed lines show the cuts with an OR. 121

Figure 7.14 Event EMF after the jet EMF cuts (step 5). Shown for path 5 (left) and path 6 (right). 122

Figure 7.15 $d\phi(\not\!\!E_T - \not\!\!H_T)$ after the event EMF cut (step 6). Shown for path 4 (left) and path 6 (right). 123

Figure 7.16 $d\phi(j_2 - \not\!\!E_T)$ vs $d\phi(j_1 - \not\!\!E_T)$ (top) and R2 vs R1 (bottom) after the $d\phi(\not\!\!E_T - \not\!\!H_T)$ cut (step 7). Shown for path 6 for SO10A (left) and total BG (right). 124

Figure 7.17 $d\phi(j_3 - \not\!\!E_T)$ vs $d\phi(j_2 - \not\!\!E_T)$ (top) and R_a2 vs R_a1 (bottom) after the R2 cut (step 8). Shown for path 5 for SO10A (left) and total BG (right). 125

Figure 7.18 $d\phi(j_2 - \not\!\!E_T)$ distribution after R_a1 cut (step 9). Shown for path 4 (left) and path 6 (right). 126

Figure 7.19 $d\phi(j_1 - \not\!\!E_T)_{min}$ distribution shown after $d\phi(j_2 - \not\!\!E_T)$ cut (step 10). Shown for path 4 (left) and path 6 (right). 127

Figure 7.20 1st jet η distribution after $d\phi(j_1 - \not{E}_T)$ cut (step 11). Shown for path 3 (left) and path 6 (right). 127

Figure 7.21 H_{20} (top) after the $j_1|\eta|$ cut (step 12). Shown for path 3 (left) and path 6 (right). H_{30} for path 3 (bottom left) and H_{40} (bottom right), again after the $j_1|\eta|$ cut. 129

Figure 7.22 b tag discriminators from jet probability algorithm shown after the Fox-Wolfram cuts (step 13, the final cut). 2nd jet discriminator (left) and event discriminator (right). Shown for path 6. 133

Figure 7.23 1st jet $|\eta|$ vs $d\phi(j - \not{E}_T)_{min}$ for SO10A (left) and total background (right) for path 6 with b triggers, excluding the cuts on d$\phi(j - \not{E}_T)_{min}$ and 1st jet η. A, B, C, D regions are shown. 141

Figure 7.24 $d\phi(j - \not{E}_T)_{min}$ distribution in different 1st jet $|\eta|$ bins: $0 < |\eta| < 0.42$ (top left), $0.42 < |\eta| < 0.85$ (top right), $0.85 < |\eta| < 1.7$ (bottom left), $1.7 < |\eta| < 3$ (bottom right. Shown for path 5 + b triggers, excluding the cuts on d$\phi(j - \not{E}_T)_{min}$ and 1st jet η. 141

Figure 7.25 $(d\phi(j - \not{E}_T)_{min} > 0.3)/(d\phi(j - \not{E}_T)_{min} < 0.3)$ ratio versus 1st jet $|\eta|$ for true background and $S + B$ for all signals. Shown for path 6 + b triggers excluding the cuts on d$\phi(j - \not{E}_T)_{min}$ and 1st jet η, with $\mathcal{L} = 1$ fb^{-1}. 142

Figure 7.26 Distributions of $S + B$, true background and estimated background versus 1st jet $|\eta|$ for all six signal benchmarks. where estimation for G2s, SO10s and FPs are made using different variables and for different paths. For G2s $\not{E}_T$ was used on path 2 without b triggers, for SO10s $d\phi(j - \not{E}_T)_{min}$ was used on path 6 including b triggers and for FPs $\not{E}_T$ was used on path 6 including b triggers and aplanarity. . 143

Figure 7.27 Effect of event-averaged jet over and undermeasurements on the $\not{E}_T$ tails calculated as described in the text for QCD (left) and SO10A(right). Results shown for $\delta = 5, 10, 15$. 145

Figure 7.28 Signal signiicance $S/\sqrt{S + B}$ corresponding to an integrated luminosity of 100 pb^{-1} versus gluino mass, showing all the signals for all paths including significance errors whose calculation was described in the text. Also shown are the results for fits to the function $y = a/x^b$. 148

Figure 7.29 Integrated luminosity required for a 5σ signiicance versus gluino mass, showing signals for all paths including luminosity errors whose calculation was described in the text. G21 is not shown for low $\not{E}_T$ paths due to its extreme errors. Also shown are the results for fits to the function $y = ax^b$. 149

Figure B.1 Aplanarity distribution after the Fox-Wolfram cuts (step 13, the final cut). Shown for path 3 (left) and path 6 (right). 166

CHAPTER 1

INTRODUCTION: QUEST FOR A NEW THEORY

"There is a theory which states that if ever anybody discovers exactly what the Universe is for and why it is here, it will instantly disappear and be replaced by something even more bizarre and inexplicable. There is another theory which states that this has already happened."

–Douglas Adams, from Hitchiker's Guide to the Galaxy

Throughout the past decades, predictions of the Standard Model (SM) [1], [2], [3] have been tested strictly by various experimental means, and they have survived these tests with dignity. All particles proposed by the SM (except Higgs) were discovered and their interactions were thoroughly examined.

One main quantitative test of the QCD theory arises from the measurement of the strong coupling $\alpha_s(Q^2)$, for which most precise results come from LEP measurements of inclusive Z decays, inclusive hadronic τ decays and event shapes as well as from scaling violations in Deep Inelastic Scattering (DIS). DIS measurements also provide information on parton distribution functions (PDFs) which are used while computing cross sections of hard pp processes at hadron colliders. The predictions for such cross sections and distributions of outcoming large p_T jets and photons are in good agreement with experiment.

In the electroweak (EW) sector, stringent tests were performed by combining measurements from different experiments and then fitting the results to the SM theory predictions. Precision fits to the LEP and SLC Z pole measurements such as cross sections, masses and various couplings of the heavy EW gauge bosons show that there is no significant deviation from the SM theory expectations provided the contributions from radiative corrections are taken into account [4]. SM is further tested by predicting the masses of heavy fundamental particles, such as the top quark and EW gauge bosons, and comparing the fitted values with the direct mass measurements, and again was found to be consistent.

Nature of flavor physics in the quark sector has been investigated by frontier experiments

at the accelerators and B factories. Their current results show that B mixing and CP violation agree very well with SM predictions based on the CKM matrix [5]. There also exist measurements such as $BR(b \to s\gamma)$ which might signal discrepencies from the SM large enough to accommodate contributions from new physics. But turning to the leptonic sector of flavor physics confronts us with the first strong hint pointing out to the existence of a theory beyond the SM (BSM) [6]. Both solar and atmospheric neutrino observations among with long baseline neutrino experiments show evidence of neutrino oscillations, which require neutrinos to have small masses of the order of eV. SM does not provide a unique explanation for neutrino masses and one has to seek formulations beyond the SM to naturally accommodate candidate solutions such as the see-saw mechanism. The unknown origin of the different quark or charged lepton masses in different generations also constitutes a puzzle.

Another phenomenological requirement is an explanation for the dark matter and dark energy. Measurements on the rotational curves of galaxies and examination of fluctuations in the spectrum of the cosmic microwave background provide strong evidence for dark matter while recent observations on the Bullet Cluster point out that dark matter constitutes of particles. Meanwhile, observations on both type 1a supernovae and cosmic microwave background fluctuations suggest that the Universe is accelerating and this is caused by dark energy, which is a novel form of energy density exerting negative pressure on spacetime. Two leading models to explain dark energy are the cosmological constant and quintessence. Standard Model is rather silent when confronted with such dark questions. It can not provide a neutral, massive dark matter candidate whose relic density would be compatible with measurements and its attempts to explain dark energy through vacuum energy fluctuations fail since the cosmological constant calculated from vacuum energy is 120 orders higher than the measured dark energy density. A further cosmology-related issue to address is that CP violation generated in the SM EW sector cannot account for the baryon assymmetry in the Universe.

It is obvious that the SM is incomplete and that a more comprehensive theory is required. At this point, one can actually get hints from the conceptual/theoretical defficiencies of the SM to shape the nature of this more fundamental theory. To fill in the missing parts of SM, the candidate theory should be able to clarify issues such as origin of mass and origin of flavor, which the SM can explain only via choices of arbitrary introduction of scalar fields or extra free parameters. The ultimate theory should also reconcile general relativity with quantum mechanics, thus unifying gravitation with the other three interactions.

Before aiming at ultimate unification, one still needs to clear the problems with Grand

Unification. Aesthetic interests motivate physicists to think that the Standard Model gauge group $SU(3)_C \times SU(2)_L \times U(1)_Y$, as a direct product of three different groups is not elegant enough and should rather be considered as a subgroup of a more generic single group. The consequences of the new theory related to this generic group would manifest themselves at the Grand Unification Theory (GUT) scale and beyond. For this assumption to be true, the couplings associated with the three gauge groups must unify at a single value at the GUT scale. This was tested by taking the LEP measurements of the couplings and running them up to the GUT scale using the SM renormalization group equations. This test showed that unification was found to be excluded with more than 8 standard deviations. This concludes that in case Grand Unification is imposed, the SM has to be modified somewhere between the EW and GUT scales.

So, at which scale could this modification occur? A rather constraining prediction is offered by the Hierarchy Problem and its consequences. Here the hierarchy refers to the orders of magnitude between the Planck and the EW scales (or Newton and Fermi constants). Current structure of the SM has no natural explanation for the hierarchy. But the more severe problem arises when the self energy corrections to the Higgs mass are considered. Higgs field that couples to fermions with mass m_F as $\sim \lambda_f H \bar{f} f$ receives a correction

$$\delta m_{h|F}^2 \simeq \frac{-|\lambda_F|^2}{16\pi^2}\Lambda^2 + O(m_F^2 \ln(\Lambda/m_F)) + ... \tag{1.1}$$

where Λ is the cut-off scale up to which the SM is valid. If $\Lambda \sim M_{Pl}$, correction becomes $\sim$ 30 orders of magnitude larger than the expected physical Higgs mass of $\sim$ 100 GeV. The correction can be cancelled by setting the tree level Higgs mass to a similarly large value, but this would result in an extreme fine tuning of the values, which is principally disfavored. For the correction to not exceed the physical Higgs mass, Λ must be around 1 TeV. Hence, a new theory is expected to reveal itself close to the TeV scale.

Over the years, scientific imagination has introduced many candidate theoretical models to address the above puzzles, but none has been yet justified. In this study, we will focus on "supersymmetry", a much appreciated theoretical framework that offers natural solutions to most of the above questions.

In essence, supersymmetry relates fermionic and bosonic degrees of freedom via fermionic spacetime transformations. In its simplest realization, it doubles the number of currently known particles, predicting a new boson for every SM fermion and a new fermion for every SM boson. However present experimental observations did not yet meet the traces of these

new particles, which leads to the conclusion that supersymmetry must be a broken symmetry and the supersymmetric particles (sparticles) must be heavier than their SM counterparts.

But how heavy can the sparticles be? The answer depends on the mechanism of supersymmetry breaking. So far various mechanisms have been proposed, each of which is characterized by a distinct phenomenology that emerges from the resulting specialized regions of the vast supersymmetry parameter space. But the variaty of choices renders the decision difficult, and the difficulty is enhanced by the lack of a robust experimental clue.

At this point we trace hints of favored scenarios in the theoretical claims which can be considered as indirect requirements, and we seek the guidance of phenomenological consequences. A well-motivated starting point could be the quest for a unified theory. Frameworks of varying scope have been proposed as candidate scenarios, whose degrees of generality are marked by the energy scale in which they are realized.

In this thesis, we make a journey from the Planck scale to the GUT scale, from the utterly fundamental to the more modest and applicable, and consider three theoretical frameworks on our way that consequently lead to a similar phenomenology: A low energy supersymmetry featuring (very) heavy scalars with masses $\gtrsim$ 2 TeV and light gauginos with masses $\mathcal{O}(100)$ GeV. The first stop is close to the Planck scale, where according to some thought strings might dwell. We first present a string scenario defined through fluxless compactification of M theory on a G_2 manifold, which gives a consistent low energy effective supersymmetric theory called G_2-MSSM. Next we approach the GUT scale and examine the case of a simple supersymmetric GUT ruled by the SO(10) gauge group which binds all matter fields in a single representation, the Higgs doublets in another single representation and unifies Yukawa couplings at the GUT scale. The final destination is a simple supergravity with universal masses called the focus point scenario which is less concerned about the high fundamental questions but prefers to make a more practical contribution via offering solutions robustly consistent with naturalness. Of course, all along this journey we will pay our respects to cosmology and always take into account the question of dark matter. We will aim to make sure that the supersymmetry scenarios of our interest are capable of providing a cosmologically consistent dark matter candidate. All this will prepare us for the Final Act in which we will take the challange of tracing these scenarios on the stage of LHC at 14 TeV, making the Compact Muon Solenoid detector our tool, and see how discoverable they are in the all inclusive jets plus missing transverse energy channel.

...

The manuscript is organized as follows: After describing supersymmetry as it is in Chapter 2, phenomenologies of G_2-MSSM, SO(10) SUSY GUT and focus point mSUGRA will be presented respectively in Chapters 3, 4 and 5. A technical interlude on the Large Hadron Collider and the Compact Muon Solenoid detector will follow in Chapter 6. Chapter 7 then will present the CMS discovery analysis of these scenarios, which will be followed by the conclusions.

CHAPTER 2

SUPERSYMMETRY

"Theory helps us bear our ignorance of facts."
–George Santayana, from The Sense of Beauty

2.1 Introducing supersymmetry

By definition supersymmetry (SUSY) is a fermionic spacetime symmetry which proposes that every existing fermionic field has a bosonic partner and vice versa. This symmetry is generated by supersymmetric transformations which are distinguished from the other transformations on the basis that they convert particles with different spins into each other such as

$$Q\,|\text{fermion}\rangle = |\text{boson}\rangle \qquad Q\,|\text{boson}\rangle = |\text{fermion}\rangle \tag{2.1}$$

where Q is the generator of transformations.

The outcome of this concept has immediate consequences on the quadratic divergency problem in Higgs mass corrections. For example, a heavy complex scalar particle S with mass m_S coupling to Higgs as $-\lambda_S |H|^2 |S|^2$ results in a Higgs mass correction

$$\delta m^2_{h|S} \simeq \frac{|\lambda_B|^2}{16\pi^2}(\Lambda^2 - 2m_S^2\, ln(\Lambda/m_S) + ...). \tag{2.2}$$

Since contributions from bosonic and fermionic loops would have opposite signs, having an equal number of fermionic and bosonic degrees of freedom cancels the quadratic terms and reduces the 1-loop correction to

$$\delta m^2_H \simeq O(m^2_{boson} - m^2_{fermion}). \tag{2.3}$$

A correction of the order of physical Higgs mass requires $|m^2_{boson} - m^2_{fermion}| \sim$ TeV.

However the idea of supersymmetry did not originate from the motivation to solve the quadratic divergency problem. It was proposed as an independent mathematical framework

that resulted from the numerous attempts in 60s to combine internal symmetries with external Lorentz symmetries. Coleman and Mandula showed in 1967 that no non-trivial combination of internal and external symmetries can be achieved by using only bosonic charges [7]. On the other hand, in 1968 Zeldovich suggested a symmetry between fermions and bosons while addressing the problem of vacuum energy. This was an independent request from the cosmology side [8]. Then in 1971, Golfard and Likhtman developed the first non-trivial extension of the Poincare algebra with fermionic charges [9]. About the same time Neveu and Schwarz [10] and Ramond [11] came up with supersymmetric string theories as they were trying to make fermionic string theories that could accommodate baryons. The fundamental formalisms started to develop when in 1973-74 Wess and Zumino started to write renormalizable four-dimensionl supersymmetric field theories to describe mesons and baryons [12],[13],[14]. Later, together with Iliopulos and Ferrera they showed that quadratic and other divergences that arise in conventional field theories were absent in supersymmetry [15],[16]. Physical applications were afterwards motivated by the discovery of local supersymmetry which unifies the graviton with the other particles [17],[18].

There exist extensive reviews of supersymmetry in the literature. We would refer to [19], [20],[21],[22],[23],[24] as comprehensive introductions.

In the following we will shortly examine the Wess-Zumino model to illustrate the theoretical construction of supersymmetry. Suppose we have a Lagrangian

$$\mathcal{L} = \mathcal{L}_{kin} + \mathcal{L}_{mass} \tag{2.4}$$

with kinetic and mass terms given as

$$\mathcal{L}_{kin} = \frac{1}{2}(\partial_\mu A)^2 + \frac{1}{2}(\partial_\mu B)^2 + \frac{1}{2}\bar{\psi}\partial\!\!\!/\psi + \frac{1}{2}(F^2 + G^2) \tag{2.5}$$

$$\mathcal{L}_{mass} = -m\frac{1}{2}\bar{\psi}\psi - GA - FB). \tag{2.6}$$

Here A, B, F and G are pseudoscalar fields and ψ is a 4-component Majorana spinor. F and G are auxillary fields, whose equations of motion $F = -mB$ and $G = -mA$ can be used to eliminate them from the Lagrangian, which then becomes

$$\mathcal{L} = \frac{1}{2}(\partial_\mu A)^2 + \frac{1}{2}(\partial_\mu B)^2 + \frac{1}{2}\bar{\psi}\partial\!\!\!/\psi - \frac{1}{2}(A^2 + B^2) - \frac{1}{2}m\bar{\psi}\psi. \tag{2.7}$$

Wess and Zumino found that the following transformations change the Lagrangian only by a

total derivative, hence leaving the theory invariant:

$$\begin{aligned}
\delta A &= i\bar{\alpha}\gamma_5\psi \\
\delta B &= -\bar{\alpha}\psi \\
\delta\psi &= -F\alpha + iG\gamma_5\alpha + \partial\!\!\!/\gamma_5 A\alpha + i\partial\!\!\!/ B\alpha \\
\delta F &= i\bar{\alpha}\partial\!\!\!/\psi \\
\delta G &= \bar{\alpha}\gamma_5\partial\!\!\!/\psi. \qquad (2.8)
\end{aligned}$$

Here α is a spacetime-independent Majorana spinor. Such linear transformations between fermions and bosons are called supersymmetric transformations. One can equivalently write the Lagrangian in terms of fields

$$S = \frac{1}{\sqrt{2}}(A + iB), \quad \psi_L = \frac{1-\gamma_5}{2}\psi, \quad \mathcal{F} = \frac{1}{2}(F + iG) \qquad (2.9)$$

which transform under the SUSY transformations respectively like

$$\delta S = i\sqrt{2}\tilde{\alpha}\psi_L \qquad (2.10)$$

$$\delta\psi_L = -\sqrt{2}\mathcal{F}\alpha_L + \sqrt{2}\partial\!\!\!/ S\,\alpha_R \qquad (2.11)$$

$$\delta\mathcal{F} = i\sqrt{2}\tilde{\alpha}\partial\!\!\!/\psi_L. \qquad (2.12)$$

In general, infinitesimal SUSY transformations will change a field S as

$$S \to S' = e^{i\bar{\alpha}Q} S\, e^{-i\bar{\alpha}Q} \approx S + [i\bar{\alpha}Q, S] = S + \delta S \equiv (1 - i\bar{\alpha}Q)S \qquad (2.13)$$

where Q is the Majorana spinor generator of the SUSY transformations. To derive an algebra for the SUSY generators, commutator of two consequetive transformations can be applied to the complex scalar field S, which gives

$$(\delta_2\delta_1 - \delta_1\delta_2)S = -2i\bar{\alpha}_2\gamma^\mu\alpha_1[P^\mu, S] \qquad (2.14)$$

where P_μ is the Poincare group generator of spacetime translations. Same commutator can alternatively be calculated using $\delta S = [i\tilde{\alpha}Q, S]$, which gives

$$(\delta_2\delta_1 - \delta_1\delta_2)S = -\bar{\alpha}_{2a}\alpha_{1b}[[Q_a, \bar{Q}_b], S]. \qquad (2.15)$$

Equating the right hand sides of Eq. 2.14 and Eq. 2.15 results in the following relation:

$$\left\{Q_a, \bar{Q}_b\right\} = 2(\gamma^\mu)_{ab}P_\mu \qquad (2.16)$$

showing the distinct mark of SUSY as a spacetime symmetry. Moreover conservation of SUSY implies

$$\{Q_a, P^\mu\} = 0. \tag{2.17}$$

The Wess-Zumino model can be enriched by adding the following interaction terms:

$$\mathcal{L}_{int} = -\frac{g}{\sqrt{2}} A\bar{\psi}\psi + \frac{ig}{\sqrt{2}} B\bar{\psi}\gamma_5\psi + \frac{g}{\sqrt{2}}(A^2 - B^2)G + g\sqrt{2}ABF. \tag{2.18}$$

Auxillary fields F and G can again be eliminated by replacing them with their equations of motion $F = -mB - g\sqrt{2}AB$ and $G = -mA - \frac{g}{\sqrt{2}}(A^2 - B^2)$. This leads to a total Lagrangian in terms of the dynamical fields

$$\begin{aligned}\mathcal{L} \;=\; & \frac{1}{2}(\partial_\mu A)^2 + \frac{1}{2}(\partial_\mu B)^2 + \frac{1}{2}\bar{\psi}\partial\!\!\!/\psi - \frac{1}{2}(A^2 + B^2) - \frac{1}{2}m\bar{\psi}\psi \\ & -\frac{g}{\sqrt{2}} A\bar{\psi}\psi + \frac{ig}{\sqrt{2}} B\bar{\psi}\gamma_5\psi - gm\sqrt{2}AB^2 - \frac{gm}{\sqrt{2}}A(A^2 - B^2) \\ & -g^2A^2B^2 - \frac{1}{4}g^2(A^2 - B^2)^2.\end{aligned} \tag{2.19}$$

This Lagrangian shows the interactions of two scalars with a Majorana spinor as well as the trilinear and quartic interactions of the scalars. It displays the important feature of having a single mass parameter m for all fields and having the same coupling g for all interactions. Overall, this toy example illustrates the main principle of SUSY which is applicable to specific cases.

In a most generic case, the possible number of SUSY generators is $N \leq S$ where S is the maximal spin in the theory. Theories with $S > 1$ are non-renormalizable and theories with $S > 5/2$ do not couple to gravity, therefore one can have $N \leq 4$ for a renormalizable theory and $N \leq 8$ for SUSY unified with gravity (supergravity). However models with $N > 1$ do not lead to a low energy theory with chiral fermions and hence cannot explain the real world. A SUSY model to explain fundamental particles needs to have a single charge. The simplest such model which is the direct extension of the SM formed by adding only the complementary fields to the existing SM fields is called the Minimal Supersymmetric Standard Model (MSSM), the which we will consider in the following.

2.2 Superfields

To accomodate the fermionic and bosonic degrees of freedom within the same framework, the idea of superspace has been conceptualized. A superspace is the extended version of an

Euclidean space with Grassmannian coordinates, such that

$$x^\mu \rightarrow (x^\mu, \theta, \bar{\theta}). \tag{2.20}$$

The supertranslations conducted by the now extended group element $G(x, \theta, \bar{\theta}) = e^{i(-x^\mu P_\mu + \theta Q + \bar{\theta}\bar{Q}}$ will lead to the following supertranslations

$$x_\mu = x_\mu + i\theta\sigma_\mu\bar{\epsilon} + i\epsilon\sigma_\mu\bar{\theta} \tag{2.21}$$

$$\theta = \theta + \epsilon \tag{2.22}$$

$$\bar{\theta} = \bar{\theta} + \epsilon \tag{2.23}$$

where ϵ and $\bar{\epsilon}$ are Grassmannian transformation parameters. The supercharges can then be expressed as

$$Q_\alpha = \frac{\partial}{\partial\theta^\alpha} - i\sigma^\mu_{\alpha\dot{\alpha}}\bar{\theta}^{\dot{\alpha}}\partial_\mu, \quad \bar{Q}_\alpha = -\frac{\partial}{\partial\theta^{\dot{\alpha}}} - i\theta^\alpha\sigma^\mu_{\alpha\dot{\alpha}}\partial_\mu \tag{2.24}$$

A superfield then is a function $\Phi(x_\mu, \theta, \bar{\theta})$ of the superspace coordinates. The superfield can be expanded in powers of θ, $\bar{\theta}$, where the coefficients give the 4-dimensional fields which will then determine the particle content. However due to the anticommuting nature of Grassmanian variables, series will be finite, terminating at the quartic term. This feature distinguishes SUSY from the Kaluza-Klein models. Expansion in terms of $\bar{\theta}\gamma_5$, $\bar{\theta}\theta$, $\bar{\theta}\gamma_5\theta$, $\bar{\theta}\gamma_\mu\gamma_5\theta$, $\bar{\theta}\gamma_5\tilde{\theta}\theta$ and $(\bar{\theta}\gamma_5\theta)^2$ would manifestly show the Lorentz properties of the coefficient fields. When SUSY transformations are applied, these fields which are vectors, spinors or scalars, transform to each other.

At this point, one could check the irreducibility of the expansion by trying to find subsects of components which only transform among each other. The chiral multiplet in Eq. 2.9 hints that there should be an irreducible representation without a vector field. Applying a gauge that sets the necessary components to zero in order to get rid of the vector field strength, we are left with the following **chiral superfield**.

$$\Phi(x, \theta) = \phi(x) + \sqrt{2}\theta\psi(x) + \theta\theta F(x) \tag{2.25}$$

where $x = x' + i\theta\sigma\bar{\theta}$ with x' the spacetime coordinate. Here $\phi(x)$ is a chiral fermion, either a quark, lepton or a Higgsino, which is the fermionic superpartner of the Higgs; $\psi(x)$ is either a complex scalar that acts as the superpartner of chiral fermions, which receive nemes as squarks and sleptons or is the Higgs; and $F(x)$ is an auxillary field.

Table 2.1: Field content of the MSSM

Chiral supermultiplets $(SU(3)_C \times SU(2)_L \times U(1)_Y$	Quarks spin 1/2	Squarks spin 0
$Q(3, 2, 1/6)$	$q = (u, d)$	$\tilde{q} = \tilde{u}, \tilde{d}$
$U^c(3, 1, -2/3)$	u^c	$\tilde{u}^c$
$D^c(3, 1, 1/3)$	d^c	$\tilde{d}^c$
	Leptons	Sleptons
$L(1, 2, -1/2)$	$l = (\nu, e)$	$\tilde{l} = \tilde{\nu}, \tilde{e}$
$E^c(1, 1, 1)$	e^c	$\tilde{e}^c$
	Higgs bosons	Higgsinos
$(1, 2, -1/2)$	(H_d^0, H_d^-)	$\tilde{H}_d^0, \tilde{H}_d^-$
$(1, 2, 1/2)$	(H_u^+, H_u^0)	$\tilde{H}_u^+, \tilde{H}_u^0$
Vector supermultiplets $(SU(3)_C \times SU(2)_L \times U(1)_Y$	Gauge bosons spin 1	Gauginos spin 1/2
$(8, 1, 1)$	g	$\tilde{g}$ (gluino)
$(1, 3, 1)$	$W^\pm, Z$	$\tilde{W}^\pm, \tilde{W}^0$ (Winos)
$(1, 1, 1)$	γ	$\tilde{B}$ (Bino)
Gravity supermultiplet $(SU(3)_C \times SU(2)_L \times U(1)_Y$	Graviton spin 2	Gravitino spin 3/2
$(1, 1, 1)$	$g_{\mu\nu}$	$\tilde{G}$

By imposing the Wess-Zumino gauge one can get to another irreducible representation which is the **vector superfield**

$$V(x, \theta, \bar{\theta}) = \theta\sigma^\mu\bar{\theta}v_\mu(x) - i\bar{\theta}\bar{\theta}\theta^\alpha\lambda_\alpha(x) + i\theta\theta\bar{\theta}_{\dot{\alpha}}\bar{\lambda}^{\dot{\alpha}}(x) + \frac{1}{2}\theta\theta\bar{\theta}\bar{\theta}D(x) \tag{2.26}$$

where $v_\mu(x)$ is a vector boson, either a gauge boson or a graviton; $\lambda_\alpha(x)$ and $\bar{\lambda}^{\dot{\alpha}}(x)$ are Majorana fermions, making either a gaugino, the spin-$1/2$ superpartners of the gauge bosons or a gravitino, the spin-$3/2$ superpartner of the graviton; and $D(x)$ is an auxillary field.

Table 2.2 lists the field content of the MSSM. Superfield formalism provides a convenient way to construct supersymmetric Lagrangians, even for theories with non-Abelian gauge symmetry. Using superfields guarantee writing supersymmetric Lagrangians.

2.3 Supersymmetry Lagrangian

The SUSY Lagrangian consists of a part invariant under SUSY transformations and a part that breaks SUSY:

$$\mathcal{L} = \mathcal{L}_{SUSY} + \mathcal{L}_{soft}. \tag{2.27}$$

The supersymmetric part consists of the following terms:

$$\mathcal{L}_{SUSY} = \mathcal{L}_{chiral} + \mathcal{L}_{gauge} + \mathcal{L}_{interaction}. \tag{2.28}$$

2.3.1 Lagrangian for the chiral superfield

The aim is to form a Lagrangian invariant under SUSY transformations using the chiral fields. This means the variation of the Lagrangian should at most be a total derivative. Examining the chiral superfields shows that the two terms that transform as a total derivative are the coefficient of $(\bar{\theta}\gamma_5\theta)^2$ of a product of any number of chiral superfields, which is called the "D term" and the coefficient of $\bar{\theta}\theta_{L/R}$ of the product of only the left chiral or only the right chiral superfields, which is called the "F term". These are the candidates for the terms in $\mathcal{L}_{chiral}$.

One defines a potential of the generic form

$$K(\Phi^\dagger, \Phi) = \sum_{i=1}^{N} \Phi_i^\dagger \Phi_i \tag{2.29}$$

to represent the case of the product of general superfields. This is called the Kahler potential. Then from the combination of only the left chiral or the right chiral fields, one defines another potential of the generic form

$$\mathcal{W} = L^i\phi_i + \frac{1}{2}M^{ij}\phi_i\phi_j + \frac{1}{6}y^{ijk}\phi_i\phi_j\phi_k \tag{2.30}$$

which is called the superpotential. This is actually the power series expansion of the chiral superfield Φ for a renormalizable theory. Bringing together the F term of the Kahler potential and the D term of the superpotential leads to

$$\begin{aligned}\mathcal{L}_{chiral} &= \partial_\mu\phi_j^*\partial^\mu\phi_j + \psi^{\dagger j}i\bar{\sigma}.\partial\psi_j + F^{*j}F_j \\ &\quad +(F_j\frac{\partial\mathcal{W}}{\partial\psi_j} - \frac{1}{2}\psi_j\psi_k\frac{\partial^2\mathcal{W}}{\partial\phi_j\partial\phi_k}) + h.c.\end{aligned} \tag{2.31}$$

where the first line is derived from the Kahler potential and gives the kinetic terms while the second line is derived from the superpotential whose first term gives the scalar masses and second term gives the fermion masses and Yukawa interactions. The equation of motion for F_i gives

$$F_i = \frac{\partial\mathcal{W}(\phi_i)}{\partial\phi_i}, \tag{2.32}$$

which shows it as an auxillary field dependent on only the scalar fields.

The superpotential for MSSM is given as

$$\mathcal{W} = \sum_{i,j=1}^{3}[(y_E)_{ij}H_dL_iE_j^c + (y_D)_{ij}H_dQ_iD_j^c + (y_U)_{ij}H_uQ_iU_j^c] + \mu H_dH_u \tag{2.33}$$

where i and j are generator indices.

2.3.2 Lagrangian for the vector superfield

The gauge transformations of the components of vector superfield are

$$\delta_{gauge} v_\mu^\alpha = \delta_\mu \Lambda^a + g f^{abc} v_\mu^b \Lambda^c \tag{2.34}$$

$$\delta_{gauge} \lambda^a = g f^{abc} \lambda^b \Lambda^c \tag{2.35}$$

where the indices run over the adjoint representations of the gauge group at hand, g is the gauge coupling and f^{abc} are the structure constants.

One must ask for local gauge invariance in a realistic theory. Impoing local gauge invariance to the chiral Lagrangian results in additional interactions involving components of the vector superfield. The kinetic terms for the gauge fields make up the gauge part, which is

$$\mathcal{L}_{gauge} = -\frac{1}{4} F_{\mu\nu}^a F^{\mu\nu a} + i\lambda^{\dagger a} \bar{\sigma}^\mu D_\mu \lambda^a + \frac{1}{2} D^a D^a \tag{2.36}$$

where $F_{\mu\nu}^a = \partial_\mu A_\nu^a - \partial_\nu A_\mu^a - g f^{abc} A_\mu^b A_\nu^c$ is the Yang-Mills field strength and $D_\mu \lambda^a = \partial_\mu \lambda^a - g f^{abc} A_\mu^b \lambda^c$ is the covariant derivative for the gaugino field.

2.3.3 Interaction Lagrangian

We asume the chiral supermultiplets transform under the gauge group in a representation with hermitian matrices $(T^a)_i^j$ satisfying $[T_a, T_b] = i f^{abc} T^c$. As SUSY and gauge transformations commute, components of the chiral superfield must all be in the same representation of the gauge group, giving

$$\delta_{gauge} X_i = ig\Lambda^a (T^a X)_i \tag{2.37}$$

where $X_i = \phi_i, \psi_i, F_i$. The gauge invariance can be imposed on the chiral Lagrangian by changing the ordinary derivatives there with the following covariant derivatives.

$$\partial_\mu \phi_i \rightarrow D_\mu \phi_i = \partial_\mu \phi_i - igA_\mu^a (T^a \phi)_i \tag{2.38}$$

$$\partial_\mu \psi_i \rightarrow D_\mu \psi_i = \partial_\mu \psi_i - igA_\mu^a (T^a \psi)_i. \tag{2.39}$$

As a result, we get interaction terms that couple vector bosons in the gauge supermultiplets to the scalars and fermions in the chiral supermultiplets. Moreover when looked further, one can see that there are three more possible renormalizable interaction terms $(\phi^* T^a \psi)$, $\lambda^{\dagger a}(\psi^\dagger T^a \phi)$ and $(\phi^* T^a \phi) D^a$ which are also allowed by gauge invariance. One adds these to the Lagrangian as well and reguires that the Lagrangian be real and supersymmetric, which in the end can be

achieved by also changing the derivatives in the SUSY transformations by covariant derivatives. The resulting Lagrangian is

$$\begin{aligned}\mathcal{L} &= \mathcal{L}_{chiral} + \mathcal{L}_{gauge} \\ &\quad - \sqrt{2}g[(\phi^* T^a \psi)\lambda^{\dagger a} + \lambda^{\dagger a}(\psi^\dagger T^a \phi] \\ &\quad + g(\phi^* T^a \phi) D^a \end{aligned} \tag{2.40}$$

where all derivatives in $\mathcal{L}_{chiral}$ are replaced by covariant derivatives. First two terms in the second line have couplings g that are fixed by the supersymmetry requirement. These terms express the direct coupling of gauginos to matter fields. The last term forms an equation of motion when combined with $\frac{1}{2}D^a D^a$ from $\mathcal{L}_{gauge}$, whose solution is $D^a = -g(\phi^* T^a \phi)$, meaning that D^a is totally dependent on the other fields.

The scalar potential can be defined using the F and D fields as

$$\mathcal{V}(\phi^*, \phi) = F^{*i} F_i + \frac{1}{2}\sum_a D^a D^a = \mathcal{W}_i^* \mathcal{W}^i + \frac{1}{2}\sum_a g_a^2 (\phi^* T^a \phi)^2. \tag{2.41}$$

Contrary to the SM, where the scalar potential is arbitrarily chosen, in MSSM it is automatically defined by the theory.

Given a superpotential, this Lagrangian is the starting point for SUSY model building.

2.3.4 Soft SUSY breaking Lagrngian

If SUSY existed, it should have been for long waving to us from detectors. As this is not the current case, we arrive to the phenomenological conclusion that supersymmetric particles must be heavier than their SM counterparts. Heavy sparticles can be obtained by taking SUSY as an exact symmetry that breaks spontaneously. The Lagrangian is invariant under SUSY transformations, but there exists a vacuum state that is not. Though diverse scenarios exist which will be shortly mentioned, the exact source and nature of SUSY breaking is not yet known. However in any case SUSY breaking involves extra interactions at high scale which would introduce new terms to the Lagrangian. As SUSY breaking mechanism is ambiguous, one can as well take a more generic approach and define a most generic list of SUSY breaking terms to be part of the effective Lagrangian. The SUSY breaking couplings should be soft (of positive mass dimension) in order to be able to naturally maintain a hierarchy between the EW and Planck scales. The collection of such suitable terms is given by

$$\mathcal{L}_{soft} = -\left(\frac{1}{2}M_a \lambda^a \lambda^a + \frac{1}{6}a^{ijk}\phi_i\phi_j\phi_k + \frac{1}{2}b^{ij}\phi_i\phi_j + t_i\phi_i\right) + c.c. - (m^2)^i_j \phi^j \phi_i, \tag{2.42}$$

which consists of gaugino mass parameters M_a, scalar mass parameters m^2, bi- and trilinear couplings a^{ijk}, b^{ij} and tadpole coupling t^i [1]. $\mathcal{L}_{soft}$ is proven to be free of all quadratic divergences. It only involves scalars and gauginos and breaks SUSY by giving masses to these even when the corresponding chiral fermion masses are negligibly small. $\mathcal{L}_{soft}$ takes the following form for the MSSM:

$$\begin{aligned}\mathcal{L}_{soft}^{MSSM} &= \frac{1}{2}M_1\tilde{B}\tilde{B} + \frac{1}{2}M_2\tilde{W}\tilde{W} + \frac{1}{2}M_3\tilde{g}\tilde{g} + m_{H_d}^2|H_d|^2 + m_{H_u}^2|H_u|^2 \\ &+ m_{\tilde{Q}}^2|\tilde{Q}_L|^2 + m_{\tilde{U}}^2|\tilde{U}_R^c|^2 + m_{\tilde{D}}^2|\tilde{D}_R^c|^2 + m_{\tilde{L}}^2|\tilde{L}_L|^2 + M_{\tilde{E}}^2|\tilde{E}_R^c|^2 \\ &+ \left(y_e A_e H_d \tilde{L}_L \tilde{E}_R^c + y_d A_d H_d \tilde{Q}_L \tilde{D}_R^c + y_u A_u H_u \tilde{Q}_L \tilde{U}_R^c + h.c.\right) \\ &+ (B\mu H_u H_d + h.c.) \end{aligned} \tag{2.43}$$

MSSM Lagrangian receives this form after SUSY breaking which occurs at a certain high energy scale. Here M_1, M_2 and M_3 are U(1), SU(2) and SU(3) gaugino masses. m_Q^2, m_U^2, m_D^2, m_L^2 and m_E^2 are the scalar masses, which are 3×3 hermitian matrices in flavor space. Also $y_u A_u$, $y_d A_d$ and $h_e A_e$ are generic 3×3 matrices. $m_{H_u}^2$, $m_{H_d}^2$ and $B\mu$ are Higgs mass terms. The parameters can be taken as complex, and by this assumption, total number of free parameters in the MSSM becomes 124. All these terms then can be run down to their values at the weak scale using the renormalization group equations (RGEs), which are a set of coupled differential equatons governing the relations among values that a quantity takes in different energy scales [2]

2.4 Supersymmetry breaking

Intuitively, 124 is too big a number to be the number of parameters of a model that claims to be the fundamental theory. Thus MSSM is thought to be embedded in a simpler and more fundamental framework fully relevant at a higher scale that would consequently restrict the MSSM parameters. SUSY breaking governs the transition mechanism between this fundamental theory and MSSM. In a spontaneous breaking of SUSY, vacuum state $|0\rangle$ is not invariant under SUSY transformations so that $Q_a|0\rangle \neq 0$ and $Q_a^\dagger|0\rangle \neq 0$. This directly implies $\langle 0|H|0\rangle > 0$, meaning that the vacuum has positive energy as is the case in the Higgs mechanism. To a

[1] $t_i\phi_i$ is possible only in case a gauge singlet field ϕ_i exists. Hence this is absent from the MSSM.

[2] Perturbative calculations in QFT are done taking into account a renormalized perturbation theory instead of a bare perturbation theory. One replaces the bare fields, mass terms and couplings which are perturbatively divergent with finite, renormalizable fields, mass terms and couplings, pushing away the divergent terms into counterterms whose forms are determined by specifying renormalization conditions at the energy scale Q (the renormalization scale.

good approximation one can say that $\langle 0|H|0\rangle = \langle 0|\mathcal{V}|0\rangle$. Thus, SUSY is broken if one has a non-vanishing $\langle 0|F|0\rangle$ or $\langle 0|F|0\rangle$.

Spontaneous breaking of a global symmetry leads to a massless Nambu-Goldstone mode which should have the same quantum numbers as the broken symmetry generator. In SUSY, generator Q_a of the broken symmetry is a fermion, so it leads to a massless neutral Weyl fermion called the "goldstino". Moreover, when local SUSY invariance is imposed, the longitudional components of the goldstino are absorbed by the gravitino which then acquires a mass

$$m_{3/2} \sim \frac{\langle F\rangle}{M_{Planck}} \tag{2.44}$$

as a result of the "super-Higgs mechanism".

None of the MSSM fields however are capable of acquiring a non-zero VEV without spoiling the gauge invariance. It is for this reason that SUSY breaking must be invoked via some other fields. The most commonly accepted scenario proposes that SUSY is broken in a "hidden sector". However no renormalizable tree level interactions between the hidden sector and the "visible" sector are known that could involve the usual matter fields. Instead, SUSY breaking is mediated between the two sectors through interactions via some fields called "messengers". Some mediation mechanisms proposed so far are gravity mediation (SUGRA), gauge mediation, anomaly mediation and gaugino mediation. We next discuss the first two in some detail.

2.4.1 Gravity-mediated SUSY breaking (SUGRA)

In SUGRA [25] two sectors interact via gravity. Here, the F terms F_T and F_S of moduli fields T that appear as a result of compactification from higher dimensions, and a dilaton field S, which is a part of the SUGRA multiplet would acquire VEVs. The resulting SUSY breaking scale is of the order of gravitino mass:

$$M_{SUSY} = \frac{\langle F_T\rangle}{M_{Pl}} + \frac{\langle F_S\rangle}{M_{Pl}} \sim m_{3/2}. \tag{2.45}$$

Since gravity is involved, the supergravity effective Lagrangian is expected to contain some non-renormalizable terms that communicate between the two sectors, such as

$$\begin{aligned}\mathcal{L}_{NR} &= -\frac{1}{M_{Pl}}\left(\frac{1}{2}F_S\, f_a\lambda^a\lambda^a + \frac{1}{6}F_{T,S}y'^{ijk}\phi_i\phi_j\phi_k + \frac{1}{2}\mu'^{ij}\phi_i\phi_j\right) + c.c.\\ &\quad -\frac{1}{M_{Pl}^2}F_S F_S^* k^i_j\phi_i\phi'^j\end{aligned} \tag{2.46}$$

where f^a, y'^{ijk} and μ'^{ij} are dimensionless constants. Soft terms are determined from the coefficients of ϕ_i and λ^a, which are the MSSM scalar and gaugino fields. To have soft terms of the order of ~TeV, we must have $\sqrt{\langle F_{T,S} \rangle}$ ~10^{11} GeV. This scenario implies a heavy gravitino of the order of ~ TeV that decouples from the LHC physics.

For the sake of simplicity, and also to comply with more fundamental underlying scenarios which favor unification, it is a custom to assume that the soft terms are universal. At the GUT scale, one assumes single universal values m_0 for the scalar masses, $m_{1/2}$ for the gaugino masses and A_0 for the trilinear couplings. Additionally one takes $\tan\beta$ (to be explained in the next section) and sign of μ in place of B. This is the famous minimal SUGRA (mSUGRA) model, examples of which are widely investigated in collider SUSY search studies.

2.4.2 Gauge-mediated SUSY breaking (GMSB)

In an alternative approach, it is possible to assume that ordinary gauge interactions are responsible for gauge mediation [26]. The messengers are ordinary gauge bosons and matter fields of the SM and of some GUT theory. At one side they couple to a gauge singlet chiral superfield S whose scalar component S and auxillary F-term acquire VEVs $\langle S \rangle$ and $\langle F \rangle$. On the other side messengers also couple indirectly to MSSM through ordinary gauge interactions. In GMSB

$$m_{soft} \sim \frac{g_a^2}{16\pi^2} \frac{\langle F \rangle}{M_{mess}}. \tag{2.47}$$

The MSSM soft terms arise from loop diagrams involving the messengers where gaugino masses are generated at 1-loop and scalar masses are generated at 2-loop as follows

$$M_a = \frac{g_a^2}{16\pi^2} \frac{\langle F \rangle}{M_{mess}} \tag{2.48}$$

$$m_\phi^2 = 2 \sum_a C_a^\phi \left(\frac{g_a^2}{16\pi^2} \right)^2 \left(\frac{\langle F \rangle}{M_{mess}} \right)^2. \tag{2.49}$$

Considering a characteristic M_{mess}, GMSB has a lower SUSY breaking scale of $\sqrt{\langle F \rangle}$ ~ 10^4 – 10^5 GeV. This implies a very light gravitino with mass $m_{3/2}$ ~eV-keV, making it the lightest sparticle. This leads to special LHC signatures. For the cases where $\tilde{\chi}_1^0$ is the next-to-lightest sparticle, one expects prompt photons from the $\tilde{\chi}_1^0 \to \gamma \tilde{G}$ decays. The other case with $\tilde{\tau}_1$ as next-to-lightest sparticle has a signature of long-lived charged particles.

2.5 Electroweak symmetry breaking

The scalar potential for the Higgs fields is

$$\begin{aligned}\mathcal{V}_H &= (|\mu|^2 + m_{H_u}^2)(|H_u^0|^2 + |H_u^+|^2) + (|\mu|^2 + m_{H_d}^2)(|H_d^0|^2 + |H_d^-|^2) \\ &\quad + \left[b(H_u^+ H_d^- - H_u^0 H_d^0) + c.c.\right] \\ &\quad + \frac{1}{8}(g^2 + g'^2)(|H_u^0|^2 + |H_u^+|^2 - |H_d^0|^2 - |H_d^-|^2)^2 + \frac{1}{2}g^2|H_u^+ H_d^{0*} + H_u^0 H_d^{-*}|^2 \quad (2.50)\end{aligned}$$

where terms proportional to $|\mu|^2$ come from the F terms, terms proportional to g_1^2 and g_2^2 come from the D terms after some rearrangament, and terms proportional to m_{H_u}, m_{H_d} and b come from soft SUSY breaking. Other terms involving squarks and slepton in $\mathcal{V}$ are not considered here since due to RGE running, they do not acquire VEVs because of their large positive squared masses.

First we can use $SU(2)_L$ gauge transformations to freely rotate away a possible VEV for one of the weak isospin components of one of the scalar fields. The VEV of H_u can be rotated to its lower component, which would imply taking $H_u^+ = 0$ at the potential minimum. Then $\partial\mathcal{V}_H/\partial H_u^+$ requires $\left\langle H_d^- \right\rangle$ as well. Remaining part of the scalar potential

$$\begin{aligned}\mathcal{V}_H &= (|\mu|^2 + m_{H_u}^2)(|H_u^0|^2) + (|\mu|^2 + m_{H_d}^2)(|H_d^0|^2) - \left[B\mu(H_u^0 H_d^0) + c.c.\right] \\ &\quad + \frac{1}{8}(g^2 + g'^2)(|H_u^0|^2 - |H_d^0|^2)^2 \quad (2.51)\end{aligned}$$

only allows charge conserving vacua. Next, the only complex phase dependent term b can be chosen as real and positive through a redefinition of H_u and H_d phases by adjusting them to absorb the b phases. Then requiring $\partial\mathcal{V}_H/\partial H_u = \partial\mathcal{V}_H/\partial H_u = 0$ leads to the following condition for a local minimum away from the origin

$$(B\mu)^2 > (|\mu|^2 + m_{H_u}^2)(|\mu|^2 + m_{H_d}^2. \quad (2.52)$$

Moreover, the scalar potential needs to have a stable minimum and should be bounded from below, which can be satisfied by the condition

$$2B\mu < 2|\mu|^2 + m_{H_u}^2 + m_{H_d}^2. \quad (2.53)$$

Both conditions can be satisfied simultaneously only if $m_{H_u} \neq m_{H_d}$. High scale scenarios with universality motivate $m_{H_u} = m_{H_d}$ at tree level. The inequality is introduced by the difference in RGE equations for m_{H_u} and m_{H_d}, where each RGE receives large contributions from terms involving scalar masses, trilinear and Yukawa couplings which can drive m_{H_u} and/or m_{H_d}

negative close to the EW scale. The symmetry breking thus achieved via quantum corrections is called radiative electroweak symmetry breaking (REWSB). Large top mass creates a larger effect on m_{H_u}, favoring $m^2_{H_u} < m^2_{H_d}$. Then the VEVs at the minimum $v_u = \left\langle H^0_u \right\rangle$ and $v_d = \left\langle H^0_d \right\rangle$ can be related to the known mass of the Z boson and the EW gauge couplings as

$$v_u^2 + v_d^2 = v^2 = 2m_Z^2/(g^2 + g'^2) \approx (174\text{GeV})^2. \tag{2.54}$$

Here, ratio of the two VEVs can be defined as a free parameter

$$\tan\beta \equiv v_u/v_d \tag{2.55}$$

through which the minimization conditions can be re-written as

$$|\mu|^2 + m^2_{H_d} = B\mu\tan\beta - (m_Z^2/2)\cos 2\beta \tag{2.56}$$

$$|\mu|^2 + m^2_{H_u} = B\mu\cot\beta + (m_Z^2/2)\cos 2\beta. \tag{2.57}$$

As a result, $\tan\beta$ and m_Z can be expressed in terms of b and μ.

The two complex $SU(2)_L$ Higgs doublets have eight degrees of freedom. Three of these are the would-be Nambu-Goldstone bosons G^0, $G^\pm$, which become the longitudional modes of the now massive Z and $W^\pm$ vector bosons. The remaining five scalar mass eigenstates become the physical Higgs bosons: two CP-even Higgses h, H, one CP-odd Higgs A and the charged Higgses $H^\pm$. The relation between mass and gauge eigenstates are given by

$$\begin{pmatrix} G^0 \\ A \end{pmatrix} = \sqrt{2}\begin{pmatrix} \sin\beta & \cos\beta \\ -\cos\beta & \sin\beta \end{pmatrix}\begin{pmatrix} Im[H^0_u] \\ Im[H^0_v] \end{pmatrix} \tag{2.58}$$

$$\begin{pmatrix} G^+ \\ H^+ \end{pmatrix} = \begin{pmatrix} \sin\beta & \cos\beta \\ -\cos\beta & \sin\beta \end{pmatrix}\begin{pmatrix} H^+_u \\ H^{-*}_v \end{pmatrix} \tag{2.59}$$

$$\begin{pmatrix} h \\ H \end{pmatrix} = \sqrt{2}\begin{pmatrix} \cos\alpha & -\sin\alpha \\ \sin\alpha & \cos\alpha \end{pmatrix}\begin{pmatrix} Re[H^0_u] - v_u \\ Re[H^0_v] - v_d \end{pmatrix}. \tag{2.60}$$

The tree level physical Higgs masses are then found to be

$$m_A^2 = 2B\mu/\sin 2\beta \tag{2.61}$$

$$m^2_{h,H} = \frac{1}{2}(m^2_{A_0} + m_Z^2 \mp \sqrt{(m_A^2 - m_Z^2)^2 + 4m_Z^2 m_A^2 \sin^2(2\beta)}) \tag{2.62}$$

$$m^2_{H^\pm} = m_A^2 + m_W^2. \tag{2.63}$$

Thus m_A and $\tan\beta$ serve as the free parameters of the Higgs sector. The mixing angle α at tree level in terms of these masses is then expressed as

$$\frac{\sin(2\alpha)}{\sin(2\beta)} = -\left(\frac{m_H^2 + m_h^2}{m_H^2 - m_h^2}\right), \qquad \frac{\tan(2\alpha)}{\tan(2\beta)} = -\left(\frac{m_A^2 + m_Z^2}{m_A^2 - m_Z^2}\right) \tag{2.64}$$

and is conventionally chosen as negative. In principle m_A, m_H and $m_{H^\pm}$ can be arbitrarily large. However the tree level definition of m_h introduces the upper bound

$$m_h < \min(m_Z, m_A)|\cos(2\beta)|. \tag{2.65}$$

However m_h also receives large radiative corrections which increase the upper limit to

$$m_h < 130 \text{ GeV}. \tag{2.66}$$

Top, charm and up quark masses are proportional to $v_u = v\sin\beta$ while bottom, strange and down quark among with charged lepton masses are poportional to $v_d = v\cos\beta$. The tree level relation between quark and lepton masses with Yukawa couplings are given as

$$f_t = \frac{gm_t}{\sqrt{2}m_W \sin\beta}; \qquad f_b = \frac{gm_b}{\sqrt{2}m_W \cos\beta}; \qquad f_\tau = \frac{gm_\tau}{\sqrt{2}m_W \cos\beta}. \tag{2.67}$$

which implies $f_b/f_t = (m_b/m_t)\tan\beta$ and $f_\tau/f_t = (m_\tau/m_t)\tan\beta$. Requiring that f_t does not diverge at high scales introduces a lower limit on $\sin\theta$ which translates as $\tan\beta \gtrsim 1.2$ while requiring non-divergence for f_b and f_τ leads to $\tan\beta \lesssim 60$.

2.6 Sparticle mixing and masses

After REWSB, gauge eigenstates with same $\mathrm{SU(3)_C} \times \mathrm{U(1)_{EM}}$ quantum numbers can mix with each other, just as B^0 and W_i mix into γ, Z and $W^\pm$ in the SM. In the MSSM, other than the Higgses explained in Section 2.5, sleptons, gauginos and higgsinos are also effected by the mixing. We next summarize the mass eigenstates and the MSSM mass spectrum.

2.6.1 Squarks and sleptons

Charged SM leptons have left- and right-handed states f_L, f_R in each family which have the sfermionic partners $\tilde{f}_L$, $\tilde{f}_R$ with different isospins $I = 1/2, 0$. However after the breaking of $\mathrm{SU(2)_L} \times \mathrm{U(1)_Y}$, $\tilde{f}_L$ and $\tilde{f}_R$, can mix through the matrix of form

$$\mathcal{L} \ni -\begin{pmatrix} \tilde{f}_L^* & \tilde{f}_R^* \end{pmatrix} \mathcal{M}^2_{\tilde{f}} \begin{pmatrix} \tilde{f}_L \\ \tilde{f}_R \end{pmatrix} \tag{2.68}$$

where

$$\mathcal{M}^2_{\tilde{f}} = \begin{pmatrix} m_{\tilde{f}_{LL}} & m_{\tilde{f}_{LR}} \\ m_{\tilde{f}_{RL}} & m_{\tilde{f}_{RR}} \end{pmatrix}. \tag{2.69}$$

The diagonal terms have the form

$$m^2_{\tilde{f}_{LL,RR}} = m^2_{\tilde{f}_{L,R}} + m^{D^2}_{\tilde{f}_{L,R}} + m^2_f \tag{2.70}$$

where m_f is the corresponding SM fermion mass, $m^2_{\tilde{f}_{L,R}}$ is the soft SUSY-breaking term from $\mathcal{L}_{soft}$, and $m^{D^2}_{\tilde{f}_{L,R}}$ is the contribution that comes from the quartic D terms in the effective potential:

$$m^{D^2}_{\tilde{f}_{L,R}} = m_Z^2 \cos 2\beta (I_3 + \sin^2\theta_W Q_{em}) \tag{2.71}$$

which has the I_3 contribution non-zore for only $\tilde{f}_L$. On the other hand, the off-diagonal terms take the form

$$m^2_{\tilde{f}_{L,R}} = m_f (A_f + \mu^{\tan\beta}_{\cot\beta}) \text{ for } f = ^{e,\mu,\tau,d,s,b}_{u,c,t} . \tag{2.72}$$

This shows that the effects of left-right mixing is important especially for the stops due to the large top mass, and also might become significant for the sbottoms and staus for large $\tan\beta$. Also, contributions from non-negligible t, b, τ masses create a difference in the 3rd generation diagonal terms even when the soft mass terms are universal. Moreover Yukawa effects in renormalization of the 3rd generation soft masses also enhance the non-universality of $m^2_{\tilde{t}_{LL,RR}}$ (as well as $m^2_{\tilde{b}_{LL,RR}}$ and $m^2_{\tilde{\tau}_{LL,RR}}$ for large $\tan\beta$). On the other hand, mixing is insignificant for the first two generations due to negligible fermion masses and hence is not generally considered in spectrum calculations.

2.6.2 The gluino

The gluino is the only octet fermion. Since $SU(2)_C$ is not broken, gluino gauge eigenstate will not mix with other fermionic states, and hence is a mass eigenstate as well, whose mass term arises from the gaugino mass term in $\mathcal{L}_{soft}$:

$$\mathcal{L} \ni -\frac{1}{2} M_3 \tilde{g}\tilde{g}. \tag{2.73}$$

Its tree level mass is $m_{\tilde{g}} = |M_3|$. The RG running of M_3 is swift due to the dependence on the strong SU(3) coupling. A better estimate for gluino mass would be the pole mass, which, including 1-loop corrections becomes for the $\overline{\text{DR}}$ renormalization scheme,

$$m_{\tilde{g}} = M_3 \left(1 + \frac{\alpha_s}{4\pi}[15 + 6\ln(Q/M_3) + \sum A_q]\right) \tag{2.74}$$

where

$$A_{\tilde{g}} = \int_0^1 dx\, x \ln[x m^2_{\tilde{g}} + (1-x) m_q^2/M_3^2 - x(1-x) - i\epsilon] \tag{2.75}$$

and the sum in Eq. 2.74 is over all 12 squark-quark supermultiplets.

2.6.3 Neutralinos

The complete set of mass terms involving neutral gauginos and higgsinos can be written in the compact form

$$\mathcal{L} \ni -\frac{1}{2}(\psi^0)^T \mathcal{M}_{neutral} \psi^0 + c.c. \tag{2.76}$$

Here $\psi^0 = (\tilde{B}, \tilde{W}^0, \tilde{H}_d^0, \tilde{H}_u^0)$, the vector of neutral gauge eigenstate basis, and $\mathcal{M}_{neutral}$ is a matrix with the mass terms

$$\mathcal{M}_{neutral} = \begin{pmatrix} M_1 & 0 & -c_\beta s_W m_Z & s_\beta s_W m_Z \\ 0 & M_2 & c_\beta c_W m_Z & -s_\beta c_W m_Z \\ -c_\beta s_W m_Z & c_\beta c_W m_Z & 0 & -\mu \\ s_\beta s_W m_Z & -s_\beta c_W m_Z & -\mu & 0. \end{pmatrix} \tag{2.77}$$

where $s_\beta = \sin\beta$, $c_\beta = \cos\beta$, $s_W = \sin\theta_W$ and $c_W = \cos\theta_W$. Eq. 2.77 shows the mixing between the gauge eigenstates. This mass matrix can be diagonalized by a unitary matrix N such that

$$N^* \mathcal{M}_{neutral} N^{-1} = \mathcal{M}_{\tilde{\chi}^0} \tag{2.78}$$

which gives the mass eigenstates

$$\tilde{\chi}_i^0 = N_{ij} \psi_{ji}^0, \quad i, j = 1, 2, 3, 4, \tag{2.79}$$

where (i,j) indices stand for (mass, gauge). To ensure positive mass eigenvalues, one can define N by choosing to diagonalize $\mathcal{M}_{neutral}^\dagger \mathcal{M}_{neutral}$ instead, such that

$$N^* \mathcal{M}_{neutral}^\dagger \mathcal{M}_{neutral} N^{-1} = \mathcal{M}_{\tilde{\chi}^0}^2 = \text{diag}(m_{\tilde{\chi}_1^0}^2, m_{\tilde{\chi}_2^0}^2, m_{\tilde{\chi}_3^0}^2, m_{\tilde{\chi}_4^0}^2). \tag{2.80}$$

Yet, assuming CP conservation, one can allow for negative mass eigenvalues. Then choosing N as real and orthogonal, we get

$$\mathcal{M}_{\tilde{\chi}^0} = \text{diag}(\varepsilon_1 m_{\tilde{\chi}_1^0}, \varepsilon_2 m_{\tilde{\chi}_2^0}, \varepsilon_3 m_{\tilde{\chi}_3^0}, \varepsilon_4 m_{\tilde{\chi}_4^0}) \tag{2.81}$$

where $\varepsilon_i = \pm 1$. The mass eigenstates $\tilde{\chi}_i^0$ are called "neutralinos" and are ordered such that $0 \leq m_{\tilde{\chi}_1^0} \leq m_{\tilde{\chi}_2^0} \leq m_{\tilde{\chi}_3^0} \leq m_{\tilde{\chi}_4^0}$. Analytical diagonalization of $\mathcal{M}_{neutral}$ is possible, but resulting formulas are long and complicated. Therefore numerical methods are preferred in spectrum computations.

2.6.4 Charginos

Similarly, the complete set of mass terms involving neutral gauginos and higgsinos can be written in the compact form

$$\mathcal{L} \ni -\frac{1}{2}(\psi^{\pm})^T \mathcal{M}_{charge} \psi^{\pm} + c.c. \tag{2.82}$$

Here $\psi^{\pm} = (\tilde{W}^+, \tilde{H}_u^+, \tilde{W}^-, \tilde{H}_d^-)$, the vector of charged gauge eigenstate bases, and $\mathcal{M}_{charge}$ is a 2×2 block matrix with the mass terms

$$\mathcal{M}_{charge} = \begin{pmatrix} 0 & X^{\mathrm{T}} \\ X & 0 \end{pmatrix} \quad \text{where} \quad X = \begin{pmatrix} M_2 & \sqrt{2} s_\beta m_W \\ \sqrt{2} c_\beta m_W & \mu \end{pmatrix}. \tag{2.83}$$

This time the mass matrix can be diagonalized by two unitary matrices U and V such as

$$U^* X V^{-1} = \mathcal{M}_{\tilde{\chi}^{\pm}} \tag{2.84}$$

which give the mass eigenstates

$$\tilde{\chi}_i^+ = V_{ij} \psi_j^+, \quad \tilde{\chi}_i^- = U_{ij} \psi_j^-, \quad i, j = 1, 2. \tag{2.85}$$

As seen, the mixing matrix for the positively charged left-handed fermions is different from that for the negatively charged left-handed fermions. Again, one can solve for positive mass eigenvalues by diagonalizing the 4×4 matrix $\mathcal{M}_{charge}^{\dagger} \mathcal{M}_{charge}$, or equivalently $X^{\mathrm{T}} X$, which gives

$$V X^{\dagger} X V^{-1} = U^* X X^{\dagger} U^T = \mathcal{M}_{\tilde{\chi}^{\pm}}^2 = \mathrm{diag}(m_{\tilde{\chi}_1^{\pm}}^2, m_{\tilde{\chi}_2^{\pm}}^2). \tag{2.86}$$

But as in the neutralino case we can allow

$$U^* X V^{-1} = \mathcal{M}_{\tilde{\chi}^{\pm}} = \mathrm{diag}(\varepsilon_1 m_{\tilde{\chi}_1^{\pm}}, \varepsilon_2 m_{\tilde{\chi}_2^{\pm}}) \tag{2.87}$$

where $\varepsilon_i = \pm 1$. The mass eigenstates are called "charginos" and are ordered such that $0 \leq m_{\tilde{\chi}_1^{\pm}} \leq m_{\tilde{\chi}_2^{\pm}}$. Contrary to the neutralino case, analytical diagonalization of X is much easier due to its 2×2 nature and gives the following chargino masses

$$m_{\tilde{\chi}_1^{\pm}}^2, m_{\tilde{\chi}_2^{\pm}}^2 = \frac{1}{2}[|M_2|^2 + |\mu|^2 + 2m_W^2 \tag{2.88}$$

$$\mp \sqrt{(|M_2|^2 + |\mu|^2 + 2m_W^2)^2 - 4|\mu M_2 - m_W^2 \sin 2\beta|^2}] \tag{2.89}$$

at tree level.

2.7 Experimental bounds on sparticle masses

Since its proposal supersymmetry was enthusiastically sought by experiment. While collider experiments LEP, HERA and Tevatron directly looked for sparticles, also non-collider experiments, especially those searching for dark matter chased after indirect hints. However as of 2008, the result of these vast efforts is only a set of lower bounds on sparticle masses.

Current estimated [3] lower bounds on masses of neutralinos are $m_{\tilde{\chi}_1^0}$ >46 GeV, $m_{\tilde{\chi}_2^0}$ >62.4 GeV (for $1 < \tan\beta < 40$), $m_{\tilde{\chi}_3^0}$ >99.9 GeV (for $1 < \tan\beta < 40$), $m_{\tilde{\chi}_4^0}$ >116 GeV (for $1 < \tan\beta < 40$); of charginos is $m_{\tilde{\chi}_1^\pm}$ >94 GeV (for $\tan\beta < 40$ and $m_{\tilde{\chi}_1^\pm} - m_{\tilde{\chi}_1^0} > 3$ GeV); of gluino is $m_{\tilde{g}}$ >308 GeV; of sleptons are $m_{\tilde{e}}$ >73 GeV, $m_{\tilde{\mu}}$ >94 GeV (for $1 \leq \tan\beta \leq 40$ and $m_{\tilde{\mu}_R} - m_{\tilde{\chi}_1^0} > 10$ GeV), $m_{\tilde{\tau}}$ >81.9 GeV (for $m_{\tilde{\tau}_1} - m_{\tilde{\chi}_1^0} > 15$ GeV); and of squarks are $m_{\tilde{q}}$ >379 GeV (for $\tan\beta = 2$, $\mu < 0$, $A_0 = 0$), $m_{\tilde{b}} > 89$ GeV (for $m_{\tilde{b}_1} - m_{\tilde{\chi}_1^0} > 8$ GeV), $m_{\tilde{\tau}}$ >95.7 GeV (with $\tilde{\tau}_1 \to c\tilde{\chi}_1^0$, for $m_{\tilde{t}_1} - m_{\tilde{\chi}_1^0} > 10$ GeV) [27].

Now we all wait for the LHC.

2.8 Reasons to favor SUSY

Besides its much quoted ”elegance”, SUSY is principally and practically capable of offering answers to prominent questions in particle physics. First, as discussed in Chapter 1 and Section 2.1, introduction of sparticles cancels out the quadratic divergencies in quantum corrections to the Higgs mass, hence solving the Hierarchy Problem.

Then there is the unification issue: 1-loop RGEs for the gauge couplings have the generic form

$$\frac{d}{dt} = \beta(g) = \frac{b_a}{16\pi^2} g_a^3 \tag{2.90}$$

with $t = \ln(Q/M_x)$ and $a = 1, 2, 3$, where Q is the renormalization scale and and M_x is the input scale. Here $\beta(g)$ are evaluated by calculating the logarithmically divergent parts of diagrams that contribute to coupling constant renormalization, then taking the logarithmic derivative with respect to Q. The constants b_a depend on the field content of the theory. For SM, $b_{1,2,3} = (41/10, -19/6, 7)$. But as mentined earlier, running the couplings up with SM RGEs does not yield Grand Unification. In MSSM however, the contributions from sparticles modify the constants to $b_a = (33/5, 1, -3)$ and RGE running actually achieves Grand Unification at $\sim 10^{16}$ GeV. This is a great motivation for SUSY. Although MSSM is much critisized for the many free parameters it has at weak scale, gauge coupling unification hints

[3] Calculations assume $\tilde{\chi}_1^0$ as lightest sparticle, $m_{\tilde{q}_R} = m_{\tilde{q}_L}$ and universal gaugino masses at the GUT scale.

that SUSY is much likely embedded in a simpler theory which reveals its true nature above the GUT scale. Meanwhile SUSY plays the role of the required ”transition theory” between the weak and the GUT scales.

SUSY takes a further step towards a fundamental theory by unifying gravity with other interactions. This goal, made impossible for the SM by the no-go theorems that forbid unification of spin-1 gauge and spin-2 graviton fields within a unique algebra can be realized in SUSY, because requiring SUSY to be a local symmetry naturally presents it as a local coordinate transformation, hence re-defining it as a theory of gravity called ”supergravity”. SUSY serves the fundamental theory concept also by constituting a strong basis for the much-studied superstring theory.

And then, there is that whole story about SUSY dark matter.

2.9 R parity and supersymmetric dark matter

The MSSM superpotential leads to a Lagrangian which is invariant under the discrete symmetry

$$R = (-1)^{L+3B+2S} \tag{2.91}$$

called ”R-parity” where L is the lepton number, B is the baryon number and S is the spin. R-parity is in fact more of a ”choice” then a model requirement since one can as well introduce R-parity violating terms consistent with supersymmetry. However this implies breaking of lepton and/or baryon number which would lead to rapid proton decay. This imposes stringent constraints on the couplings of the R-parity breaking terms due to the current limits on proton lifetime and thus establishes R-parity conservation as the more favored case.

$R = 1$ for particles and $R = -1$ for sparticles. As phenomenological consequences, sparticles are always produced in pairs and a sparticle always decays to an odd number of sparticles.

The second implication is important for cosmology: According to this, the lightest supersymmetric particle (LSP) has to be stable, which makes it possible that a multitude of them remaining from the Big Bang era could still be lingering around the Universe, playing the long sought dark matter [28]. In the early Universe, when temperatures are much greater then particle masses, dark matter particles are created and annihilated at the same rate. Then through expansion, Universe cools and eventually temperature drops below dark matter mass, rendering dark matter production impossible. Finally there comes a temperate where expan-

sion rate of the Universe goes beyond that of dark mater annihilation, freezing out the relic density of dark matter.

To stand for dark matter, LSP should be neutral and uncolored, since charged or colored supersymmetric relics would combine with ordinary matter to form heavy, exotic baryons which already would have been observed by astrophysics experiments. However such exotics are excluded for the few TeV mass range. In MSSM, SUGRA leads to $\tilde{\chi}_1^0$ and GMSB leads to $\tilde{G}$ dark matter.

Consequently, the LSP relic density of a candidate SUSY model has a role when deciding on that model's feasibility. It is calculated by solving the Boltzmann equation for a Friedmann-Robertson-Walker (FRW) Universe

$$\frac{dn}{dt} = -3Hn - \langle\sigma v\rangle (n^2 - (n^{eq})^2). \tag{2.92}$$

Here n is the number density, t is the time, H is the Hubble constant, $\langle\sigma v\rangle$ is the thermally-averaged annihilation cross section and n^{eq} is the equilibrium number density which is

$$n^{eq} = g\left(\frac{mT}{2\pi}\right)^{3/2} e^{-m/T} \tag{2.93}$$

in the non-relativistic limit, for heavy particles. Here g is the number of degrees of freedom, m is the particle mass and T is the temperature. Defining the scaled inverse temperature $x = m/T$, the freeze-out point is given by the iterative solution of the equation

$$x_f = \ln \frac{0.038 g M_{Pl} m \langle\sigma v\rangle}{g_*^{1/2} x_f^{1/2}} \tag{2.94}$$

where g_* is the value at freeze-out. Finally the relic density $\Omega_{CDM}h^2$ is found to be

$$\Omega_{CDM}h^2 \approx \frac{1.07 \times 10^9 \text{GeV}^{-1}}{J(x_f) g_*^{1/2} M_{Pl}} \quad \text{where} \quad J(x_f) = \int_{x_f}^{\infty} \frac{\langle\sigma v\rangle}{x^2} dx. \tag{2.95}$$

Dark matter relic density can be quantitively predicted by measuring the temperature fluctuations of Cosmic Microwave Background (CMB) radiation. Most precise estimates come from the Wilkinson Microwave Anisotropy Probe (WMAP) experiment, which stated

$$\Omega_{CDM}h^2 = 0.1143 \pm 0.0034 \tag{2.96}$$

after 5-year data taking in 2008 [29]. However in earlier work in this thesis, we use the limits

$$0.094 < \Omega_{CDM}h^2 < 0.136 \tag{2.97}$$

found by a different analysis on the 3-year WMAP data [30].

2.10 Spectrum and relic density comparisons

Now we present the results of a study which compares the numerical computations of SUSY spectra with different codes and impacts of the differences on relic density calculations [31], [32]. This study which in part was an update of [33] and [34] was done through a request by the CMS SUSYBSM group and served to determine the choice of spectrum calculators during Summer 2007 and 2008 Monte Carlo data productions.

The four public codes considered are ISAJET 7.75 [35], SOFTSUSY 2.0.14 [36], SPHENO 2.2.3 [37] and SUSPECT 2.3.4 [38], Besides the moderate parameter regions, we investigate the regions with known difficulties such as i) large m_0, ii) large $\tan\beta$ and iii) large A_0. Relic density is calculated using micrOMEGAs 2.0 [39]. We base the study on a simple mSUGRA benchmark P with $m_0 = 500$ GeV, $m_{1/2} = 300$ GeV, $A_0 = 0$, $\tan\beta = 10$ and $\mu > 0$. For the SM input parameters, we take $m_t = 175$ GeV, $\alpha_{\rm em}^{-1} = 127.908957$, $G_F = 1.16637 \times 10^{-5}$, $\alpha_s(M_Z)^{\overline{\rm MS}} = 0.1172$, $M_Z^{\rm pole} = 91.1876$ GeV and $m_b(m_b) = 4.2$ GeV in all four codes. The relative difference in any quantity X is expressed as

$$\delta X \equiv (X_{max} - X_{min})/X_{mean}. \tag{2.98}$$

where *min* and *max* refer to the minimum and maximum values achieved by the four codes.

The moderate region and effects of stau co-annihilation: Figure 2.1 shows a scan in the moderate regions of $m_0 - m_{1/2}$ plane for $A_0 = 0$, $\tan\beta = 10$ and $\mu > 0$ comparing the WMAP upper bounds $\Omega_{\tilde\chi_1^0}h^2 = 0.136$ for the four codes. Also shown are regions where $\delta\Omega_{\tilde\chi_1^0}h^2$ is $< \%4$, $\%4 - 10$, $\%10 - 30$ and $> \%30$. Though the differences in WMAP bounds do not seem too dramatic, $\delta\Omega_{\tilde\chi_1^0}h^2$ becomes large near $m_{\tilde\tau_1} = m_{\tilde\chi_1^\pm}$ boundary. Here the effects of $\tilde\tau_1$ co-annihilation that appears as $\tilde\chi_1^0\tilde\tau_1 \to X$ processes contribute vastly to $\Omega_{\tilde\chi_1^0}h^2$, helping to reduce it below the WMAP bound, and a small difference in $m_{\tilde\tau_1} - m_{\tilde\chi_1^0}$ translates as a large $\delta\Omega_{\tilde\chi_1^0}h^2$. For example, $m_{\tilde\tau_1} - m_{\tilde\chi_1^\pm} = 0.6$ GeV leads to $\Omega_{\tilde\chi_1^0}h^2 = \%15$.

Large m_0 case: Figure 2.2 shows μ (left) and top Yukawa coupling y_t (right) versus m_0 with other parameters fixed to values in P. While differences in y_t are small, variances such as $\delta y_t = \%0.85$ for $m_0 = 1$ TeV and $\%1.08$ for $m_0 = 3$ TeV induce large discrepencies in μ, giving $\delta\mu \simeq \%10,\ \%25,\ \%60$ for $m_0 = 1, 2, 3$ TeV. Also the limit of REWSB is reached at different values. So computations in this region need further improvement for compatibility. We do not present a relic density comparison here since relic density is generally above the WMAP upper bound except for the special focus point case, which will be discussed in Chapter 6.

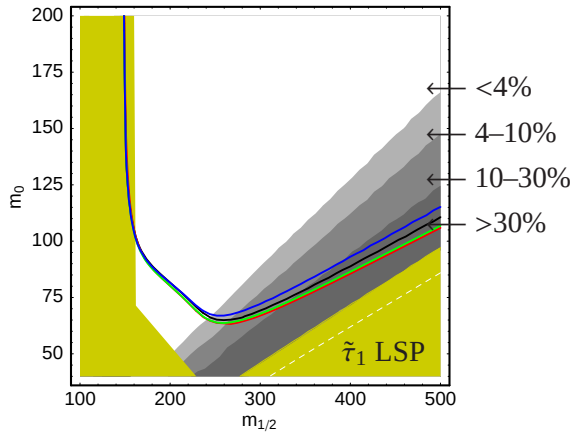

Figure 2.1: Upper bound from the relic denisty, $\Omega_{\tilde{\chi}_1^0}h^2 = 0.136$, on the $m_{1/2}$–m_0 plane for $\tan\beta = 10$, $A_0 = 0$, $\mu > 0$ and $m_t = 175$ GeV. The black, red, green and blue lines are for ISAJET, SOFTSUSY, SPHENO and SUSPECT respectively. Also shown is the corresponding $\delta\Omega_{\tilde{\chi}_1^0}h^2$. The yellow regions are excluded by LEP measurements or because of a stau LSP.

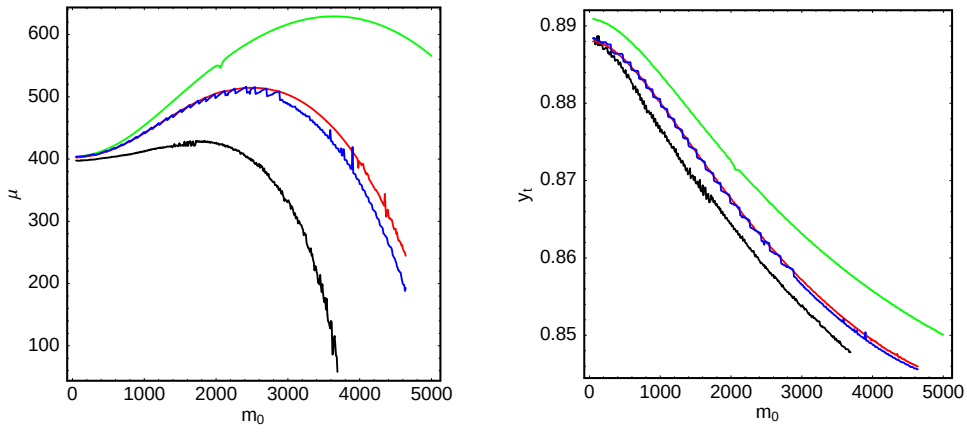

Figure 2.2: Higgs mass parameter μ (left) and top Yukawa coupling $y_t(M_{\rm SUSY})$ (right) as functions of m_0; the black, red, green and blue lines are for ISAJET, SOFTSUSY, SPHENO and SUSPECT respectively.

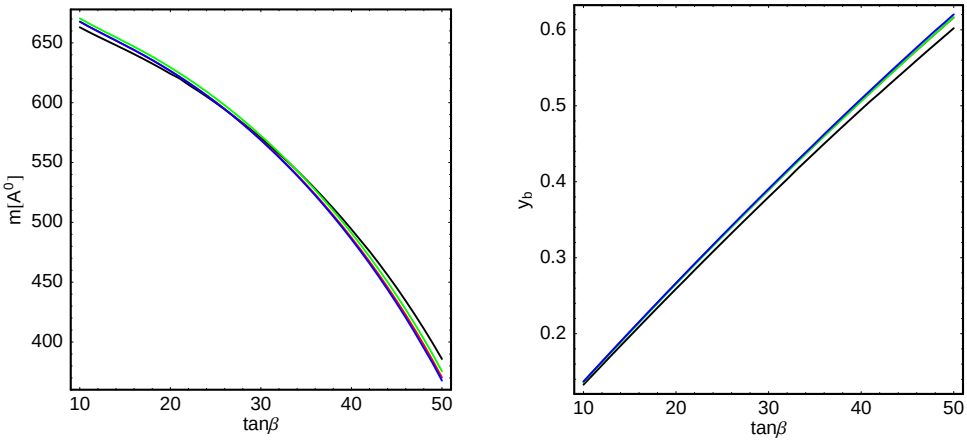

Figure 2.3: Pseudoscalar Higgs mass m_A (left) and bottom Yukawa coupling $y_b(M_{\rm SUSY})$ (right) as functions of $\tan\beta$ for $m_0 = 500$ GeV, $m_{1/2} = 300$ GeV, $A_0 = 0$, $\mu > 0$ and $m_t = 175$ GeV; the black, red, green and blue lines are for ISAJET, SOFTSUSY, SPHENO and SUSPECT respectively.

Large $\tan\beta$ case and effects of Higgs annihilation: Figure 2.3 shows pseudoscalar Higgs mass m_A and bottom Yukawa coupling $y_b(M_{\rm SUSY})$ versus $\tan\beta$ with other parameters fixed to values in P. Due to recent improvements, the four codes seem to be in good agreement with each other. However, the generic small difference of %10 in m_A will neverthless induce considerable discrepencies in $\Omega_{\tilde\chi_1^0}h^2$ when $\tan\beta$ is large, because at that region neutralino annihilation through s-channel pseudoscalar Higgs exchange becomes significant and Higgs annihilation is sensitive to $m_A - 2m_{\tilde\chi_1^0}$. This is illustrated in Figure 2.4 which shows the WMAP upper bound in the $m_0 - m_{1/2}$ plane for $\tan\beta = 50$, with $A_0 = 0$ on the right and $A_0 = -m_{1/2}$ on the left. Even the small $\sim$ %10 variations in m_A are able to generate significant discrepencies in $\Omega_{\tilde\chi_1^0}h^2$.

Large A_0 case and effects of stop co-annihilation: Figure 2.5 shows on the left $m_{\tilde t_1}$ vs A_0 with other parmeters as in P. As $|A_0|$ gets large, $m_{\tilde t_1}$ decreases, becoming close to $m_{\tilde\chi_1^0}$ and $\delta m_{\tilde t_1}$ also increases, where especially ISAJET gives a lower $m_{\tilde t_1}$ value. At $m_{\tilde t_1} \sim m_{\tilde\chi_1^0}$, contribution from stop co-annihilation ($\tilde\chi_1^0\tilde t_1 \to X$) dominate in $\Omega_{\tilde\chi_1^0}h^2$ calculation, hence $\Omega_{\tilde\chi_1^0}h^2$ will be sensitive to small differences in $m_{\tilde t_1}$, as shown in the right panel of Figure 2.5. The visibly low $m_{\tilde t_1}$ from ISAJET has a drastic impact, pushing the ISAJET $m_{\tilde\chi_1^0} = m_{\tilde t_1}$ boundary up to $m_0 \sim 250 - 300$, that increases with increasing $m_{1/2}$. Even when ISAJET is excluded, the uncertainties in $\Omega_{\tilde\chi_1^0}h^2$ still can reach beyond %30.

We conclude that the precise measurement of mass differences $m_{\tilde\tau_1} - m_{\tilde\chi_1^0}$, $m_A - 2m_{\tilde\chi_1^0}$ and

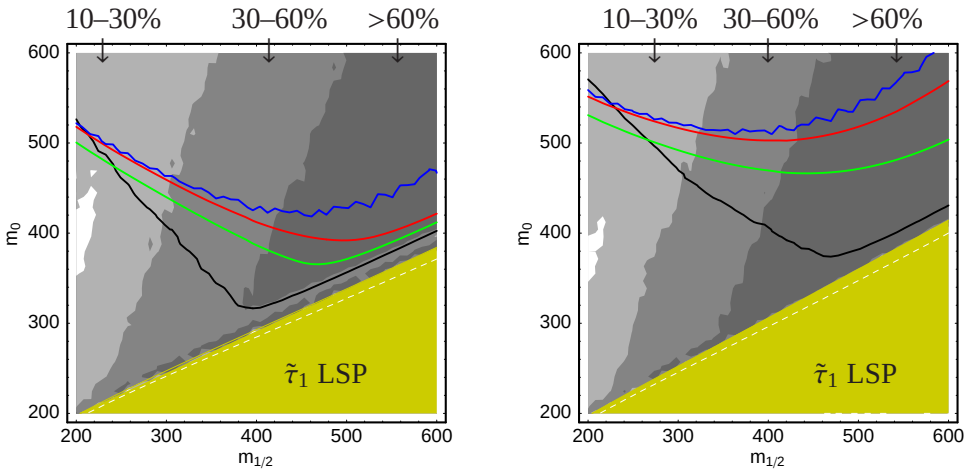

Figure 2.4: Upper bound from the relic denisty, $\Omega_{\tilde{\chi}_1^0}h^2 = 0.136$, on the $m_{1/2}$–m_0 plane for $\tan\beta = 50$ and $A_0 = 0$ (left) and $A_0 = -m_{1/2}$ (right). The black, red, green and blue lines are for ISAJET, SOFTSUSY, SPHENO and SUSPECT respectively. Also shown is the corresponding $\delta\Omega_{\tilde{\chi}_1^0}h^2$ in grey. The triangular yellow regions are excluded by stau LSP.

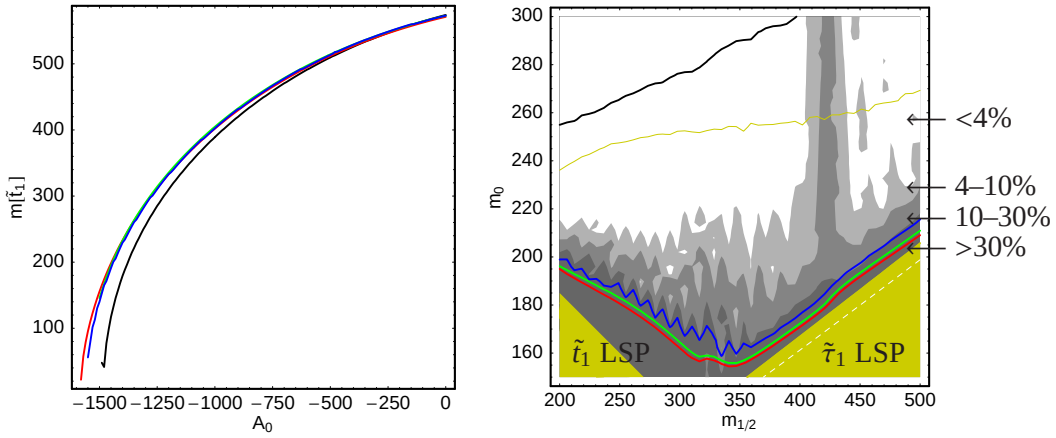

Figure 2.5: Light stop mass $m_{\tilde{t}_1}$ as a function of A_0 for $m_0 = 500$ GeV, $m_{1/2} = 300$ GeV, $\tan\beta = 10$, $\mu > 0$ and $m_t = 175$ GeV (left) and upper bound from the relic denisty, $\Omega_{\tilde{\chi}_1^0}h^2 = 0.136$, in the $m_{1/2}$–m_0 plane for $\tan\beta = 10$, $A_0 = -4m_{1/2}$, $\mu > 0$ and $m_t = 175$ GeV (right). The black, red, green and blue lines are for ISAJET, SOFTSUSY, SPHENO and SUSPECT respectively. Also shown are the corresponding $\delta\Omega_{\tilde{\chi}_1^0}h^2$ for SOFTSUSY, SPHENO and SUSPECT. The yellow regions are excluded because of a stau or stop LSP for the above 3 codes. The yellow line gives the $m_{\tilde{t}_1} = m_{\tilde{\chi}_1^0}$ boundary for ISAJET.

$m_{\tilde{t}_1} - m_{\tilde{\chi}_1^0}$ is crucial for a reliable determination of $\Omega_{\tilde{\chi}_1^0}h^2$, especially in judging the compatibility of a given SUSY scenario with dark matter. We also extended the study by comparing spectra for models with non-universal Higgs masses. The details will not be given here, but we found very good agreement in moderate regions for spectra and $\Omega_{\tilde{\chi}_1^0}h^2$. Only in the edges of parameter space, e.g., for large $m_{H_d}^2 - m_{H_u}^2$ we found up to %10 differences in slepton masses.

CHAPTER 3

PHENOMENOLOGY OF THE G_2-MSSM

3.1 Introducing strings

We mentioned that even SUSY can be a subset of a more fundamental framework which offers descriptions for physics beyond the GUT scale. One developing and much debated approach is string theory, which aims to unify quantum mechanics and general relativity and formulate the quantum theory of gravity [40],[41],[42],[43]. String theory proposes that fundamental elements are not 0-dimensional points, but 1-dimenstional extended objects called strings, whose different modes of vibrations embody particles with specific charge, flavor, mass and spin. It can be formulated by an action principle that can be solved to achieve the motion of strings in spacetime, which are described by worldsheets. The interactions of particles are given by splittings and recombinations of strings.

Over the years, five distinct supersymmetric, 10-dimensional string theories were formulated, and it was thought that only one of those would survive as the correct theory. But in 1995, M theory emerged from 11 dimensions, and showed that those distinct theories were in fact different descriptions of the same fundamental phenomenon. It connected the five theories to each other via dualities in distance scales and coupling strengths.

However, though it is a prominent mathematical framework, string theory faces the great challange of making a unique prediction for the observable low energy world. There are numerous ways to compactify the extra dimensions on various manifolds and end up with the 4 spacetime dimensions. The string theory landscape is vast, with $\sim 10^{500}$ vacua, and it is not clear if there is a decisive principle to choose a metastable vacuum that leads to the known laws of physics, i.e: the Standard Model and General Relativity with a positive cosmological constant - to a configuration of string theory consistent with observation.

But this is exactly what we care for: a phenomenologically consistent theory. To achieve

this, a class of string vacua arising from compactification to four dimensions need to

- have $N = 1$ supersymmetry and produce SUSY breaking,
- generate hierarchy between EW and Planck scales by stabilizing the moduli [1] in a metastable dS vacuum,
- have a visible sector that hosts the MSSM particle content and gauge group (maybe plus additional matter fields and gauge groups) and their properties,
- have an electoweak symmetry breaking mechanism,
- unify gauge couplings.

If MSSM visible content is realized in these constructions, then a set of soft supersymmetry breaking parameters will be generated after SUSY breaking, which are defined by the internal parameters of the string model. Recently there have been considerable attempts to construct a stringy framework which addresses the above issues within the Type IIB or M theory setup. Examples include visible sector construction via Type IIB KKLT vacua [45],[46],[47], Type IIB LARGE volume vacua [48],[49] and fluxless M theory vacua on G_2 manifolds [50],[51]. A generic description of these models among with a prospective LHC study has been given in [52]. Here we will concentrate on the final case, that has come to be known as the G_2-MSSM, detailed calculations of which can be found in [53].

3.2 The G_2-MSSM

G_2-MSSM is a low energy limit of M theory. It was shown that through fluxless [2] compactifications of M theory on a G_2 manifold, it is possible to achieve $N = 1$ SUSY in 4 dimensions with non-Abelian gauge groups and chiral fermions; generate the hierarchy and stabilize all moduli in a dS vacuum. In the simplest case, the G_2 manifold consists of two hidden sectors that live on two 3-dimensional submanifolds with asymptotically free gauge groups. These undergo strong gauge dynamics, and at least one contains light charged matter fields Q and

[1] Moduli are scalar fields whose different values are equally good since potential energy for moduli are constant. In string theory, they are used for parametrizing string backgrounds, which are defined as a set of classical values of quantum fields in spacetime that correspond to classical solutions of string theory. Physics of string theory is imagined as a set of infinitely many quantum fields expanded around a given string background. Examples for string backgrounds are the dilaton field expectation value, various coupling constant values, allowed shape (radius and complex structure) of the internal manifold and Wilson lines of the gauge fields around non-trivial cycles.

[2] Zero flux generates an entirely non-perturbative moduli superpotential, and is necessary to obtain a small mass scale of the order of TeV.

$\tilde{Q}$. Then there is the usual visible sector living on another three-dimensional submanifold. G_2-MSSM is defined by the following hidden sector superpotential

$$\mathcal{W} = m_p^3 \left(C_1 P \phi^{-(2/P)} e^{ib_1 f_1} + C_2 Q e^{ib_2 f_2} \right);\ b_1 = \frac{2\pi}{P},\ b_2 = \frac{2\pi}{Q}. \tag{3.1}$$

Here $\phi \equiv \det(Q\tilde{Q})^{1/2} = (2Q\tilde{Q})^{(1/2)}$ is the effective hidden sector meson field that generates the spontaneous SUSY breaking, P and Q are the ranks of the hidden sector gaugino condensation groups, C_1, C_2 are normalization constants that depend on the specific choice of G_2 manifold and f_1, f_2 are the hidden sector gauge kinetic functions which are two different linear combinations of the N geometric moduli s_i of the G_2 manifold. As mentioned in Chapter 2, the superpotential, which here depends on the microscopic parameters of G_2 compactification determines the Lagrangian of the low energy effective theory where the phenomenologically relevant parameters are defined.

In G_2 compactification, SUSY breaking is mediated via the higher-dimensional gravity multiplet, which gives rise to gravity (moduli) mediation. However anomaly mediation also makes significant contribution to gaugino masses.

Consequently, the high scale gaugino masses take the form

$$M_a \approx \frac{1}{4\pi(\alpha_{unif}^{-1} + \delta)} \left\{ b_a + \left(\frac{4\pi\alpha_M^{-1}}{P_{\text{eff}} - b'_a \phi_0^2} \right) \left(1 + \frac{2}{\phi_0^2 (Q+P)} \right) \right\} m_{3/2} \tag{3.2}$$

with $b_1 = 33/5$, $b_2 = 1.0$, $b_3 = -3.0$, $b'_1 = -33/5$, $b'_2 = -5.0$, $b'_3 = -3$, where α_M is the tree-level universal gauge coupling, δ is the threshold correction from the Kaluza-Klein modes, which comes as a contribution from the anomaly mediation, ϕ_0 is the VEV of the meson field, which is order of unity and $P_{\text{eff}} \equiv P(C_1/C_2)$. Low scale SUSY can only be obtained for $Q - P = 3$. Also $50 < P_{\text{eff}} < 84$ should be taken to get a gravitino mass $m_{3/2} < 100$ TeV. $m_{3/2}$ also depends largely on V_7, the volume of the compactification manifold. Gaugino masses are light, with $M_a \leq$TeV. The scalar masses, Higgsino masses and trilinear couplings turn out to be $m_0 \sim A_0 \sim m_{H_u} \sim m_{H_d} \sim \mathcal{O}(m_{3/2})$ and are around 30-100 TeV.

At the weak scale, scalars are very heavy with masses $\mathcal{O}(10)$TeV where exceptionally lightest stop is significantly light ($\leq$ 1TeV) due to RGE running. Gauginos are light, and have masses $\leq$TeV. Moreover $\tan\beta$ is predicted from the high scale theory to be $\mathcal{O}(1)$. The value of m_Z however is fine tuned. G_2-MSSM is consistent with GUT scale gauge unification and the consistent solutions lead to a wino LSP, which annihilate more efficiently than binos due to stronger $SU(2)$ coupling g_2. This leads to a dark matter relic density much lower than the WMAP upper limit, and means that G_2-originating LSPs must be produced by non-thermal

mechanism, details of which is related to the cosmological evolution of moduli after inflation. A future study is expected to address this issue more elaborately [54].

A SUSY model which is a direct descendent of strings would be an interesting prize to chase at the LHC. To exercise this, we will adopt two of the four benchmarks proposed in Table 1 of [53], namely the Points 1 and 4, for which we list the microscopic parameters, important EW scale parameters and $\Omega_{\tilde{\chi}_1^0}h^2$ in Table 3.2.

Table 3.1: Microscopic parameters (first 5 columns) as explained in the text, some EW scale parameters (columns 6-10) and $\Omega_{\tilde{\chi}_1^0}h^2$ for benchmark Points 1 and 4 from Table 1 of [53] which are renamed as G21 and G24 respectively. $P-Q=3$ and $P_{eff}=83$. Here Z_{eff} is the effective Higgs bilinear coefficient, which is a complex values function of all hidden sector chiral fields in general and is used in determination of the pases μ and $B\mu$. $\Omega_{\tilde{\chi}_1^0}h^2$ is computed using micrOMEGAs 2.0.7.

Point	δ	$m_{3/2}$	V_7	$\alpha^{-1}_{\text{unif}}$	Z_{eff}	$\tan\beta$	μ	A_t	A_b	A_τ	$\Omega_{\tilde{\chi}_1^0}h^2$
G21	-4	67558	14	26.7	1.58	1.44	87013	14267	3114	1935	3.66×10^{-4}
G24	-10	17091	35	26.0	1.77	1.45	22309	2379	805	468.7	3.15×10^{-4}

In Chapter 7 we will present a discovery analysis with the full CMS detector simulation for these two benchmarks in the all inclusive jets+ missing E_T channel.

CHAPTER 4

PHENOMENOLOGY OF THE SIMPLE SO(10) SUPERSYMMETRIC GUTs

4.1 Introduction and motivation

Yet there is so much way to go until we reach the distant, dreamy realm of strings. Meanwhile it is a good idea to also consider theories built upon simpler and relatively more ground-based assumptions, such as that of the Grand Unification requirement of gauge couplings.

Grand Unification is an inspirational indgredient of models that claim to explain the laws of nature. It is constructed by embedding the EW scale SM gauge group into a larger local symmetry which should be valid above the GUT scale (M_{GUT}). The theoretical understanding of Grand Unification would lead to a unified description of gauge interactions in terms of a single coupling constant as well as a possible quark-gluon unification through whose mechanism the seemingly seperate interactions of these two types of fields could be clarified.

As mentioned in Chapter 2, SM alone cannot unify the gauge couplings at M_{GUT} while supersymmetric contributions introduce modifications to the running of gauge couplings which can make the unification possible. Then beyond M_{GUT}, physics is ruled by a Grand Unified Theory. The main question here is to determine the nature of that Grand Unified Theory.

The simplest candidate is based on the SU(5) group. Here $\hat{D}^C$ and $\hat{L}$ superfields are members of a $\bar{5}$ superfield $\hat{\phi}$ while $\hat{Q}$, $\hat{U}^C$ and $\hat{E}^C$ superfields are assigned to a **10** dimensional representation $\bar{\psi}$. The Higgs sector consists of the supermultiplets $\hat{\mathcal{H}}_1(\bar{5})$ and $\hat{\mathcal{H}}_2(5)$ which contain the MSSM Higgs doublets $\hat{H}_d$ and $\hat{H}_u$ respectively and $\hat{\Sigma}(24)$ which breaks the SU(5) symmetry. The resulting superpotential is given as

$$\begin{aligned} \mathcal{W} &= \mu_\Sigma Tr\hat{\Sigma}^2 + \frac{1}{6}\lambda_\Sigma Tr\hat{\Sigma}^3 + \mu_H\hat{\mathcal{H}}_1\hat{\mathcal{H}}_2 + \lambda\hat{\mathcal{H}}_1\Sigma\hat{\mathcal{H}}_2 \\ &\quad + \frac{1}{4}y_l\epsilon_{ijklm}\hat{\psi}^{ij}\hat{\psi}^{kl}\hat{\mathcal{H}}_2^m + \sqrt{2}y_b\hat{\psi}^{ij}\hat{\phi}_i\hat{\mathcal{H}}_{lj} + \dots . \end{aligned} \tag{4.1}$$

Despite being a predictive scenario that simplifies the MSSM a great deal, SU(5) SUSY GUTs suffer from some problems. For example, they predict the unrealistic mass relation $m_d/m_s = m_e/m_\mu$ at all scales. Furthermore, SU(5) cannot conserve the R-parity naturally and hence does not have a stable candidate for cold DM. There is also no natural mechanism for generating neutrino masses in the SU(5) models, to get which, one would have to introduce right-handed singlet neutrino superfields by hand.

All these issues are succesfully handled when one considers the gauge group SO(10) instead [55]. Here all matter fields in each generation are grouped together with a heavy singlet right-handed neutrino state $\hat{N}^C$ in a 16-dimensional spinorial representation $\bar{\psi}_{16}$, hence leading to matter unification. Furthermore, the two Higgs doublets H_u and H_d lie in a 10-dimensional fundamental representation $\bar{\phi}_{10}$. Such a formalism automatically generates neutrino masses via the see-saw mechanism. The resulting structure of the nuetrino sector implies a successful theory of baryogenesis via intermediate scale leptogenesis. Moreover, the SO(10) group is left-right symmetric, which enables the SO(10) models to provide a solution to the strong CP problem and to naturally induce R parity conservation.

SO(10) contains the maximal subgroups SU(5) $\times$ U(1) and $SO(4)_C \times SU(2)_L \times SU(2)_R \times Z_2$ where the Z_2 group corresponds to charge conjugation. The SU(4) contains the subgroup $SU(3)_C \times U(1)_{B-L}$. Such a rich subgroup structure leads to various alternatives for SO(10) breaking such as

$$\begin{aligned} SO(10) &\rightarrow SU(5) \rightarrow G_{SM} \\ SO(10) &\rightarrow SU(2)_L \times SU(2)_R \times SU(4)_C \times Z_2 \rightarrow G_{SM} \end{aligned} \tag{4.2}$$

where G_{SM} is the SM gauge group. However the idea of gauge coupling unification at M_{GUT} motivates the assumption that SO(10) directly breaks to G_{SM}.

An important characteristic here is that the rank of the SO(10) group (defined as the largest number of mutually commuting generators) is one higher than that of the MSSM gauge group meaning that there should exist an extra $U(1)_X$ symmetry. This excess $U(1)_X$ should be broken far above the EW scale. The U(1) D-term in the scalar potential that determines the VEVs of the fields breaking the extra $U(1)_X$ has an impact on the physics through its contribution to the soft SUSY breaking (SSB) terms at M_{GUT}.

The SSB masses are constrained by the SO(10) symmetry in the GUT scale. Here, the unified scalar fields have the universal soft breaking mass m_{16} at M_{GUT} while the unified Higgs fields have the common mass m_{10}. These are complemented by A_0, $\tan\beta$ and $sgn(\mu)$.

D-term m_D that comes from the breaking of the extra $U(1)_X$ symmetry is an additional free input of the order of EW scale which, according to the U(1) breaking scenario, contributes to the soft scalar or Higgs terms and generates non-universalities.

A very distinguishing feature of the SO(10) models is the additional requirement of the unification of 3rd generation Yukawa couplings at the GUT scale. This is implied by the superpotential which includes the following term

$$\mathcal{W} \ni y\hat{\psi}_{16}\hat{\psi}_{16}\hat{\phi}_{10} + \cdots . \tag{4.3}$$

An exact unification ($y = y_t = y_b = y_\tau = y_{\nu_\tau}$) occurs at the tree level while several percent corrections arise at the loop level due to gauge exchange for $\hat{\psi}_{16}$ and $\hat{\phi}_{10}$, Yukawa exchange with color triplet Higgs fields and with heavy right-handed neutrinos in the loop. Yukawa unification has its direct consequence on the value of $\tan\beta$. Considering the relation

$$\frac{m_t}{m_b} \sim \frac{y_t v_u}{y_b v_t}, \tag{4.4}$$

right hand side can have $y_t \sim y_b$ only if $v_u/v_b = \tan\beta$ is around 50.

These features of SO(10) SUSY GUTs makes them worthy of being investigated in detail. In the following sections we present studies that examine the realization of WMAP-compatible SO(10) scenarios, their collider phenomenology, consequences for axino dark matter and aspects for fine tuning.

4.2 Search for DM-allowed scenarios for Yukawa-unified SO(10) SUSY GUTs

The primary necessity here is to determine the range of SSB parameters that might have originated from the SO(10) SUSY GUTs and the sparticle spectrum resulting from those parameters. In other words, we would like to investigate the characteristics that arise in a SUSY model when the constraints from SO(10) symmetry are imposed.

In this context, we assume a theoretical framework where nature is explained by an SO(10) symmetry above M_{GUT}, which breaks to MSSM plus some heavy right-handed neutrino states at M_{GUT}. Then at the EW scale, content of the theory is equal to that of the MSSM. The main constraint to impose on the parameters besides the universalities explained above is the trademark Yukawa unification quantified as

$$R = \frac{max(y_t, y_b, y_\tau)}{min(y_t, y_b, y_\tau)}. \tag{4.5}$$

One immediate consequence follows from the concern of accommodating radiatively broken electroweak symmetry (REWSB) which, as explained in Chapter 2 should be realized due to

the large top quark mass. REWSB in Yukawa-unified SO(10) SUSY scenarios is achieved by a soft Higgs mass splitting which has $m_{H_U}^2 < m_{H_d}^2$. This splitting can be parametrized using the D-term contribution from the extra $U(1)_X$ symmetry as

$$m_{U,D}^2 = m_{10}^2 \mp 2M_D^2. \tag{4.6}$$

and is a crucial ingredient in search for Yukawa-unified scenarios.

There have been two lines of approach in imposing Yukawa unification: One method by Blazek, Derimsek and Raby (BDR) [56] uses a top-down approach in which they assume exact unification at M_{GUT}, and give the three gaugino parameters M_G, gauge couplings $\alpha_G(M_{GUT})$, the unification uncertainty ϵ_3, unified Yukawa coupling y and 7 SSB parameters μ, $m_{1/2}$, A_0, $\tan\beta$, m_{16}, m_{10} and an arbitrary Higgs splitting Δm_H^2 as input. They evolve down these parameters with 2-loop gauge and Yukawa running and 1-loop soft term running. Then they make a χ^2 fit of the resulting low energy parameters α_{EM}, G_F, $\alpha_s(m_Z)$, m_Z, m_W, ρ, m_t, $m_b(m_b)$ and m_τ to the central observed values (within the experimental uncertainties) and determine the parameter regions that minimize the χ^2.

The other method used by Auto, et. al. [57] considered a bottom-up approach where there were no apriori assumptions of GUT scale Yukawa unification during spectrum computation. Instead, the measured values of the EW precision observables mentioned above were given as input among with the GUT scale SUSY parameters. The spectrum computation was done using ISAJET 7.64 where the RGE running first starts with the inputs at weak scale. Then the unification degree of the resulting Yukawa couplings are checked and those points having $R < 1.1$ were identified as potential SO(10) scenarios.

Both groups tried the two different realizations of SO(10), namaly the D-term scenario where the $U(1)_X$ D-term invokes non-universalities in scalars and the Higgs splitting (HS) scenario where only m_{H_u} and m_{H_d} are non-universal. Both studies showed that Yukawa-unification was harder to reach for the D-term scenario. Auto et. al. reported that $R \sim$ %5 was possible for $\mu < 0$, however latest results reported by BNL on the value of the anomolous magnetic moment of muon favor positive μ solutions in which the best R reached is $\sim$ %30 – 50. For the HS model, BDR found Yukawa-unified results for $m_A \sim 100$ GeV and $\mu \sim 100 - 200$ GeV. These however are in contrast with findings of [58] which claims that solutions with valid REWSB could only occur for $\mu \sim m_A \sim m_{\tilde{t}_1} \sim 1$ TeV. On the other side, Auto et. al. reported down to few percent Yukawa unification only for very large values of $m_{16} > 5 - 10$ TeV and low values of $m_{1/2} < 100$ GeV for positive μ.

Driven by these results we performed a study following the Auto et.al. approach which aimed a more detailed search for Yukawa-unified solutions in the HS parameter space [59]. For this study we used ISAJET 7.75 where spectrum calculation begins with inputting $\overline{\text{DR}}$ gauge couplings and y_b, y_τ at $Q = M_Z$. Also taking y_t on the way at $Q = m_t$, the six couplings run to M_{GUT} (where $g_1 = g_2$) using 2-loop RGEs. Here, the boundary conditions from SSB parameters are imposed and the resulting 26 MSSM RGEs are run down back to $Q = M_Z$. Soft terms are run with full 2-loop RGEs while gauge and Yukawa running is done by 1-loop RGEs that include threshold effects in the beta functions to achieve a smooth transition of couplings from MSSM to SM at different mass scales. Once tree-level sparticle masses are computed, full 1-loop radiative corrections are calculated for all sparticle and Higgs masses, including complete 1-lopp weak scale threshold corrections for the t, b and τ masses at $Q = M_{SUSY} = \sqrt{m_{\tilde{t}_L} m_{\tilde{t}_R}}$. As GUT scale Yukawa couplings are modified by the threshold corrections, the RGEs are applied iteratively to account for these until a convergent solution is reached.

We examined the outcome of two different methods to generate the required Higgs splitting, of which first is the parametrization given by Eq. 4.6. The parameters of this GUT-scale Higgs input (GSH) scenario are

$$m_{16},\ m_{10},\ M_D^2,\ m_{1/2},\ A_0,\ \tan\beta,\ sign(\mu). \tag{4.7}$$

The second approach was put forward in order to generate BDR-like solutions with low μ and m_A. ISAJET allows a case where the EW scale values of μ and m_A can be input by hand. Thus one can force small values of μ and m_A to examine the consequences. Here we start with a set of GSH parameters at M_{GUT} plus μ and m_A as inputs. Then soft Higgs masses m_{H_u} and m_{H_d} are evaluated down, and at $Q = M_{SUSY}$, the values that m_{H_u} and m_{H_d} should have taken in order to give our input μ and m_A are computed using the following two 1-loop EW symmetry breaking minimization conditions.

$$B = \frac{(m_{H_u}^2 + m_{H_d}^2 + 2\mu^2)\sin 2\beta}{2\mu} \tag{4.8}$$

$$\mu^2 = \frac{m_{H_d}^2 - m_{H_u}^2 \tan^2\beta}{\tan^2\beta - 1} - \frac{M_Z^2}{2} \tag{4.9}$$

These boundary conditions are used to run back to the GUT scale resulting in the output of GUT scale m_{H_u} and m_{H_d}. This process is repeated at each iteration until a stable solution is found. This weak scale Higgs (WSH) input scenario is defined by the following parameters

$$m_{16},\ m_{10},\ M_D^2,\ m_{1/2},\ A_0,\ \tan\beta,\ \mu,\ m_A. \tag{4.10}$$

We searched the parameter spaces of GSH and WSH scenarios to look for regions having a good Yukawa unification as well as a WMAP-compatible DM relic density. We adopted the Markov Chain Monte Carlo technique that allows for a much efficient scan with respect to regular random parameter scans. Besides the RGE code ISASUGRA of ISAJET 7.75, we used a specially adopted version of micrOMEGAs 2.0.7 [60] for relic density computations that can accommodate the WSH input [1]. The input top mass was taken as 171 GeV.

4.2.1 The Markov Chain Monte Carlo method

A Markov Chain [62] is a discrete-time, random process having the Markov property, which is defined such that given the present state, the future state only depends on the present state, but not on the past states. This can be expressed as

$$P(X^{t+1} = x|X^t = x^t, ..., X^1 = x^1) = P(X^{t+1} = x|X^t = x_t). \tag{4.11}$$

An MCMC constructs a Markov chain through sampling from a parameter space with the help of a specified algorithm. In this study, we have applied the Metropolis-Hastings algorithm [63] which generates a candidate state x^c from the present state x^t using a proposal density $Q(x^t; x^c)$. The candidate state is accepted to be the next state x^{t+1} if the ratio

$$p = \frac{P(x^c)Q(x^t; x^c)}{P(x^t)Q(x^c; x^t)} \tag{4.12}$$

(where $P(x)$ is the probability calculated for the state x) is greater than a uniform random number $a = U(0, 1)$. If the candidate is not accepted, the present state x^t is retained and a new candidate state is generated. For the proposal density we use a Gaussian distribution that is centered at x^t and has a width σ. This simplifies the p ratio to $P(x^c)/P(x^t)$.

Once taking off from a starting point, Markov chains are aimed to converge at a target distribution $P(x)$ around a point with the highest probability. The time needed for a Markov chain to converge depends on the width of the Gaussian distribution used as the proposal density. This width can be adjusted during the run to achieve a more efficient convergence.

While searching the SO(10) parameter space, we assume flat priors and we approximate the likelihood of a state to be $e^{-\chi^2(x)}$. We define the χ^2 for R as

$$\chi^2_R = \left(\frac{R(x) - R_{unification}}{\sigma_R}\right)^2 \tag{4.13}$$

[1] This triggered some modifications in SUSY Les Houches Accord II [61], resulting in an arrangement that allows to input parameters at different scales

where $R_{unification} = 1$ and σ_R is the discrepancy we allow from absolute Yukawa unification, which in this case we take to be 0.05. On the other hand, for $\Omega_{\tilde{\chi}_1^0}h^2$ we define

$$\chi^2_{\Omega_{\tilde{\chi}_1^0}h^2} = \begin{cases} 1, & (0.094 \leq \Omega_{\tilde{\chi}_1^0}h^2 \leq 0.136) \\ \left(\frac{\Omega_{\tilde{\chi}_1^0}h^2(x) - \Omega_{\tilde{\chi}_1^0}h^2_{mean}}{\sigma_{\Omega_{\tilde{\chi}_1^0}h^2}}\right)^2, & (\Omega_{\tilde{\chi}_1^0}h^2 < 0.094 \text{ or } \Omega_{\tilde{\chi}_1^0}h^2 > 0.136) \end{cases} \tag{4.14}$$

where $\Omega_{\tilde{\chi}_1^0}h^2_{mean} = 0.115$ is the mean value of the range $0.094 < \Omega_{\tilde{\chi}_1^0}h^2 < 0.136$ proposed in [30], and $\sigma_{\Omega_{\tilde{\chi}_1^0}h^2} = 0.021$. This way, the MCMC primarily searches for regions of Yukawa-unification, and within these regions, for solutions with a good relic density.

For each search, we select a set of ~ 10 starting points in order to ensure a more thorough investigation of the parameter space. Then we run the MCMC, aiming to maximize the likelihood of either R alone, or R and $\Omega_{\tilde{\chi}_1^0}h^2$ simultaneously. For the case of simultaneous maximization, we compute the p ratios for R and $\Omega_{\tilde{\chi}_1^0}h^2$ individually, requiring both $p_R > a$ and $p_{\Omega_{\tilde{\chi}_1^0}h^2} > a$ separately. We do not strictly seek convergence to an absolute maximal likelihood, but we rather use the MCMC as a tool to reach compatible regions and to investigate the amount of their extension in the SO(10) parameter space.

4.2.2 The GSH solutions

We begin our MCMC scans by selecting 10 starting points "pseudorandomly" –that is, selecting them from different m_{16} regions to cover a wider range of the parameter space– and imposing some loose limits (defined by previous works and random scans) on the rest of their parameters to achieve a more efficient convergence. Our initial scan is directed to look for points only with R as close to 1.0 as possible by maximizing solely the likelihood of R. Based on the results of the first MCMC scan, we then pick a new set of 10 starting points with low R and also low $\Omega_{\tilde{\chi}_1^0}h^2$, and direct the second set of scans to look for points with both $R = 1.0$ and $\Omega_{\tilde{\chi}_1^0} < 0.136$ by maximizing the likelihoods of R and $\Omega_{\tilde{\chi}_1^0}h^2$ simultaneously. For MCMC scans, the code is interfaced to the micrOMEGAs package to evaluate the relic density and low-energy constraints.

Figure 4.1 shows the compatible regions as projections in the planes of various input parameter pairs. Here the light-blue dots have $R < 1.1$, the dark blue dots have $R < 1.05$, the orange dots have $R < 1.1$ plus $\Omega_{\tilde{\chi}_1^0}h^2 < 0.136$ and the red dots have $R < 1.05$ plus $\Omega_{\tilde{\chi}_1^0}h^2 < 0.136$. On the m_{10} vs m_{16} plane Yukawa unification is seen only at the regions having the correlation $m_{10} \simeq 1.2m_{16}$. A good R is feasable for m_{16} values from ~ 3 TeV to

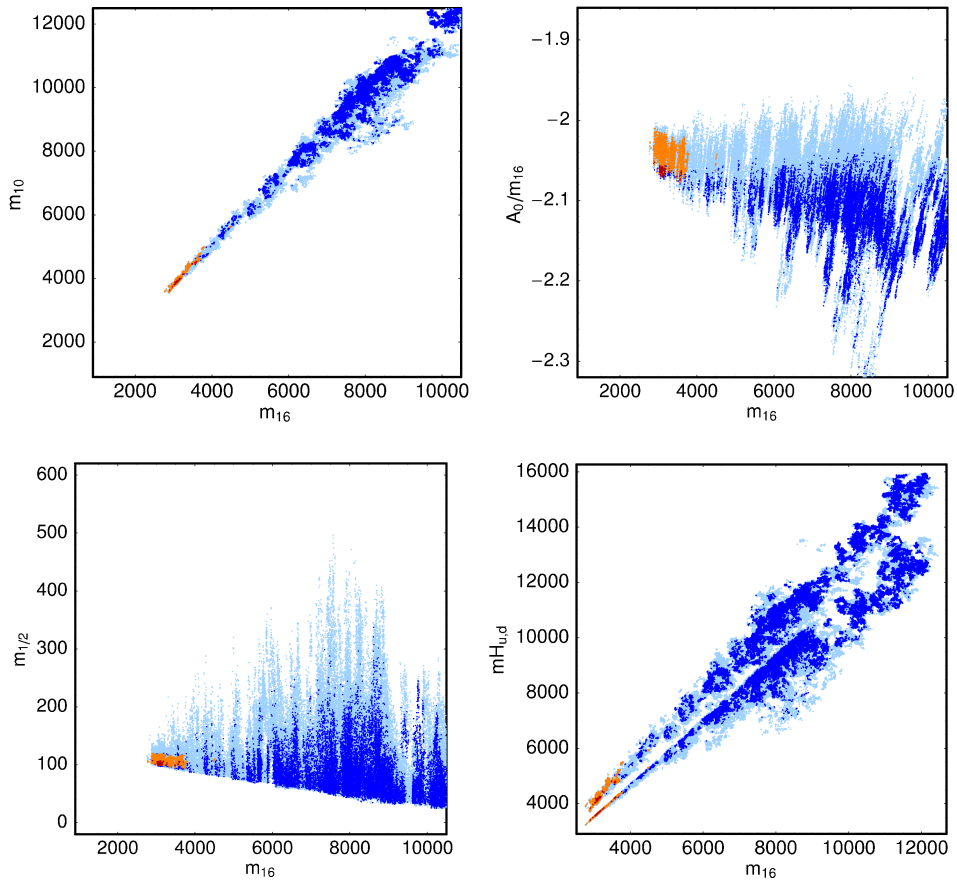

Figure 4.1: Yukawa-unified GSH points found by MCMC on the m_{10} vs. m_{16} (top left), A_0/m_{10} vs. m_{16} (top right), $m_{1/2}$ vs m_{16} (bottom left) and $m_{H_{u,d}}$ vs. m_{16} (bottom right) planes; the light-blue (dark-blue) points have $R < 1.1$ (1.05), while the orange (red) points have $R < 1.1$ (1.05) plus $\Omega_{\tilde{\chi}_1^0}h^2 < 0.136$.

$>$ 10 TeV, however a good relic density is achieved only for $m_{16} \sim 3-4$ TeV. Concerning A_0, the Yukawa unified solutions obey the relation $A_0 \simeq -(2-2.1)m_{16}$. The $m_{16} - m_{10}$ and $m_{16} - A_0$ correlations agree with those suggested in a study by Bagger et. al. [64] in the context of radiatively driven inverted scalar mass hierarchy models where RG running of multi-TeV GUT scale scalar masses cause 3rd generation masses to be driven to weak scale values while 1st/2nd generation soft terms remain in the multi-TeV regime. These models, which also required Yukawa unification were designed to maintain low fine-tuning by having light 3rd generation scalars while solving the SUSY flavor and CP problems via multi-TeV 1st/2nd generation scalars.

On the bottom left plot, we see that $m_{1/2}$ takes the lowest possible values for a given m_{16}, generally giving $\sim$ 100 GeV, and it decreases steadily with increasing m_{16}. The final plot shows the individual GUT-scale values of Higgs soft terms m_{H_u} and m_{H_d} which proves that $m_{H_u} < m_{H_d}$ is a requirement to achieve solutions in the Yukawa-unified cases.

This MCMC search discovered a new class of Yukawa-unified solutions with WMAP-compatible relic density where the relic density is adjusted by an efficient annihilation of $\tilde{\chi}_1^0$s via a light Higgs resonance. This can be seen from Figure 4.2 which shows $m_A - 2m_{\tilde{\chi}_1^0}$ vs. $m_h - 2m_{\tilde{\chi}_1^0}$. Here all solutions with $\Omega_{\tilde{\chi}_1^0}h^2 < 0.136$ uniquely lie along the $m_h = 2m_{\tilde{\chi}_1^0}$ line. On the other hand, annihilation via an A-resonance does not assume a special role since the WMAP-compatible solutions are scattered randomly along the y-axis and there is no accumulation close to $m_A = 2m_{\tilde{\chi}_1^0}$. The h-resonance solutions with $R < 1.1$ occur at the $m_{16} \sim 3-4$ TeV region since higher m_{16} values cannot accommodate a sufficient decrease in $\Omega_{\tilde{\chi}_1^0}h^2$. On the other hand, lowest R values favor larger m_{16} regions and the best R we get for the $3-4$ TeV, h-resonance solutions is $\sim$ 1.03.

The highly confined SO(10) parameter regions lead to strongly constrained mass spectra, and hence to significant LHC signatures. We see that Yukawa-unified solutions are distinguished by their heavy 1st/2nd generation scalars ($>$ 2 TeV), lighter 3rd generation scalars ($\sim$TeV) and light gauginos (few hundred GeV). All Higgsses except h are about $1-3$ TeV. Figure 4.3 shows the distribution of selected points on $m_{\tilde{t}_1}$ vs $m_{\tilde{g}}$ plane (left), and on m_h vs $m_{\tilde{\chi}_2^0} - m_{\tilde{\chi}_1^0}$ plane (right) for the GSH scenario. The requirement of $\Omega_{\tilde{\chi}_1^0}h^2 < 0.136$ favors a gluino mass range around $350-450$ GeV, which means we would expect a large amount of gluino pair production at the LHC with cross sections about $\sim$ 100 pb. These gluinos decay via 3-body channels such as $\tilde{g} \to \tilde{\chi}_1^0 b\bar{b}, \tilde{\chi}_2^0 b\bar{b}, \tilde{\chi}_1^{\pm} t\bar{b}/b\bar{t}$, because 2-body channels are closed due to the high squark masses. Favored $\tilde{\chi}_2^0 \simeq \tilde{\chi}_1^{\pm}$ mass range is $100-150$ GeV, which

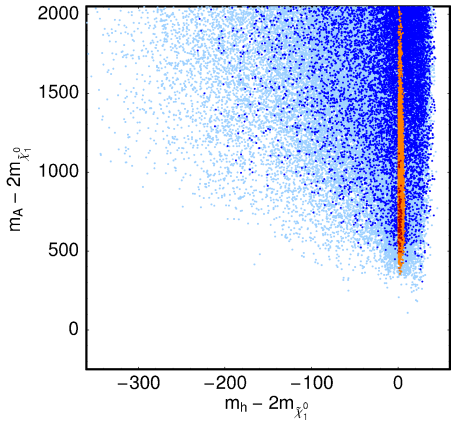

Figure 4.2: Plot of MCMC scan points on the $m_A - 2m_{\tilde{\chi}_1^0}$ vs. $m_h - 2m_{\tilde{\chi}_1^0}$ plane with $R <$ 1.1 (1.05) for dark-blue (light-blue) dots. We also show points with both $\Omega_{\tilde{\chi}_1^0}h^2 < 0.136$ and $R <$ 1.1 (1.05) as orange (red) dots.

leads to gaugino pair production cross sections about $\sim$ 10 pb, while the preferred $m_{\tilde{\chi}_1^0}$ is $\sim 50 - 75$ GeV. This results in a signature mass difference $m_{\tilde{\chi}_2^0} - m_{\tilde{\chi}_1^0}$ of $52 - 65$ GeV which is smaller than $m_{Z,h}$, therefore $\tilde{\chi}_2^0$ decays are dominated again by 3-body channels such as $\tilde{\chi}_2^0 \to b\bar{b}\tilde{\chi}_1^0, q\bar{q}\tilde{\chi}_1^0, l\bar{l}\tilde{\chi}_1^0$. Two sample GSH benchmarks will be explored in detail in the coming parts of this work.

4.2.3 The WSH solutions

Previous searches by Auto et. al. as well as our MCMC scans with the GSH input were not able to reproduce the low μ–low m_A BDR solutions, the smallest values found for μ and m_A being around 1 TeV. We made a further study with the MCMC using the weak scale Higgs (WSH) input explained above to see if one can generate these solutions with ISAJET despite the differences in spectrum computations.

Here again we start with 10 points pseudorandomly selected from the WSH parameter space and implement two MCMC scans on them: one that searches for solutionss with lowest R values by maximizing the likelihood of R, and the other that serches for solutions with both good R and $\Omega_{\tilde{\chi}_1^0}h^2$ by minimizing likelihoods of R and $\Omega_{\tilde{\chi}_1^0}h^2$ simultaneously.

Figure 4.4 shows the distribution of solutions in the WSH parameter space. The $m_{16} - A_0$ correlation is similar to GSH case, respecting the Bagger et. al. condition of $A_0 \approx -(2 - 2.1)m_{16}$, but differing from GSH in the sense that now there are additional good dark matter solutions scattered in $m_{16} \sim 3 - 6$ TeV range which will be discussed soon. The second frame

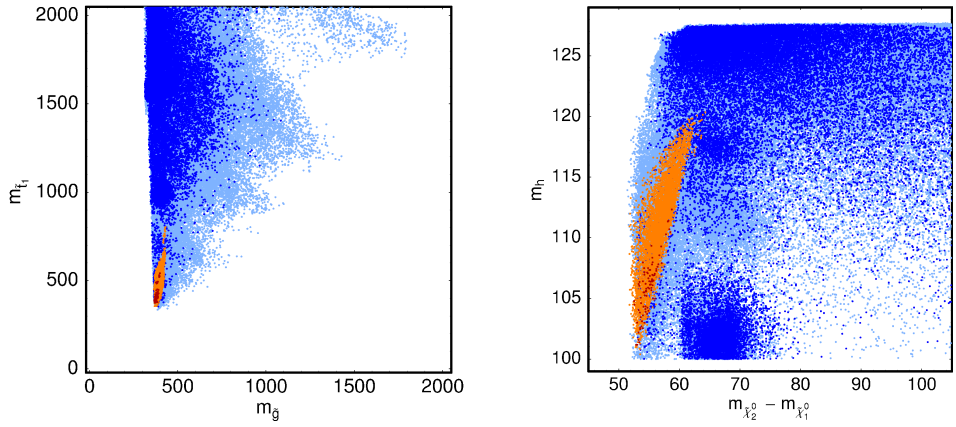

Figure 4.3: Plot of MCMC results for the GSH scenario on the $m_{\tilde{t}_1}$ vs. $m_{\tilde{g}}$ plane (left) and the m_h vs. $m_{\tilde{\chi}_2^0} - m_{\tilde{\chi}_1^0}$ plane (right); the light-blue (dark-blue) points have $R < 1.1$ (1.05), while the orange (red) points have $R < 1.1$ (1.05) plus $\Omega_{\tilde{\chi}_1^0} h^2 < 0.136$.

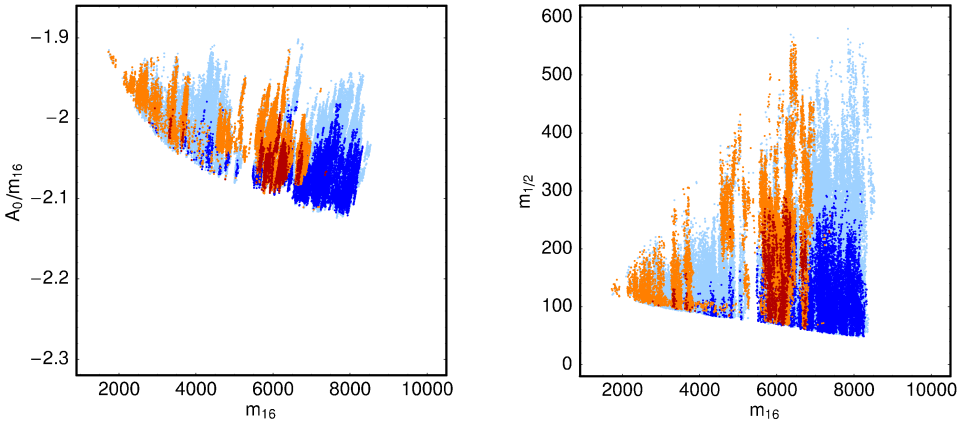

Figure 4.4: Plot of MCMC scan points using WSH boundary conditions on the A_0/m_{16} vs. m_{16} plane (left) and $m_{1/2}$ vs. m_{16} plane (right) with $R < 1.1$ (1.05) for dark-blue (light-blue) dots. We also show points with both $\Omega_{\tilde{\chi}_1^0} h^2 < 0.136$ and $R < 1.1$ (1.05) as orange (red) dots.

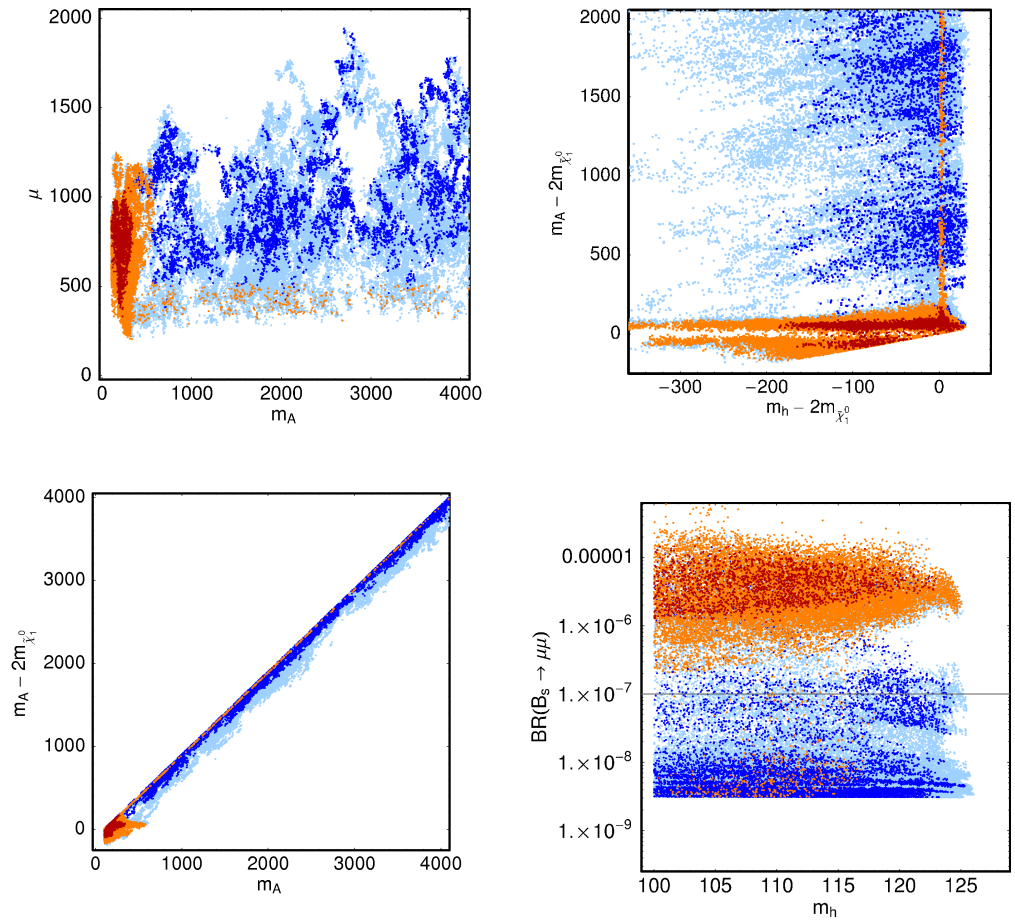

Figure 4.5: Plot of MCMC scan points using WSH boundary conditions on the μ vs. m_A (top left), $m_A - 2m_{\tilde{\chi}^0_2}$ vs. $m_h - 2m_{\tilde{\chi}^0_2}$ plane (top right), $m_A - 2m_{\tilde{\chi}^0_2}$ vs. m_A (bottom left) and $BD(B_s - \mu\mu)$ (botttom right) planes with $R < 1.1$ (1.05) for dark-blue (light-blue) dots. We also show points with both $\Omega_{\tilde{\chi}^0_1}h^2 < 0.136$ and $R < 1.1$ (1.05) as orange (red) dots.

shows $m_{1/2}$ vs m_{16} where we see that for the WSH case larger values of $m_{1/2}$, ranging up to 600 GeV are WMAP compatible.

Figure 4.5 shows the solutions on the $\mu - m_A$ plane on the top left. Most of the DM-allowed solutions are accumulated in the $m_A \sim 130 - 250$ GeV range. Since those solutions were not hinted by the GSH search, one can conclude that they are highly fine-tuned. To investigate the source of WMAP compatibility, we plot $m_A - 2m_{\tilde{\chi}^0_1}$ vs $m_h - 2m_{\tilde{\chi}^0_1}$ on the top right. The vertical narrow strip corresponds to $m_h \sim 2m_{\tilde{\chi}^0_1}$, where the efficient neutralino annihilation is provided by light Higgs exchange whereas the horizontal thick bunch corresponds to the neutralino annihilation via A-resonance. In the down-left plot we show $m_A - 2m_{\tilde{\chi}^0_1}$ vs m_A, which confirms that it is the A-resonance mechanism that dominates the $\Omega_{\tilde{\chi}^0_1}h^2$ reduction at

the low values of m_A.

The fact that A-resonance solutions simultaneously have a large $\tan\beta$ of ~ 50 along with the low A masses raises the issue of agreement with the measured limit of $BR(B_s \to \mu\mu)$ since this BR is a function of $\tan^6\beta/m_A^4$. To check this we plot $BR(B_s \to \mu\mu)$ versus m_h in down right plot of Figure 4.5 and see that all A-resonance solutions are in fact excluded by the current CDF limit of 10^{-7} as expected. Therefore we conclude that, despite finding some low μ-low m_A solutions with ISAJET we can not straightforwardly reproduce a physically consistent BDR case. One can seek optional ways to achieve low m_A solutions with a consistent $BR(B_s \to \mu^+\mu^-)$ through introducing flavor violating soft terms. This class of solutions would lead to wider perspective of LHC signatures: e.g.: in the dark matter allowed regions, $m_{\tilde{\chi}_1^0}$ goes up to $\sim$ 250 GeV and $m_{\tilde{g}}$ goes up to 260 GeV. The mass difference $m_{\tilde{\chi}_2^0} - m_{\tilde{\chi}_1^0}$ would go up to $\sim$ 150 GeV for $R < 1.05$ and $\sim$ 230 GeV for $R < 1.1$, which are greater than $m_{h,Z}$, so the two body decays that are forbidden for the GSH case can now be realized.

4.2.4 Adjusting the DM relic density

The plots in the previous two sections, especially for the GSH case show us that majority of the Yukawa-unified solutions give an excess DM relic density. Below we propose some ideas, which either present a point of view where the DM excess is not a problem or in case it is perceived so, suggest a method to reduce $\Omega_{\tilde{\chi}_1^0}h^2$ below the WMAP upper limit.

4.2.4.1 $\tilde{\chi}_1^0$ may not be the LSP...

The first way out of the situation is to assume that $\tilde{\chi}_1^0$ is not the LSP, but is the next to lightest sparticle (NLSP) and can actually decay to lighter modes like gravitinos ($\tilde{G}$) or axinos ($\tilde{a}$). The decays can be realized via the mode $\tilde{\chi}_1^0 \to \gamma\tilde{G}/\tilde{a}$. The relic density of the axinos/gravitinos thus non-thermally produced from neutralino decays [2] are given by

$$\Omega_{\tilde{G}/\tilde{a}}h^2 = \frac{m_{\tilde{G}/\tilde{a}}}{m_{\tilde{\chi}_1^0}}\Omega_{\tilde{\chi}_1^0}h^2. \tag{4.15}$$

Knowing that the Yukawa-unified solutions generally have a relic density range between $10 - 10^4$, an order of $\sim 10^2 - 10^5$ reduction would be needed to reach below the WMAP upper limit.

[2] DM candidate axinos or gravitinos would also be produced thermally by scattering processes of other particles during thermal equilibrium, contributing more to the relic density. Thermal relic abundance depends on the thermal re-heat temperature T_R which is constrained by the gravitino mass and non-thermal leptogenesis. See Section 4.5 for details.

As explained in Chapter 2, in SUGRA, gravitino mass is given by $m_{3/2} \sim \langle F \rangle / M_{Pl} \sim m_{soft}$, which generally leads to $m_{3/2} \sim O(\text{TeV})$. However sometimes $m_{3/2} < m_{\tilde{\chi}_1^0}$, leading to $\tilde{\chi}_1^0$ decays to $\tilde{G}$. But even then, $m_{\tilde{G}}$ is at most only a few times smaller than $m_{\tilde{\chi}_1^0}$, which is not enough to reduce the relic density beneath the WMAP limit.

Axinos, on the other hand are allowed to have masses as low as $\sim keV$ and could lead to a convenient relic density. Details of a further study on an axino DM solution for SO(10) scenarios with excess relic density will be given in Section 4.5.

4.2.4.2 Solution via non-universal gaugino masses

If one increases the GUT scale value of the U(1) gaugino mass M_1 to values higher than $m_{1/2}$, the weak scale M_1 also gets increased enough so that $m_{\tilde{\chi}_1^0}$ approaches $m_{\tilde{\chi}_1^\pm}$. As a result $\tilde{\chi}_1^0$ becomes more wino-like. Contrary to the case with SU(2) and SU(3) gaugino masses, moving M_1 up does not have a large effect on R. For $m_{\tilde{\chi}_1^0} > m_W$, this would lead to annihilation to WW pairs. For our case where $m_{\tilde{\chi}_1^0} < M_W$, the relic density is rather lowered by bino-wino coannihilation.

4.2.4.3 Solution via non-universal scalar masses

Another method would be to lower the 1st/2nd generation scalar masses $m_{16}(1,2)$ while keeping $m_{16}(3)$ fixed. The non-universality thus generated leads to an increase in the S term in the scalar mass RGEs

$$S = m_{H_u}^2 - m_{H_d}^2 + Tr[m_Q^2 - m_L^2 - 2m_U^2 + m_D^2 + m_E^2] \tag{4.16}$$

that influences the scalar mass running. Resulting increased S term helps to suppress right squark masses. If $m_{16}(1,2)$ is low enough, then $m_{\tilde{u}_R} \simeq m_{\tilde{e}_R} \simeq m_{\tilde{\chi}_1^0}$. This way both the neutralino annihilation into squark pairs and neutralino-squark coannihilation is increased and relic density is decreased.

However despite the last two possibilities we favor and work with the universal solutions.

4.2.5 LHC scenarios for SO(10)

Guided by the results of the MCMC scans using the GSH and WSH input, we point out and examplify in Table 4.1 five different scenarios that might be realized at the LHC. Table 4.1 also lists $\Omega_{\tilde{\chi}_1^0} h^2$, $R(b \to s\gamma)$, Δa_μ, $BR(B_s \to \mu^+\mu^-)$ and the neutralino-proton direct DM detection cross section $\sigma(\tilde{\chi}_1^0 p)$, where the first four are computed by both IsaReD/Isatools (upper)

and micrOMEGAs (lower) while $\sigma(\tilde{\chi}_1^0 p)$ is computed only with IsaReD/Isatools. There is generally a good agreement between the two codes except in the cases of relic density computation where the neutralinos annihilate through h or A resonance. Variances arise due to different treatment of Higgs resonances. For example, Yukawa couplings used for annihilation through the A resonance and evaluation of the heavy Higgs widths are computed at scale $Q = M_{SUSY} = \sqrt{m_{\tilde{t}_L} m_{st_R}}$ in IsaReD while at $Q = 2m_{\tilde{\chi}_1^0}$ in micrOMEGAs.

SO10A is a generic Yukawa-unified GSH model with $\sim$ 10 TeV scalars and 100 – 400 GeV neutralinos/charginos. $\Omega_{\tilde{\chi}_1^0} h^2$ here is high, so this model requires an axino DM solution. $\tilde{\chi}_1^0$ has a lifetime of ~ 0.3 sec and a resulting decay distance of 10^4 km, so it is able to escape the LHC detectors before it decays, leading to the usual missing energy signature. SO10B and SO10C are derived from SO10A and demonstrate the cases where $\Omega_{\tilde{\chi}_1^0} h^2$ is adjusted by increasing GUT scale M_1 or decreasing GUT scale $m_{16}(1,2)$ respectively. SO10D examplifies the new class of GSH solutions found by the MCMC scans, where $m_{16} \sim 3{-}4$ TeV and a good $\Omega_{\tilde{\chi}_1^0} h^2$ is reached by annihilation through h resonance. SO10E shows a case of WSH input where a good $\Omega_{\tilde{\chi}_1^0} h^2$ is achieved by annihilation through a pseudoscalar A resonance.

The heavy scalars in SO10A are decoupled from the LHC physics leaving the ground mainly to a dominant $\tilde{g}\tilde{g}$ pair production followed by subsequent 3-body decays to b-rich final states. The %56 branching ratio of $\tilde{g} \to b\bar{b}\tilde{\chi}_2^0 \to b\bar{b}l\bar{l}\tilde{\chi}_1^0$ allows for a possible prediction of sparticle masses through observation of endpoints. Additionally there will be production of $\tilde{\chi}_1^+\tilde{\chi}_1^-$, $\tilde{\chi}_1^\pm\tilde{\chi}_2^0$ and $\tilde{\chi}_1^\pm\tilde{\chi}_1^0$ pairs which can be pursued in the exclusive leptonic channels. In SO10B, $m_{\tilde{\chi}_1^0}$ is increased to 125.4 GeV and $m_{\tilde{\chi}_2^0} - m_{\tilde{\chi}_1^0}$, and hence the $m(ll)$ edge is decreased to $\sim$ 13 GeV, while the branching ratio of the radiative decay $\tilde{\chi}_2^0 \to \gamma\tilde{\chi}_1^0$ can go up to %10 and be spotted if one observes hard, isolated photons. SO10C, on the contrary, has very low 1st/2nd generation scalars which would dominate the LHC stage. Light right squarks will decay to very soft jets via $\tilde{q}_R \to q\tilde{\chi}_1^0$ due to the 18 GeV mass difference $\tilde{q}_R - \tilde{\chi}_1^0$, while left squarks will decay to $\tilde{\chi}_2^0$ and $\tilde{\chi}_1^\pm$ which again lead to soft jet activity. SO10D is similar to SO10A, but additionally has lighter $\tilde{t}_1$, $\tilde{\chi}_3^0$, $\tilde{\chi}_4^0$, $\tilde{\chi}_2^\pm$ and heavy Higgses that can be produced at the LHC. The WSH point SO10E violates the Tevatron limits of $BR(B_s \to \mu\mu)$, but in case this point is allowed due to other flavor-violating interactions, its very light Higgs spectrum (which is also quite close to the Tevatron limits, e.g.: for $m_A > 170$ GeV) will easily be discovered.

In Section 4.3 and Chapter 7, detailed studies on the observation of SO10A and SO10D will be presented. These points were favored since we prefer to keep universality and would

Table 4.1: Masses and parameters in GeV units for five benchmark Yukawa unified points using Isajet 7.75 and $m_t = 171.0$ GeV. The upper entry for the $\Omega_{\tilde{\chi}_1^0}h^2$ etc. come from IsaReD/Isatools, while the lower entry comes from micrOMEGAs; $\sigma(\tilde{\chi}_1^0 p)$ is computed with Isatools.

parameter	SO10A	SO10B	SO10C	SO10D	SO10E
m_{16}	9202.9	9202.9	5018.8	2976.5	5877.3
$m_{1/2}$	62.5	62.5	160	107.0	113.6
A_0	-19964.5	-19964.5	-10624.2	-6060.3	-12052.6
m_{10}	10966.1	10966.1	6082.1	3787.9	—
$\tan\beta$	49.1	49.1	47.8	49.05	47.4
M_D	3504.4	3504.4	1530.1	1020.8	—
M_1	—	195	—	—	—
$m_{16}(1,2)$	—	—	603.8	—	—
y_t	0.51	0.51	0.49	0.48	0.49
y_b	0.51	0.51	0.41	0.47	0.49
y_τ	0.52	0.52	0.47	0.52	0.49
μ	4179.8	4186.3	1882.6	331.0	865.3
$m_{\tilde{g}}$	395.6	395.4	495.5	387.7	466.6
$m_{\tilde{u}_L}$	9185.4	9185.4	622.1	2970.8	5863.0
$m_{\tilde{u}_R}$	9104.1	9104.2	98.3	2951.4	5819.2
$m_{\tilde{t}_1}$	2315.1	2310.5	1048.4	434.5	944.7
$m_{\tilde{b}_1}$	2723.1	2714.9	1894.0	849.3	1452.7
$m_{\tilde{e}_L}$	9131.9	9132.0	311.9	2955.8	5833.6
$m_{\tilde{e}_R}$	9323.7	9323.9	891.8	3009.0	5945.8
$m_{\tilde{\chi}_1^\pm}$	128.8	128.8	165.7	105.7	141.3
$m_{\tilde{\chi}_2^0}$	128.6	128.1	165.1	105.1	140.9
$m_{\tilde{\chi}_1^0}$	55.6	115.9	80.2	52.6	65.7
m_A	3273.6	3266.0	1939.9	776.8	177.8
m_h	125.4	125.4	123.2	111.1	113.4
$\Omega_{\tilde{\chi}_1^0}h^2$	423 220	0.09 0.08	0.11 0.11	0.10 0.06	0.15 0.08
$BF(b\to s\gamma)$	3.0×10^{-4} 3.3×10^{-4}	3.0×10^{-4} 3.3×10^{-4}	6.2×10^{-4} 3.7×10^{-4}	1.9×10^{-4} 4.0×10^{-4}	2.5×10^{-4} 2.2×10^{-4}
Δa_μ	5.0×10^{-12} 5.1×10^{-12}	5.0×10^{-12} 5.0×10^{-12}	3.0×10^{-10} 2.8×10^{-10}	2.2×10^{-10} 2.2×10^{-10}	4.1×10^{-11} 4.1×10^{-11}
$BF(B_s\to\mu^+\mu^-)$	5.0×10^{-9} 4.4×10^{-9}	5.0×10^{-9} 4.4×10^{-9}	11.8×10^{-9} 6.9×10^{-9}	5.8×10^{-8} 6.2×10^{-8}	2.0×10^{-5} 2.0×10^{-5}
$\sigma_{sc}(\tilde{\chi}_1^0 p)$ [pb]	1.3×10^{-15}	1.9×10^{-17}	1.5×10^{-6}	2.7×10^{-9}	5.3×10^{-8}

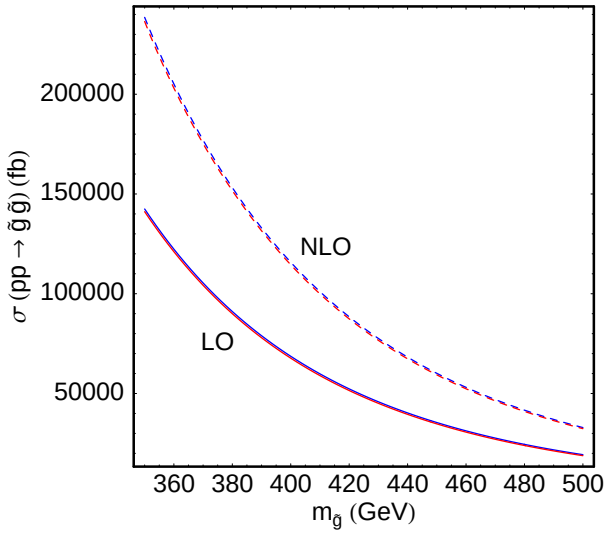

Figure 4.6: $\sigma(pp \to \tilde{g}\tilde{g})$ at $\sqrt{s} = 14$ TeV versus $m_{\tilde{g}}$ for $m_{\tilde{g}} = 350{-}500$ GeV using PROSPINO with scale $Q = m_{\tilde{g}}$. Solid (dashed) lines show LO (NLO) values. Red (lower) lines have 10 TeV squarks (SO10A-like) and blue (upper) lines have 3 TeV squarks (SO10D-like).

also like to stay below the Tevatron $BR(B_s \to \mu^+\mu^-)$ limit. At the LHC, gluinos in the 350-500 GeV range will be pair-produced via $q\bar{q}$ and gg fusion subprocesses. Figure 4.6 shows the LO and NLO cross sections for such light gluinos at 14 TeV calculated using PROSPINO as a function of the gluino mass for two values of squark mass $m_{\tilde{q}} = 3$ and 10 TeV. The NLO cross sections are a factor of ~ 1.6 greater then the LO results, but considering different squark masses lead only to insignificant differences in cross sections. So, in the case of Yukawa-unified SO(10) SUSY $pp \to \tilde{g}\tilde{g}X$ events are produced with 30 – 150 pb cross sections at the LHC.

Figure 4.7 then shows LO cross sections for the process $pp \to \tilde{\chi}\tilde{\chi}$ computed with ISAJET 7.75 versus $m_{\tilde{\chi}_1^\pm}$. Here $\tilde{\chi}_1^\pm\tilde{\chi}_2^0$ production cross section dominates and reaches up to 10 – 20 pb for the mass ranges of SO10A and SO10D.

Guided by these, we will mostly focus on the $\tilde{g}\tilde{g}$ pair production while stating some brief comments on the 3-lepton final state from the $\tilde{\chi}_2^0\tilde{\chi}_1^\pm$ channel. In the next section, we give the results of a study featuring inclusive dilepton and exclusive trilepton channels for $\sqrt{s} = 14$ TeV at the LHC based on a toy simulation while in Chapter 7 we present an analysis performed based on a full CMS simulation.

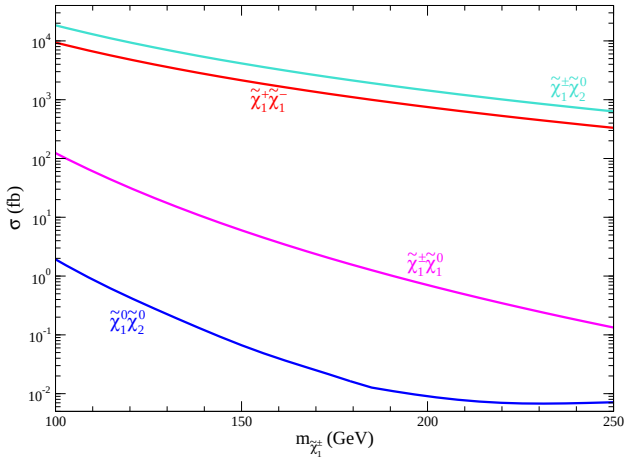

Figure 4.7: Various $\sigma(pp \to \tilde{\chi}\tilde{\chi})$ at $\sqrt{s} = 14$ TeV versus $m_{\tilde{\chi}_1^\pm}$ for $m_{\tilde{q}} = 3$ TeV and $\mu = m_{\tilde{g}}$ with $\tan\beta = 49$ and $\mu > 0$ (Plot by H. Summy).

4.3 Search for SO(10) scenarios using the lepton channels at $\sqrt{s} = 14$ TeV at the CERN LHC

We studied the feasibility of discovering Yukawa-unified SUSY at the lepton channels at $\sqrt{s} = 14$ TeV at the LHC as well as prospects for measuring the sparticle masses [65]. Signal events for SO10A and SO10D plus the backgrounds QCD (in five different p_T bins), W+n jets, $Z + n$ jets, $t\bar{t}$ ($m_t = 171$ GeV) and the dibosons WW, ZZ, WZ were generated using ISAJET 7.75. Detector effects were modeled using a toy detector simulation with calorimeter cell size $\Delta\eta\times\Delta\phi = 0.05\times0.05$ and $-5 < \eta < 5$. The hadron calorimeter energy resolution was taken to be $\%80/\sqrt{E} + \%3$ for $|\eta| < 2.6$ and for forward calorimeter was $\%100/\sqrt{E} + \%5$ for $|\eta| > 2.6$ while the electromagnetic calorimeter energy resolution was assumed to be $\%3/\sqrt{E} + \%0.5$. An UA1-like jet finding algorithm with jet cone size $R = 0.4$ was used and $E_T(jet) > 50$ GeV and $|\eta(jet)| < 3.0$ were required for the jets. Leptons were considered isolated if they have $p_T(e \text{ or } \mu) > 20$ GeV and $|\eta| < 2.5$ with visible activity within a cone of $\Delta R < 0.2$ of $\Sigma E_T^{cells} < 5$ GeV. Furthermore, a lepton identification efficiency of %75 was assumed for leptons with 20 GeV$< p_T(l) <$ 50 GeV, and %85 for leptons with $p_T(l) > 50$ GeV.

A hadronic cluster with $E_T > 50$ GeV and $|\eta(j)| < 1.5$ was taken as a b jet if it contains a B hadron with $p_T(B) > 15$ GeV and $|\eta(B)| < 3$ within a cone of $\Delta R < 0.5$ about the jet axis. The generic b tagging efficiency of %60 was adopted and it was assumed that light quark and gluon jets can be mis-tagged as b jets with a probability $1/150$ for $E_T \leq 100$ GeV and $1/50$ for $E_T \geq 250$ GeV, with a linear interpolation for 100 GeV$< E_T <$ 250 GeV [66].

4.3.1 The $\tilde{g} \to b\bar{b}\tilde{\chi}_2^0 \to b\bar{b}(l\bar{l}/b\bar{b})\tilde{\chi}_1^0$ chain

Here we try to identify the gluino decay chains. In order to eliminate the huge SM backgrounds we first use the following simple set of cuts dubbed C1':

$$n(jets) \geq 4, \tag{4.17}$$

$$E_T(j1, j2, j3, j4) \geq 100,\ 50, 50, 50\ \text{GeV}, \tag{4.18}$$

$$S_T \geq 0.2. \tag{4.19}$$

where S_T is the transverse sphericity. The transverse sphericity matrix is given as

$$S = \begin{pmatrix} \sum p_x^2 & \sum p_x p_y \\ \sum p_x p_y & \sum p_y^2 \end{pmatrix} \tag{4.20}$$

from which S_T is defined as $2\lambda_1/(\lambda_1 + \lambda_2)$, where $\lambda_{1,2}$ are the larger and smaller eigenvalues of S. Table 4.2 shows the generated events with their cross sections among with the situation after cuts C1' and C1'+ missing E_T (denoted as $\not{E}_T$) > 150 GeV. These rough cuts including jets and $\not{E}_T$ seem to provide a good significance however the interpretation of jets and $\not{E}_T$ is subject to uncertainties when the true detector effects are taken into account. Furthermore, the QCD background, which stays significant in lepton blind jet-MET channels creates ambiguities to deal with for which special analysis techniques need to be implied. A much detailed full simulation study of the Jet-MET channel for the CMS detector addressing all these issues will be presented in Chapter 7. Here, in order to concentrate on the prospects of mass determination in SO(10) SUSY observations comfortably with only a toy simulation, we rather choose to work with multi b jet and lepton channels. These channels are applicable at the later stages of the LHC, after 5-10 fb^{-1} of data after the detector is better understood. Requirement of multi leptons (≥ 2) or multi b jets (≥ 4) eliminates the QCD background and provides a high S/B relevant for discovering the signal properties.

The specialized spectrum of SO10A and SO10D-type scenarios allow extraction of information on the sparticle mass relations. First of all, $\tilde{g}\tilde{g}$ signal is not obscured by squark production. Second, the spoiler 2-body modes $\tilde{\chi}_2^0 \to \tilde{\chi}_1^0 Z$, $\tilde{\chi}_2^0 \to \tilde{\chi}_1^0 h$ are kinematically forbidden, leaving the stage only to the 3-body modes $\tilde{\chi}_2^0 \to x\bar{x}\tilde{\chi}_1^0$. Among these the mode $\tilde{\chi}_2^0 \to l^+l^-\tilde{\chi}_1^0$ is a good tool, since it leads to a typical triangular l^+l^- invariant mass distribution $m(l^+l^-)$ whose endpoint gives the mass difference $m_{\tilde{\chi}_2^0} - m_{\tilde{\chi}_1^0}$. Despite the low $\tilde{\chi}_2^0 \to l^+l^-\tilde{\chi}_1^0$ branching ratios of %4.6 and %6.6 for SO10A and SO10D, requirement of a pair of same-flavor-oppposite-sign (SFOS) leptons reduce the background to a negligible level and leave us

Table 4.2: Events generated and cross sections (in fb) for various signal and SM background processes before and after cuts. C1' and C1' + $\not{E}_T$ cuts are specified in the text. $W + n$ jets and $Z + n$ jets backgrounds have been computed within the restriction $p_T(W, Z) > 100$ GeV.

process	events	σ (fb)	C1'	C1'+$\not{E}_T$
QCD (p_T : 0.05 – 0.1 TeV)	10^6	2.6×10^{10}	4.1×10^5	–
QCD (p_T : 0.1 – 0.2 TeV)	10^6	1.5×10^9	1.4×10^7	–
QCD (p_T : 0.2 – 0.4 TeV)	10^6	7.3×10^7	6.5×10^6	2199
QCD (p_T : 0.4 – 1.0 TeV)	10^6	2.7×10^6	2.8×10^5	1157
QCD (p_T : 1 – 2.4 TeV)	10^6	1.5×10^4	1082	25
$W \to l\nu_l + n$ jets	5×10^5	3.9×10^5	3850	1275
$Z \to \tau\bar{\tau} + n$ jets	5×10^5	1.4×10^5	1358	652
$t\bar{t}$	3×10^6	4.9×10^5	8.2×10^4	2873
WW, ZZ, WZ	5×10^5	8.0×10^4	197	7
Total BG	9.5×10^6	2.76×10^{10}	2.13×10^7	8188
Point A:	10^6	7.6×10^4	3.6×10^4	8914
$S/B \to$	–	–	0.002	1.09
$S/\sqrt{S+B}\,(1\,\text{fb}^{-1}) \to$	–	–	–	68
Point D:	10^6	9.0×10^4	3.7×10^4	10843
$S/B \to$	–	–	0.002	1.32
$S/\sqrt{S+B}\,(1\,\text{fb}^{-1}) \to$	–	–	–	78

with a clean signal. Furthermore one can apply the "flavor subtraction" technique where the different-flavor-opposite-sign (DFOS) dilepton invariant mass distribution is subtracted from the SFOS distribution in order to eliminate $e^+\mu^-$ and $e^-\mu^+$ pairs from chargino pairs produced in cascade decays. The $m(l^+l^-)$ distribution after these cuts and flavor subtraction is shown in Figure 4.8 where solid red (dashed blue) curves show point A (D) and the gray shade is the background. The significant peak at $m(l^+l^-) \approx m_Z$ comes mainly from W and Z radiation within the QCD background events. The $m_{\tilde{\chi}_2^0} - m_{\tilde{\chi}_1^0}$ for both points are seen to coincide well with endpoints.

The next step is to estimate $m_{\tilde{g}} - m_{\tilde{\chi}_2^0}$ and $m_{\tilde{g}} - m_{\tilde{\chi}_1^0}$ mass differences for which we would need the endpoints of $m(b\bar{b})$ and $m(b\bar{b}l^+l^-)$ mass distributions for the $\tilde{g} \to b\bar{b}\tilde{\chi}_2^0$ and $\tilde{g} \to b\bar{b}\tilde{\chi}_2^0 \to b\bar{b}l^+l^-\tilde{\chi}_1^0$ decays. Figure 4.9 shows the ideal $m(b\bar{b})$ distributions plotted in generator level with PYTHIA 6 using the quarks for SO10A. The black curve shows the distribution only with $b\bar{b}$ pairs from direct $\tilde{g} \to b\bar{b}\tilde{\chi}_1^0$ decays, the red curve shows the distribution with $b\bar{b}$ pairs from inclusive $\tilde{g} \to b\bar{b}\tilde{\chi}_2^0$ decays and the black curve shows the special case where the $b\bar{b}$s come from the exclusive $\tilde{g} \to b\bar{b}\tilde{\chi}_2^0 \to b\bar{b}l^+l^-\tilde{\chi}_1^0$ decays. The gray area, which is the sum of the red and blue curves accounts for the total distribution of all correct $b\bar{b}$ pairs from gluino decays. The two-edge structure, where the first shows $m_{\tilde{g}} - m_{\tilde{\chi}_2^0} \sim 268$ GeV and the second

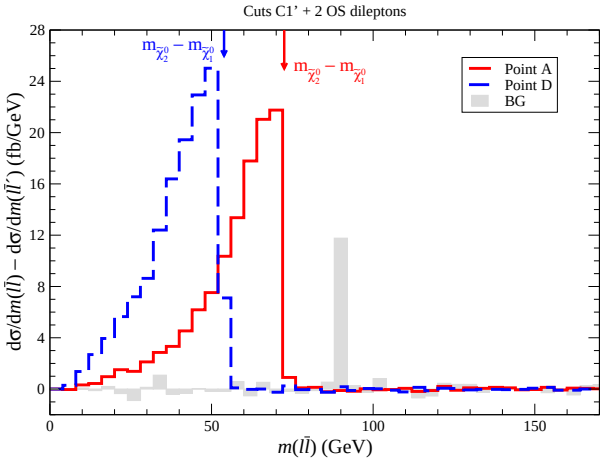

Figure 4.8: Dilepton invariant mass distribution for SFOS leptons after cuts C1' for SO10A (red, solid) and SO10D (blue, dashed) (Plot by H. Summy).

shows $m_{\tilde{g}} - m_{\tilde{\chi}_1^0} \sim 340$ GeV can be clearly seen in this ideal depiction.

However in real life we face a big problem regarding both the tagging and correct combination of b jet pairs coming from the gluino decays and this will smear the ideal spectrum greatly. There is always the unwanted possiblity to combine 2 b's from different gluinos or include b's from $\tilde{\chi}_2^0 \rightarrow b\bar{b}\tilde{\chi}_1^0$ decays. We did some generator level studies using b quarks to find a most feasable method to get the correct bb combinations. The events targeted were those with both gluinos decaying to bb pairs so we require $n_b \geq 4$. Since we would first like to examine the purest case, we only use the b's coming from the gluinos and reject the b's from neutralinos. We first worked with individual b quarks and checked if those pairs minimizing $\Delta\phi(bb)$, $\Delta R(bb)$, $avg(p_T(b_1)p_T(b_2))$, $m(bb)$ or maximizing $\Delta p_T(bb) = (p_T(b_1) - p_T(b_2))/avg(p_T(b_1)p_T(b_2))$ or $p_T(X(bb)$ give the right combinations, where $X(bb)$ is a combined object made from the two b's. It was seen that two b's from $\tilde{g} \rightarrow b\bar{b}\tilde{\chi}_i^0$ were not necessarily azimuthally close. None of these variables showed a considerable discriminating power.

Next we worked with objects $X_1(b_1b_2)$ and $X_2(b_3b_4)$ made by combining the 4-momenta of b-pairs. Figure 4.10 shows the distribution of $\Delta\phi(X_1 - X_2)$, $\Delta R(X_1 - X_2)$, $\Delta p_T(X_1 - X_2)$, $avg(p_T(X_1) - p_T(X_2))$, $\Delta m(X_1 - X_2 = (m(X_1) - m(X_2))/avg(m(X_1) - m(X_2))$ and $avg(m(X_1) - m(X_2))$. Here red curve gives the correct $b\bar{b}$ combinations, the green curve gives the wrong $b\bar{b}$ combinations where b and $\bar{b}$ come from different gluinos, and the blue curve gives the wrong bb or $\overline{bb}$ combinations. According to these distributions, one can expect the most efficient

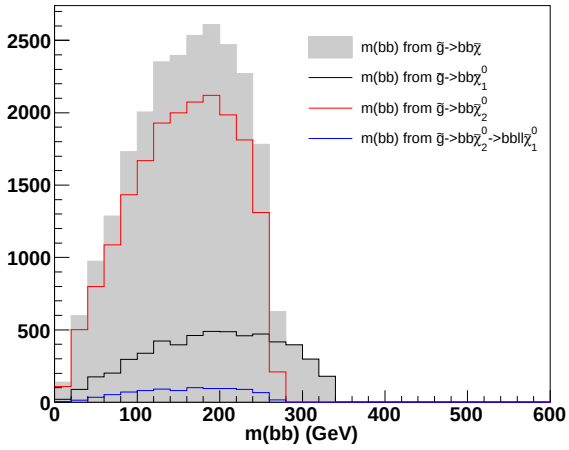

Figure 4.9: Parton level $m(bb)$ distributions with PYTHIA for SO10A using bb pairs coming from $\tilde{g} \to bb\tilde{\chi}$ (shaded), $\tilde{g} \to bb\tilde{\chi}_1^0$ (black), $\tilde{g} \to bb\tilde{\chi}_2^0$ (red) and $\tilde{g} \to bb\tilde{\chi}_2^0 \to bbll\tilde{\chi}_1^0$ (blue) decay modes.

selection of correct combinations by choosing the X_1X_2 pairs that have minimum $\Delta m(X_1 - X_2)$ and $avg(m(X_1) - m(X_2))$. Furthermore one can pick the X_1X_2 maximizing $\Delta\phi(X_1X_2)$ or $\Delta R(X_1X_2)$ since $b\bar{b}$ pairs from different gluinos are supposed to be back to back. Likewise one can select the pairs with minimum $\Delta p_T(X_1 - X_2)$ (which doesn't seem to have much discriminating power with respect to the others) or maximum $avg(p_T(X_1) - p_T(X_2))$.

Next, again by using the 4 b quarks from the 2 gluinos, we plot some $m(bb)$ distributions in Figure 4.11 for SO10A. The red curves (which are the same in each plot) show the $m(bb)$ made from the correct $b\bar{b}$ combinations, green curves show $m(bb)$ from the wrong $b\bar{b}$ combinations and blue curves show $m(bb)$ from the wrong $bb/\overline{bb}$ combinations. The black curves are drawn by taking the X_1 and X_2 objects such that they give $\Delta\phi(X_1X_2)^{min}$, $\Delta\phi(X_1X_2)^{min}$, $\Delta p_T(X_1 - X_2)^{min}$, $avg(p_T(X_1) - p_T(X_2))^{max}$, $\Delta m(X_1 - X_2)^{min}$ and $avg(m(X_1) - m(X_2))^{min}$ where both $m(bb)_{X_1}$ and $m(bb)_{X_2}$ contribute. The different color fills under the black curves show the components from right and wrong distributions for the selected pair. Light red/brown component from right $b\bar{b}$, green component from wrong $b\bar{b}$ and blue/gray component from wrong $bb/\overline{bb}$ combinations. It is seen that for each case, the selections accept almost equal amounts of right, wrong $b\bar{b}$ and wrong $bb/\overline{bb}$ combinations. However we see that the wrong combinations accepted do not actually spoil the $m(bb)$ distributions catastrophically. Maxima of the black curves are generally shifted to the low $m(bb)$ values, but the endpoints

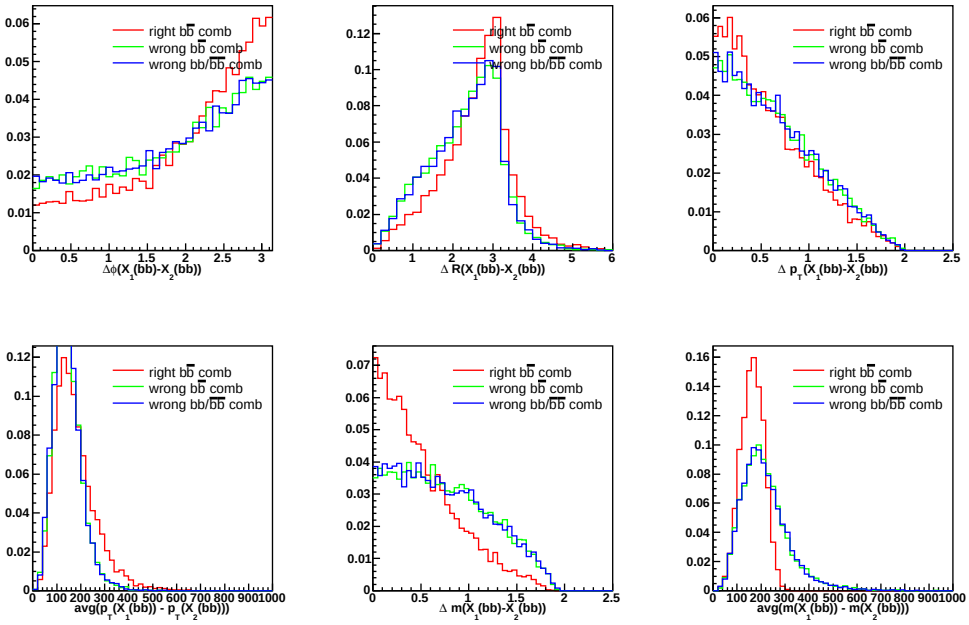

Figure 4.10: Combinations of all $X_1(bb) - X_2(bb)$s. Selection variables for right $X_1(b\bar{b}) - X_2(b\bar{b})$ (red), wrong $X_1(b\bar{b}) - X_2(b\bar{b})$ (green) and wrong $X_1(bb) - X_2(\bar{b}\bar{b})$ (blue).

mostly tend to agree. Furthermore, the yellow curves are the results of inverse selections, e.g.: $\Delta\phi(X_1 - X_2)^{min}$. Obviously the inverse selections pick the spoiler wrong combinations.

The $m(bb)$ curve with closest resemblance to the ideal distribution is given by the selection $\Delta m(X_1 - X_2)^{min}$, so we proceed with this choice. These generator level studies also pointed out that generally two hardest b's come from two different gluinos. Thus while forming the combined objects, we additionally require that the hardest b jet should belong to X_1 and the second hardest to X_2. However there is still a chance of getting the b's from $\tilde{\chi}_2^0$ decays plus there will be a significant contribution from the b-rich SM backgrounds such as QCD and $t\bar{t}$, so it is helpful to constrain this selection further by additionally requiring two SFOS leptons. Figure 4.12 shows the resulting distribution with ISAJET b jets for SO10A and SO10D. Here the SM background is very low and both $m_{\tilde{g}} - m_{\tilde{\chi}_2^0}$ and $m_{\tilde{g}} - m_{\tilde{\chi}_1^0}$ mass edges are clearly visible.

Finally we reconstruct $m(bbl^+l^-)$ by combining l^+l^- with X_1 or X_2 and choose the X_i that minimizes $m(X_i l^+ l^-)$. Resulting distribution is seen in Figure 4.13. Here altough an edge is located near the maximum, it is hard to precisely predict its position due to the low statistics.

Exact positions of the edges can be determined by making fits to the $m(l^+l^-)$, $m(bb)$ and

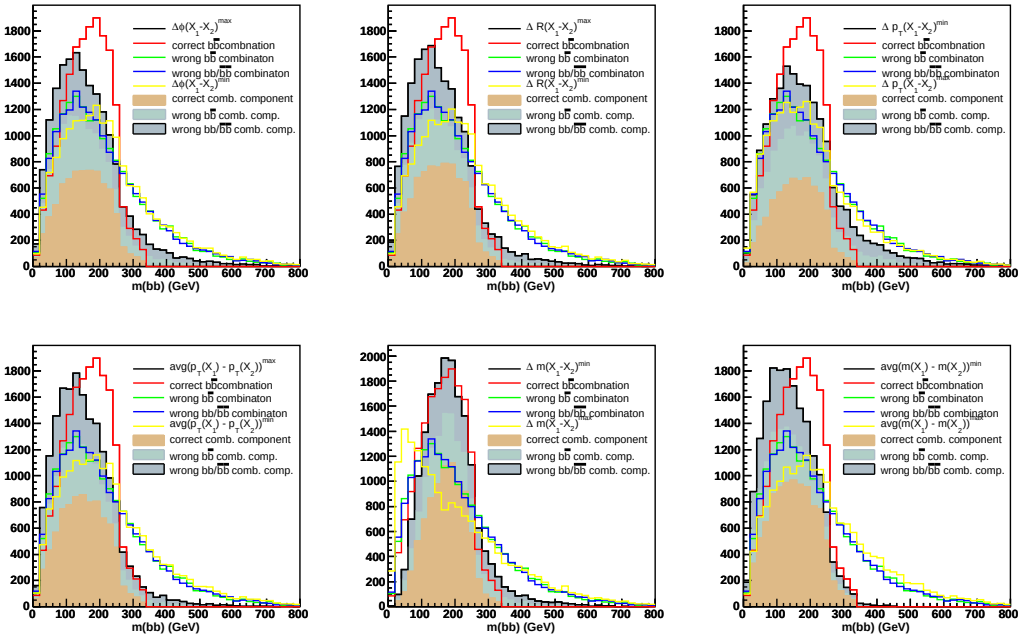

Figure 4.11: $m(bb)$s for both pairs in the $X_1 - X_2$ combination determined according to different selections. Black curves respectively for: $\Delta\phi(X_1 - X_2)^{max}$, $\Delta R(X_1 - X_2)^{max}$, $\Delta p_T(X_1 - X_2)^{min}$, avg $(p_T(X_1) - p_T(X_2))^{max}$, $\Delta m(X_1 - X_2)^{min}$, avg $(m(X_1 - m(X_2))^{min}$. The different color fills under the black curves show the components from right and wrong distributions for the selected pair: light red/brown component from right $b\bar{b}$, green component from wrong $b\bar{b}$ and blue-gray component from wrong $bb/\bar{b}\bar{b}$. The red curve shows the total right $b\bar{b}$ distribution, green curve shows the total wrong $b\bar{b}$ distribution and the blue curve shows the wrong $bb/\bar{b}\bar{b}$ distribution. The yellow curve shows the case of inverse selection: $\Delta\phi(X_1 - X_2)^{min}$, $\Delta R(X_1 - X_2)^{min}$, $\Delta p_T(X_1 - X_2)^{max}$, avg $(p_T(X_1) - p_T(X_2))^{min}$, $\Delta m(X_1 - X_2)^{max}$, avg $(m(X_1 - m(X_2))^{max}$. This shows that even when one selects a wrong combination with a certain requirement, that wrong combination does not generally have an invariant mass which spoils the distribution. The combinations with spoiler masses are generally those combinations made by inverse selections.

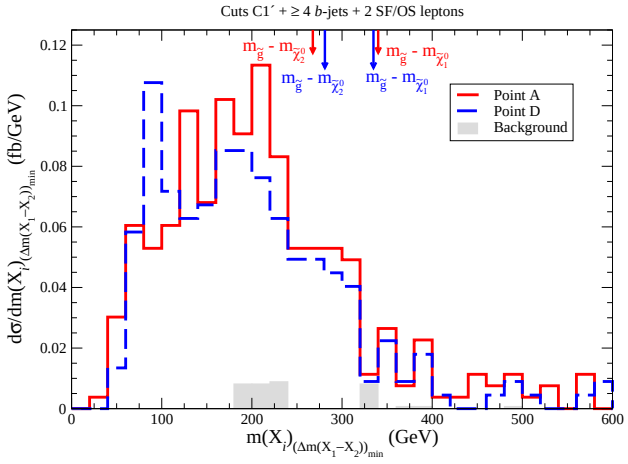

Figure 4.12: Plot of $m(X_{1,2}\ell^+\ell^-)_{min}$ from SO10A (red, solid) and SO10D (blue, dashed), minimizing $\Delta m(X_1 - X_2)$ as explained in the text, along with SM backgrounds (Plot by H. Summy).

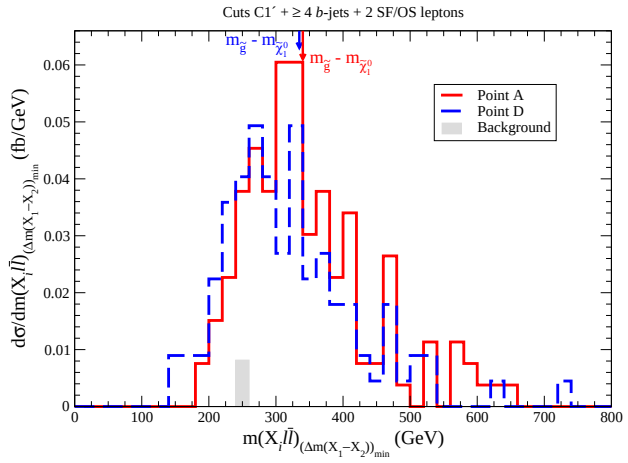

Figure 4.13: Plot of $m(X_{1,2}\ell^+\ell^-)_{min}$ from SO10A (red, solid) and SO10D (blue, dashed), minimizing $\Delta m(X_1 - X_2)$ as explained in the text, along with SM backgrounds (Plot by H. Summy).

$m(bbl^+l^-)$ distributions. For example a triangle convoluted with a gaussian function would approximately give the dilepton edge. In this study involving only a toy simulation, we will not exercise any of the fit methods existing in literature or propose any new fitting methods, but just will quote the generic precision of hadronic mass edge measurements, which amounts to ~ %10. If determined, the three edges would still not be sufficient to find $m_{\tilde{g}}$, $m_{\tilde{\chi}_2^0}$ and $m_{\tilde{\chi}_1^0}$. In such models where $\tilde{g}\tilde{g}$ pair production dominates, one could complement the edge values with $\tilde{g}\tilde{g}$ cross section and dominant branching ratio measurements from which the absolute gluino mass can be determined. Knowing $m_{\tilde{g}}$, the neutralino masses can be extracted from the edges.

4.3.2 A note on trileptons signal from $\tilde{\chi}_2^\pm\tilde{\chi}_1^0$ production

Discovery of SO(10) SUSY in the $\tilde{g}\tilde{g}$ channels can be complemented by investigating $\tilde{\chi}\tilde{\chi}$ production. According to Figure 4.7, especially $\tilde{\chi}_1^\pm\tilde{\chi}_2^0$ production is worth analyzing. The $\tilde{\chi}_1^+\tilde{\chi}_1^-$ production also has considerable cross section, however would be hard to see at the LHC because it would be buried under the SM backgrounds due to its relatively soft final states.

$\tilde{\chi}_2^0\tilde{\chi}_1^\pm$ can combine $\tilde{\chi}_2^0 \to l^+l^-\tilde{\chi}_1^0$ and $\tilde{\chi}_1^\pm \to l^\pm\tilde{\chi}_1^0$ to give a trileptons plus $\not{E}_T$ signature above the SM backgrounds for which the prospective LHC reach is shown in [67]. In this study, after applying the following list of cuts from [68]

- three isolated leptons with $p_T(l) > 20$ GeV and $|\eta_l| < 2.5$,
- OS/SF dilepton mass 20 GeV $< m(l^+l^-) <$ 81 GeV, to avoid BG from photon and Z poles in the $2 \to 4$ process $q\bar{q}' \to l\bar{l}'\bar{\nu}_l$,
- a transverse mass veto 65 GeV $< M_T(l, \not{E}_T) <$ 80 GeV to reject on-shell W contributions, and
- $\not{E}_T > 25$ GeV,
- veto events with jets $n(jets) \geq 1$.

we obtained the results in Table 4.3 where we see that ~ 5 fb signal events will be visible over a 0.7 fb SM background.

Table 4.3: Clean trilepton signal after cuts listed in the text.

process		events	σ (fb)	after cuts (fb)
$t\bar{t}$		3×10^6	4.9×10^5	–
WW, ZZ, WZ		5×10^5	8.0×10^4	–
$W^*Z^*,\ W^*\gamma^* \to l\bar{l}'\nu_{l'}$		10^6	–	0.7
Total BG		4.5×10^5	–	0.7
Point A:	–	10^6	7.6×10^4	3.4
	$S/B \to$	–	–	4.86
	$S/\sqrt{S+B}\,(10\,\text{fb}^{-1}) \to$	–	–	5.31
Point D:	–	10^6	9.0×10^4	4.1
	$S/B \to$	–	–	5.86
	$S/\sqrt{S+B}\,(10\,\text{fb}^{-1}) \to$	–	–	5.92

In the end, we conclude that di- and trilepton channels provide a clean signature for the SO(10) scenarios at the LHC, allowing significant discovery using ~1 fb^{-1} and reconstruction of $m_{\tilde{g}}$, $m_{\tilde{\chi}_1^0}$ and $m_{\tilde{\chi}_2^0}$ to O(%10) accuracy using ~100 fb^{-1}.

4.4 Sensitivity of Yukawa unification to small variances in input parameters

We also comment on a study that quantifies the sensitivity of SO(10) solutions and Yukawa unification with respect to small changes in input parameters [84]. Figure 4.14 shows the Yukawa coupling evolution from weak scale to GUT scale for SO10A and SO10D. The kinks seen at $M_{SUSY} \sim 3$ TeV and ~ 10 TeV at SO10D and SO10A respectively are due to MSSM threshold corrections (e.g.: the steep slopes for y_t and y_b for $Q < M_{SUSY}$ occur mainly because the coefficient of the QCD g_s^2 contribution to $y_{t/b}$ running changes from 16/3 in the MSSM to 8 in the SM - specially the big jump of y_b was found to be due to $\tan\beta$-anhanced chargino-stop loop). This illustrates the effect of correct implementation of the MSSM threshold corrections on determination of the degree of Yukawa unification.

To see how SO(10) solutions are effected by small variations in parameters, we took SO10A and SO10D, and varied the GUT scale input parameters m_{16}, m_{10}, m_D, $m_{1/2}$, A_0 and $\tan\beta$ simultaneously within %10 around the central parameter values using a random uniform distribution. Figures 4.15 and 4.16 show the results for SO10A and SO10D respectively for 500000 randomly tried points. Plots on the left hand side show the efficiency of getting an RGE solution (where efficiency is defined as the number of points with a RGE solution divided by the number of tried points) in planes of δm_{10}, δm_D, $\delta m_{1/2}$, δA_0, $\delta\tan\beta$ versus m_{16}. Plots on the right hand side show the ranges of resulting R parameters.

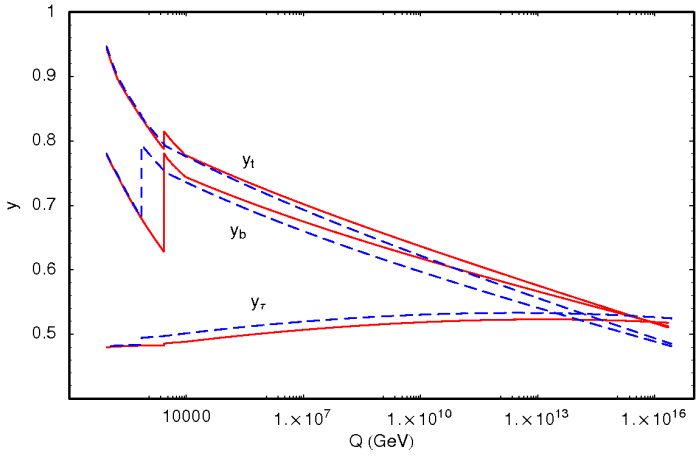

Figure 4.14: Plot of y_t, y_b and y_τ evolution from the weak scale to the GUT scale for SO10A (red, solid) and SO10D (blue, dashed). The large jumps around 3 TeV correspond to the MSSM threshold corrections.

From the efficiency plots for both SO10A and SO10D, we see that lowering m_{16} significantly reduces the efficiency. Furthermore m_{10} and $\tan\beta$ allow more solutions when increased and A_0 allows more solutions when decreased. Then, as seen on the right hand side of Figure 4.15, R values of every range are evenly distributed for m_{10} vs m_{16}, m_D vs m_{16} and $m_{1/2}$ vs m_{16} planes, showing that R is not sensitive to variations in m_{10}, m_{10} and $m_{1/2}$. On the other hand Yukawa-unified points with $R < 1.05$ and $R < 1.1$ are obviously constrained on the A_0 vs m_{16} and $\tan\beta$ vs m_{16} planes, further justifying the Bagger et. al. condition $A_0 \simeq -2.2m_{16}$ and favoring $47 \lesssim \tan\beta \lesssim 51$, in agreement with Eq. 4.4. In general, a %10 variation in SO10A parameters easily produces Yukawa-unified points, however variations of SO10D, as seen in Figure 4.16, generally result in $R > 1.15$. Also in SO10D, the condition $m_{10} \sim 1.2m_{16}$ is more emphasized and the actual point SO10D lies almost on the very boundary of REWSB, illustrating the more fine-tuned nature of the case where WMAP-compatible $\Omega_{\tilde{\chi}_1^0}h^2$ is achieved by annihilation via light Higgs.

4.5 Cosmological consequences of SO(10) models with mixed axion/axino cold and warm dark matter

As promissed earlier, we finally present a study which proposes the possibility of mixed axion/axino cold and warm dark matter in order to solve the excess relic density issue that comes up in most of the Yukawa-unified SO(10) solutions [69].

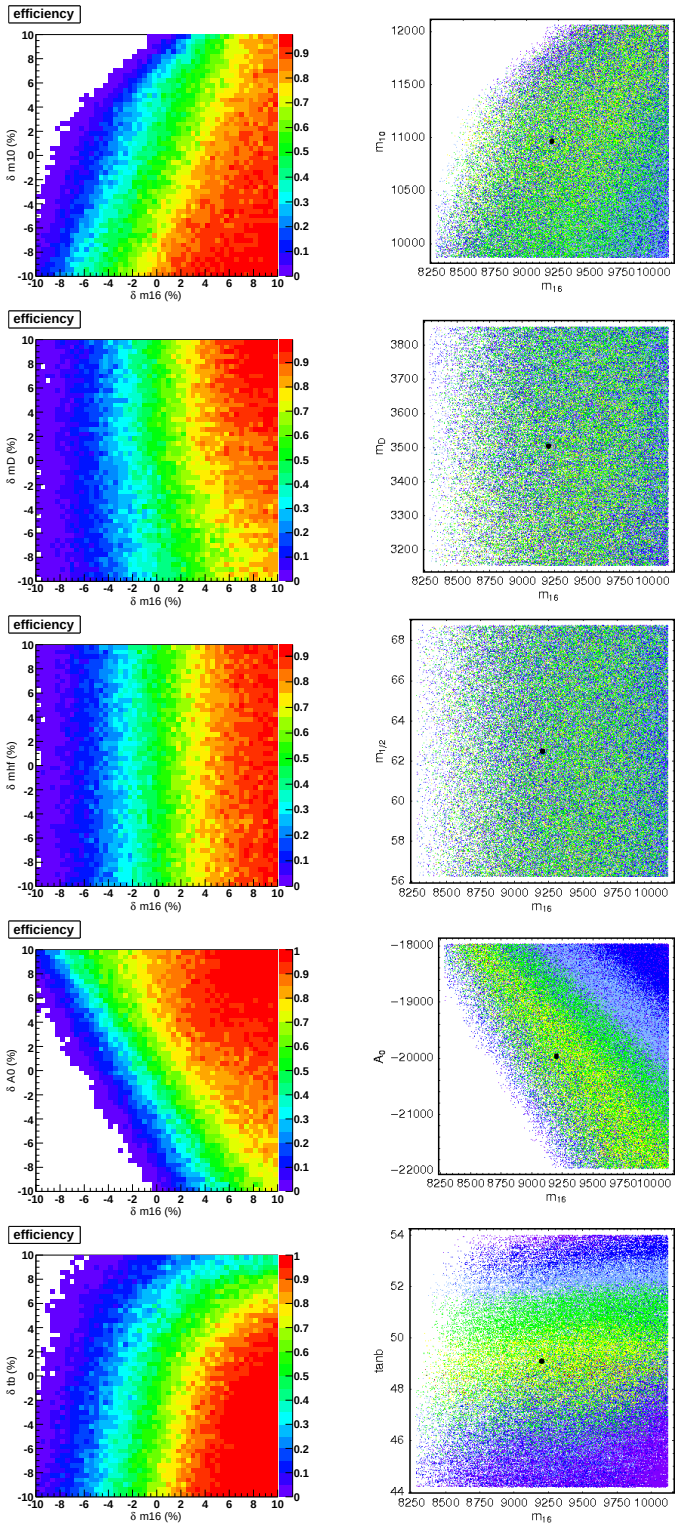

Figure 4.15: Efficiency of finding RGE solutions as explained in the text (left) and R values (right) on input GUT scale parameter planes, obtained by varying the input parameters of SO10A randomly in a uniform distribution of %10 around the central values. R ranges shown are $1 \leq R \leq 1.01$ (red), $1.01 < R \leq 1.05$ (yellow), $1.05 < R \leq 1.1$ (green), $1.1 < R \leq 1.15$ (light blue), $1.15 < R \leq 1.20$ (blue) and $1.20 < R$ (purple). Black dot marks the position of SO10A.

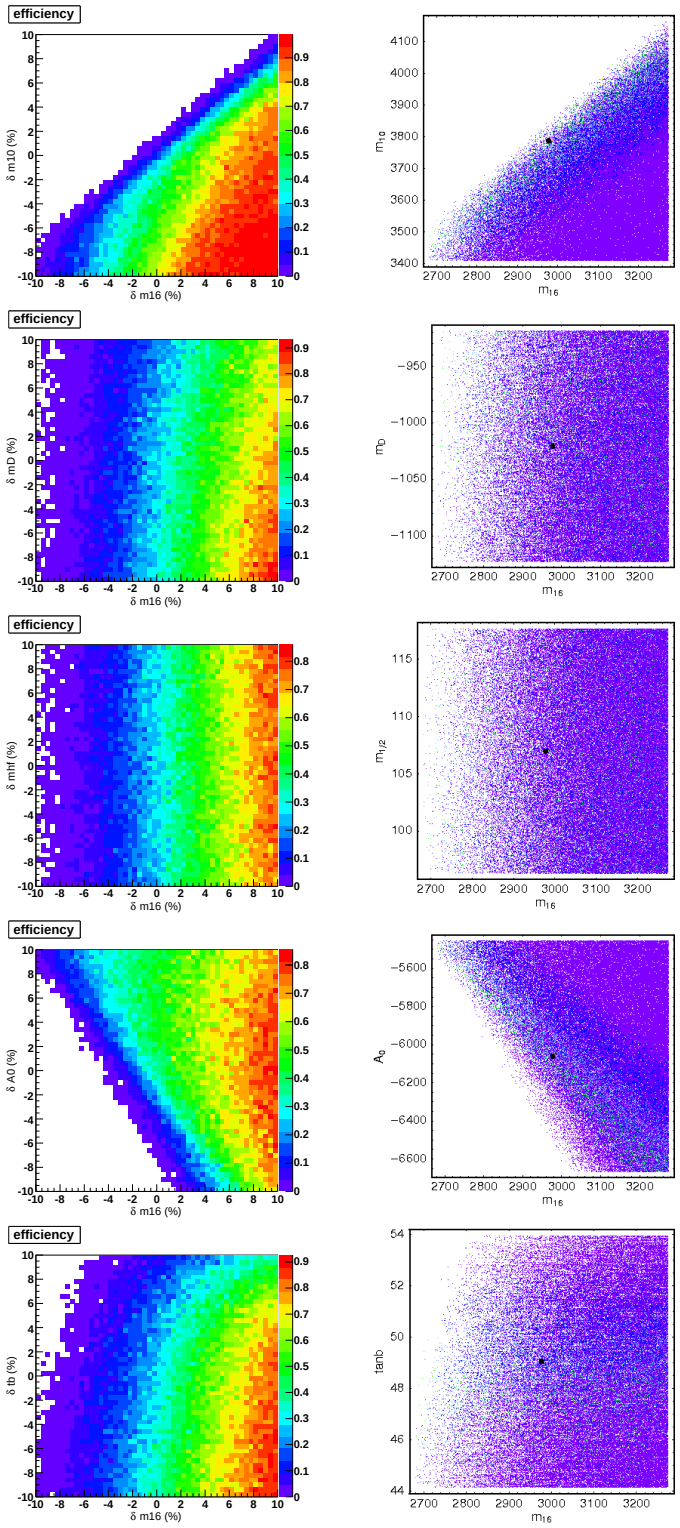

Figure 4.16: Efficiency of finding RGE solutions as explained in the text (left) and R values (right) on input GUT scale parameter planes, obtained by varying the input parameters of SO10D randomly in a uniform distribution of %10 around the central values. R ranges shown are $1 \leq R \leq 1.01$ (red), $1.01 < R \leq 1.05$ (yellow), $1.05 < R \leq 1.1$ (green), $1.1 < R \leq 1.15$ (light blue), $1.15 < R \leq 1.20$ (blue) and $1.20 < R$ (purple). Black dot marks the position of SO10D.

4.5.1 Introducing axions and axinos

QCD Lagrangian has the following CP-violating term:

$$\mathcal{L} \ni \frac{\theta g^2}{32\pi^2} G^a_{\mu\nu} \tilde{G}^{a\mu\nu} \tag{4.21}$$

where $G^a_{\mu\nu}$ is the gluon field strength tensor. This can be cured by imposing a global U(1) symmetry [70],[71]. This so-called Peccei-Quinn (PQ) symmetry is classically valid, but breaks down spontaneously due to quantum anomalies, resulting in a pseudo-Goldstone boson called "axion" (a(x)) [72],[73], through which the Lagrangian becomes

$$\mathcal{L} \ni \frac{1}{2}\partial_\mu a \partial^\mu a + \frac{g^2}{32\pi^2}\frac{a(x)}{f_a} G^a_{\mu\nu}\tilde{G}^{a\mu\nu}. \tag{4.22}$$

Here f_a is the scale where PQ symmetry breaks. The axion mass can be given as

$$m_a \simeq 6 \text{ eV} \frac{10^6 \text{ GeV}}{f_a}. \tag{4.23}$$

Astrophysical limits from cooling of red giant stars and supernova 1987a require $f_a \gtrsim 10^9$ GeV, or $m_a \lesssim 3 \times 10^{-3}$ eV.

Then within a supersymmetric framework, the axion will be embedded in an axion left chiral scalar superfield

$$\hat{\phi}_a = \frac{(s(\hat{x}) + ia(\hat{x}))}{\sqrt{2}} + i\sqrt{2}\bar{\theta}\psi_{a_L}(\hat{x}) + i\bar{\theta}\theta_L \mathcal{F}_a(\hat{x}), \tag{4.24}$$

where s is a spin-0 field "saxion" which gets a mass of order of weak scale and $\psi_a \equiv \tilde{a}$ is the spin-1/2 "axino", whose mass is model dependent and extends over the keV-GeV range [74],[78],[79].

4.5.2 Axions and axinos as dark matter

It turns out that axions and axinos make suitable dark matter candidates. Axions can be produced in the early Universe, and for the thermal re-heat temperature bound of $T_R \lesssim 10^9$ K (which we will shortly discuss), the production mechanism is unique, and is via vacuum misallignment. Axions have lifetimes longer then the age of Universe, so can constitute dark matter, whose current relic density is

$$\Omega_a h^2 \simeq \frac{1}{4}\left(\frac{6 \times 10^{-6} \text{ eV}}{m_a}\right)^{7/6}. \tag{4.25}$$

Axions generated via vacuum misallignment make up cold dark matter.

Axinos, on the other hand, can be produced either non-thermally through decays of heavier particles, such as $\tilde{\chi}_1^0$s or thermally in the early Universe.

The decay width for the process $\tilde{\chi}_1^0 \to \tilde{a}\gamma$ is given as

$$\Gamma(\tilde{\chi}_1^0 \to \tilde{a}\gamma) = \frac{\alpha_{em}^2 C_{aYY} v_4^{(1)2}}{128\pi^3 \cos^2\theta_W} \frac{m_{\tilde{\chi}_1^0}^3}{(f_a/N)^2} \left(1 - \frac{m_{\tilde{a}}^2}{m_{\tilde{\chi}_1^0}^2}\right)^3, \tag{4.26}$$

where $v_4^{(1)}$ is the bino fraction of neutralino $\tilde{\chi}_1^0$, N is the axion model-dependent anomaly factor (*e.g.* $N = 1$ (6) for KSVZ[75] (DFSZ[76]) axions), and C_{aYY} is a model-dependent coupling factor (*e.g.* $C_{aYY} = 8/3$ in the DFSZ model). Thus produced axinos will constitute the non-thermal relic abundance, and the relic density directly inherited from $m_{\tilde{\chi}_1^0}$ becomes

$$\Omega_{\tilde{a}}^{\rm NTP} h^2 = \frac{m_{\tilde{a}}}{m_{\tilde{\chi}_1^0}} \Omega_{\tilde{\chi}_1^0} h^2. \tag{4.27}$$

which means that smaller the ratio $m_{\tilde{a}}/m_{\tilde{\chi}_1^0}$, larger the reduction in $\Omega^{\rm NTP}h^2$. According to [77] where rms velocity profile of axino DM coming from $\tilde{\chi}_1^0$ decays were calculated, non-thermally produced axinos with $m_{\tilde{a}} \lesssim 1$ GeV contribute to *warm* dark matter.

Axinos have weak couplings to other matter fields and so cannot be in thermal equilibrium. However they can be produced via scattering processes of other particles in thermal equilibrium. The relic abundance for thermally produced axinos are given by [78],[79],[80]

$$\Omega_{\tilde{a}}^{\rm TP} h^2 \simeq 5.5 g_s^6 \ln\left(\frac{1.108}{g_s}\right)\left(\frac{10^{11}\ {\rm GeV}}{f_a/N}\right)^2 \left(\frac{m_{\tilde{a}}}{0.1\ {\rm GeV}}\right)\left(\frac{T_R}{10^4\ {\rm GeV}}\right) \tag{4.28}$$

where g_s is the strong coupling evaluated at $Q = T_R$ (*e.g.* $g_s = 0.915$ at $Q = 10^6$ GeV from our ISAJET RGE calculations). The thermally produced axinos qualify as *cold* dark matter as long as $m_{\tilde{a}} \gtrsim 100$ keV.

4.5.2.1 Cosmological bounds on T_R

The thermal axino relic abundance is directly dependent on the re-heat temperature T_R. Here we introduce two bounds on T_R which will restrict our final results. T_R is bound by constraints from gravitino mass and non-thermal leptogenesis.

The gravitino couplings to matter are suppressed by the Planck scale. As in the axino case, such weakly coupling gravitinos cannot be in thermal equilibrium, but still can get produced in the early Universe via scatterings of particles involved in thermal equilibrium. These heavy gravitinos would then decay, but with lifetimes <1 sec, exceeding the time scale that Big Bang Nucleosynthesis begins. This is dangerous, since the high energies that come

from heavy gravitino decay would hinder a successful production of light nuclei. Results from the calculation of BBN constraints on gravitino give an upper limit on T_R as a function of $m_{\tilde{G}}$ [81]. These depend on $\tilde{G}$ lifetime, which is the time of the energy release, and the dominant $\tilde{G}$ decay modes. For $m_{\tilde{G}} \sim 5 - 50$ TeV, which is consistent with our SO(10) case, the re-heat upper bound is $T_R \lesssim 10^9$ GeV.

Second constraint is related to leptogenesis [82], which emerged as a candidate mechanism for generating the baryon asymmetry. Leptogenesis requires the presence of heavy right-handed gauge-singlet Majorana neutrino states $\psi_{N_i^c}(\equiv N_i)$ with masses M_{N_i} (where $i = 1, 2, 3$ is a generation index). The N_i states may be produced either thermally in the early universe, or non-thermally [83] via inflaton decay $\phi \rightarrow N_i N_i$. Then N_i would generate the asymmetry by CP violating, asymmetric decays to + and − states. Thermal leptogenesis predicts a $T_R \gtrsim 10^{10}$ GeV, which is inconsistent with $T_R \lesssim 10^9$ GeV from gravitino constraint. On the other hand non-thermal leptogenesis predicts a much lower, compatible value $T_R \gtrsim 10^6$ GeV. Here we adopt the constraint from non-thermal leptogenesis.

4.5.3 Mixed axion/axino cold and warm dark matter scenarios for SO(10)

We consider a dark matter coctail composed of the following ingredients

$$\Omega_{DM}h^2 = \Omega_a h^2 + \Omega_{\tilde{a}}^{\rm TP} h^2 + \Omega_{\tilde{a}}^{\rm NTP} h^2 \tag{4.29}$$

and investigate various scenarios made by assigning different fractional amounts to different components. The main decisive factor here is the input choice of the model dependent parameter f_a/N, which in turn determines $\Omega_a h^2$. We take Yukawa-unified SO(10) benchmarks, and inputting $m_{\tilde{\chi}_1^0}$ and $\Omega_{\tilde{\chi}_1^0}h^2$, we calculate $m_{\tilde{a}}$ from the assigned value of $\Omega_{\tilde{a}}^{\rm NTP}h^2$. Then we input $m_{\tilde{a}}$ along with our proposal values of f_a/N and $\Omega_{\tilde{a}}^{\rm NTP}h^2$, and calculate T_R from the expression for $\Omega_{\tilde{a}}^{\rm NTP}h^2$. In our search for Yukawa-unified SO(10) solutions, we upgrade to ISAJET 7.79 and to the more recently announced top mass 172.6 GeV. We again make use of the MCMC technique to search for solutions with $R < 1.05$, but to be able to present our results more clearly, we make fixed-m_{16} scans for $m_{16} = 5, 8, 10, 15$ GeV. Using the solutions, we check the feasibility of the following four cosmological cases and plot the resulting T_R versus $m_{\tilde{a}}$ for each case in Figure 4.17. Figure also shows two bounds on re-heat temperature: $T_R = 10^6$ GeV, values smaller than which are not preferred by non-thermal leptogenesis, and $T_R = 10^4$ GeV, below which the calculations for thermal production become invalid.

- Case 1 (C1): $f_a/N = 10^{11}$ GeV from which $\Omega_a h^2 = 0.017$. Axino components are cho-

sen to be $\Omega_{\tilde{a}}^{\rm TP}h^2 \sim 0.083$ and $\Omega_{\tilde{a}}^{\rm NTP}h^2 \sim 0.01$. Here only a few solutions are preferred by non-thermal leptogenesis but still the axino mass in the allowed region is less then 10^{-4} GeV meaning that the axinos make up warm dark matter. This is inconsistent with the current cosmological model, therefore this scenario is cosmologically difficult.

- Case 2 (C2): $f_a/N = 4 \times 10^{11}$ GeV from which $\Omega_a h^2 = 0.084$. Axino components are chosen to be equal, with $\Omega_{\tilde{a}}^{\rm TP}h^2 = \Omega_{\tilde{a}}^{\rm NTP}h^2 \sim 0.013$. $m_{16} = 8 - 10$ TeV gives solutions above the non-thermal leptogenesis bound, and this time solutions with $m_a < 10^{-4}$ GeV do not create a problem since relic abundance is already dominated by the cold axions.

- Case 3 (C3): $f_a/N = 10^{12}$ GeV but we further assume a factor of $1/3$ error on $\Omega_a h^2$ so that $\Omega_a h^2 = 0.084$. Axino components are again chosen equal, with $\Omega_{\tilde{a}}^{\rm TP}h^2 = \Omega_{\tilde{a}}^{\rm NTP}h^2 \sim 0.013$. In this case more solutions are allowed by non-thermal leptogenesis due to larger f_a/N, and again there is no danger coming from warm axinos below $m_{\tilde{a}} < 10^{-4}$ GeV. Therefore Case 3 is also cosmologically consistent.

- Case 4 (C4): $f_a/N = 10^{12}$ GeV, but we assume a case of a tiny axion relic abundance due to accidental vacuum allignment. Here dark matter is only made of axinos. We take $\Omega_{\tilde{a}}^{\rm TP}h^2 = 0.1$ and $\Omega_{\tilde{a}}^{\rm NTP}h^2 \sim 0.01$. This case gives allowed solutions for the whole mass range $5 - 15$ GeV, but again we need to exclude warm axinos with $m_{\tilde{a}} < 10^{-4}$ GeV. But even then, Case 4 allows solutions covering $m_{16} = 5 - 15$ GeV.

In the end we conclude that mixed axion/axino cold and warm dark matter solutions provide a cosmologically consistent possibility to accommodate SO(10) scenarios with excess relic density. We also show that the larger Peccei-Quinn breaking scales f_a lead to wider allowed m_{16} ranges.

The SO(10) SUSY GUTs are considered as well-motivated models, offering a scheme with matter unification as well as $t - b - \tau$ Yukwa coupling unification at the GUT scale. In the studies summarized here, we addressed searches for Yukawa-unified SO(10) GUTs, search strategies for such scenarios in leptonic channels at the LHC, and consequences for a cosmology with mixed axion/axino cold and warm dark matter, All these build up a consistent phenomenology with rich prospects for experimental observation.

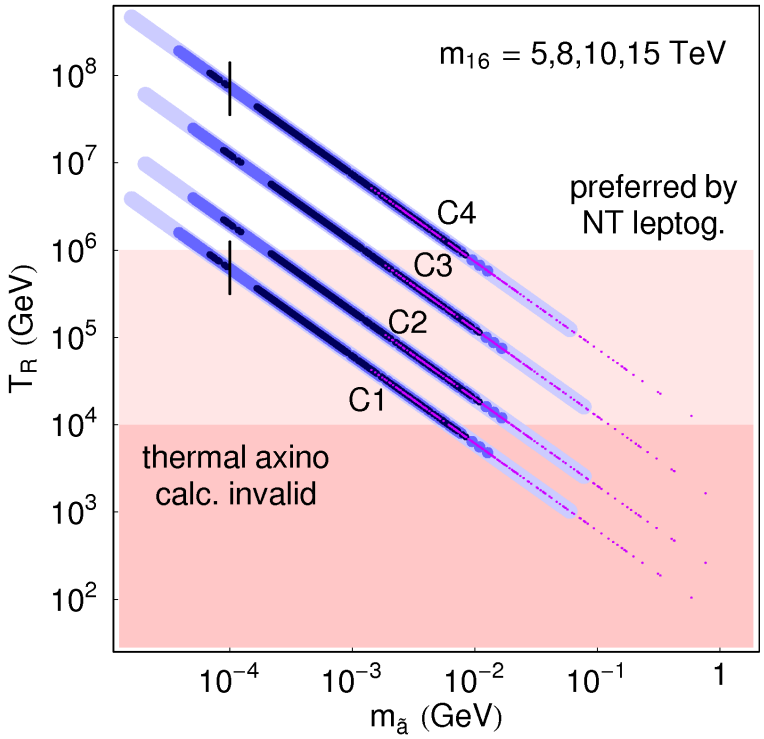

Figure 4.17: Plot of locus in the T_R vs. $m_{\tilde{a}}$ plane of four Yukawa-unified cases of mixed axion/axino dark matter, along with four different m_{16} values. Purple (small), dark blue (medium), blue (large) and light blue (very large) dots show solutions with $m_{16} = 5, 8, 10, 15$ TeV. The thermally produced axino relic density calculation is only valid for $T_R \gtrsim 10^4$ GeV. Non-thermal leptogenesis prefers the region with $T_R \gtrsim 10^6$ GeV. The black, vertical lines intersecting C1 and C2 show the axino mass limit $m_{\tilde{a}} = 10^{-4}$ GeV below which axinos constitute warm dark matter.

CHAPTER 5

PHENOMENOLOGY OF THE FOCUS POINT mSUGRA

5.1 Introducing focus point mSUGRA

After the string-inspired and GUT-inspired models, we now move on to a special case of SUGRA, called the focus point scenario.

Sparticle masses are favored to be typically below ∼1 TeV due to constraints from naturalness. Above 1 TeV SUSY is challanged by fine tuning. However for a reliable decision on compliance with naturalness, the amount of fine tuning needs to be quantified. A conventionally used measure of fine-tuning is the sensitivity of weak scale Z mass to the variations in the fundamental parameters, such that

$$\frac{\Delta M_Z^2}{M_Z^2} = c_i \frac{\Delta a_i}{a_i} \tag{5.1}$$

where a_i are the GUT scale input parameters and c_i is the fine tuning parameter. In a previous study, Feng et. al. examined this sensitivity arising from different input parameters [85]. Besides justifying the naturalness of parameter regions with sparticle masses less then ∼ TeV, they also discovered that for a special case, the fine tuning for regions with m_0 ∼2-3 TeV can be as small as that for $m_0 \lesssim 1$ TeV. This class of solutions with $m_0 >> m_{1/2}$ possess the "focus point" property, which means that the RGE trajectories of a parameter converge at a point at the weak scale for varying inputs at the GUT scale. Such behavior is caused by the form that RGE equations take due to the $m_0 - m_{1/2}$ results in fixed solutions for a family of ultraviolet boundary conditions. Ref [85] examined the case where m_{H_u} has a focus point. It was shown that as the weak scale value of m_{H_u} is insensitive to its GUT scale value, the REWSB conditions are also stable and result in a Z mass that is also insensitive, thus making the focus point (FP) scenario consistent with naturalness. FP regions were also found to be

slightly favored by gauge coupling unification [1].

The FP solutions are obtained for both moderate and large $\tan\beta$. They are settled right at the back of the region excluded by REWSB. Here $|\mu|$ becomes small, with $\mu \sim m_{\tilde{\chi}_1^0} \sim m_{\tilde{\chi}_1^\pm}$, and hence $\tilde{\chi}_1^0$ becomes Higgsino-like. This has an important consequence for cosmology, because a large Higgsino component enhances the rate of $\tilde{\chi}_1^0\tilde{\chi}_1^0$ annihilation into WW, ZZ and Zh pairs, that result in a much efficient reduction of $\Omega_{\tilde{\chi}_1^0}h^2$, easily pushing it below the WMAP upper bound [87]. As one gets closer to the REWSB-excluded region, $\tilde{\chi}_1^0\tilde{\chi}_1^\pm$ and $\tilde{\chi}_1^0\tilde{\chi}_2^0$ coannihilation effects also contribute to the adjustment of $\Omega_{\tilde{\chi}_1^0}h^2$.

A follow-up study [88] then showed that FP solutions are able to suppress unwanted contributions to proton decays and electric dipole moments which can emerge in other SUSY models. This leads to an α_s prediction which is more consistent with experiment and also enhances the allowed CP-violating phases by an order of magnitude or two. It was also seen that the heavy stops and sbottoms triggered by the large m_0 single-handedly generate a natural light Higgs mass ≥ 115 GeV.

As a result, FP solutions are worthwhile consideration as a promissing mSUGRA subcase with heavy scalars.

5.2 Focus point scenarios for the LHC

Inspired by this, we set out to determine FP scenarios that are feasable for observation at the LHC [89]. With a large $m_0 \sim 2-3$ TeV and small-to-moderate $m_{1/2}$, scalars should be at the edge or beyond the LHC reach, while gauginos and gluinos mostly lie within the LHC reach. Here we choose to focus on the case where gluinos are light enough to be produced at the LHC. We again ask the help of the Markov Chain Monte Carlo (MCMC) method introduced in Section 4.2.1. Taking off from points that have $m_0 \sim 2$ TeV and $m_{1/2} \sim 200$ GeV, we perform a scan in the mSUGRA parameter space with $\mu > 0$ to look for regions with light gluinos having $m_{\tilde{g}} \sim 500$ TeV and a WMAP compatible $\Omega_{\tilde{\chi}_1^0}h^2$. In order to avoid heading towards bino-LSP or τ_1 coannihilation regions, we further restrict m_0 to be above 1.5 TeV. The observational limits on sparticle masses were also imposed. We use SOFTSUSY 2.0.14 for RGE calculations and micrOMEGAs 2.0.7 for relic density calculations.

Figure 5.1 shows the distribution of WMAP-compatible focus point-like solutions on

[1] An earlier study by Chan et. al. [86] followed a different approach, taking μ^2/m_Z^2 as a fine tuning measure. They found that for $\tan\beta \geq 10$ there is a hyperboloid-like $m_0 - m_{1/2}$ region above $m_0 \sim 1$ TeV which gives a fixed, moderate fine tuning. It is referred to as the hyperbolic branch (HB) region.

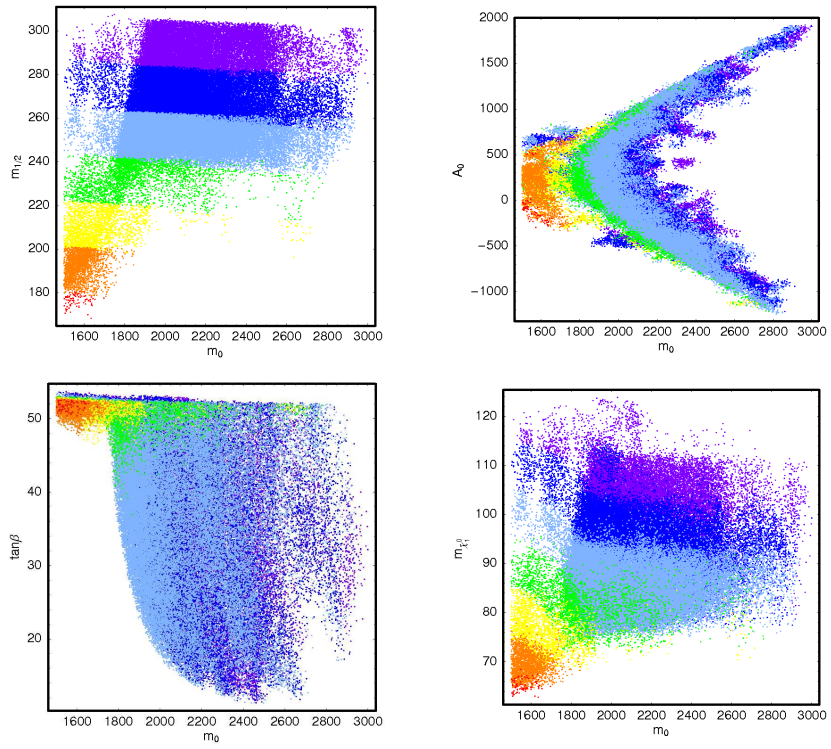

Figure 5.1: Focus point solutions found by MCMC scans using SOFTSUSY 2.0.14 + micrOMEGAs 2.0.7 on the $m_{1/2}$ vs. m_0 (top left), A_0 vs. m_0 (top right), $\tan\beta$ vs. m_0 (bottom left) and $m_{\tilde{\chi}_1^0}$ vs. m_0 (bottom right) planes. Different colors represent diferent gluino masses: $m_{\tilde{g}} \leq 500$ (red), $500 < m_{\tilde{g}} \leq 550$ (orange), $550 < m_{\tilde{g}} \leq 600$ (yellow), $600 < m_{\tilde{g}} \leq 650$ (green), $650 < m_{\tilde{g}} \leq 700$ (light blue), $700 < m_{\tilde{g}} \leq 750$ (blue) and $750 m_{\tilde{g}} \leq 800$ (purple).

the $m_{1/2}$ vs. m_0, A_0 vs. m_0, $\tan\beta$ vs. m_0 and $m_{\tilde{\chi}_1^0}$ vs. m_0 planes, where different colors show different gluino mass ranges. Generically we observe that higher $m_{\tilde{g}}$ solutions are more favored by the FP case. As expected, lower $m_{\tilde{g}}$ solutions are found for lower m_0 and $m_{1/2}$. We further see that a free variation of A_0 opens the possibility of finding more solutions, allowing the range $-1200 \lesssim A_0 \lesssim 2000$ especially for $m_{\tilde{g}} > 650$ GeV. FP solutions were found for a wide range of $\tan\beta$ from ~ 10 up to ~ 55, but $m_{\tilde{g}} < 650$ GeV restricts $\tan\beta$ to $\sim 45 - 55$. The $\tilde{\chi}_1^0$ mass range to achieve WMAP-compatible $\Omega_{\tilde{\chi}_1^0} h^2$ is $\sim 65 - 125$ GeV, but $m_{\tilde{g}} < 650$ TeV implies $m_{\tilde{\chi}_1^0} < 80$ GeV.

Figure 5.2 then shows μ vs. m_0 and the higgsino component of $\tilde{\chi}_1^0$ vs. μ. As expected, FP solutions are possible for a low μ, where low $m_{\tilde{g}}$ solutions are especially favored by $\mu < 200$. It is also seen that higgsino content increases steeply with decreasing μ. The focus point behavior is obviously enhanced with increasing $m_{\tilde{g}}$. Solutions with $m_{\tilde{g}} \lesssim 500$ GeV have a small higgsino component ~ 0.2, but this nevertheless is enough to generate an efficient relic

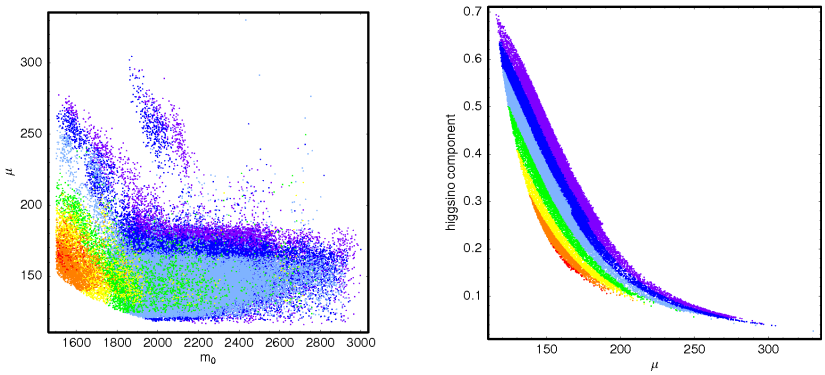

Figure 5.2: Focus point solutions found by MCMC scans using SOFTSUSY 2.0.14 + micrOMEGAs 2.0.7 on the μ vs. m_0 (left) and higgsino content vs. μ (right) planes. Different colors represent diferent gluino masses: $m_{\tilde{g}} \leq 500$ (red), $500 < m_{\tilde{g}} \leq 550$ (orange), $550 < m_{\tilde{g}} \leq 600$ (yellow), $600 < m_{\tilde{g}} \leq 650$ (green), $650 < m_{\tilde{g}} \leq 700$ (light blue), $700 < m_{\tilde{g}} \leq 750$ (blue) and $750 m_{\tilde{g}} \leq 800$ (purple).

density reduction. Solutions we found reach up to a higgsino content of ~ 0.7, but such utterly FP scenarios favor $m_{\tilde{g}} > 800$ GeV which makes them more difficult to chase at the LHC.

Guided by this information we select two benchmarks as candidate scenarios for the LHC. These are listed in Table 5.2. FP1 is a benchmark with a low gluino mass $m_{\tilde{g}} = 495.2$ GeV while FP2 has heavier gluinos with $m_{\tilde{g}} = 682.5$ GeV. FP1 will lead to gluino production with high cross sections at the LHC while FP2 will cause a lower rate of production due to the heavier gluinos. However the FP2 LSPs with $m_{\tilde{\chi}_1^0} = 64.92$ GeV are also heavier with respect to the FP1 LSPs with $m_{\tilde{\chi}_1^0} = 80.21$ GeV. As a result FP2 will compensate its lesser gluino production by having more events that will survive the cuts on missing E_T.

Table 5.1: GUT scale input parameters, μ, higgsino component, $m_{\tilde{g}}$, $m_{\tilde{\chi}_1^0}$ and $\Omega_{\tilde{\chi}_1^0}h^2$ for the two selected FP benchmarks FP1 and FP2. $m_t = 172.5$. Spectra are calculated using SOFTSUSY 2.0.14 and $\Omega_{\tilde{\chi}_1^0}h^2$s are computed using micrOMEGAs 2.0.7.

Point	m_0	$m_{1/2}$	A_0	$\tan\beta$	μ	Hggsn	$m_{\tilde{g}}$	$m_{\tilde{\chi}_1^0}$	$\Omega_{\tilde{\chi}_1^0}h^2$
FP1	1606.0	176.8	50.8	-161.9	159.6	0.184	495.2	64.92	0.106
FP2	2544.6	248.6	47.6	-865.8	128.9	0.502	682.5	80.21	0.094

Finally for the sake of complementarity we examine the sensitivity of obtaining RGE solutions with respect to changes in the GUT scale input parameters and check if the solutions in the vicinity of the two benchmarks have WMAP-compatible $\Omega_{\tilde{\chi}_1^0}h^2$ as well as gluinos

observable at the LHC. As in Section 4.4, we move the input parameters within %10 variation of a uniform random distribution. Figures 5.3 and 5.4 show the efficiencies of getting valid RGE solutions on the left and resulting $\Omega_{\tilde{\chi}_1^0}h^2$ on the right on $m_{1/2}$ vs. m_0, A_0 vs. m_0 and $\tan\beta$ vs m_0 planes for FP1 and FP2 respectively. As a generic feature, increasing the m_0 makes getting valid solutions much harder, and this effect gets more emphasized for FP2, meaning that the focus point behaviour is constrained to a narrower m_0 band for higher m_0 values. Then for a fixed m_0, higher $m_{1/2}$ and lower A_0 are preferred. For FP1, since $\tan\beta$ is already high, pushing it higher gets us to a strict boundary of no REWSB.

Gluino masses around FP1 vary from 449 GeV to 540 GeV and thus gluinos are within the LHC reach. Variations in FP1 almost always result in $\Omega_{\tilde{\chi}_1^0}h^2 < 0.136$, though as $m_{1/2}$ goes up for low values of m_0, there is a significant possibility of getting $\Omega_{\tilde{\chi}_1^0}h^2$ larger than the WMAP upper limit. There are a considerable amount of solutions with $\Omega_{\tilde{\chi}_1^0}h^2$, especially condensed at the REWSB boundary at large $\tan\beta$, meaning that this class of scenarios easy to observe at the LHC possess a significant amount of fine tuning.

Gluino masses around FP2 vary from 619 GeV to 749 GeV. Gluinos are heavier than 700 GeV for $m_0 \gtrsim 2.7$ TeV, and this region is much harder to observe at the LHC. FP2 lies in the midst of a neat band of solutions having $\Omega_{\tilde{\chi}_1^0}h^2$. This band has a width of $\delta m_0 \sim 300$ GeV and the major part of it lies on the left of $m_0 \sim 2.7$ TeV, so it consists of LHC-accessible solutions. FP2-like points also lead to solutions with $\Omega_{\tilde{\chi}_1^0}h^2 < 0.001$ however these are constrained to a very narrow region at the REWSB boundary at large $\tan\beta$, so FP2 is less fine-tuned and shows constitutes a more robust focus point scenario.

We will resume the FP scenarios later by presenting the discovery potential of PP1 and FP2 with the inclusive jets and missing E_T channel at the LHC in Chapter 7.

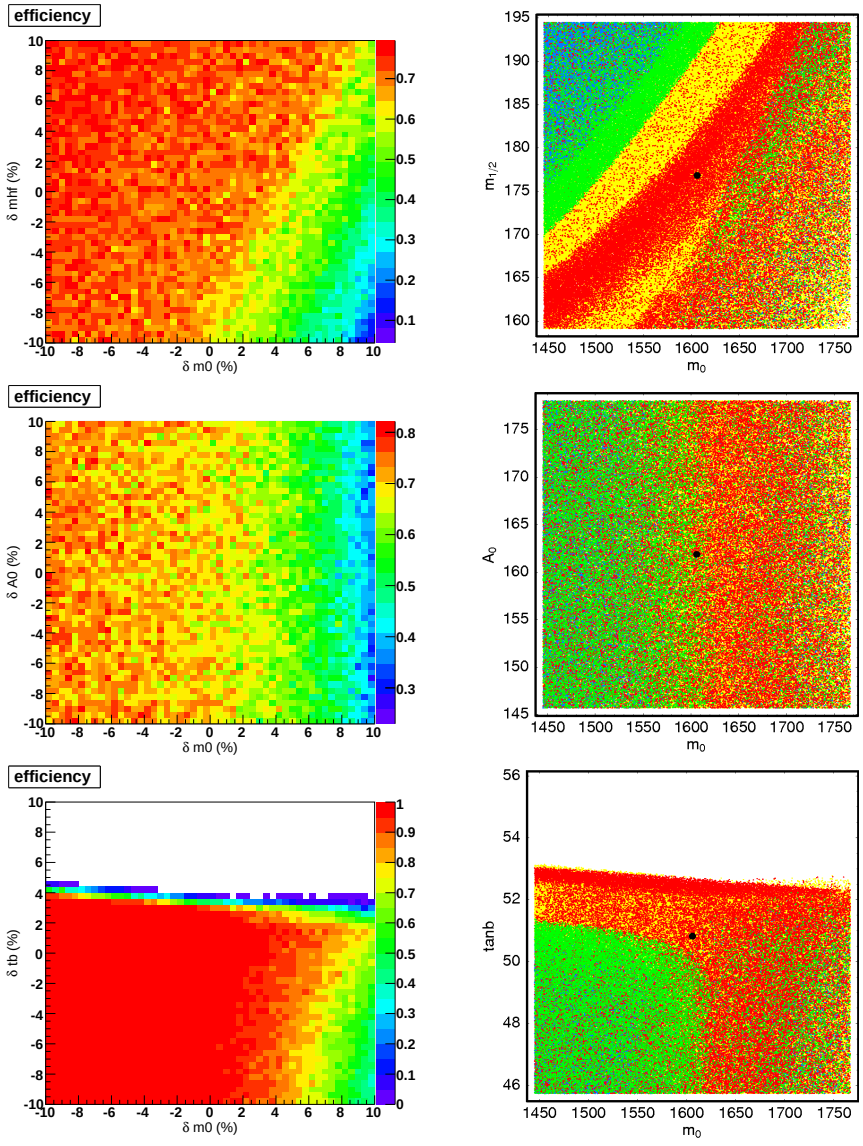

Figure 5.3: Efficiency of finding RGE solutions (left) and values of $\Omega_{\tilde{\chi}^0_1}h^2$ (right) on input GUT scale parameter planes, obtained by varying the input parameters of FP1 randomly in a uniform distribution of %10 around the central values. Different relic density ranges shown are: $\Omega_{\chi^1}h^2 \leq 0.001$ (red), $0.001 < \Omega_{\chi^1}h^2 \leq 0.094$ (yellow), $0.094 < \Omega_{\chi^1}h^2 \leq 0.136$: WMAP range (green), $0.136 < \Omega_{\chi^1}h^2 \leq 1$ (blue), $1 < \Omega_{\chi^1}h^2 \leq 10$ (purple) and $10 < \Omega_{\chi^1}h^2 \leq 100$ (pink). The black dot marks the position of FP1.

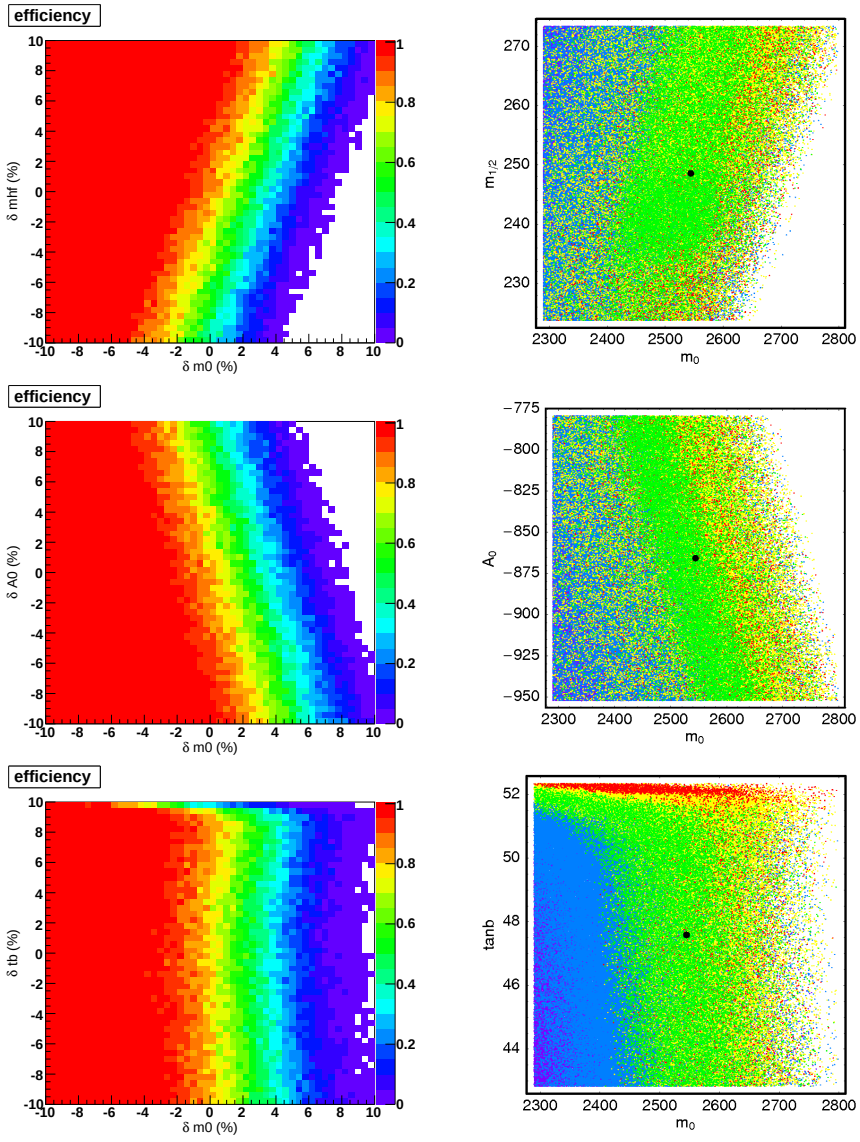

Figure 5.4: Efficiency of finding RGE solutions (left) and values of $\Omega_{\tilde{\chi}^0_1}h^2$ (right) on input GUT scale parameter planes, obtained by varying the input parameters of FP2 randomly in a uniform distribution of %10 around the central values. Different relic density ranges shown are: $\Omega_{\chi^1}h^2 \leq 0.001$ (red), $0.001 < \Omega_{\chi^1}h^2 \leq 0.094$ (yellow), $0.094 < \Omega_{\chi^1}h^2 \leq 0.136$: WMAP range (green), $0.136 < \Omega_{\chi^1}h^2 \leq 1$ (blue) and $1 < \Omega_{\chi^1}h^2 \leq 10$ (purple). The black dot marks the position of FP2.

CHAPTER 6

CERN LARGE HADRON COLLIDER AND THE COMPACT MUON SOLENOID EXPERIMENT

6.1 The Large Hadron Collider

On September 10, 2008, Large Hadron Collider (LHC), the newest gorgeous instrument of the quest for fundamentals of physics started operation by circulating beams in both directions successfully at CERN amidst an extraordinary attention from the whole world. Though shortly after the enthusiasm brought by recording first beam events LHC had to stop due to an incident on the 19th of September involving a large helium leak from sector 3-4 to the tunnel caused by a faulty electrical connection, it is planned to re-start operations in summer 2009 after the necessary repairs and the winter maintenance shut-down.

LHC [90],[91], is a 27 km long circular proton-proton collider to operate at maximal center-of-mass energy of 14 TeV. It lies 50-175 m underground in Geneva at the Swiss-French border. Starting with the first foreseen collisions in 2009, LHC will investigate the fundamental questions, acting more as a discovery machine that will aim to unravel the nature of new physics beyond the Standard Model. In addition, a part of LHC program consists of colliding lead ions with 5.5 TeV c.o.m energy per nucleon-nucleon collision.

Various physical, financial and historical consequences shaped the current design of the LHC. Going one step further from the LEP discoveries of the SM EW sector would require much higher energies impossible to reach through simple upgrades on LEP. Main difficulty would lie in synchrotron radiation which increases with increasing energy, and increases much more for light particles such as electrons as seen in the synchrotron energy loss formula for highly relativistic particles:

$$-\Delta E = \frac{4\pi\alpha}{3R}\beta^3\gamma^4. \tag{6.1}$$

Here m is the mass, E is the energy and R is the radius of curvature of the particle and α is the fine structure constant. The two options to avoid huge energy losses by synchrotron radiation were either to build a linear collider for electrons or to use the existing LEP tunnel as a stage for the new machine and introduce the heavy protons as its new actors. The latter was found technically and financially more convenient. Properties of protons, radius of the LEP tunnel and maximal amount of magnetic field technically achievable can be combined to determine the maximum collision energy using

$$p[GeV/c] = 0.3B[T]R[m] \tag{6.2}$$

where LEP-LHC tunnel radius of curvature R equals 4.3 km. The very high magnetic fields necessary for providing energies high enough for new discoveries could only be reached by using the superconductor technology. A special magnet system has been designed for the LHC which consists of $\sim$ 9600 magnets of various types, such as dipoles to bend the beam, quadrupoles to focus the beam near collision points as well as sextupoles, octupoles, decapoles, etc. used as correction magnets. Total energy stored in the LHC magnets is $\sim$ 11 GJ. LHC has 1232 dipoles, each with a length of 14.3 m and weight of 35 tonnes, which will provide the 8.33 T magnetic field. Dipoles use finely structured Niobium-Titanium (NiTi) cables that transport a very high current of 11700 A

The NiTi dipoles of LHC will operate at a temperature of 1.9 K which will be provided by a cryogenic system that uses superfluid helium. Helium is first cooled to 80 K with the help of liquid nitrogen, then to 4.5 K by the refrigerator turbines. After this, helium is injected into the magnet cold masses and further cooled to 1.9 K. The complete cool down process takes up to several weeks. LHC uses $\sim$ 120 tonnes of superfluid helium and the cryogenic system transports $\sim$ 150 kW for refrigeration at 4.5 K and $\sim$ 20 kW at 1.9 K.

Protons are driven first by a linear accelerator (linac) to 50 MeV, then by a booster up to 1.4 GeV. Next, protons will be transferred to the Proton Synchrotron (PS) where they will reach 25 GeV, and to Super Proton Synchrotron, where they will reach 450 GeV. Finally protons wil be injected into the LHC ring, where they will be accelerated to the nominal energy of 7 TeV. The LHC consists of 8 arc-shaped sectors and 8 straight insertions in between. Two beams travel in two seperate vacuum pipes with a vacuum pressure of 10^{-13} atm. Beams are designed to collide at four different points around which the four major LHC detectors Compact Muon Solenoid (CMS), A Toroidal LHC Apparatus (ATLAS), LHCb, and A Large Ion Collider Experiment at CERN (ALICE) are located.

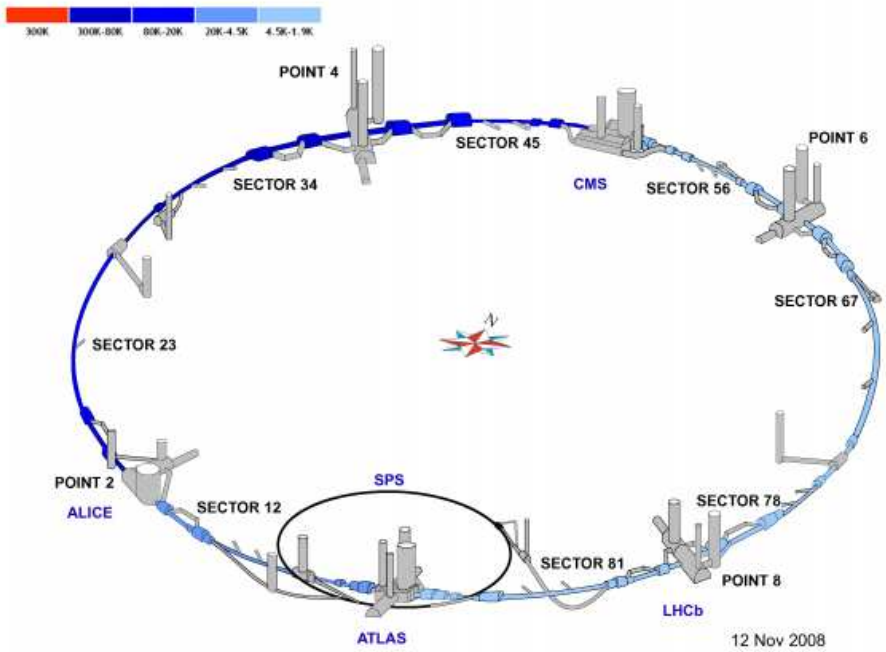

Figure 6.1: Large Hadron Collider and its experiments. Figure shows the cooldown status on 12 November 2008 [91]

Each beam is supported by 8 radiofrequency (RF) cavities that architect the bunch structure and deliver RF power to boost the beam and keep it at constant energy by compensating energy losses. The cavities will provide 16 MeV per turn in a peak alternating electric field of 5.5 MV/m osciallating at 400 MHz, and they will operate at 4.5 K. Total energy stored in a beam is $\sim$ 350 MJ. Beams can circulate for about 10 hours.

Each beam comes in 2808 bunches seperated by 25 ns (or 7.5 m). Each bunch has a length of 11.24 cm and a transverse dimension of $\sim$ 1 mm at injection. Bunch length will be reduced to 7.55 cm and bunch width to 16 microns at the interaction points. Each bunch will consist of $\sim 1.15 \times 10^{11}$ protons. Frequency of bunch crossing (at each interaction point) corresponds to $\sim$ 40 MHz.

The luminosity of a collider which collides bunches containing n_1 and n_2 particles at a frequency is given by

$$\mathcal{L} = F(\theta)\frac{\nu n_b N_1 N_2}{4\pi\sigma_x\sigma_y} \tag{6.3}$$

where ν is the bunch crossing frequency, $F(\theta)$ is the correction factor due to non-zero crossing angle and σ_x and σ_y characterize Gaussian transverse beam profiles. For the LHC, $F(\theta) \sim$

Table 6.1: Important LHC parameters

Parameter	Value
c.o.m. energy	14 TeV
Circumference	26.659 km
Dipole operating temperature	1.9K
Number of dipoles	1232
Number of quadrupoles	858
Number of correcting magnets	6208
Number of RF cavities	8/beam
Peak magnetic dipole field	8.33 T
Min. distance between bunches	$\sim$ 7 m
Design luminosity	$10^{34} cm^{-2} s^{-1}$
Nr of bunches per proton beam	2808
Bunch spacing	25 ns
Nr of protons per bunch	1.1×10^{11}
Nr of collisions per crossing	$\sim$ 20

%85. LHC design value at high luminosity running is to be $\mathcal{L} = 10^{34}$ cm^{-2}s^{-1}, while for the early runs after one year $\mathcal{L} = 2 \times 10^{33}$ cm^{-2}s^{-1} will be adopted. $L \sim 50$ fb^{-1} is expected for the first 3 years running.

Number of events for a process i with cross section σ_i is then found from

$$N_i = \int \sigma_i \mathcal{L} dt = \sigma_i L \tag{6.4}$$

where integration is performed upon the running time of the machine with luminosity $\mathcal{L}$. Here L is the integral luminosity. The total pp cross section expected at the LHC is $\sim$ 110 mb, $\sim$ 60 mb of which comes from inelastic collisions, $\sim$ 40 mb of which comes from elastic collisions and $\sim$ 10 mb of which comes from single diffractive events.

LHC is designed to be a discovery machine. One of its main goals is to investigate EWSB through detection of one or more Higgs bosons. LHC will also look for new particles that might originate from supersymmetry or other beyond the Standard Model (BSM) physics. Studies of QCD in multijet and top physics will as well be carried out, which are supposed to provide further information on the SM. Moreover CP violation in B sector will be explored in order to obtain precise measurements of the CKM matrix. The heavy ion collisions on the other hand will be used to search for the quark-gluon plasma.

Figure 6.1 shows the LHC complex with its experiments and Table 6.1 lists important LHC parameters.

6.2 The Compact Muon Solenoid Experiment

The Compact Muon Solenoid (CMS) [92] is one of the two general purpose detectors of LHC, especially designed to look for signatures of the Higgs boson and other new particles proposed by BSM theories such as supersymmetry. Opposed to ATLAS, it has adopted a compact detector design with a strong solenoidal magnetic field of 4 Tesla, which will be very helpful while distinguishing particles in high multiplicity events that are a common signature of the BSM physics.

CMS lies $\sim$ 100 m underground, at LHC collision point 5 in Cessy, France. It is a cylindrical detector with a length of 21.5 m and a diameter of 15 m and consists of a barrel and two endcaps. About 100 million seperate detecting elements make up its weight of 12500 tonnes. CMS has a multilayer structure resembling an onion, where different layers are subdetector elements specialized for differents tasks and measurements. From inside to outside, these subdetectors are the pixel detector and the silicon strip detector that make up the tracker, electromagnetic calorimeter (ECAL), hadronic calorimeter (HCAL), the superconducting magnet coil and the muon system.

Besides its advantageous strong magnet and compactness, the emphasis in CMS design was on having an accurate and efficient muon system. Muon detection is important since muons have a high penetrating power in the detector and a robust muon observation has great role while deciphering any new physics. Muon system was complemented by other features required by a generic purpose detector that aims BSM research: A high performance ECAL was planned for an efficient electron and photon detection, which becomes critical especially in Higgs observation in $\gamma\gamma$ decays. An HCAL complemented with forward detectors to provide 4π coverage and a "tail catcher" in the barrel region for energetic hadronic showers was designed for precise jet and missing energy measurements, which are crucial for SUSY observations. Calorimeters were complemented by a high resolution tracking system for an accurate reconstruction of tracks and secondary vertex reconstruction which are directly used during b and τ jet identification.

The CMS convention for coordinates is as follows: Origin is at the interaction point, x axis points to the center of the LHC ring, y axis points upwards and z axis points parallel to the beam in northwest direction towards the Jura mountains from Point 5. Azimuthal angle ϕ is defined with respect to the positive x axis and polar angle θ is defined with respect to positive z axis. Pseudorapidity is defined as $\eta = -\ln\tan(\theta/2)$.

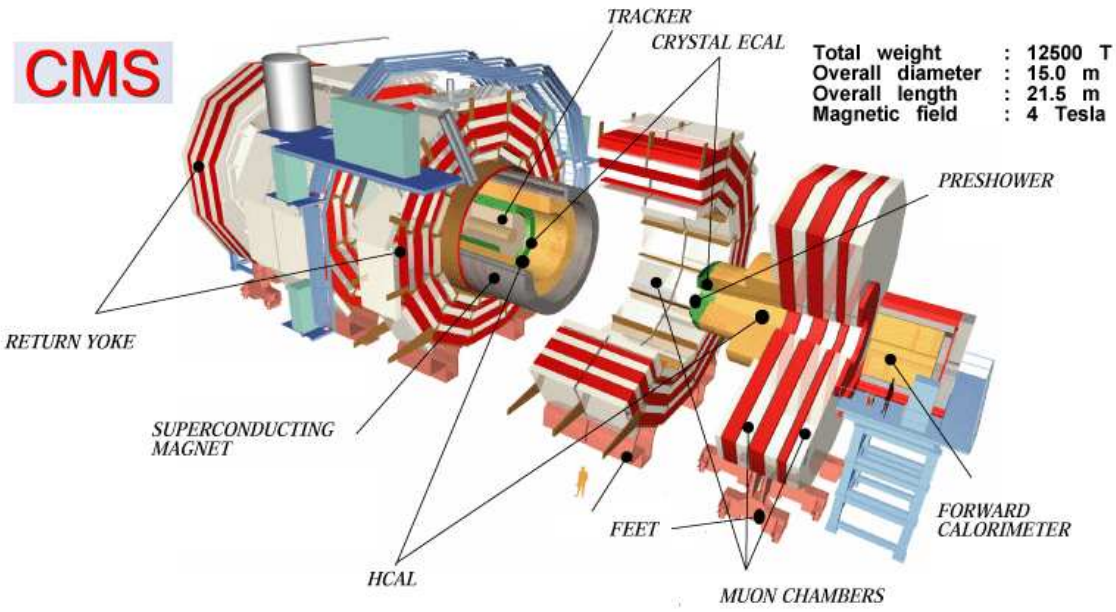

Figure 6.2: Schematic view of the Compact Muon Solenoid detector.

Figure 6.2 shows a detailed depiction of the CMS detector.

6.2.1 Tracker

A reliable measurement of charged objects depends on a precise identification of charged particle tracks and vertices. CMS tracking system [93], which constitues the innermost part of CMS, measures the momenta of charged particles bent by the 4 Tesla magnetic field through accurately determining their trajectories from the ionization they produce as they cross the tracker layers. Tracker layers consist of finely segmented silicon pixel detectors surrounded by single-sided and double-sided silicon strip detectors.

6.2.1.1 The Pixel Detector

Pixel detector is closest to the interaction point. It consists of three cylindrical layers in the barrel and two disks per endcap region. Barrel layers are situated at 4.4, 7.3 and 10.2 cm radial distances from the beam line, and have a length 53 cm. The endcap disks extend from radii 6 cm to 25 cm, and are placed at ±34.5 cm and ±46.5 cm on the z-axis. In total, there are 4.4 million square-shaped n-type silicon pixels of size $\Delta\eta \times \Delta\phi = 100\,\mu m \times 150\,\mu m$ with a thickness of $250\,\mu m$ that lead to an overall tracking precision of $\sim 15 - 20\,\mu m$ adequate for accurate charged track and vertex reconstruction in three dimensions. Barrel consists of

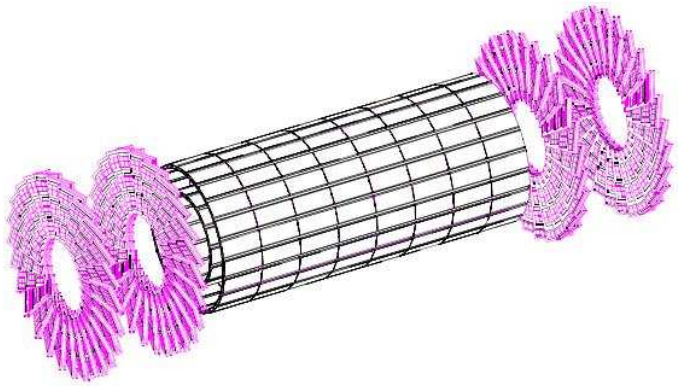

Figure 6.3: Layout of the pixel detector.

768 pixel modules arranged into half ladders made of 4 identical modules. Endcap disks are composed of 20° blades, where each blade is made of 7 pixel modules. There are 672 modules in total in the endcaps.

Figure 6.3 shows layout of the pixel detector.

6.2.1.2 The Silicon Strip Detector

The silicon strip detector is located outside the pixel detector, and is based on micro-strip silicon devices. It consists of four inner barrel layers (TIB), three inner endcap disks (TID), six outer barrel layers (TOB) and nine outer endcap disks (TEC). TIB, which extends to $|z| < 65$ cm is made of 4 layers with silicon sensors of thickness 320 μm and a strip pitch varying from 80 to 120 μm. Resulting resolution is 23-34 μm in $r - \theta$ and 230 μm in z directions. TOB extends to $|z| < 110$ cm, has 6 layers and a resolution of 35-52 μm in $r - \theta$ and 530 μm in z directions. The silicon strip modules in endcaps (TEC) are assembled on carbon fibre support wedges. Each TEC has 9 disks extending into 120 cm $< |z| <$ 280 cm and each TID has 3 disks located between the TIB and the TEC. In total there are 15400 modules that cover a $\sim 200m^2$ area and the signal is read out by $\sim$ 10 million electronic channels.

Pseudorapidity coverage of the tracker is $|\eta| < 2.4$. Low energy tracks ($p_T < 1$ GeV) are not reconstructed since they are bent too much by the magnetic field to reach the external region of the tracker. The reconstruction efficiencies are %85 and %95 for charged hadrons with $p_T > 1$ GeV and $p_T > 10$ GeV respectively while muons are reconstructed almost perfectly with an effiiency of %98 in the pseudorapidity region of $|\eta| < 2.1$. On the other

hand, electron tracks are reconstructed with %90 efficiency. Resolution in p_T measurement is given by

$$\frac{\sigma_{p_T}}{p_T} = \frac{\sigma_s}{s} = \sigma_s \frac{8 p_T}{0.3 B L^2} \tag{6.5}$$

where s is the sagitta which is the actual quantitiy measured in the tracker and thus a meaure of spatial resolution), B is the magnetic field strength and L is the coil length. Momentum resolution is parametrized as

$$\frac{\sigma_{p_T}}{p_T} \approx 15 p_T(TeV) \oplus \%0.5 \tag{6.6}$$

for $|\eta| < 1.6$ region and as

$$\frac{\sigma_{p_T}}{p_T} \approx 60 p_T(TeV) \oplus \%0.5 \tag{6.7}$$

for the $1.6 < |\eta| < 2.5$ region.

6.2.2 The Electromagnetic Calorimeter

The Electromagnetic Calorimeter (ECAL) [94] is the innermost calorimeter in CMS, designed to make accurate energy measurements of electrons and photons, and to assist HCAL in measuring jet energies. It is a homogeneous detector composed of radiation-hard lead-tungstate ($PbWO_4$) crystals that have a high density of 8.3 g/cm^3, a Moliere radius 2.2 cm and a radiation length of $X_0 = 0.89$ cm. This choice for the absorbing material enabled a compact design for the ECAL. It emits scintillation light with a time scale of the order of 25 ns, which allows measurements with time scales of the order of LHC bunch crossing.

ECAL is a combination of a barrel (EB) and two endcaps (EE). EB, which is made of 61200 cryistals, covers the region $|\eta| < 1.479$. Inner radius of the barrel cylinder reaching from the interaction point to the front faces of the crystals is 1.29 m. EB consists of 36 identical supermodules, each made of 4 modules. Cystals each cover a range of $\Delta\eta \times \Delta\phi = 0.0174 \times 0.0174$, corresponding to 22×22 mm^2 at the front face and 26×26 mm^2 at the rear face. Length of each crystal is 23 cm, which is equivalent to ~ 26 radiation lengths (X_0). To match the direction of particles coming from the interaction point, the EB crystals are arranged in a tilted structure. In η direction, cryistal longitudional axes are all inclined by -3 degrees with respect to the line joining the crystal front face center to the interaction point. In ϕ direction, the crystal axes are tangential to a circle of radius 66.7 m producing an angular tilt of 3 degrees.

EEs consist of 7134 crystals and span the pseudorapidity range $1.48 < |\eta| < 3.0$. They start at 3.170 m from the interaction point, with the crystal front faces starting at 3.205 m.

Each crystal covers 28.6×28.6 mm^2 at the front face and 30×30 mm^2 at the rear face. Length of each crystal is 22 cm that corresponds to $\sim 24.7X_0$. Each endcap has a preshower detector (ES) attached in front that have the purpose to distinguish between γs and π^0s, to help electron identification and to increase the position measurement of the electrons and photons. ES is a two-layer sampling calorimeter covering $1.653 < |\eta| < 2.6$. Its first layer is composed of lead radiators with thicknesses $2X_0$ and X_0, and its second layer is composed of silicon strip sensors that lie behind each radiator. With this setup %95 of the photons start showering before they reach the second silicon plane, providing a good discrimination against the π^0s. Photons produce an electromagnetic shower that interacts with the lead in the %95 of cases, and this contributes to a finer determination of the positions of electrons and photons.

$PbWO_4$ has a relatively low light yield, about 30 γs/MeV of deposited energy. Therefore each cryistal must be coupled with a high gain photomultiplier. In the EB case, rear face of each cryistal has two avalanche photo-diodes (APDs), each with a 5×5 mm^2 active area attached to it. In the EE case, crystals each have one vacuum phototriode (VPT) attached instead.

The energy resolution of ECAL is parametrized by

$$\left(\frac{\sigma}{E}\right)^2 \equiv \left(\frac{S}{\sqrt{E}}\right)^2 + \left(\frac{N}{E}\right)^2 + C^2 \tag{6.8}$$

where S is the stochastic term that includes the effects of the fluctuations in the photon statistics and the shower containment, N is the noise term that comes from electronics and pile up, and C is the constant term that arises due to calibration errors and various systematic errocts. The ECAL supermodule energy resolution was measured in a test beam and parameters were found as $N = 124$ Mev, $S =$ %3.63 and $C =$ %0.26.

6.2.3 The Hadron Calorimeter

Tha Hadron Calorimeter (HCAL) [95] specializes in measuring jets and missing transverse energy through which it helps to determine energies and directions of quarks/gluons and of uninteracting particles such as neutrinos and neutralinos. It also contributes to the identification of electrons, photons and muons through complementing the measurements by the ECAL and the muon system.

HCAL is a sampling calorimeter made of alternating layers of passive and active material, where the passive material serves as an absorber. Total energy measured is the sum of ionization energy deposited in the sampling layers which is then converted to an electronic

signal and digitized. HCAL surrounds ECAL and most of it is locationed within the magnet, which makes the HCAL design strongly dependent on the magnet parameters. To perform accurate $\not\!\!E_T$ measurements, HCAL is required to provide a good containment and hermeticity, and to minimize the non-Gaussian tails in energy resolution curves. This could be achieved by maximizing the material inside the magnet in terms of interaction lengths. For this, brass is chosen as the absorber material, which has a relatively short interaction length. Brass is a non-magnetic, low Z material, hence it is not magnetized in high fields and avoids multiple scattering of muons. Moreover, the space occupied by the active material is minimized by adopting the tile/fibre technology, which consists of plastic scintillator tiles read out with embedded wavelength shifting filters (WLS). The WLS convert the blue light from scintillators to green light, which is then carried by clear fibres into the corresponding pixel of Hybrid Photo Diode detectors (HPDs) that convert light to electronic signals. The tiles are arranged in projective towers with fine granularity to achieve good jet seperation and mass resolution.

HCAL consists of four subdetector parts. Hadron barrel (HB) covers $|\eta| \leq 1.4$, has a length of 9 m and extends from 1.8 to 2.9 m in the radial direction. It is an assembly of two half-barrels each composed of 18 20° wedges in the ϕ direction. HB consists of 2304 towers having a segmentation $\Delta\eta\times\Delta\phi = 0.087\times0.087$, while in the radial direction there are 15 brass plates, each 5 cm thick, mechanically supported by two external stainless steel plates. Then there are the hadron endcaps (HE) covering $1.3 \leq |\eta| \leq 3.0$, which have inner radii of 0.4 m and outer radii of 3 m. The brass plates making up HEs are 7.8 cm thick. Each HE consists of 14 η towers, where the first tower overlaps with HB, the next 5 have a ϕ segmentation of 5° and an η segmentation of 0.087 while the remaining 8 have a ϕ segmentation of 10° to accomodate the bending radius of the WLS readaout and an η segmentation that vary from 0.09 to 0.35. There are 2304 towers in total. HB and HE scintillators are 3.7 mm thick.

The thickness of HCAL corresponds to 5 interaction lengths at $|\eta| = 0$. This is not sufficient for full hadronic shower containment. To sample the tails of leaking hadron showers, 10 mm thick scintillators are placed outside the vacuum tank of the magnet coil in order to act as ”tail-catchers”. This component, called hadron outer (HO) covers the $|\eta| \leq 1.26$ region and increases the effective thickness of HCAL to about 11 interaction lengths. HO lies below the muon system and hence is effected by its geometry. Tiles are grouped in 30° sectors to match the ϕ segmentation of the drift tubes of the muon system while the η direction is divided into 5 sectors called ”rings”.

The pseudorapidity range $3 < |\eta| < 5$ is covered by the hadron forward (HF) components,

which aim to measure high energy forward jets and to complete the hermetic coverage for a better $\not\!\!E_T$ determination. Their front faces are located at 11.15 m from the interaction point and the depth of the absorber is 1.65 m. Each HF module is constructed of 18 wedges, each covering a 20° angle. The η-direction is segmented into 13 towers with size $\Delta\eta \approx 0.175$ except for the lowest and highest η towers which have $\Delta\eta \approx 0.111$ and $\Delta\eta \approx 0.301$ respectively. The ϕ-direction is segmented into 10° except for the highest-η towers that are divided into 20° segments. There are 900 towers and 1800 channels in total in the 2 HFs.

The main constraint in the design of HFs was the high radiation dose they will receive ($\sim$ 0.1 GRad/year). HFs are made of steel absorbers and radiation-hard quartz fibres that provide a fast collection of Cherenkov light, which is then channeled to photomultipliers. HFs are built with a non-projective geometry where the quartz fibres run parallel along the length of absorbers to the beam line. The fibres are 0.6 mm thick and are placed 5 mm apart in a square grid, embedded in the grooves of the absorber. HFs use 1.65 m (long) fibres that run over the full HF length and 1.43 m (short) fibres that start at a 22 cm depth, which are readout seperately in order to distinguish between electromagnetic and hadronic showers. Electromagnetic showers deposit a significant part of their energy in the first 22 cm, so they are mostly observed by the long fibres, while the hadronic showers are observed by both.

According to the 2006 test beam data, energy resolution of the combined EB+HB system for beam momenta in 2-300 GeV/c range is given as

$$\left(\frac{\sigma}{E}\right)^2 = \left(\frac{0.71}{E}\right)^2 + \left(\frac{0.97}{\sqrt{E}}\right)^2 + 0.08^2 \tag{6.9}$$

where the first term represents the electronic noise, the second term is the stochastic term determined by statistical fluctuations in the shower developement and the last term depends on the degree of non-compensation.

6.2.4 Superconducting Magnet Coil

The CMS magnet design [96] was constrained by the requirement to provide a muon momentum resolution of $\Delta p_T/p_T \sim$ %10 for muons with momentum 1 TeV/c. Eq. 6.2 shows that a better momentum resolution is achieved by increasing the B field or the magnet size. CMS implemented the former approach, targeting a 4 Tesla magnetic field which allowed for a compact design.

The 4 T magnetic field is provided by a superconducting solenoid with length 12.9 m and inner diameter 5.9 m which has 2168 turns. 19.5 kA of current is passed through it

and the total stored energy is 2.7 Gj. The conductor made of niobium-titanium is in the form of Rutherford cable co-extruded with pure aluminium and mechanically reinforced with aluminium alloy, and it adopts a four-layer coil winding, all of which are necessary to cope with the high ampere turns, forces and stored energy.

The tracking system and all calorimetry except Hadron Outer (HO) is contained within the magnet. One disadvantage of a strong B field is that it bends the low-p_T particles so much that either they cannot reach the calorimetry or they part from other particles and hit the calorimetry, producing out-of-cone depositions that smear the jet reconstruction. Particles with $p_T < 0.9$ GeV/c cannot reach the calorimeters. The magnetic flux is returned by a 1.5 m thick saturated iron yoke instrumented with four stations of muon chambers. Return yoke weighs 11000 tons and consists of two endcaps, each of which have three disks, and a barrel yoke that is made up of five rings. The magnet system is complemented by a vacuum tank and ancillaries such as cryogenics, power supplies and process controls.

6.2.5 Muon System

Most of the interesting processes related to BSM physics such as supersymmetry or extra dimensions as well as SM precesses related to electroweak, Higgs or B physics expected at the LHC provide final states rich with muons, naming muons as crucial tools of discovery and precision measurements. Therefore reconstruction, robust identification, correct charge assignment and precise p_T measurement along with efficient triggering of muons have a high priority amoung the CMS design goals which are to be achieved by the combination of CMS muon and tracker systems.

Muons are heavy ($m_\mu = 105.65$ MeV), so they do not emit as much bremstrahlung radiation as the electrons, and are relatively long-lived ($\tau = 2.2 \times 10^{-6}$ s). They are not absorbed totally by the calorimeters, depositing only a little ionizing energy there and penetrating further. A particle is identified as a muon if it passes a large amount of material suffering only a small amount of energy loss and deflection.

CMS Muon System [97] has the mission of catching the muons that survive the calorimetry, so it is placed outside the magnet coil. It consists of four muon stations interleaved with the iron magnet return yoke plates and is divided into a central barrel part (MB) covering $|\eta| < 1.2$ and two endcaps (ME) covering $0.9 < |\eta| < 2.4$. Each endcap consists of four disks that enclose both ends of the barrel cylinder. Overall thinkness of absorber before the final muon station is $\sim$ 16 interaction lengths. Three different types of detectors are used

in the muon system. Drift tubes (DTs) are dominant in the barrel region where both muon rate and neutron induced background rate is small and magnetic field is low. In the endcaps where muon and neutron background rate as well as the magnetic field are large, cathode strip chambers (CSCs) are deployed. DTs and CSCs, which have a good posiion resolution are complemented with resistive plate chambers (RPCs) both in the barrel and endcaps up to $|\eta| < 2.1$ which have a good time resolution.

DTs provide track measurement up to $|\eta| = 1.3$, p_T triggering and bunch crossing identification. They are placed at 2 m $\times$ 2 m and 40 cm thick chambers hosted in MB. DTs have a cross section of 1×4 cm^2. DTs consist of 1.2 mm thick 9.6 mm long aluminum cathodes with stainless steel anode wires at their center. DT cells are filled with a gas mixture of %85 Ar and %85 CO_2. The electrons generated in the DTs move to anode wire in the center and the high electric field close to the wire amplifies the signal. The track position is measured by looking at the time needed for the electron to reach the wire. Mean time circuits that enable a fast trigger are used. Maximum drift time is 400 ns and time resolution is 5 ns. Spatial resolution is $\sim 100\ \mu m$ in $r - \phi$ space and $\sim 150\ \mu m$ in $r - z$ space.

The CSCs, also used for tracking, p_T triggering and bunch crossing identification have a faster response and finer segmentation then the DTs. CSCs are $\sim 1 \times 2$ m^2 trapezoidal chambers in MEs that consist of six gas gaps, all having a plane of radial cathode strips and a plane of gold-plated anode wires running almost perpendicular to the strips in the middle of the chamber. They are filled with a mixture of $Ar - CO_2 - CF_4$ gas. A charged particle traversing the chamber ionizes the gas and develops an avalanche which then induces a charge on the anode wire and an image charge on a group of cathode strips. The signal on the wires is fast and is used for the Level-1 trigger, but leads to a coarser position resolution, which is compensated by a precise position measurement made by determining the center of gravity of the charge distribution induced on the cathode strips. Spatial resolution of CSCs is $\sim 200\ \mu m$ ($\sim 100\ \mu m$ for the CSCs in the closest station to the interaction point) and time resolution is 6 ns. Both DTs and CSCs have a trigger spatial resolution of $\sim 1 - 2$ mm and bunch crossing identification efficiency of %99 at maximum LHC interaction rates.

RPCs are dedicated trigger detectors with a good timing resolution of ~ 3 ns. They are not used for tracking except for resolving ambiguities. Spatial resolution is the cell size which is about a centimeter. RPCs consist of two highly resistive plate pairs made of phenolic resin and coated by a conductive graphite paint. These plates acting as electrodes are seperated by a 2 mm gap filled with a gas mixture of mostly $C_2H_2F_4$, few percent of iso-C_4H_10 and less

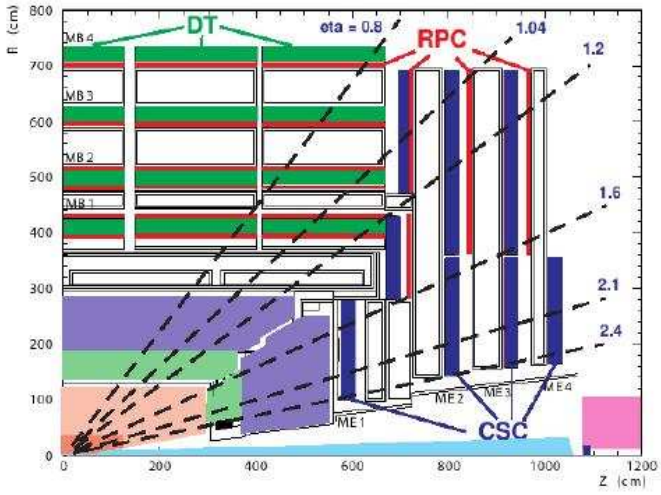

Figure 6.4: Schematic description of CMS muon system.

then a percent of SF_6. A passing muon develops an avalanche along its path. The drift of this charge towards the anodes produces a signal by inducing a fast charge on the other electrode.

A quarter of CMS muon system is shown in Figure 6.4. MB is segmented into 5 wheels in the beam direction labeled YB-2 to YB+2 from z- to z+. It consists of 4 stations of concentric detectors in the return yoke at radii of 4.0, 4.9, 5.9 and 7.0 m from the beam axis labeled MB1 to MB4 respectively. Each wheel is divided into 12 sectors in ϕ direction, each covering 30° angle. There are a total of 250 DT chambers, and chambers in different stations are staggered so that a high-p_T muon produced near a boundary passes at least 3 stations. Each DT is coupled to 1 or 2 RPCs. A high-p_T muon passing the DT system can cross up to 4 DTs and 6 RPCs, producing up to 44 measured points which are used to construct a muon-track candidate.

The endcaps consist of 4 disks perpendicular to the beam, and in concentric rings: 3 rings in the innermost station and 2 in the others. There are 36 chambers in each ring of a muon station except for the innermost ring of the second through fourth discs which have 18 chambers, making a total of 468 CSCs in 2 endcaps. All CSCs except those in the third ring of the first endcap disc are overlapped in ϕ to avoid gaps in the muon acceptance. MB+MEs have a total of 912 RPCs.

Reconstruction efficiency of a muon track is more than %90 for a 100 GeV muon in entire η range while the p_T resolution highly depends on η since for $|\eta| > 1.5$ tracks exit the solenoid and are less bent. Momentum measurement involving only the muon system which

uses the bending angle at the exit of the magnet is dominated by multiple scatterings in the material before the first muon station up to $p_T \sim 200$ GeV. Better resolution for low p_T muons are obtained from silicon tracker measurements while combination of inner tracker and muon system gives the best resolution for high-p_T muons in the $|\eta| < 2.5$ range. The muon system is also capable of measuring the muon charge (for muons with energy up to 1 TeV).

6.2.6 Trigger

Considering the 40 MHz bunch crossing and $10^{34}\text{cm}^{-2}\text{s}^{-1}$ LHC design luminosiy, CMS is expected to host $\sim$ 20 inelastic pp events per bunch crossing. A typical CMS event size is $\sim$ 1.5 MB, so hundreds of terabytes of data would be accumulated at the end of each second. However the current storage capability of CMS is $\sim$ 100 MB/s, therefore a reduction factor of $\sim 10^6$ in data is necessary. Total pp collision time per each year after 2008 will be 10^7 s, which will lead to huge amounts of data.

Among the 10^9 Hz of inelastic collisions relatively very few are physically interesting. For example SM Higgs production for $m_H \sim 100$ GeV would occur at 0.1 Hz. Figure 6.5 shows the typical cross sections and rates for different processes at the LHC. To reach the BSM physics goals, the rejection in incoming inelastic collision events needs to be of the order of $10^{-10/11}$. Since minimum bias events generally have low momentum, the strategy is to select high p_T events.

CMS will achieve such a filtering through the Trigger and Data Acquisition (DAQ) system [99], [100], whose implementation is relatively challenging with respect to the prior experiments due to both high bunch crossing rates at the LHC and low physics rate with respect to collision rate in hadron collisions. CMS triggering is done in two levels (Level 1 and High Level Trigger) and the system consists of four parts, namely the detector electronics, the Level-1 trigger processors, the readout network and an online event filter system to execute the software for the High Level Triggers. Each level reduces the data size while enabling more sophisticated analysis and algorithms to be applied to the data.

Level-1 Trigger (L1): It reduces the initial data collected at 40 MHz to 100 KHz. The triggering is done based on the information received from calorimeters (ECAL, HCAL and HF), all muon systems and the global combination of those. This information leads to the construction of trigger candidates such as photons, electrons, muons and jets, which are formed only if their p_T or E_T are above certain thresholds. Additionally, globally constructed objects as total hadronic E_T and $\not{E}_T$ are considered as trigger candidates.

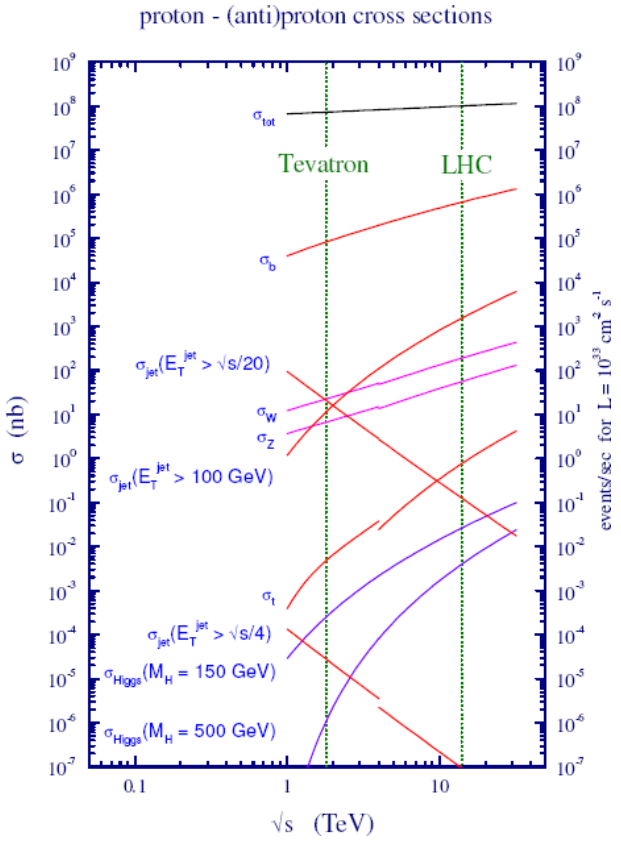

Figure 6.5: Production cross sections for various processes at hadron colliders (pp and $p\bar{p}$) as a function of c.o.m. energy. Discontinuities in some curves are due to transition from $p\bar{p}$ to pp collisions [98].

The L1 decision is made using custom-built hardware processors. Total time for L1 to come to a decision on accepting or rejecting data is 3.2 μs. Most of this period is due to the time necessary for the signal to be transferred from detector front end electronics to the L1 logic system, while the actual decision takes only $\sim 1\,\mu s$. However the special design prevents deadtime by allowing data from all detector channels to be stored in pipeline memories. After the decision, the signals accepted by L1 and the raw readout data are transferred to a computer farm through a temporary storage buffer for high level triggering.

High Level Trigger (HLT): It reduces the 100 KHz output rate recived from L1 to 100 Hz. HLT calculations are processed in a single farm of $\sim$ 1000 dual CPU computers, which enables flexibility in decision making. There are several internally-defined levels which redefine the measurements on trigger candidates and which can be optimized according to the LHC run conditions. Level 2 (L2) applies partial event reconstruction using calorimeters and the muon system and imposes L1 threshold values to more accurately reconstructed objects.

Level 2.5 optionally uses information from pixel detectors. Level 3 (L3) does full event reconstruction by including full information from tracking. An advantage of this system is that it enables usage of offline reconstruction algorithms. Eventually the data is stored for offline analysis where the specialized physics studies are to be performed.

CHAPTER 7

SEARCH FOR THE G_2-MSSM, SO(10) AND FOCUS POINT SUSY SCENARIOS IN CMS USING THE INCLUSIVE MISSING E_T+JETS SIGNATURE AT $\sqrt{s} = 14$ TeV AT THE CERN LHC

7.1 Introduction

Since the late 90s, many simulation studies have been carried out in order to test the capabilities of CMS in tracing supersymmetry. These analyses, for which summaries can be found in refs [102],[103] tried to cover a spectrum of SUSY scenarios at hand, and concentrated in various signature end topologies which would help to analyze the relevnant scenarios most efficiently. Up to now most CMS SUSY studies were focused on conventional mSUGRA scenarios having low-to-moderate mass scalars, 500 – 900 GeV gluinos and light-to-moderate gauginos and Higgses with masses < 1 TeV. These investigated the signaures related to various open or closed decay channels due to different squark-gluino, squark-gaugino or slepton-gaugino mass hierarchies. Occasional studies featured the trilepton channels for the mSUGRA benchmarks with heavier scalars.

In what follows, we will present an analysis on the CMS discovery potential of the G_2-MSSM (G2), SO(10) SUSY-GUT (SO10) and focus point (FP) scenarios that were introduced in Chapters 3, 4 and 5 [101]. Despite coming from different origins at the high scale, these three scenarios share common features at low energies: They all possess (very) heavy scalars that decouple from LHC physics, leaving gluino pair production to be the main actor. The leading order processes for gluino pair production from gluon-gluon and quark-antiquark interactions are shown in Figure 7.1. Furthermore, the light gauginos ($\tilde{\chi}_1^0$, $\tilde{\chi}_2^0$ and $\tilde{\chi}_1^\pm$) are all accessible at LHC energies, while the remaining gauginos can only be produced for some

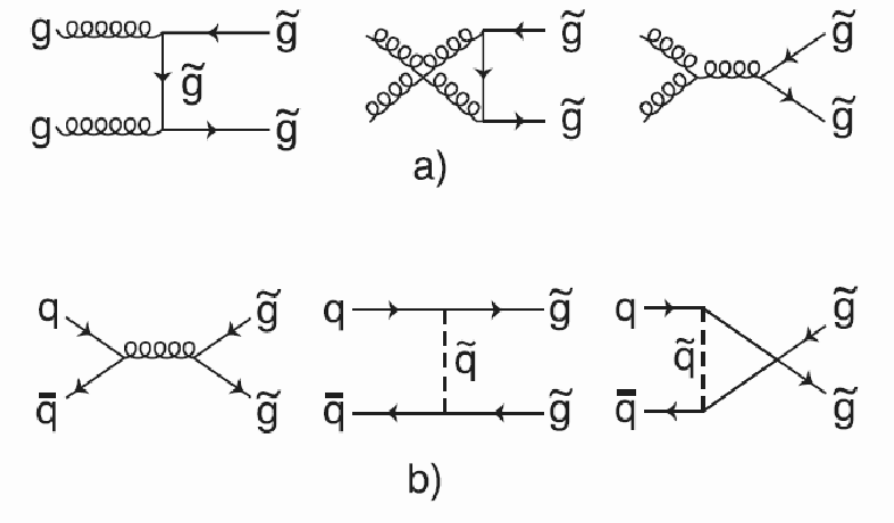

Figure 7.1: The leading order processes contributing to $pp \to \tilde{g}\tilde{g}$ production. a) gluon-gluon initial states, b) quark-antiquark initial states

SO10 scenarios as well as for the focus point case.

The gluinos decay subsequently through diverse cascades involving gauginos, tops and W/Zs into *b*-rich multi-jet states. Decays of gauge bosons and gauginos also lead to leptons. However there is no single leptonic decay with a dominant branching ratio, therefore leptonic studies that aim to extract information on SUSY spectrum would require methods to clearly distinguish between leptonic signals from different cascades. An exercise on dilepton and trilepton channels with a toy Monte Carlo was already described in Chapter 4 for the SO10 models. Recently much detailed analyses on these channels were thoroughly practiced with full simulation of the CMS detector response [104], [105]. In this study, we will rather concentrate on the all inclusive jet-MET channel, and trace the three scenarios at the multijet plus $\not{E}_T$ final states. The leptons will only be considered implicitly while introducing some cuts for background elimination through the indirect lepton veto method. This should be the reasonable approach when the diverse and entangled cascades in the three scenarios are concerned. Our aim will be to determine the LHC reach of selected benchmarks belonging to each scenario.

7.2 Selected benchmarks and signal generation

To sample the G2, SO10 and FP scenarios, two benchmarks per each were selected, as were explained in the relevant chapters for each scenario. Table 7.1 shows the mass spectra for the

six benchmarks. The G2 spectra were computed using a specialized mathematica package, SO10 spectra using ISASUGRA 7.75 and the FP spectra using SOFTSUSY 2.0.14. The trademark $m_{scalar} >> m_{\tilde{g}}$ holds for each case. As exceptions, heavy Higses are lighter than 500 GeV for FP1 and heavy gauginos are ligher than 350 GeV for SO10D, FP1 and FP2, providing them an LHC access. $\tilde{\chi}_1^0$ masses are highest ($\sim$ 110 GeV) for the G2s and lowest ($\sim$ 55 GeV) for the SO10s, hence highest SUSY $\not{E}_T$ should be expected from the G2s and the lowest from the SO10s.

Table 7.2 then shows the cross sections of various signal processes possible at the LHC as computed with PROSPINO 2.0. The $pp \to \tilde{g}\tilde{g}$ cross sections are directly dependent on the gluino mass, reaching values as high as $\sim$ 80 pb for the SO10s due to $m_{\tilde{g}} \sim 400$ GeV. Hardest case is G21, which has $\sigma(pp \to \tilde{g}\tilde{g}) = 0.25$ pb due to $m_{\tilde{g}} = 995$ GeV. $\tilde{q}\tilde{g}$ production is slightly possible for SO10D and FP2 while for FP1 where $m_{\tilde{q}} \sim 1$ TeV, it reaches 1 pb. Production of $\tilde{q}\tilde{q}/\tilde{q}\bar{\tilde{q}}$, $\tilde{\chi}^{\pm}\tilde{q}$ and $\tilde{\chi}^0\tilde{q}$ is totally suppressed due to large squark masses except the $\tilde{q}\tilde{q}/\tilde{q}\bar{\tilde{q}}$ case in FP1, which has a cross section of 0.04 pbs. $\tilde{\chi}^{\pm}\tilde{\chi}^0$ production exists for each benchmark, varying between 5-15 pb. $\tilde{\chi}^0\tilde{\chi}^0$ production is rarely possible, reaching 0.5 - 1 pb for the the FPs and 0.04 pb for the SO10D, while $\tilde{\chi}^{\pm}\tilde{\chi}^{\pm}$ pairs can be produced for all scenarios with cross sections varying between 2-8 pb for the selected benchmarks.

Next, the $\tilde{g}$, $\tilde{\chi}_2^0$ and $\tilde{\chi}_1^{\pm}$ branching ratios for the three scenarios computed using the package SUSYHIT 1.1 [106] is shown in Table 7.3. The gluinos decay dominantly to 3-body modes except for a %3.5 – 10.2 BR($\tilde{g} \to \tilde{\chi}^0 g$) in SO10D and FPs. Among the gluino decays, BR($\tilde{g} \to \tilde{\chi}_2^0 t\bar{t}$) leads with $\sim$ %35 for the G2s, BR($\tilde{g} \to b\bar{b}\tilde{\chi}_2^0$ leads with $\sim$ %56 for the SO10s and BR($\tilde{g} \to \tilde{\chi}_1^{\pm} t\bar{b}/b\bar{t}$ leads with $\sim$ %15 – 30 for the FPs. The decay modes $\tilde{g} \to \tilde{\chi}_1^{\pm} t\bar{b}/b\bar{t}$ and $\tilde{g} \to b\bar{b}\tilde{\chi}_1^0$ exist for all six benchmarks. All these lead to b and t-rich final states. Futhermore, Table 7.4 lists several important mass differences. By looking at $m_{\tilde{g}} - m_{\tilde{\chi}}$, hardest hadronic decay products from gluino decays can be expected for G21 and FP2, however, these decays are mostly lead to tops, and the momentum will be shared among the top decay products, leading to multijets with lower p_Ts. The SO10 gluinos would lead to softer jets.

The second step in gluino cascades generally involves a $\tilde{\chi}_2^0$ or a $\tilde{\chi}_1^{\pm}$. For G21, $m_{\tilde{\chi}_2^0} - m_{\tilde{\chi}_1^{\pm}} = 273.4 > m_W$, hence $\tilde{\chi}_2^0$s decay %100 to $W\tilde{\chi}_1^{\pm}$ modes. For G24, $m_{\tilde{\chi}_2^0} - m_{\tilde{\chi}_1^{\pm}} = 29.6 < m_W$, hence here $\tilde{\chi}_2^0$s decay through a virtual W. $\tilde{\chi}_2^0$s in SO10s and FP1 decay completely to $\tilde{\chi}_1^0$ through virtual Z modes with a %50 and %15 – 30 dominance of $q\bar{q}\tilde{\chi}_1^0$ and $b\bar{b}\tilde{\chi}_1^0$ final states respectively. Here $m_{\tilde{\chi}_2^0} < m_{\tilde{\chi}_1^{\pm}}$, so decays to $\tilde{\chi}_1^{\pm}$s are not allowed. For FP1, there is an approximate $\tilde{\chi}_2^0 - \tilde{\chi}_1^{\pm}$ mass degeneracy, hence decays to $\tilde{\chi}_1^{\pm}$s via virtual W modes are fully

Table 7.1: Spectra for selected G2, SO10 and FP benchmark points

Masses	G21	G24	SO10A	SO10D	FP1	FP2
Code	MATH	MATH	ISA	ISA	SOFT	SOFT
W	81	81	80.4	80.4	80.4	80.4
h^0	123.6	116.8	125.4	111.0	114.9	118.6
H	134144	34113	3294	782	434	1059
A^0	134144	34113	3273	777	434	1059
$H^\pm$	134144	34113	3296	788	427	1062
$\tilde{d}_L$	67559	17093	9186	2972	1628	2564
$\tilde{d}_R$	67559	17093	9242	2989	1628	2564
$\tilde{u}_L$	67559	17093	9185	2971	1625	2560
$\tilde{u}_R$	67559	17093	9104	2951	1627	2564
$\tilde{s}_L$	67559	17093	9186	2972	1628	2564
$\tilde{s}_R$	67559	17093	9242	2989	1628	2564
$\tilde{c}_L$	67559	17093	9185	2971	1625	2560
$\tilde{c}_R$	67559	17093	9104	2951	1627	2564
$\tilde{b}_1$	49548	12378	2723	849	1096	1763
$\tilde{b}_2$	67497	17076	2959	961	1216	1988
$\tilde{t}_1$	18819	3846	2315	434.3	965	1509
$\tilde{t}_2$	49548	12378	2870	940.6	1110	1774
$\tilde{e}_L$	67558	17091	9132	2956	1607	2543
$\tilde{e}_R$	67559	17091	9324	3009	1606	2543
$\tilde{\nu}_{e_L}$	67558	17091	9133	2955	1603	2540
$\tilde{\mu}_L$	67558	17091	9132	2955	1607	2543
$\tilde{\mu}_R$	67559	17091	9324	3009	1606	2543
$\tilde{\nu}_{\mu_L}$	67558	17091	9132	2955	1603	2540
$\tilde{\tau}_1$	67527	17084	4150	1210	1148	1931
$\tilde{\tau}_2$	67543	17097	5944	2216	1394	2254
$\tilde{\nu}_{\tau_L}$	67543	17087	6940	2214	1393	2255
$\tilde{g}$	995	573	396	387.7	495.2	682.5
$\tilde{\chi}_1^0$	116.3	107.1	55.6	52.6	64.8	80.2
$\tilde{\chi}_2^0$	389.9	137.1	128.3	105.1	109.6	130.6
$\tilde{\chi}_3^0$	87116	22319	4090	340.8	176.8	145.9
$\tilde{\chi}_4^0$	87116	22319	4090	352.0	221.5	250.5
$\tilde{\chi}_1^\pm$	116.5	107.3	128.8	105.7	105.8	109.6
$\tilde{\chi}_2^\pm$	87116	22319	4075	353.0	219.8	247.9

Table 7.2: LO (NLO) cross sections for G2, SO10 and FP points computed using PROSPINO 2.0

Point	code	$\tilde{g}\tilde{g}$	$\tilde{g}\tilde{q}$	$\tilde{q}\bar{\tilde{q}}$	$\tilde{q}\tilde{q}$	$\tilde{\chi}^{\pm}\tilde{q}$	$\tilde{\chi}^{0}\tilde{q}$	$\tilde{\chi}^{\pm}\tilde{\chi}^{0}$	$\tilde{\chi}^{0}\tilde{\chi}^{0}$	$\tilde{\chi}^{\pm}\tilde{\chi}^{\pm}$	Total
G21	MATH	0.25	0.00	0.00	0.00	0.00	0.00	10.67	0.00	5.33	16.25
		(0.40)	(0.00)	(0.00)	(0.00)	(0.00)	(0.00)	(14.17)	(0.00)	(7.00)	
G24	MATH	8.62	0.00	0.00	0.00	0.00	0.00	14.33	0.00	7.17	30.12
		(14.7)	(0.00)	(0.00)	(0.00)	(0.00)	(0.00)	(19.01)	(0.00)	(9.42)	
SO10A	ISA	73.00	0.00	0.00	0.00	0.00	0.00	7.52	0.00	3.73	84.25
		(123.00)	(0.00)	(0.00)	(0.00)	(0.00)	(0.00)	(9.98)	(0.00)	(4.90)	(137.88)
SO10D	ISA	80.60	0.07	0.00	0.00	0.00	0.00	14.36	0.04	7.08	102.15
		(136.00)	(0.09)	(0.00)	(0.00)	(0.00)	(0.00)	(19.07)	(0.05)	(9.29)	(164.5)
FP1	SOFT	19.10	1.05	0.01	0.03	0.00	0.00	10.90	0.54	4.89	36.53
		(33.70)	(1.66)	(0.01)	(0.04)	(0.00)	(0.00)	(14.61)	(0.67)	(6.37)	(57.07)
FP2	SOFT	2.73	0.06	0.00	0.00	0.00	0.00	7.86	1.03	2.87	14.55
		(4.82)	(0.09)	(0.00)	(0.00)	(0.00)	(0.00)	(10.50)	(1.40)	(3.77)	(20.58)

suppressed. For FP2, this degeneracy loosens to 21 GeV, allowing additional decays to $\tilde{\chi}_1^{\pm}$ through a virtual W. For all scenarios $\tilde{\chi}_2^0$s decay mostly to jets, however except the case of G21, these jets will be relatively soft, with p_Ts of the order of few tens of GeV.

For the G2s, $\tilde{\chi}_1^{\pm}$ and $\tilde{\chi}_1^0$ masses are nearly degenerate with $m_{\tilde{\chi}_1^{\pm}} - m_{\tilde{\chi}_1^0} < 200$ MeV. This leads to $\tilde{\chi}_1^{\pm}$ decays into $\tilde{\chi}_1^0$ plus a virtual W which subsequently decays into a soft pion or an electron/muon plus neutrino resulting in pion/lepton p_Ts of the order of 100 MeV. Due to this mass degeneracy, the $\tilde{\chi}_1^{\pm}$s are metastable, and they decay in the detector. Outcoming pions and leptons could have been observed as short track stubs in the CMS tracker. however their extremely low p_Ts renders such an observation unlikely. Therefore, $\tilde{\chi}_1^{\pm}$s in G2s are totally converted to missing energy. SO10s and FPs have $\tilde{\chi}_1^{\pm}$ modes mimicking W decays, so the $q\bar{q}\tilde{\chi}_1^0$ final states dominate with $\sim$ %67. Resulting jets will be soft (harder in SO10 case), with p_Ts similar to the p_Ts of jets coming from $\tilde{\chi}_2^0$ decays.

This detailed information points out to the dominance of hadronic activity, and hence is a jusification of our choice to work with the jet-MET topologies for a generic discovery analysis.

Signal processes for all benchmarks were produced using the parton shower generator `PYTHIA 6` [107], which has been interfaced to the CMS software framework through the package `GeneratorInterface/Pythia6Interface`. Sparticle spectra, mixings, other EW parameters and cross sections, which were computed with the various codes mentioned above were formatted as a SUSY Les Houches Accord (SLHA) [108] file and were input to the `Pythia6Interface`. Detector simulation, digitization and reconstruction were processed by

Table 7.3: BRs computed with SUSYHIT for G2, SO10 and FP benchmarks

BR	G21	G24	SO10A	SO10D	FP1	FP2
$\tilde{g} \to \tilde{\chi}_2^0 g$	–	–	–	4.7	1.3	–
$\tilde{g} \to \tilde{\chi}_3^0 g$	–	–	–	–	6.3	3.5
$\tilde{g} \to \tilde{\chi}_4^0 g$	–	–	–	–	2.6	–
$\tilde{g} \to \tilde{\chi}_1^0 q\bar{q}$	9.2	10.7	–	–	3.1	1.1
$\tilde{g} \to \tilde{\chi}_2^0 q\bar{q}$	–	–	–	–	4.6	1.7
$\tilde{g} \to \tilde{\chi}_4^0 q\bar{q}$	–	–	–	–	1.4	1.9
$\tilde{g} \to \tilde{\chi}_1^0 b\bar{b}$	8.0	9.7	16.1	16.2	11.7	9.8
$\tilde{g} \to \tilde{\chi}_2^0 b\bar{b}$	–	–	56.0	56.4	15.6	3.9
$\tilde{g} \to \tilde{\chi}_3^0 b\bar{b}$	–	–	–	–	12.5	8.7
$\tilde{g} \to \tilde{\chi}_4^0 b\bar{b}$	–	–	–	–	5.4	3.0
$\tilde{g} \to \tilde{\chi}_1^0 t\bar{t}$	4.5	–	–	–	–	1.9
$\tilde{g} \to \tilde{\chi}_2^0 t\bar{t}$	32.9	35.6	–	–	–	4.0
$\tilde{g} \to \tilde{\chi}_3^0 t\bar{t}$	–	–	–	–	–	5.0
$\tilde{g} \to \tilde{\chi}_4^0 t\bar{t}$	–	–	–	–	–	1.4
$\tilde{g} \to \tilde{\chi}_1^\pm q\bar{q}$	18.4	21.4	4.1	–	9.1	2.1
$\tilde{g} \to \tilde{\chi}_2^\pm q\bar{q}$	–	–	–	–	2.7	4.0
$\tilde{g} \to \tilde{\chi}_1^\pm t\bar{b}/b\bar{t}$	24.8	16.4	20.1	17.4	15.4	30.3
$\tilde{g} \to \tilde{\chi}_2^\pm t\bar{b}/b\bar{t}$	–	–	–	–	7.8	15.0
$\tilde{\chi}_2^0 \to \tilde{\chi}_1^\pm W$	100	–	–	–	–	–
$\tilde{\chi}_2^0 \to \tilde{\chi}_1^0 q\bar{q}$	–	–	51.6	53.6	54.0	26.6
$\tilde{\chi}_2^0 \to \tilde{\chi}_1^0 b\bar{b}$	–	–	29.1	16.5	14.6	7.0
$\tilde{\chi}_2^0 \to \tilde{\chi}_1^0 e\bar{e}$	–	–	2.3	3.3	3.4	1.7
$\tilde{\chi}_2^0 \to \tilde{\chi}_1^0 \mu\bar{\mu}$	–	–	2.3	3.3	3.4	1.7
$\tilde{\chi}_2^0 \to \tilde{\chi}_1^0 \tau\bar{\tau}$	–	–	1.9	3.3	3.5	1.7
$\tilde{\chi}_2^0 \to \tilde{\chi}_1^0 \nu_e\bar{\nu}_e$	–	–	4.5	6.6	6.8	3.4
$\tilde{\chi}_2^0 \to \tilde{\chi}_1^0 \nu_\mu\bar{\nu}_\mu$	–	–	4.5	6.6	6.8	3.4
$\tilde{\chi}_2^0 \to \tilde{\chi}_1^0 \nu_\tau\bar{\nu}_\tau$	–	–	3.6	6.5	6.8	3.4
$\tilde{\chi}_2^0 \to \tilde{\chi}_1^\pm q\bar{q}$	–	66.4	–	–	–	33.6
$\tilde{\chi}_2^0 \to \tilde{\chi}_1^\pm e\bar{\nu}_e/\bar{e}\nu_e$	–	11.1	–	–	–	5.6
$\tilde{\chi}_2^0 \to \tilde{\chi}_1^\pm \mu\bar{\nu}_\mu/\bar{\mu}\nu_\mu$	–	11.1	–	–	–	5.6
$\tilde{\chi}_2^0 \to \tilde{\chi}_1^\pm \tau\bar{\nu}_\tau/\bar{\tau}\nu_\tau$	–	11.1	–	–	–	5.4
$\tilde{\chi}_1^\pm \to \tilde{\chi}_1^0 q\bar{q}$	75	75	67.1	66.8	66.7	66.8
$\tilde{\chi}_1^\pm \to \tilde{\chi}_1^0 e\nu_e$	12.5	12.5	11.0	11.1	11.1	11.1
$\tilde{\chi}_1^\pm \to \tilde{\chi}_1^0 \mu\nu_\mu$	12.5	12.5	11.0	11.1	11.1	11.1
$\tilde{\chi}_1^\pm \to \tilde{\chi}_1^0 \tau\nu_\tau$	–	–	10.9	11.0	11.0	11.0

Table 7.4: Important mass differences for G2, SO10 and FP benchmark points

Masses	G21	G24	SO10A	SO10D	FP1	FP2
Code	MATH	MATH	ISA	ISA	SOFT	SOFT
$m_{\tilde{g}} - m_{\tilde{\chi}_2^0}$	605.1	435.9	267.7	282.6	385.6	551.9
$m_{\tilde{g}} - m_{\tilde{\chi}_1^0}$	878.7	465.9	340.4	335.1	430.4	602.3
$m_{\tilde{g}} - m_{\tilde{\chi}_1^\pm}$	878.5	465.7	267.2	282.0	389.4	572.9
$m_{\tilde{\chi}_2^0} - m_{\tilde{\chi}_1^0}$	273.6	30.0	72.7	52.5	44.8	50.4
$m_{\tilde{\chi}_2^0} - m_{\tilde{\chi}_1^\pm}$	273.4	29.8	-0.5	-0.6	3.8	21.0
$m_{\tilde{\chi}_1^\pm} - m_{\tilde{\chi}_2^0}$	-273.4	-29.8	0.5	0.6	-3.8	-21.0
$m_{\tilde{\chi}_1^\pm} - m_{\tilde{\chi}_1^0}$	0.2	0.2	73.2	53.1	41.0	29.4

Table 7.5: Generated signal samples. The event weights are calculated according to PROSPINO LO cross sections

Benchmark point	Processes	# of events	Total LO σ (pb) (PYTHIA)	Total LO σ (pb) (PRSPN)	Corr $\int \mathcal{L}dt$ (PRSPN) (fb$^-$1)	Weight for 100pb^{-1} (PRSPN) (
G21	$pp \to \tilde{g}\tilde{g}$	3900	0.236	0.25	15.600	0.00641026
G24	$pp \to \tilde{g}\tilde{g}$	18874	8.006	8.62	2.190	0.0456713
SO10A	$pp \to$ all SUSY	46000	78.07	84.25	0.546	0.183152
SO10D	$pp \to$ all SUSY	45800	96.20	102.15	0.448	0.223035
FP1	$pp \to$ all SUSY	40352	35.04	36.53	0.0905284	
FP2	$pp \to$ all SUSY	46096	14.09	14.55	3.168	0.0315646

the Geant 4 based CMS software framework CMSSW, using versions 1_6_11 for the SO10s and G2s and 1_6_12 for the FPs. Reconstruction was done using the calibration and allignment constants based on ideal detector conditions. Pile-up effects were not considered.

Information related to the produced signal samples are summarized in Table 7.5. While all SUSY processes were generated for the SO10s and FPs, only $\tilde{g}\tilde{g}$ processes were generated for the G2s, since the $\tilde{\chi}\tilde{\chi}$ processes are owerwhelmingly dominant, but have insignificant contribution to the final state of interest.

7.3 Backgrounds and background samples

As a prominent hadron collider, LHC will stage rich hadronic processes which will constitute significant backgrounds to our signals. For the jet-MET channel, main backgrounds to be considered are associated production of $W + n$ jets, $Z + n$ jets, $t\bar{t} + n$ jets, QCD, γ + jets and minimum bias processes. Additionally the contribution from muon enriched component of

QCD will be examined seperately [1]. These backgrounds were produced officially in CMS within the framework of Computing, Software and Analysis Challange 2007 (CSA07) using CMSSW 1_6_7. All subprocesses (e.g. different number of jets in associated production or different bins) belonging to each SM process above (plus someothers) were produced as individual datasets, then approppriate amounts of events were taken from each subprocess and merged into three main AllEvents datasets, the so-called "soups" Chowder, Gumbo and Stew. The events in the soups are weighted since it is impossible to generate realistic amounts of events releevant for the LHC luminosities for processes with large cross sections such as low p_T QCD.

The large amount of data to be collected by CMS challanges the computing efficiency during offline analysis. To overcome this, CMS data, after being processed by the L1 and HLT algorithms, is split into primary datasets (PDs) defined through a logical OR of subsets of HLT paths. Here we use the PDJetMET coming from the OR of 19 JetMET triggers (listed in Tables A.1 and A.2. Other selections focus on other objects, resulting in datasets like PDTau, PDMuon, PDElectron and PDPhoton. While analyzing real data, subsets of PDs called skims designed by further applying offline cuts can also be used for a more efficent analysis.

Table 7.6 summarizes the backgrounds relevant for our analysis [2].

7.3.1 Objects and reconstruction

Jet reconstruction in CMS takes place in four steps. Starting with the digitized sample, the offline reconstruction software first converts the ADC counts in each calorimeter cell in ECAL and HCAL to energy. Second, ECAL and HCAL cells are combined into projective towers corresponding to HCAL granularity. Then the CaloTowers are converted into standard offline candidate objects finally over which a selected jet clustering algorithm is run.

`CMSSW_1_6_X` implements iterative cone [109], midpoint cone [110], K_T [111] and seedless infrared safe cone (SIScone) [112] algoritms for jet reconstruction. Both CMS HLT selection and current CMS physics analyses conventionally use the iterative cone (IC) algoritm, which starts by taking an E_T ordered list of objects (CaloTowers or generated particles) over a defined seed threshold and making a cone with size $R = \sqrt{\Delta\eta^2 + \Delta\phi^2}$ around the highest E_T

[1] They will be shown in the histograms but are not added to the number of total background events in order to avoid double counting

[2] No minimum bias events survive the trigger requirements of PDJetMET, hence minimum bias events are not included in the table

Table 7.6: CSA07 background samples used in the analysis

Short name	Processes	Event generator	Dataset (soup)	Total σ (pb)	# of evts in PDJetMET
WnJ	$W + n\ jets$, $n = 1, 5$ $p_T(W) < 300$ GeV	ALPGEN	Chowder PDJetMET	5.82×10^4	1055680
ZnJ	$Z + n\ jets$, $n = 1, 5$ $p_T(Z) < 300$ GeV	ALPGEN	Chowder PDJetMET	5.78×10^3	194337
ttnJ	$tt + n\ jets$, $n = 1, 4$	ALPGEN	Chowder PDJetMET	8.37×10^2	780408
QCD	QCD	PYTHIA	Gumbo PDJetMET	2.28×10^9	5541900
PJ	$\gamma + \ jets$	PYTHIA	Gumbo PDJetMET	1.78×10^8	601307
ppMuX	μ enriched QCD	PYTHIA	Stew PDJetMET	5.50×10^{10}	10272

object to construct a proto-jet with $E_T = \sum_j E_T^j$, $\eta = \frac{1}{E_T} \sum_j \eta_j \times E_T^j$ and $\phi = \frac{1}{E_T} \sum_j \phi_j \times E_T^j$. Then another cone is casted, this time around the proto-jet direction and a second proto-jet is made from the objects inside. The procedure goes on until the energy of the proto-jet changes by $<$ %1 and direction changes by $\Delta R < 0.01$ between two iterations. The objects within the ΔR of the 1st jet thus reconstructed are taken off from the list and the algorithm restarts for making the next jet, and this goes on until no objects above the seed threshold are left.

To justify the usage of IC, we studied the performance of IC in comparison with the SIScone (SC) algorithm. SIScone was proposed to solve the infrared unsafety issue, which is defined as the inambiguity of being able to reconstruct totally different stable cones when an infinitely soft object is added to the collection. In this algorithm, supposing there are a total of N objects regardless of a seed threshold, one takes each of all possible subsets S of N, and defines η_S and ϕ_S from the objects in S. Then a cone with radius R is cast around (η_S, ϕ_S). If the cone contains all objects in S but no other objects, it is called a "stable cone". Procedure goes on until all stable cones are found and no objects are left outside.

We reconstruct the jets with a cone size of $R = 0.5$ using both algorithms where a cone seed E_T cut of 1 GeV was assumed for the IC. We take the resulting jets only if they have an uncorrected $p_T > 30$ GeV and are within $|\eta| < 3$. Electrons faking jets are not vetoed intentionally, since this is an inclusive study that aims to measure the reach through good signal-background seperation rather then making detailed mass and model parameter measurements. An indirect lepton veto will be applied during the event selection.

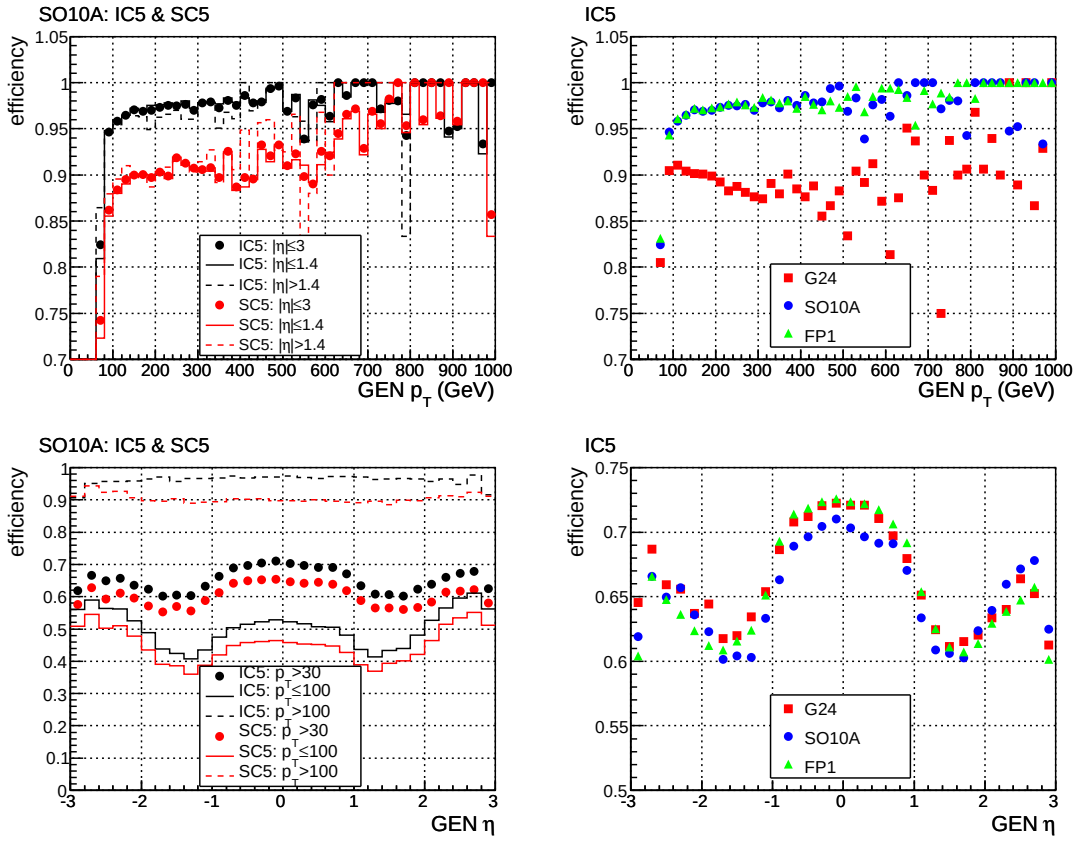

Figure 7.2: Reconstruction efficiency (# of matched GEN jets / total # of GEN jets) distribution in p_T and η for the signals. Comparison between iterative cone $R = 0.5$ and SIScone $R = 0.5$ algorithms are also shown

Figure 7.2 shows the jet reconstruction efficiencies (where efficiency is defined as the number of matched GEN jets / total number of GEN jets). Here matching is done by requiring $\Delta R \leq 0.15$ between the GEN and RECO jets. Top left plot compares efficiency versus p_T^{GEN} for IC5 and SC5 of SO10A. IC5 is seen to have a better performance at low p_T. For both algorithms, efficiencies for jets within HB ($|\eta| < 1.4$) and outside are also shown where no significant differences are observed. Bottom left plot then displays the η^{GEN} dependence of efficiencies, where again IC5 efficiencies are higher. The HB-HE intersecton region with $\eta \sim 1.5$ results in the poorest reconstruction. The cases for $p_T \leq 100$ and $p_T > 100$ jets are also shown seperately, which clearly proves that the low efficiencies in especially the central region are due to the low-p_T component. Right hand side plots display comparisons between G24, SO10A and FP2 versus p_T and η. Efficiency with respect to p_T is lower for the G24 case, which should be due to the existance of multi-top states derived from the %36 $\tilde{g} \rightarrow \tilde{\chi}_2^0 t\bar{t}$

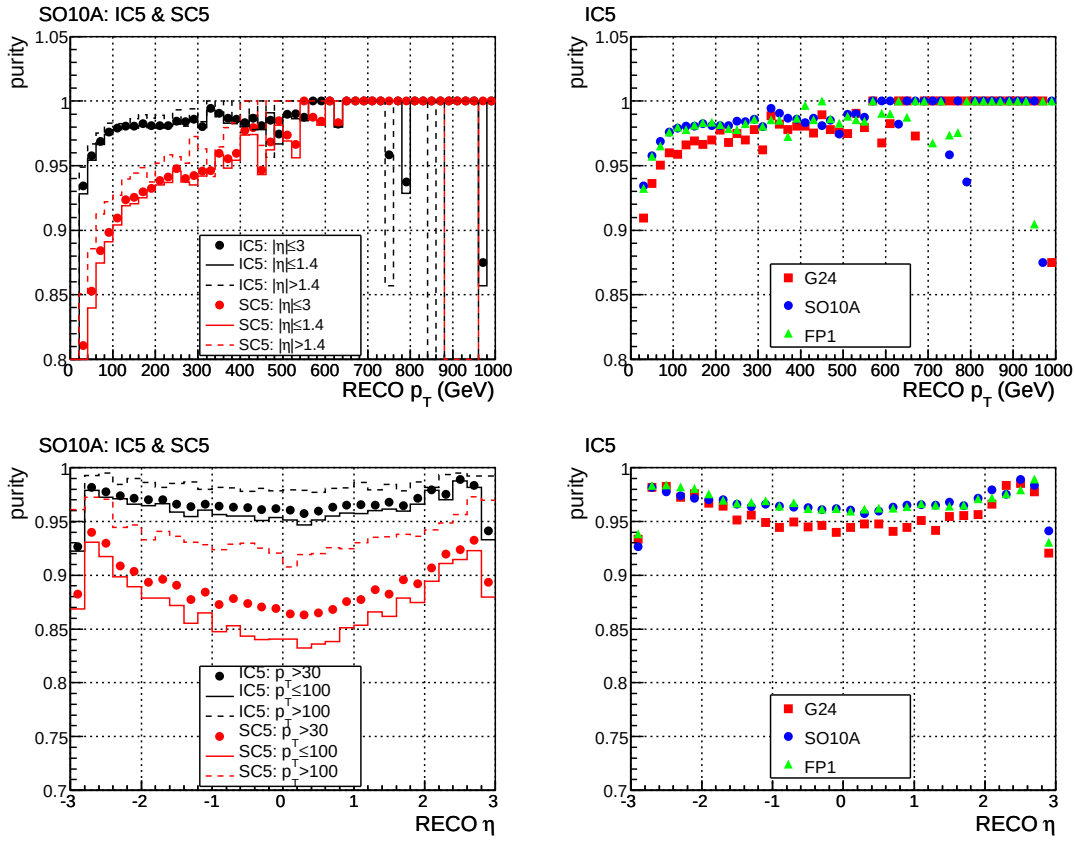

Figure 7.3: Purity (# of matched reconstructed jets / total # of reconstructed jets) distribution in p_T and η for the signals. Comparison between iterative cone $R = 0.5$ and SIScone $R = 0.5$ algorithms are also shown.

that is absent in the other scenarios while the efficiency with respect to η is similar for the three scenarios.

Left hand side plots in Figure 7.3 similarly show comparisons of jet purity (defined as the number of matched reconstructed jets / total number of reconstructed jets) of IC5 and SC5 versus p_T and η, where again IC5 is seen to perform better for low p_T. The purity is lower in the central region, which should be due to the fakes created by high p_T central electrons existing in the signals. Fake rates for central, low p_T jets for SC5 can go up to %15, while for IC5 they generally stay below %5. Right hand side plots then compare G24, SO10A and FP1, where again G24 purity is slightly lower due to dominant top final states.

Next, 1st jet p_Ts and jet multiplicities for SO10A and QCD with IC5 and SC5 can be seen in Figure 7.4. Though a significant difference is not observed in the p_T tails due to the relatively efficient reconstruction at high p_T for both algorithms, the generically poorer

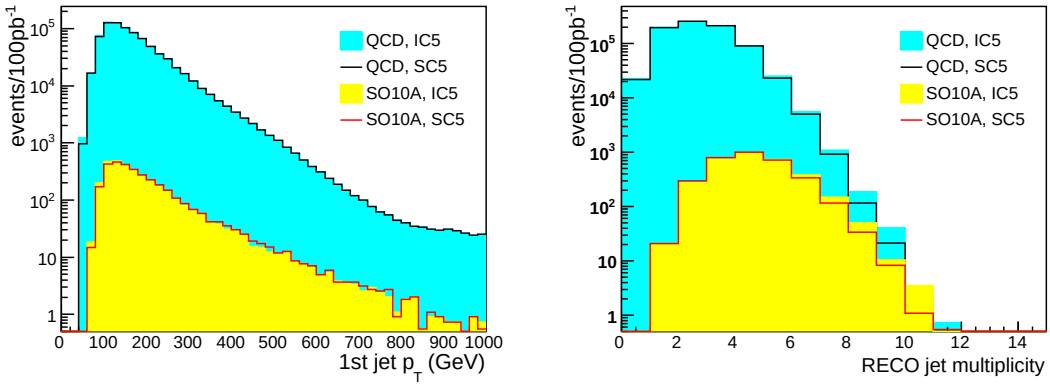

Figure 7.4: 1st jet p_T (left) and jet multiplicity (right) for jets having $p_T > 30$ GeV and $|\eta| < 3$. Comparison of iterative cone $\Delta R = 0.5$ and SIScone $\Delta R = 0.5$ calojets.

behavior of SC5 reconstruction reflects visibly to the multiplicity tails.

We also study the jet resolution for the signals using IC5. Figure 7.5 on the top left shows the detector response given as p_T^{REC}/p_T^{GEN} versus p_T^{GEN} for G24, SO10A and FP1. Here the p_T^{REC}/p_T^{GEN} distributions were taken for each p_T^{GEN} bin and were fitted to a Gaussian, and the resulting mean and width are shown. The errors are of the order of %10 and slightly decrease with increasing p_T. Top right plot then shows the resolution defined as $\sigma(p_T^{REC}/p_T^{GEN})/\left\langle p_T^{REC}/p_T^{GEN}\right\rangle$ among with the results of fits to the resolution function given as $a/p_T^{GEN} \oplus b/\sqrt{(p_T^{GEN}} \oplus c$. The three scenarios are seen to have a similar p_T resolution behavior while variance of η resolution among the scenarios is bigger, as shown on the down left plot. Down right plot shows p_T resolution curves in the $|\eta| \leq 1.4$ and $1.4 < \eta| < 3$ regions.

The missing transverse energy is calculated from the calorimetry towers. It is the negative sum of the energy E_i in each tower with angular position (θ_i, ϕ_i), given as

$$\not\!\!E_T = \sum (E_i \sin\theta_i \cos\phi_i \hat{\mathbf{i}} + E_i \sin\theta_i \sin\phi_i \hat{\mathbf{j}}). \tag{7.1}$$

The ratio $\not\!\!E_T^{REC}/\not\!\!E_T^{GEN}$ can be seen in Figure 7.6, where contribution from muons was also included in the calculation of $\not\!\!E_T^{GEN}$. The errors are again the gaussian widths resulting from a fit in each bin. At low p_T, $\not\!\!E_T$ is overestimated, which should be due to the contribution from the mismeasurements of jets. G21 has the highest overestimation since it has the highest p_T jets coming from its heavy gluinos. The resulting $\not\!\!E_T$ resolution $\sigma(\not\!\!E_T^{REC}/\not\!\!E_T^{GEN})/\left\langle \not\!\!E_T^{REC}/\not\!\!E_T^{GEN}\right\rangle$ is also displayed in the right hand side plot.

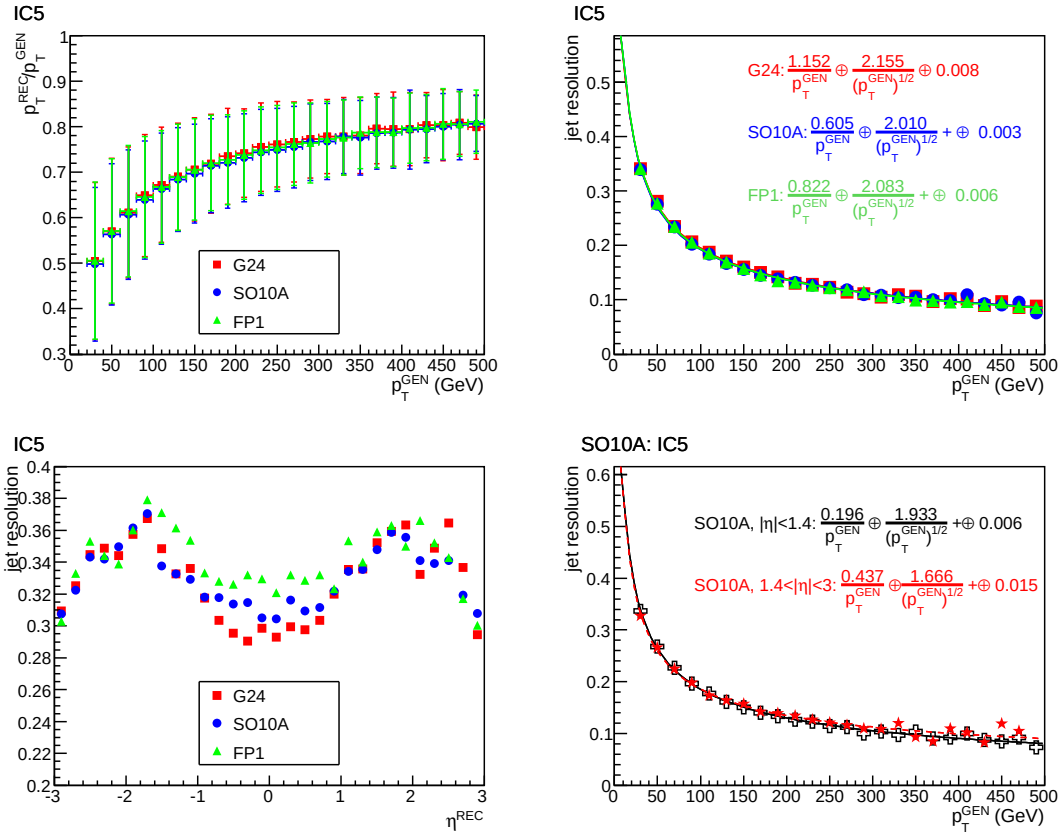

Figure 7.5: IC5 jet p_T^{REC}/p_T^{GEN} distribution versus p_T^{GEN} (top left), IC5 jet resolution versus p_T^{GEN} (top right) and η^{GEN} (bottom left) for the signals G24, SO10A and FP1. Also shown is the comparison of jet resolution curves versus p_T^{GEN} among jets having $|\eta| \leq 1.4$ and $1.4 < |\eta| < 3$ (bottom right).

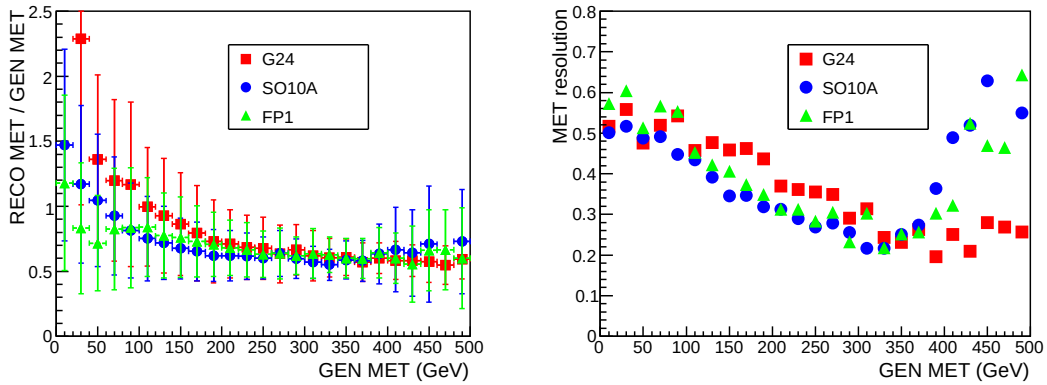

Figure 7.6: $\not{E}_T^{REC}/\not{E}_T^{GEN}$ distribution (left) and $\not{E}_T$ resolution (right) versus $\not{E}_T^{GEN}$ for the signals G24, SO10A and FP1.

7.4 Trigger studies

We adopt the trigger tables defined for CSA07 and implemented in CMSSW_1_6_X, relevant for the conditions for a physics run at 14 TeV and $\mathcal{L} = 10^{32}$ cm^{-2}s^{-1} [113]. Table 7.7 lists the first 10 unprescaled HLT paths that give the highest efficiencies for all signal benchmarks. Information related to these HLT paths is given in Tables A.1 and A.2. As expected, highest signal efficiencies are provided by the paths based on jet and $\not\!\!E_T$ requirements. This strongly justifies our choice of working with the PDJetMET.

L1 jets are defined using the transverse energy sums in 12×12 calorimeter trigger tower windows, which are arrays of 5×5 crystals of dimension $\Delta\eta \times \Delta\phi = 0.087 \times 0.087$ and correspond $1:1$ to the physical tower size of the HCAL. The algorithm uses a sliding window technique, checking the dynamic ranges of 4×4 trigger towers, which make a trigger region. The L1 $\not\!\!E_T$ calculated from the sum of x and y components of the energy deposited in each trigger region, where E_x and E_y components are calculated using the coordinates of the center of the region.

Table 7.7: First 10 unprescaled HLT paths with highest efficiency for each signal point

G21		SO10A		FP1	
HLT path	Eff	HLT path	Eff	HLT path	Eff
HLT3jet	95.59	HLT1MET	56.24	HLT1MET	55.61
HLT1MET1HT	95.41	HLT1MET1HT	55.11	HLT1MET1HT	53.99
HLT1MET	94.97	HLT4jet	52.30	HLT4jet	51.04
HLT3jet1MET	94.67	HLT3jet	48.26	HLT3jet	50.76
HLT4jet1MET	94.10	HLTBHT	47.65	HLT4jet1MET	48.99
HLT1jet	94.39	HLT4jet1MET	45.69	HLT3jet1MET	48.16
HLT4jet	93.23	HLTB4Jet	44.97	HLT1jet	44.61
HLT1jet1MET	92.97	HLT3jet1MET	43.21	HLT1jet1METAco	43.49
HLT2jet1MET	92.23	HLTB3Jet	39.54	HLT1jet1MET	43.13
CandHLT2jetAve200	91.15	HLT1jet	37.20	HLTS2jet1METAco	41.40
G24		SO10D		FP2	
HLT path	Eff	HLT path	Eff	HLT path	Eff
HLT1MET1HT	85.17	HLT1MET	54.47	HLT1MET	25.74
HLT1MET	84.83	HLT1MET1HT	53.19	HLT1MET1HT	21.15
HLT4jet1MET	78.34	HLT4jet	43.80	HLT1jet1MET	17.25
HLT4jet	77.62	HLT4jet1MET	43.00	HLT4jet1MET	17.19
HLT3jet1MET	77.58	HLT3jet	42.45	HLT1jet	17.14
HLT3jet	76.88	HLTBHT	42.34	HLT3jet	17.11
HLT1jet	69.51	HLT3jet1MET	40.70	HLT4jet	17.08
HLT1jet1MET	69.12	HLTB4Jet	38.84	HLT3jet1MET	16.86
HLT1jet1METAco	68.95	HLTS2jet1METNV	36.03	HLT1jet1METAco	15.85
HLTS2jet1METAco	68.01	HLT1jet1METAco	35.52	HLT2jet1MET	15.08

The HLT jets are reconstructed using the iterative cone algorithm with $R = 0.5$, for $|\eta| < 5$, exactly as in the offline case. HLT uses the CaloTowers constructed from one or more projected HCAL cells and corresponding projected ECAL crystals as input, where each tower should have $p_T > 0.5$ GeV and at least one tower must satisfy the jet seed requirement of $p_T > 1$ GeV. Next, jet corrections determined by a PYTHIA QCD dijet analysis are applied. $\not{E}_T$ is calculated from calotowers with $p_T > 0.5$ GeV, same as in the offline case. HLT total hadronic transverse energy (H_T) is calculated using HLT $\not{E}_T$.

With the aim to decide on a common trigger selection for the three SUSY scenarios, we list in Table 7.8 the signal and background efficiencies for individual HLT paths in PDJetMET calculated with respect to the initial number of events in PDJetMET. The paths `HLT1MET` and `HLT1MET1HT` (which we will refer to as the $\not{E}_T$&H_T set) provide the highest signal efficiency for all benchmarks. The $\not{E}_T$&H_T set is a common choice for SUSY analyses and can be safely applied in our analysis. However one can always search for other possibilities. In Table 7.9 we list the number of events remaining after HLT selection for signals and total background along with significances (defined as $S/\sqrt{S+B}$) for each signal benchmark. The HLT paths giving the highest signal significance for all benchmarks are `CandHLTSjet1MET1Aco`, `CandHLTSjet2MET1Aco` and `CandHLTS2jetAco`, which we will refer to as the "acoplanarity trio". These triggers, despite their low $\not{E}_T$ (> 70 GeV) and jet p_T (>40 to 60 GeV) thresholds perform well due to jet-jet and jet-$\not{E}_T$ acoplanarity requirements that eliminate huge amounts of QCD background.

Both $\not{E}_T$&H_T set and acoplanarity trio lead to similar results after the offline selection is applied, so they can both be used, though there exist slight differences which could lead one to favor a choice over the other in order to serve specific analysis purposes. One point is that, although some $\not{E}_T$&H_T triggers exist in the latest core start-up trigger menus, they are not the exact counterparts of the 1_6_X $\not{E}_T$&H_T set. The closest path to `HLT1MET` is `HLT_MET65`, which has a higher $\not{E}_T$ L1 seed `L1_ETM50` while the closest path to `HLT1MET1HT` is `HLT_MET35_HT350` which has a lower HLT $\not{E}_T$ threshold of 35 GeV. Though not much difference is expected after the offline, effects of these changes should be checked. Exact counterparts of the acoplanarity triggers are in the candidate trigger menus for 8E29 and 3E30 although not in the core start-up menus. High signal significance is a good feature of the $\not{E}_T$&H_T set, but this choice also leads to a higher background efficiency with respect to the acoplanarity trio after offline cuts. Therefore acoplanarity trio selection leads to slightly better signal to background ratios and signal significances in low cross section scenarios (such

as the G2s and FP2), especially when an offline selection featuring no $\not\!\!E_T$ or moderate $\not\!\!E_T$ is to be implemented. The $\not\!\!E_T\&H_T$ triggers yield slightly higher S/B and significance in the high cross section paths (such as the SO10s). On the other hand, the acoplanarity trio performs slightly better during background estimation from data. As will be explained in Section 7.8, top backgrounds cause a small amount of background underestimation. More top background survives when $\not\!\!E_T\&H_T$ set is applied, so underestimation is slightly more for this set.

Here we will implement the acoplanarity trio which provides a complementary alternative to the conventional $\not\!\!E_T\&H_T$ set for difficult cases. We require that all events satisfy the AND of the three acoplanarity paths. Figure 7.7 shows the effect of applying this HLT requirement to the SO10A dataset. Efficiency curves for the 1st and the 2nd hardest jets, $\not\!\!E_T$, $d\phi(j_1 - j_2)$ and $d\phi(j_1 - \not\!\!E_T)$ are shown, where the efficiencies are calculated with respect to the un-biassed SO10A dataset (which has no PDJetMET requirement).

Table 7.8: PDJetMET HLT path selection efficiencies for all signals and backgrounds

HLT path	G21	G24	SO10A	SO10D	FP1	FP2	WnJ	ZnJ	ttnJ	QCD	PJ	ppmuX
HLT1jet	94.385	69.510	45.974	47.718	63.693	58.510	9.756	7.741	23.938	6.564	1.241	14.447
HLT2jet	90.615	57.384	37.024	37.462	53.799	47.960	6.099	6.199	20.377	7.882	5.228	13.717
HLT3jet	95.590	77.905	59.711	57.311	72.487	58.399	4.590	7.762	41.316	6.480	0.552	15.216
HLT4jet	93.231	78.689	64.800	59.139	72.838	58.288	2.584	5.515	49.603	3.793	0.219	10.202
HLT1MET	94.974	85.963	69.516	73.550	79.408	87.843	67.581	25.305	42.415	3.949	5.512	18.682
HLT2jetAco	87.462	53.186	30.337	30.498	47.820	44.658	1.457	1.843	11.288	1.109	0.104	3.329
HLT1jet1METAco	90.333	69.870	46.030	47.966	62.114	54.076	5.608	3.334	15.199	1.302	0.374	6.318
HLT1Jet1MET	92.974	70.041	43.652	46.459	61.575	58.873	9.508	5.357	14.245	1.380	0.491	6.844
HLT2Jet1MET	92.231	65.521	38.685	40.566	57.095	51.477	3.667	2.357	11.238	0.844	0.259	4.030
HLT3Jet1MET	94.667	78.609	53.376	54.956	68.774	57.533	3.387	2.577	17.566	0.787	0.172	4.858
HLT4Jet1MET	94.103	79.366	56.434	58.054	69.959	58.681	3.214	2.518	18.954	0.736	0.138	4.683
HLT1MET1HT	95.410	86.306	68.188	71.825	77.101	72.192	16.617	8.120	34.378	2.006	0.584	12.412
HLT2jetvbfMET	0.103	0.306	0.578	0.672	0.478	0.785	1.107	0.435	0.590	0.756	0.063	2.765
HLTS2jet1METNV	76.385	65.752	44.843	48.653	54.552	51.477	11.181	5.142	18.502	0.959	0.215	6.036
HLTS2jet1METAco	86.154	68.903	44.418	47.096	59.119	51.136	5.293	2.645	13.874	0.551	0.133	2.901
CandHLTSjet1MET1Aco	70.333	56.407	36.428	39.328	48.142	43.259	6.489	2.763	11.753	0.207	0.050	2.015
CandHLTSjet2MET1Aco	85.385	68.340	42.664	45.914	57.330	50.729	5.086	2.353	12.787	0.296	0.079	1.967
CandHLTS2jetAco	72.538	59.321	37.975	41.571	50.058	44.740	5.117	2.422	12.082	0.296	0.069	2.366
CandHLTJetMET-RapidityGap	2.923	2.442	2.638	2.538	2.658	4.487	25.280	62.793	5.875	80.537	88.597	51.762

Table 7.9: Number of signal and total background events passing PDJetMET HLT paths along with HLT selection significances.

HLT path	G21		G24		SO10A		SO10D		FP1		FP2		Tot bg
	evts	sig	evts	sig	evts	sig	evts	sig	evts	sig	evts	sig	
PDJetMET	25	0.002	807	0.059	6817	0.496	7564	0.550	2150	0.156	426	0.031	189127600
HLT1jet	24	0.007	561	0.158	3134	0.885	3609	1.019	1325	0.374	249	0.070	12533255
HLT2jet	23	0.006	463	0.120	2524	0.651	2834	0.731	1119	0.289	204	0.053	15008048
HLT3jet	24	0.007	629	0.179	4070	1.156	4335	1.232	1508	0.429	249	0.071	12382870
HLT4jet	23	0.009	635	0.235	4417	1.636	4473	1.656	1515	0.561	249	0.092	7287052
HLT1MET	24	0.009	694	0.247	4739	1.683	5563	1.976	1652	0.587	375	0.133	7921213
HLT2jetAco	22	0.015	429	0.293	2068	1.413	2307	1.576	995	0.680	190	0.130	2140872
HLT1jet1METAco	23	0.014	564	0.351	3138	1.953	3628	2.257	1292	0.804	231	0.144	2579793
HLT1Jet1MET	23	0.014	565	0.341	2976	1.796	3514	2.121	1281	0.773	251	0.152	2742186
HLT2Jet1MET	23	0.018	529	0.409	2637	2.037	3068	2.370	1188	0.918	219	0.169	1673270
HLT3Jet1MET	24	0.019	634	0.503	3638	2.883	4157	3.294	1431	1.135	245	0.194	1588157
HLT4Jet1MET	24	0.020	641	0.525	3847	3.148	4391	3.592	1455	1.191	250	0.205	1489794
HLT1MET1HT	24	0.012	697	0.347	4648	2.310	5433	2.699	1604	0.797	308	0.153	4045483
HLT2jetvbfMET	0	0.000	2	0.002	39	0.032	51	0.042	10	0.008	3	0.002	1466445
HLTS2jet1METNV	19	0.014	531	0.381	3057	2.191	3680	2.638	1135	0.814	219	0.157	1943025
HLTS2jet1METAco	22	0.021	556	0.528	3028	2.874	3562	3.380	1230	1.168	218	0.207	1107025
CandHLTSjet1MET1Aco	18	0.027	455	0.681	2483	3.706	2975	4.438	1001	1.497	184	0.275	446330
CandHLTSjet2MET1Aco	21	0.027	552	0.706	2908	3.710	3473	4.428	1193	1.524	216	0.276	611565
CandHLTS2jetAco	18	0.023	479	0.608	2589	3.283	3144	3.985	1041	1.322	191	0.243	619307
CandHLTJetMET-RapidityGap	1	0.000	20	0.002	180	0.015	192	0.016	55	0.004	19	0.002	151686346

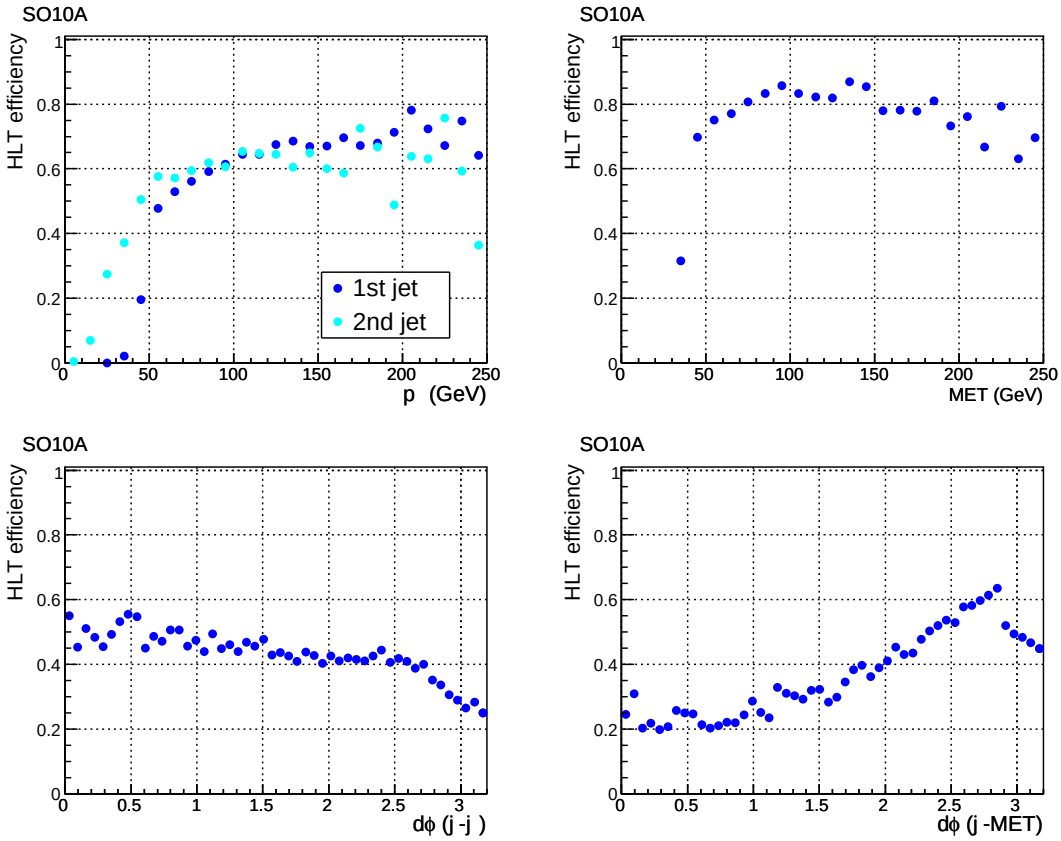

Figure 7.7: HLT efficiency curves for SO10A for $p_T(j_1)$ and $p_T(j_2)$ (top left), $\not{E}_T$ (top right), $d\phi(j_1 - j_2)$ (bottom left) and $d\phi(j_1 - \not{E}_T)$ (bottom right) after applying the acoplanarity trio requirement.

7.5 Offline event selection

Since gluino pair production followed by three-body decays into diverse channels lead to rich high multiplicity final states with diverse objects, an early data analysis looking for a specific end topology would not be feasable. Therefore we aim at an inclusive jet-MET analysis, which however has the disadvantage that various aspects of the different signal topologies will suffer from being easily imitated by different SM processes. In what follows we present a step-by-step event selection procedure, proposing a generic set of cuts specialized to eliminate different backgrounds, which should be applicable for all the selected benchmarks. Instead of considering a single selection path, we will take a multi-path approach and work with several jet-MET selection paths in order to have alternatives to confirm a signal excess. Analysis assumes 100 pb^{-1} of data.

7.5.1 Defining the paths

Since R-parity conserving SUSY events are all destined to have two $\tilde{\chi}_1^0$s in their final states, $\not{E}_T$ is a key signature for them. It must be noted however that SO10 and FP scenarios have low $m_{\tilde{\chi}_1^0} \sim 50 - 80$ GeV, hence they have moderate $\not{E}_T$ with respect to typical mSUGRA LHC scenarios featuring $m_{\tilde{\chi}_1^0} > 100$ GeV. Top row plots in Figure 7.8 show the $\not{E}_T$ and jet multiplicity distrbutions after the HLT selection, where G24, SO10A and FP1 are taken as example signals. $X + n$ jets $\not{E}_T$ shapes resemble the signals closely while QCD and γ+jets peak at lower values. Though all backgrounds in the jet multipliciy distribution peak at lower multiplicities then the signals, the background distributions have a broader range. To decide on optimal starting points for the cuts, we also plot on the 2nd and 3rd rows the S/B ratio and the Punzi significance S_P, which is defined as

$$S_P = \frac{\epsilon(t)}{a/2 + \sqrt{(B(t))}} \tag{7.2}$$

where t is the set of cuts, $\epsilon(t)$ is the signal efficiency after cuts, $B(t)$ is the number of background events remaining after cuts and a is the number of sigmas (we take 3). These were calculated assuming that a $\not{E}_T$ or jet multiplicity cut was put at the values seen on the x-axis.

Both S/B and Punzi significance distributions show that a cut on $\not{E}_T$ will be more effective as a starting point compared to jet multiplicity. Thus to characterize the different paths we first use a $\not{E}_T$ requirement and select events with $\not{E}_T > 0, 100, 150, 200$ or 300 GeV. Having selections with different $\not{E}_T$ choices also enables the inspection of $\not{E}_T$ bias effects on different

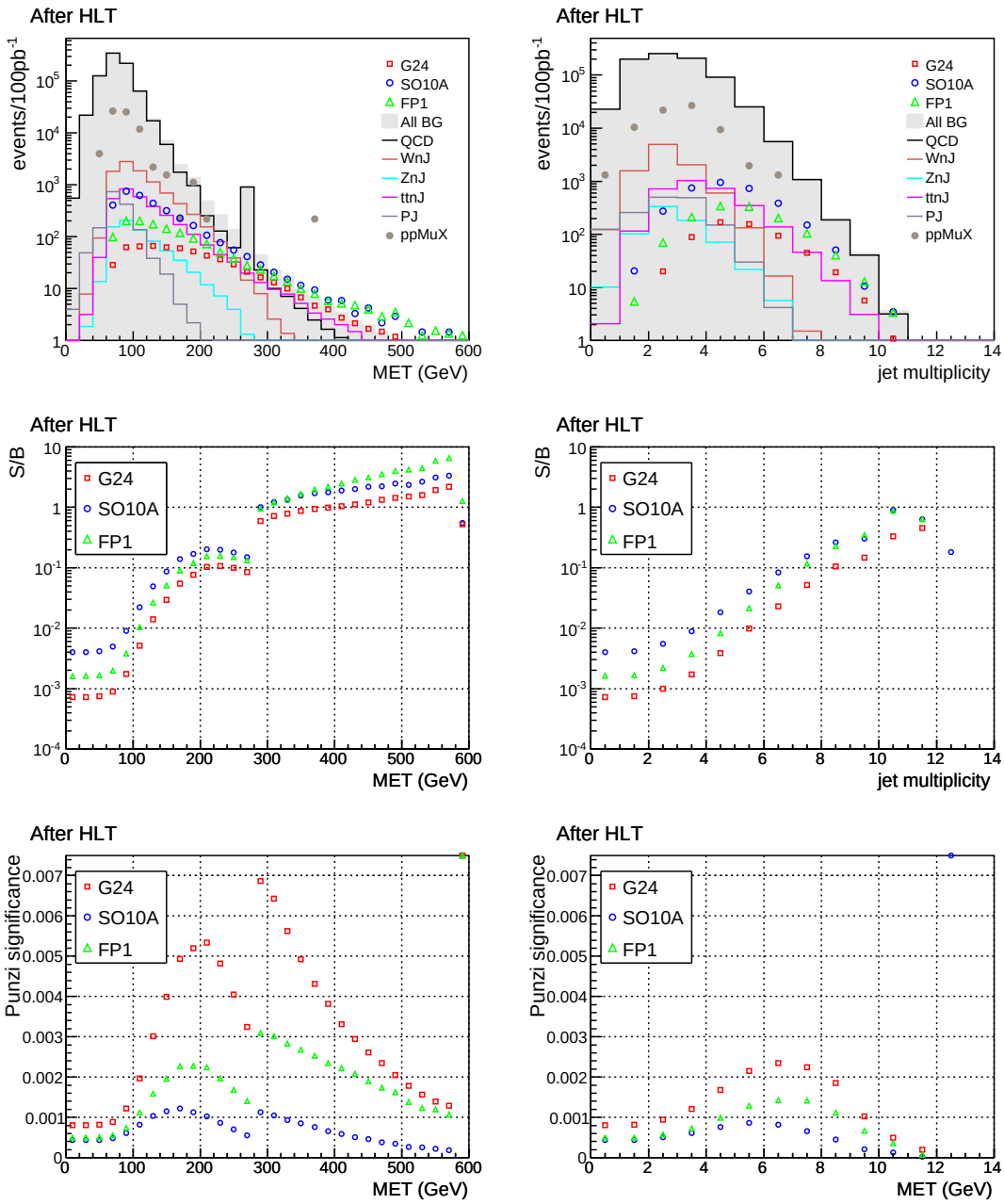

Figure 7.8: $\not\!\!E_T$ (left) and jet multiplicity (right) distributions after HLT selection (1st row) for signals and backgrounds. Also shown are the S/B ratio (2nd row) and Punzi significance (3rd row) calculated assuming that a cut was put at the value seen on the x-axis.

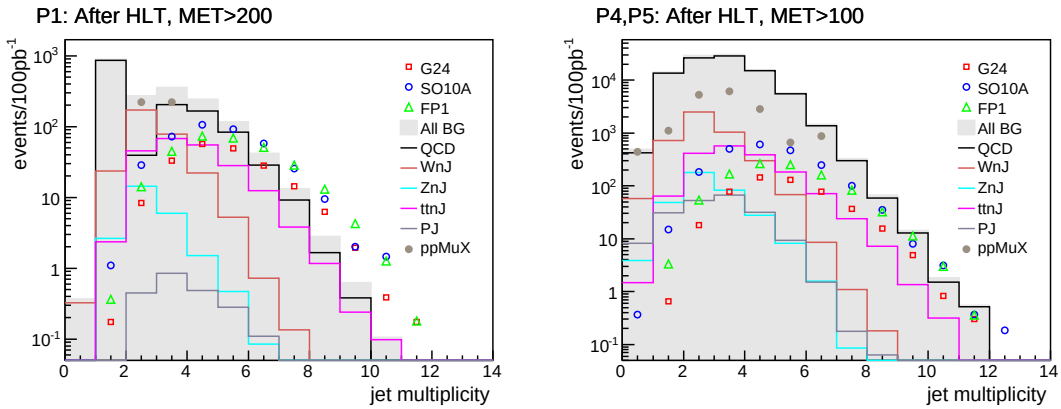

Figure 7.9: Jet multiplicity distributions after the $\not\!\!E_T$ cut (step 1). Shown for path 1: $\not\!\!E_T > 200$ (left) and paths 4 and 5: $\not\!\!E_T > 100$ (right).

kinematic variables. A non-$\not\!\!E_T$ case is also considered in order to probe the discovery possibility in a channel which is free of $\not\!\!E_T$ measurement disambiguities, where one would need to seek more creative ways to eliminate the large QCD backgrounds.

Figure 7.9 then shows the signal and background jet multiplicity distributions after requiring $\not\!\!E_T > 200$ GeV (left) and $\not\!\!E_T > 100$ GeV (right). Higher $\not\!\!E_T$ requirements are seen to eliminate the backgrounds with higher jet multiplicites (especially QCD), pushing the BG peaks to the left. We develop the paths further by adding a requirement of $n_{jets} \geq 4$ to $\not\!\!E_T > 100, 200$ and 300 cases, $n_{jets} \geq 5$ to $\not\!\!E_T > 0$ and 100 cases, and $n_{jets} \geq 3$ to $\not\!\!E_T > 150$ case.

Conventional SUSY jet-MET analyses implement high p_T cuts on the 1st and 2nd jets (where the jets are p_T ordered). To test the feasibiliy of such a requirement for our case, we plot in Figure 7.10 the 1st (left) and 2nd (right) jet p_Ts after applying the $\not\!\!E_T > 100$ and $n_{jets} \geq 5$ cuts. Signal jet p_Ts are seen to have low values, mimicking the backgrounds. This is expected since gluinos make 3-body decays contrary to conventional scenarios with $m_{\tilde{q}} < m_{\tilde{g}}$ and $\tilde{g} - \tilde{\chi}$ mass differences are small for SO10As and FPs. Such behavior is similar for the other paths, and also endures after the full event selection is applied. Therefore jet p_T cuts are not applied in this analysis.

$\not\!\!E_T$ in QCD dijet events is mainly due to jet mismeasurements. Hard QCD processes may result in high amounts of $\not\!\!E_T$ that cannot be eliminated by the $\not\!\!E_T$ requirements. Since the 1st and 2nd jet distributions display a harder spectrum for QCD, the QCD events are expected to posses larger amounts of fake $\not\!\!E_T$ than the signals. To spot such QCD events,

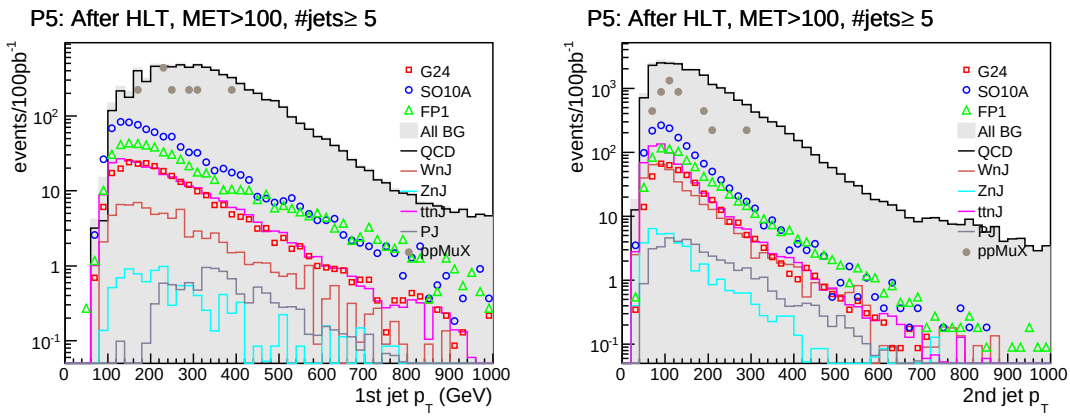

Figure 7.10: 1st (left) and 2nd (right) jet p_T distributions after the jet multiplicity cut (step 2). Shown for path 5: $\not\!\!E_T > 100$, $n_{jets} \geq 5$.

Table 7.10: Offline prototype selection paths characterized by $\not\!\!E_T$, jet multiplicity and $\not\!\!E_T/H_T$ requirements proposed as alternatives to be used during signal excess searches

Step	var	P1	P2	P3	P4	P5	P6
S1	$\not\!\!E_T$	> 200	> 300	–	> 100	> 100	> 150
S2	n_{jets}	≥ 4	≥ 4	≥ 5	≥ 4	≥ 5	≥ 3
S3	$\not\!\!E_T/H_T$	–	–	> 0.1	> 0.1	> 0.1	–

we check the $\not\!\!E_T/H_T$ ratio, where hadronic transverse energy H_T is the scalar sum of all jet p_Ts. The largeness of H_T in QCD - which creates the large amount of QCD $\not\!\!E_T$ - pushes the ratio to low values for QCD, while the $\tilde{\chi}_1^0$ contribution to $\not\!\!E_T$ in signals pulls this ratio up even when the signal jets are also hard. Figure 7.11 shows the $\not\!\!E_T/H_T$ distributions for signals and backgrounds after $\not\!\!E_T > 0$ and $n_{jets} \geq 5$ (left) and $\not\!\!E_T > 100$ and $n_{jets} \geq 5$ (right), where a large QCD accumulation is seen at $\not\!\!E_T/H_T < 0.1$. This effect disappears for $\not\!\!E_T > 150$. As a result we add the $\not\!\!E_T/H_T > 0.1$ requirement to the paths having $\not\!\!E_T > 150$ GeV, thus introducing an implicit $\not\!\!E_T$ cut to the no-$\not\!\!E_T$ path. This $\not\!\!E_T/H_T$ cut can be considered as a tool to indirectly eliminate high-$\not\!\!E_T$ QCD events in a way that does not drasticlly effect the signals.

These three steps complete the definition of the six alternative prototype selection paths, which are summarized in Table 7.10. Selection criteria considered afterwards will be applied to all of these six paths.

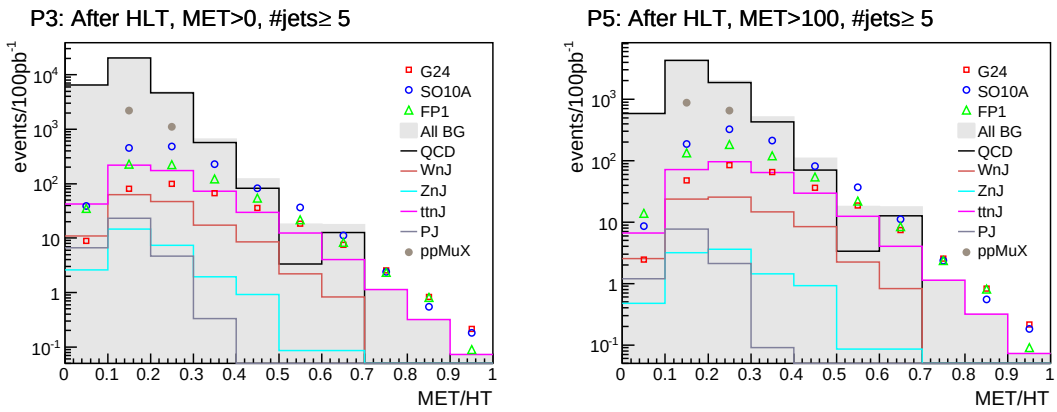

Figure 7.11: $\not{E}_T$/HT distributions after the jet multiplicity cut (step 2). Shown for path 3: $\not{E}_T > 0$, $n_{jets} \geq 5$ (left) and path 5: $\not{E}_T > 100$, $n_{jets} \geq 5$ (right).

7.5.2 Cleaning the lepton-rich backgrounds

$pp \rightarrow W, Z, \bar{t}t$ processes associated with multiple jets constitute significant backgrounds. Ws and Zs decay to hadronic channels with BRs of %67 and %69, but these final states are mostly eliminated by the $\not{E}_T$ requirements. The $Z + n$ jets backgrounds are already dropped to 10-30 evts/100 pb^{-1} after HLT plus the prototype paths. However $W/\bar{t}t + n$ jets events for which Ws decay to $l\nu$ survive, mainly due to $\not{E}_T$ produced by νs from the W and τ decays. Such leptonic W decay events should have a lepton as their hardest object.

This analysis does not make use of lepton objects, so an explicit identification of such background events is not possible. However there exists a method called ”indirect lepton veto” (ILV), practiced in Tevatron SUSY searches, which makes use of combined tracker and calorimeter information to spot and eliminate these events having leptons as their hardest object [114],[115]. The ILV algorithm is implemented in two steps, where one introduces respective checks on the leading track isolation and jet and event electromagnetic fraction.

7.5.2.1 Leading track isolation

Leptons as elementary particles leave single tracks as they pass through the tracker. If the hardest object in an event is a lepton, it must be responsible for a single hard track. The strategy here is to examine the hardest track, and if it is isolated, conclude that it belongs to a hardest lepton, and subsequently veto the event.

We work with events having at least one primary vertex (PV). The tracks associated with

the first PV (which is the PV with the highest $\sum p_T$ of associated tracks) are considered as good tracks if they satisfy the following conditions

- $p_T^{trk} > 1.2$ GeV and $p_T^{trk} < 500$ GeV (the high p_T tracks tend to be straight and hence have a high Δp/p. Therefore they are rejected.)
- $\chi^2/d.o.f < 20$
- Number of valid hits ≥ 5
- $|\eta|_{trk} < 2.4$
- transverse impact parameter $|d_{xy}| \leq 600\ \mu m$
- $|z^{pv} - z^{trk}| < 1$ mm

We select the hardest track from the relevant tracks, and if it has $p_T > 15$ GeV, we construct a cone with radius $R = 0.35$ around it. The p_Ts of tracks falling into the cone are then summed up, and the track isolation parameter which is defined as

$$P_{trkIso} = \frac{\sum_{i \leq LeadTrk}^{n_{trks}} p_T^{trk_i}}{p_T^{LeadTrk}} \tag{7.3}$$

is calculated. The leading track p_T threshold and the cone radius were optimized in earlier studies to provide the best S/B ratios for generic SUSY analyses [116]. Figure 7.12 shows the P_{trkIso} variable for path 6 after the $\not{E}_T/H_T$ cut. While QCD distribution is approximately constant with a slight downward slope towards high P_{trkIso}, half of the $W/t\bar{t}$+ n jets and almost all $Z + n$ jets events sharply peak at $P_{trkIso} < 0.1$, strongly indicating the distinction between the presence and absence of isolated leptons as hardest objects. Signals also peak significantly, but since the signal leptons are produced at the lower parts of gluino cascade decays, they have less chance to be harder than jets and be the hardest object. This results in a relatively small loss in signals of about %10-15. We therefore consider the leading track as isolated if it has $P_{trkIso} < 0.1$ and reject such events with isolated leading tracks.

7.5.2.2 Jet and event electromagnetic fraction

A further measure against the $W/t\bar{t} + n$ jets backgrounds can be taken by considering the electromagnetic fraction (EMF) of jets, which is defined as the ratio of jet energy deposited in ECAL to the total jet energy. Energetic electrons or photons faking jets would have high EMFs close to 1. We can observe this in Figure 7.13 which shows the leading versus second

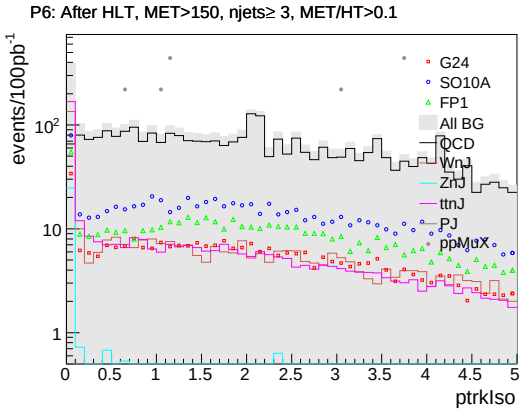

Figure 7.12: P_{trkIso} distributions after the $\not\!\!E_T/H_T$ cut (step 3). Shown for path 6.

leading jet EMFs for SO10A, QCD, $W+n$ jets and $t\bar{t}+n$ jets for path 5 after the isolated track rejection cut, where especially $t\bar{t}+n$ jets has distinct jet accumulations at EMF>0.9. Though it is less pronounced, a similar effect is observed for the signals.

The better motivated reason to use a jet EMF cut is to identify and veto cosmic muon events where cosmic muons leave energy deposits either in the HCAL or ECAL, hence leading to jet EMFs closer to 0 or 1 respectively. Jet EMF also is essential in cleaning up the beam halo events that involve highly energetic particles associated with beam losses around the beam core or produced in collisions of the beam with gas molecules within the beam pipe which is a slightly imperfect vacuum. Such particles, mainly protons and muons, overlap with the normal collision events and produce a large $\not\!\!E_T$, hence constituting backgrounds to the multijet $+\not\!\!E_T$ signals. An earlier study has shown that beam halo particle energies are mainly deposited in HCAL, leading to very low jet EMFs [117]. It also demonstrated the benefit of using the event EMF, which is the p_T-weighted average of jet EMFs given as

$$\text{EEMF} = \frac{\sum_{i=1}^{n_{jet}} p_T^{j_i} \text{EMF}^{j_i}}{\sum_{i=1}^{n_{jet}} p_T^{j_i}} \tag{7.4}$$

and concluded that most beam halo events have EEMF < 0.2. Figure 7.14 shows the EEMF distribution after the jet EMF cut for path 6 where signals and backgrounds are seen to follow a similar trend.

As a result, in the second step of ILV we require that $j_1\text{EMF} > 0.1 \wedge j_2\text{EMF} > 0.1 \wedge (j_1\text{EMF} < 0.9 \vee j_2\text{EMF} < 0.9)$ along with an EEMF less than 0.175.

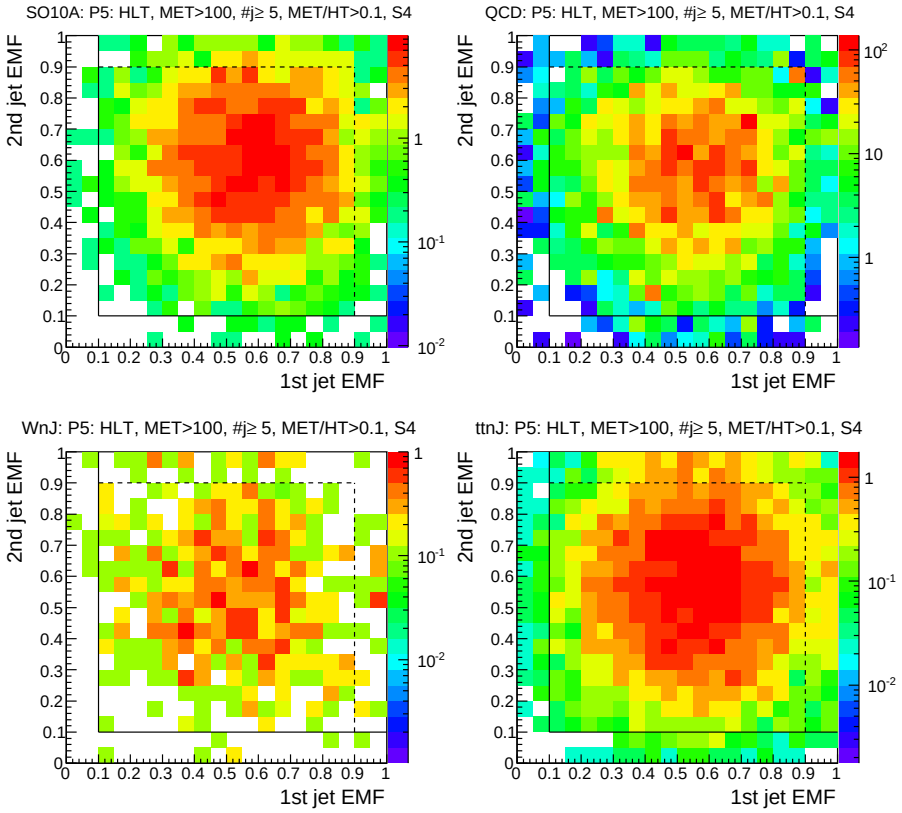

Figure 7.13: 2nd jet EMF vs 1st jet EMF after the leading track isolation cut (step 4). Shown for path 5 for SO10A (top left), QCD (top right), $W+n$ jets (bottom left) and $t\bar{t}+n$ jets (bottom right). Solid lines show the strict cuts while dashed lines show the cuts with an OR.

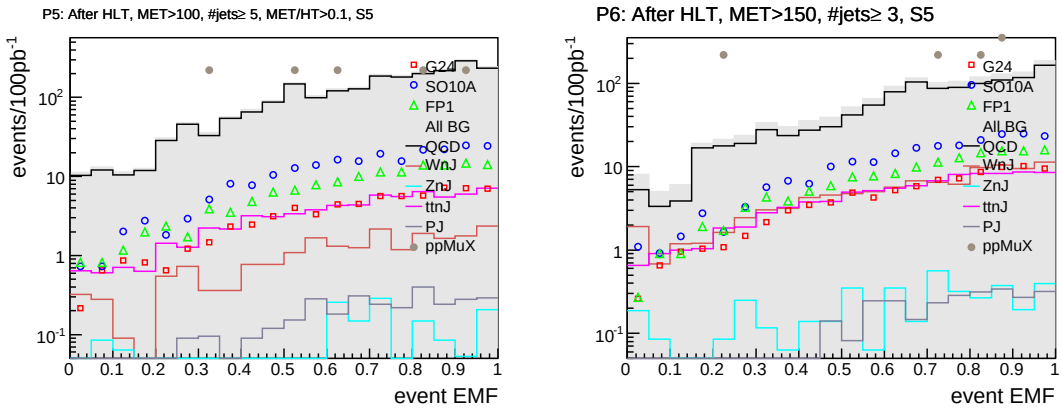

Figure 7.14: Event EMF after the jet EMF cuts (step 5). Shown for path 5 (left) and path 6 (right).

7.5.3 Cleaning the QCD background

Being a prominent pp machine, LHC will host a large amount of QCD events that consist of hard scattering processes among the partons of colliding protons, such like $qq \to qq$, $q\bar{q} \to q\bar{q}, gg$, $qg \to qg$ and $gg \to q\bar{q}, gg$. These events which have 2 jets in their purest form are enriched by other jets from initial and final state QCD radiation, thus becoming multi-jet events. On the other hand, existence of $gg \to c\bar{c}, b\bar{b}$ processes along with jet mismeasurements and detector resolution constitute sources of missing energy, establishing QCD as a major background in the SUSY jet-MET searches. In what follows we will present methods to eliminate these QCD processes.

7.5.3.1 Missing hadronic transverse energy

We first try to make use of the missing hadronic transverse energy $\not{H}_T$ to distinguish the events that have fake $\not{E}_T$ from jet mismeasurements. It is defined as the negative vectorial sum of the jet p_Ts:

$$\not{H}_T = -\sum_{i=1}^{n_{jet}} \vec{p}_T^{\,j_i}, \tag{7.5}$$

where we still use the jets with $p_T > 30$ GeV and $|\eta| < 3$. The difference between $\not{E}_T$ and $\not{H}_T$ comes from four sources. First, the leptons and photons are not included in the $\not{H}_T$ calculation. Second, the low-p_T high $|\eta|$ jets are also not present in $\not{H}_T$. Third, contributions from jet misreconstruction and mismeasurements to $\not{E}_T$ and $\not{H}_T$ are different, and fourth, $\not{E}_T$ is more effected by the detector noise and pile-up with respect to $\not{H}_T$.

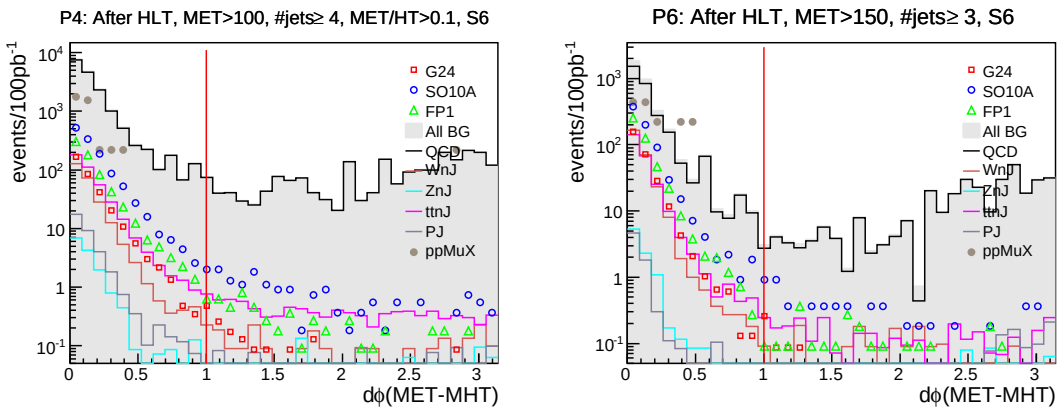

Figure 7.15: $d\phi(\not{E}_T - \not{H}_T)$ after the event EMF cut (step 6). Shown for path 4 (left) and path 6 (right).

Here we investigate the distribution of $d\phi$ between $\not{E}_T$ and $\not{H}_T$ which is shown in Figure 7.15 for paths 4 and 6 after the event EMF cut. In the cases where we have true missing energy such as in signals or $W/Z/t\bar{t} + n$ jets events with ν final states, the above differences serve only as different augmentations to the true missing energy. Here, the fake missing energy is a relatively small percentage of the total missing energy, therefore $\not{E}_T$ and $\not{H}_T$ are relatively close. On the other hand, for the cases with only fake missing energy the above contirbutions will reflect in considerably different ways to the $\not{E}_T$ and $\not{H}_T$ calculations. Especially when the fake missing energy is small, slight fluctuations in jet mismeasurements and detector effects could easily cause $\not{E}_T$ and $\not{H}_T$ to face at opposite directions. Therefore events where $\not{E}_T$ and $\not{H}_T$ have a large $d\phi$ can be interprated as sources of purely fake missing energy whose quantification is totally dependent on sensitivty due to detector effects and mismeasurements. QCD is a prime example for this case, as seen in Figure 7.15. As a result, we introduce the cut $d\phi(\not{E}_T - \not{H}_T) < 1$, which eliminates a good fraction of QCD but has an insignificant effect on the signals.

7.5.3.2 $d\phi(jet - \not{E}_T)$ cuts

The fact that QCD $\not{E}_T$ primarily comes from the jet mismeasurements can be used further to discriminate the QCD events. In such processes, the two jets originating from hard scattering are close in p_Ts and are back-to-back. These jets can be mismeasured, either resulting in an increase or a decrease of the jet p_T. The resulting enhancement in the difference of p_Ts of these two jets would reveal itself as the $\not{E}_T$, which then will naturally allign with the jet that

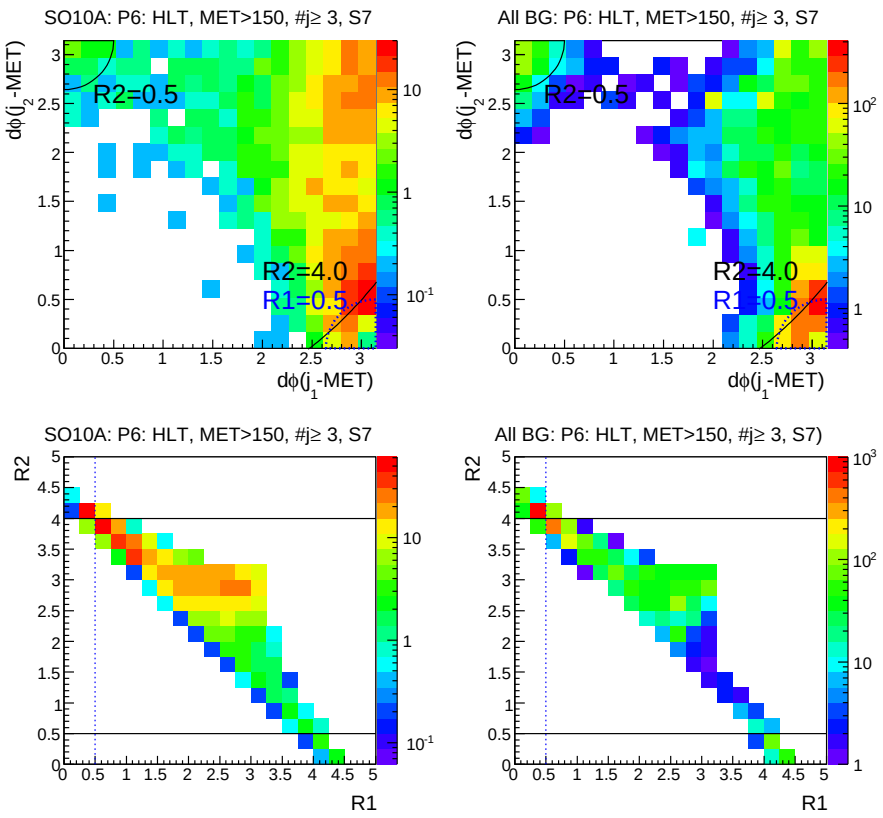

Figure 7.16: $d\phi(j_2 - \not{E}_T)$ vs $d\phi(j_1 - \not{E}_T)$ (top) and R2 vs R1 (bottom) after the $d\phi(\not{E}_T - \not{H}_T)$ cut (step 7). Shown for path 6 for SO10A (left) and total BG (right).

has now become the 2nd jet. Moreover, since 1st and 2nd jets are back-to-back, the $\not{E}_T$ is also expected to be back-to-back with the 1st jet. The upper two plots in Figure 7.16 show $d\phi(j_1 - \not{E}_T)$ vs. $d\phi(j_2 - \not{E}_T)$ after the $d\phi(\not{E}_T - \not{H}_T)$ cut of path 6 for SO10A (left) and total BG (right) events. The majority of the BG events are accumulated at the intersection of high $d\phi(j_1 - \not{E}_T)$ and low $d\phi(j_2 - \not{E}_T)$. A more moderate, but still significant fraction of events are seen at the opposite corner with low $d\phi(j_1 - \not{E}_T)$ and high $d\phi(j_2 - \not{E}_T)$, which illustrates the cases where the mismeasurements lead to a smaller $|p_T^{j_1} - p_T^{j_2}|$ than the original difference.

Tevatron studies have defined the following radial variables to quantify the j_1, j_2 and $\not{E}_T$ correlation [114],[115]:

$$R1 = \sqrt{(d\phi(j_2 - \not{E}_T))^2 + (\pi - d\phi(j_1 - \not{E}_T))^2} \quad (7.6)$$

$$R2 = \sqrt{(d\phi(j_1 - \not{E}_T))^2 + (\pi - d\phi(j_2 - \not{E}_T))^2}. \quad (7.7)$$

The bottom plots show R2 versus R1. Conventionally $R1 > 0.5$ and $R2 > 0.5$ are adopted as selection criteria, however in our case S/B and significance optimization performs better

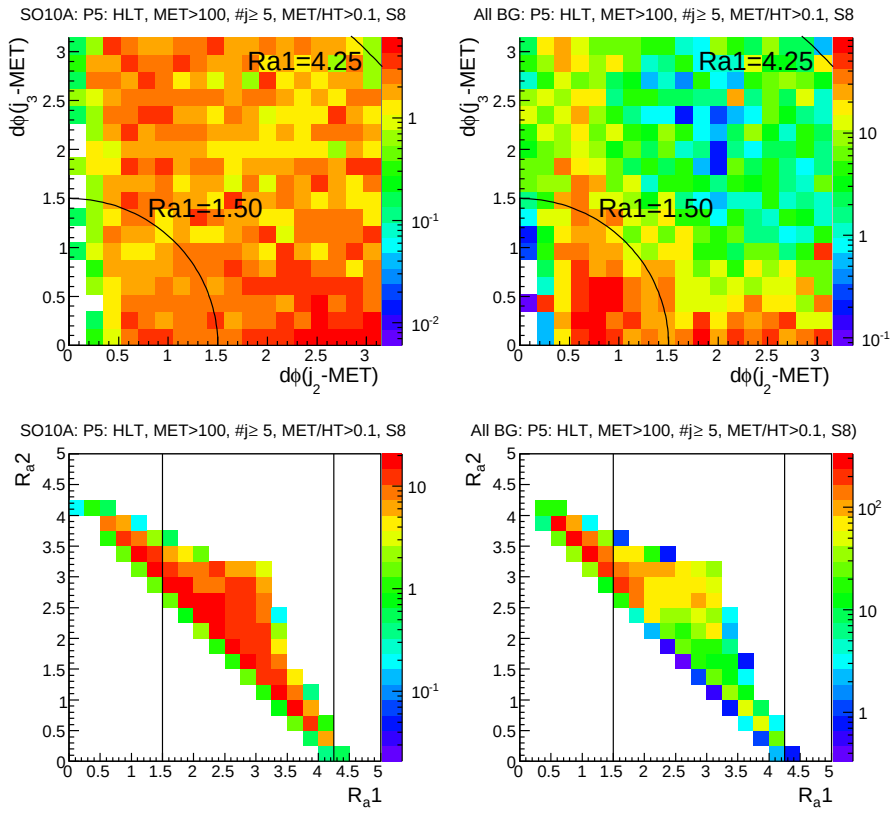

Figure 7.17: $d\phi(j_3 - \not{E}_T)$ vs $d\phi(j_2 - \not{E}_T)$ (top) and R_a2 vs R_a1 (bottom) after the R2 cut (step 8). Shown for path 5 for SO10A (left) and total BG (right).

when $R2 < 4$ was applied instead of $R1 > 0.5$. Therefore $0.5 < R2 < 4$ will be used.

Similarly Figure 7.17 shows $d\phi(j_3 - \not{E}_T)$ versus $d\phi(j_2 - \not{E}_T)$ on top plots after the $R2$ cut for path 5. The artificial $\not{E}_T$ from mismeasurements clearly manifests itself in QCD case by alligning either with 2nd or 3rd jet, while in signals the distributions are uniform.

Inspired by this we define the following R_a variables in order to quantify the relation between j_2, j_3 and $\not{E}_T$:

$$R_a1 = \sqrt{(d\phi(j_2 - \not{E}_T))^2 + (d\phi(j_3 - \not{E}_T))^2} \quad (7.8)$$

$$R_a2 = \sqrt{(\pi - d\phi(j_2 - \not{E}_T))^2 + (\pi - d\phi(j_3 - \not{E}_T))^2}. \quad (7.9)$$

The bottom plots show R_a2 vs. R_a1. For all paths and all benchmarks $1.5 < R_a1 < 4.25$ manages a good QCD rejection so we implement the cut.

Figure 7.18 then shows the resulting $d\phi(j_2 - \not{E}_T)$ signal and background distributions for paths 4 and 6 after the $R2$ and R_a1 cuts. As seen, especially for the low $\not{E}_T$ paths there is some residual QCD at low $d\phi(j_2 - \not{E}_T$. We clean these by additionally requiring $d\phi(j_2 - \not{E}_T) > 0.35$.

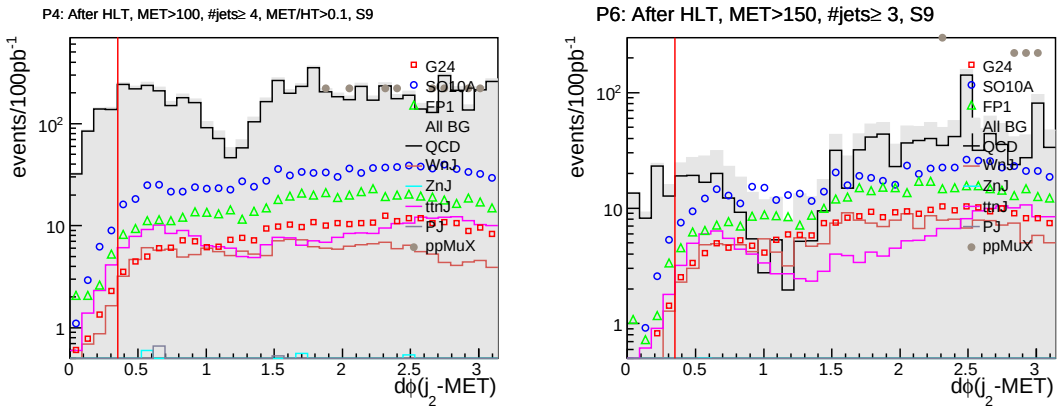

Figure 7.18: $d\phi(j_2 - \not{E}_T)$ distribution after R_a1 cut (step 9). Shown for path 4 (left) and path 6 (right).

As mentioned, the $\not{E}_T$ in QCD is generally expected to allign with the mostly mismeasured jet which is not always the 2nd jet. We define the mostly mismeasured jet as the jet that has the minimum $d\phi$ with the $\not{E}_T$. Figure 7.19 shows $d\phi(j_i - \not{E}_T)_{min}$ distributions for paths 4 and 6 after the $d\phi(j_2 - \not{E}_T)$ cut. Here QCD background strongly peaks close to $d\phi \sim 0$ and makes a distinctive sharp descent while signals and $W/t\bar{t}+n$ jets display a broader distribution. As a result we select the events that have $d\phi(j_i - \not{E}_T)_{min} > 0.3$.

Overall, the $d\phi(j - \not{E}_T)$ cuts prove to be very powerful tools in QCD rejection since $\sim$ %80-90 of QCD events present after the $d\phi(\not{E}_T - \not{H}_T)$ cut are rejected for the various paths while these angular cuts preserve $\sim$%55 of the signals.

7.5.4 Cleaning further

In what follows we will refine the event selection further by introducing supplementary cuts on the 1st jet η and event shape variables.

7.5.4.1 1st jet η

We accept the events with 1st jet $|\eta| < 1.7$. The reasons are three-fold: Firstly, SUSY processes produce central jets. This can be seen in Figure 7.20 which shows the η distribution for paths 3 and 6 after the $d\phi(j_i - \not{E}_T)_{min}$ cut. Signals peak at $\eta \sim 0$ which QCD backgrounds behave contrarily, having more excess at $\eta \sim 3$, especially for the no-$\not{E}_T$ path.

Secondly we would like to stay close to the HB/EB common region in order to have a better visualization of the physics. The third motivation is to veto the beam halo events that

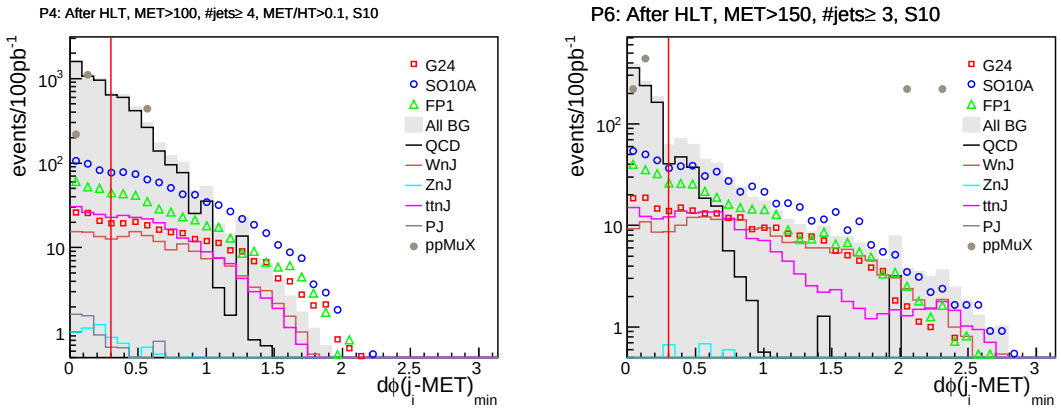

Figure 7.19: $d\phi(j_1 - \not{E}_T)_{min}$ distribution shown after $d\phi(j_2 - \not{E}_T)$ cut (step 10). Shown for path 4 (left) and path 6 (right).

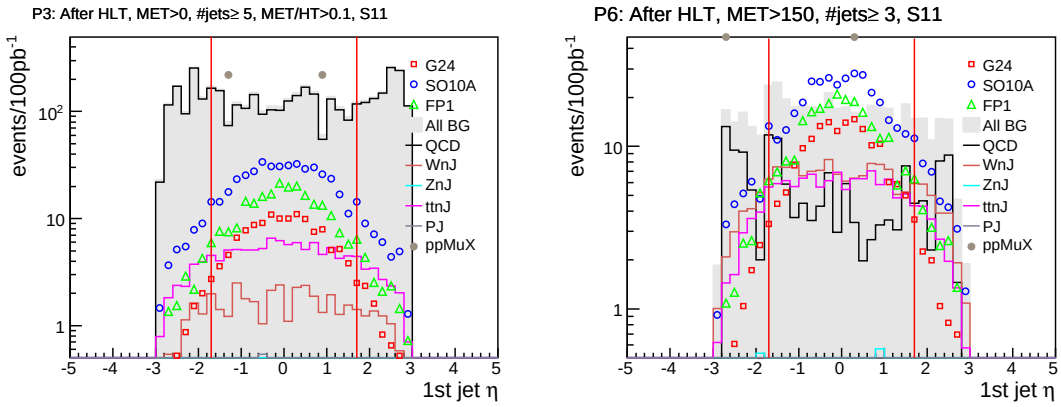

Figure 7.20: 1st jet η distribution after $d\phi(j_1 - \not{E}_T)$ cut (step 11). Shown for path 3 (left) and path 6 (right).

generate high energetic jets at the forward region. As shown in [117], beam halo particles deposit most of their energy at the HF which is positioned at $3 < |\eta| < 5$. Beam halo events should mostly be rejected by jet $|\eta| < 3$ cut, however $|\eta| < 1.7$ cut is a further measure to clean the fraction of such events surviving the $|\eta| < 3$ and EEMF cuts.

7.5.4.2 Event shape variables

Past e^+e^- and ep experiments have used event shape variables to study QCD processes, utilizing these to probe the structure of the hadronic final states. Event shapes are defined in terms of the 4-momenta of selected objects, which may be partons, hadrons, tracks, calorimeter energy deposits or jets. Here we investigate the discriminating power of the event shape variables between SUSY signals and SM backgrounds. By using the IC5 jets with $p_T > 30$ GeV and $|\eta| < 3$, we calculate the conventional event shapes spehericity, transverse sphericity, aplanarity [118], thrust [119] and the Fox-Wolfram moments [120]. Among these, aplanarity and Fox-Wolfram moments seem to possess discriminating powers.

The Fox-Wolfram moments H_l are defined as

$$H_l = \sum_{i,j} \frac{|p_i||p_j|}{E_{vis}^2} P_l(\cos\theta_{ij}) \tag{7.10}$$

where the summation is over any two jets i and j (including $i = j$), $P_l(\cos\theta_{ij})$ are the Legendre polynomials as functions of θ_{ij} which is the θ between two jets j_i, j_j and E_{vis} is the total visible energy of the jets in the event. The moments are generally normalized to H_0 and given as $H_{l0} = H_l/H_0$. Figure 7.21 shows H_{20} and H_{30} on the left for path 2 after $j_1|\eta|$ cut and H_{20} and H_{40} for path 6 on the right. Signals tend to have lower Fox-Wolfram moments than either the QCD or $W/t\bar{t}+n$ jets backgrounds which is valid for all the remaining paths as well. Therefore a selection criteria of $H_{20} < 0.8$, $H_{30} < 0.7$ and $H_{40} < 0.65$ is implemented.

This finalizes our event selection. Nevertheless an alternative case could be to further implement an aplanarity cut which can increase S/B by $\sim$ %20 − 35 of the current value at the expense of loosing $\sim$ %5 − 10 from significance $S/\sqrt{S+B}$ (corresponding to values up to 2 sigmas) and a %1 loss in final signal efficiency. More information on the aplanarity cut is given in Appendix B.

7.6 Selection results

Table 7.11 summarizes the results of the above selection for all paths for all signal points and backgrounds. Number of events are given for $\mathcal{L} = 100$ pb^{-1}. Signal efficiencies are highest

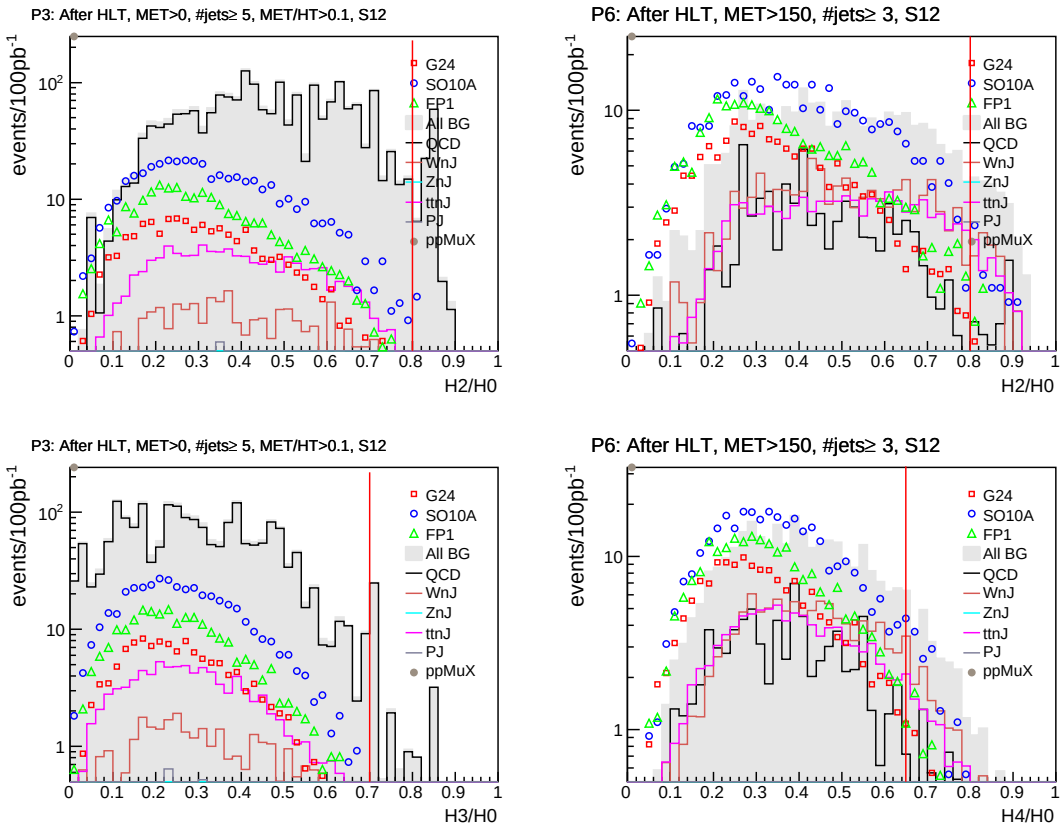

Figure 7.21: H_{20} (top) after the $j_1|\eta|$ cut (step 12). Shown for path 3 (left) and path 6 (right). H_{30} for path 3 (bottom left) and H_{40} (bottom right), again after the $j_1|\eta|$ cut.

for the G2s and lowest for the SO10s. Path 2 (with $\not{E}_T > 300$ GeV and $n_{jets} \geq 4$) leads to the lowest signal efficiencies while path 4 (with $\not{E}_T > 100$ GeV, $n_{jets} \geq 4$ and $\not{E}_T/H_T > 0.1$) leads to the highest. $\not{E}_T > 200$ and $\not{E}_T > 300$ cuts are survived most by $t\bar{t} + n$ jets, while the other backgrounds are almost totally eliminated. For paths with $\not{E}_T < 200$, QCD rejection depends more on the increase of $\not{E}_T$, while $W/Z/t\bar{t} + n$ jets rejection depends more on the number of jets required rather than the $\not{E}_T$. For example number of remnant events is 5 times more for path 6 ($\not{E}_T > 150$ and $n_{jets} \geq 3$) than path 5 ($\not{E}_T > 100$, $n_{jets} \geq 5$ and $\not{E}_T/H_T > 0.1$) for $W + n$ jets and 2 times for $t\bar{t} + n$ jets. All background efficiencies are less then %1.

The signal over background ratio is maximum for path 2 for all signals followed by path 1. These channels will be especially feasable at higher luminosities like 1 fb^{-1}. The non-$\not{E}_T$ path 3 suffers from a large QCD contamination. Highest significance $S/\sqrt{(S+B)}$ for the low cross section scenarios G21 and FP2 is given by path 2 while the lowest by path 3. On the other hand the higher cross section scenarios G24, SO10s and FP1 yield highest significances for path 6 while lowest for path 2. The decision for an optimal path choice for each scenario can be guided by the Punzi significance, which is a compromise between the S/B and the significance. Highest Punzi significances are given by path 2 for G21 which has the lowest cross section; by path 1 for G24 and FP2 whose cross sections are 2-3 times greater than G21; and by path 6 for SO10s and FP1.

The analysis flow for path 6 for all signals and backgrounds is displayed in Table 7.12. Cuts that reduce the background most efficiently are seen to be $\not{E}_T > 150$ and $d\phi(j - \not{E}_T)_{min} > 0.3$.

In the end, all six paths prove to be implementable in SUSY jet-MET analyses of scenarios having moderate $\not{E}_T$ and moderate p_T jets. They would also serve as alternatives to each other in order to justify a possible discovery. Moreover these paths can still be improved, as in the example to be presented next.

Table 7.11: Selection results for all paths for signal and backgrounds after the offline selection. The numbers of events represent 100 pb^{-1} of integrated luminosity.

Point		PDJM	HLT	path1	path2	path3	path4	path5	path6
G21:	nevts	25	23	7	4	7	9	7	9
	efficiency (%)	100.00	92.00	28.00	16.00	28.00	36.00	28.00	36.00
	S/B (%)	0.00	0.00	0.23	1.33	0.00	0.01	0.02	0.03
	Sgnf $S/\sqrt{S+B}$	0.00	0.03	1.15	1.51	0.16	0.27	0.33	0.55
	Punzi sgnf $\times 10^4$	0.73	10.13	401.31	495.04	61.25	103.22	123.92	204.26
G24:	nevts	807	597	74	19	124	179	107	155
	efficiency (%)	100.00	73.98	9.17	2.35	15.37	22.18	13.26	19.21
	S/B (%)	0.00	0.00	2.47	6.33	0.06	0.16	0.24	0.60
	Sgnf $S/\sqrt{S+B}$	0.06	0.66	7.26	4.05	2.72	4.98	4.55	7.61
	Punzi sgnf $\times 10^4$	0.72	8.04	129.66	71.87	33.16	62.74	57.89	107.51
SO10A:	nevts	6817	3323	86	15	414	523	265	308
	efficiency (%)	100.00	48.75	1.26	0.22	6.07	7.67	3.89	4.52
	S/B (%)	0.00	0.00	2.87	5.00	0.21	0.47	0.60	1.18
	Sgnf $S/\sqrt{S+B}$	0.50	3.66	7.98	3.54	8.51	12.93	9.95	12.92
	Punzi sgnf $\times 10^4$	0.59	4.34	14.63	5.51	10.75	17.80	13.92	20.74
SO10D:	nevts	7564	3975	116	21	436	638	295	411
	efficiency (%)	100.00	52.55	1.53	0.28	5.76	8.43	3.90	5.43
	S/B (%)	0.00	0.00	3.87	7.00	0.22	0.57	0.66	1.58
	Sgnf $S/\sqrt{S+B}$	0.55	4.37	9.60	4.29	8.92	15.24	10.84	15.87
	Punzi sgnf $\times 10^4$	0.54	4.29	16.28	6.36	9.34	17.91	12.78	22.83
FP1:	nevts	2150	1329	81	23	219	295	174	210
	efficiency (%)	100.00	61.81	3.77	1.07	10.19	13.72	8.09	9.77
	S/B (%)	0.00	0.00	2.70	7.67	0.11	0.26	0.39	0.81
	Sgnf $S/\sqrt{S+B}$	0.16	1.46	7.69	4.51	4.70	7.86	6.99	9.69
	Punzi sgnf $\times 10^4$	0.53	4.93	39.09	23.96	16.13	28.48	25.93	40.12
FP2:	nevts	426	243	26	7	50	61	44	48
	efficiency (%)	100.00	57.04	6.10	1.64	11.74	14.32	10.33	11.27
	S/B (%)	0.00	0.00	0.87	2.33	0.03	0.05	0.10	0.18
	Sgnf $S/\sqrt{S+B}$	0.03	0.27	3.47	2.21	1.12	1.78	1.99	2.74
	Punzi sgnf $\times 10^4$	0.21	1.84	25.61	14.89	7.52	12.02	13.38	18.72
WnJ	nevts	115196	9432	6	0	29	87	16	96
	eff (%)	100.00	8.19	0.01	0.00	0.03	0.08	0.01	0.08
ZnJ	nevts	19624	725	0	0	2	3	1	3
	eff (%)	100.00	3.69	0.00	0.00	0.01	0.02	0.01	0.02
ttnJ	nevts	18559	3134	17	3	86	128	47	86
	eff (%)	100.00	16.89	0.09	0.02	0.46	0.69	0.25	0.46
QCD	nevts	185288380	807170	7	0	1834	894	380	75
	eff (%)	100.00	0.44	0.00	0.00	0.00	0.00	0.00	0.00
PJ	nevts	1408307	1557	0	0	4	2	1	0
	eff (%)	100.00	0.11	0.00	0.00	0.00	0.00	0.00	0.00
Total BG	nevts	186850066	822018	30	3	1955	1114	445	260
	eff (%)	100.00	0.44	0.00	0.00	0.00	0.00	0.00	0.00

Table 7.12: Analysis flow for path 6 corresponding to $\mathcal{L} = 100$ pb^{-1} for signals and backgrounds. Number of RAW events for backgrounds are estimated from cross sections (since no AllEvents datasets for the backgrounds are available).

Cut		G21	G24	SO10A	SO10D	FP1	FP2	WnJ	ZnJ	ttnJ	QCD	PJ	All BG
R	RAW	25	862	8425	10215	3504	1455	5.82×10^{6}	5.78×10^{5}	8.37×10^{4}	2.28×10^{11}	1.78×10^{10}	2.40×10^{11}
P	PDJetMET	25	807	6817	7564	2150	426	115196	19624	18559	185288380	1408307	186850066
H	HLT (Acoplanarity trio)	23	597	3323	3975	1329	243	9432	725	3134	807170	1557	822018
S1	$\not{E}_T > 150$	19	342	936	1209	578	131	1309	105	614	5839	18	7885
S2	$n_{jets} \geq 5$	18	329	853	1072	549	125	439	36	454	3837	10	4776
S3	$\not{E}_T/H_T > 0$	18	329	853	1072	549	125	439	36	454	3837	10	4776
S4	trkiso=0	15	288	760	962	485	104	294	11	275	3692	10	4282
S5	j_1EMF$> 0.1 \wedge j_2$EMF$> 0.1\wedge$												
S5	$(j_1$EMF$< 0.9 \vee j_2$EMF$< 0.9)$	15	285	755	954	480	103	284	10	267	3395	8	3964
S6	EEMF> 0.175	15	277	738	929	467	101	272	9	257	3301	8	3847
S7	$(d\phi(\not{E}_T - MHT) < 1$	15	276	732	922	465	100	271	9	254	2979	7	3520
S8	$0.5 < R_2 < 4$	14	261	657	838	431	93	241	8	217	1658	4	2128
S9	$1.5 < R_a1 < 4.25$	13	238	571	735	379	84	198	6	183	988	1	1376
S10	$d\phi(j_2 - \not{E}_T) > 0.35$	13	235	561	723	373	83	196	6	180	930	1	1313
S11	$d\phi(j_i - \not{E}_T) > 0.3$	9	177	397	528	253	54	164	5	135	155	0	459
S12	$j_1\|\eta\| < 1.7$	9	161	331	438	220	50	117	3	102	82	0	304
S13	$H_{2/0} < 0.8 \wedge H_{3/0} < 0.7$												
	$\wedge H_{4/0} < 0.65$	9	155	308	411	210	48	96	3	86	75	0	260
Efficiency wrt RAW (%)		36.0	18.0	3.66	4.02	5.93	3.30	1.65×10^{-3}	5.19×10^{-4}	1.03×10^{-1}	3.29×10^{-8}	0.00	1.08×10^{-7}
Efficiency wrt PDJetMET (%)		36.0	19.2	4.52	5.43	9.77	11.3	8.33×10^{-2}	1.53×10^{-2}	4.63×10^{-1}	4.05×10^{-5}	0.00	1.39×10^{-4}

7.7 Making use of the *b* triggers

As mentioned, the SUSY signatures of our interest are rich with *b*-jets. Therefore using an effective probe for *b*-rich signatures could prove very helpful in signal discrimination. CMS has developed several *b* tagging algorithms where a discriminator is calculated by exploiting either the long *B* hadron lifetimes, or the semi-leptonic *B* decay modes, or other kinematic variables related to high *B* hadron mass and hard *b* fragmentation function.

The algorithm with best performance for `CMSSW_1_6_X` was shown to be the jet probability algorithm that is based on the lifetime of *B* hadrons, whose discriminator is equal to the negative logarithm of the confidence level that all the tracks in the jet are consistent with originating from the primary vertex. Here the confidence level is calculated from the signed impact parameter significances of all good tracks. As an example we plot in Figure 7.22 the 2nd jet discriminator and event discriminator for path 6 after the final selection, where we define the event discriminator as the p_T weighted sum of all jet discriminators in the event. The signal excess at high values is obvious for both cases. The next step would be to put a cut on the discriminator to distinguish *b* jets from non-*b* jets. However the cut decision varies for each discriminator, is made upon the efficiency and rejection distributions and is dependent on the nature of analysis.

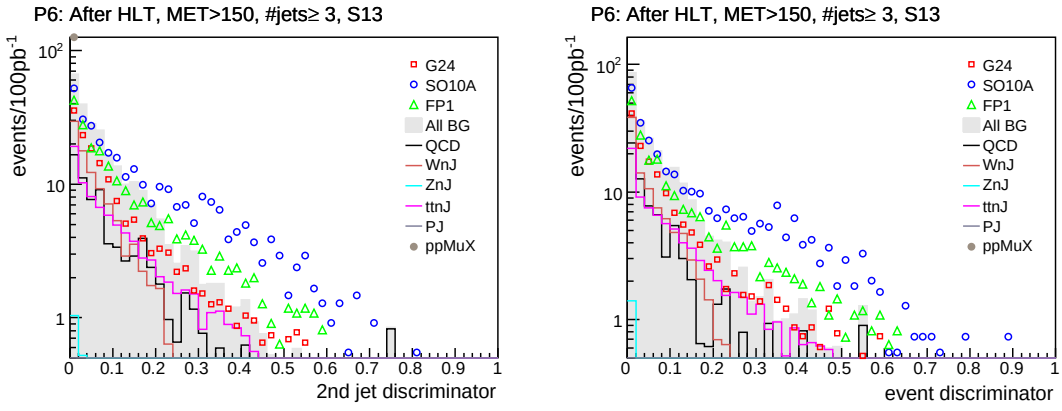

Figure 7.22: *b* tag discriminators from jet probability algorithm shown after the Fox-Wolfram cuts (step 13, the final cut). 2nd jet discriminator (left) and event discriminator (right). Shown for path 6.

In this study we rather follow a simpler and more robust approach and exploit the effect of *b* triggers instead. Tables C.1 and C.2 in Appendix C list the *b* triggers implemented in `CMSSW 1_6_X`, relevant for the conditions for a physics run at 14 TeV and $\mathcal{L} = 10^{32}$ cm^{-2}s^{-1} (which also exist in the more recent candidate trigger tables implemented in `CMSSW 2_1_X`) and Table C.3 shows their L1 seeds. *b* triggers take the L2 calorimeter information for jets and find *b*-tag discriminators using PV, track and muon information on L2.5 and L3. Currently lifetime triggers based on the track counting *b* tag algorithm and soft muon triggers based on the soft muon algoritm are implemented.

We accept a PDJetMET event if it also passes any of the unprescaled *b* triggers along with the usual acoplanarity trio requirement [3]. In other words, we take the intersection of the acoplanarity trio with the OR of all unprescaled *b* triggers. Table 7.13 shows the change in final results when the *b* trigger requirement is added. %40-70 of the signals survive with respect to the non-*b* trigger cases, where SO10s, with $\sim$ %72 $\tilde{g} \rightarrow bb\tilde{\chi}^0$ decays show the best performance. $\sim$ %90 of $W + n$ jets, $\sim$ %50 of $t\bar{t} + n$ jets and $\sim$ %80 of QCD with respect to non-*b* case are rejected. The S/B is increased for all paths. Moreover, the no-$\not\!\!E_T$ path can be considered as a more reliable alternative now.

Overall, although the *b* trigger requirement is not compulsory for our analysis, it greatly improves the final S/B ratios and signal significances. The combined OR approach of a multi-*b* trigger requirement seems much more efficient than a single cut on a single discriminator since as also seen from Figure 7.22, a single cut would eliminate a relatiely large amount of signal. Therefore using the *b* triggers can be considered as a good alternative to offline *b* tagging. The improvement can be further optimized by considering different subsets of *b* triggers instead of the whole unprescaled set.

7.8 Background estimation from data

In what follows, we try to estimate the background remaining after all selection cuts via implementing the so-called "ABCD" method [121]. The procedure starts with choosing two variables x and y among those used for event selection, which are as uncorrelated in the case of backgrounds as possible. After applying all cuts except those on x and y, the remaining events are histogrammed in the x-y plane. Then one divides the x-y plane into four regions from the values where x and y are cut, and labels the regions such that A is the intersection

[3] Here we do not make use of a different *b*-specific datastream neither do we combine more than one primary datasets, we rather select a subset of PDJetMET events that would have fired a *b* trigger.

Table 7.13: Selection results including the *b* trggers requirement for all paths for signal and backgrounds after the offline selection. The numbers of events represent 100 pb^{-1} of integrated luminosity.

Point		PDJM	HLT	path1	path2	path3	path4	path5	path6
G21:	nevts	25	23	3	2	3	4	3	4
	efficiency (%)	100.00	92.00	12.00	8.00	12.00	16.00	12.00	16.00
	S/B (%)	0.00	0.00	0.25	2.00	0.01	0.02	0.03	0.06
	Sgnf $S/\sqrt{S+B}$	0.00	0.03	0.77	1.15	0.15	0.25	0.31	0.46
	Punzi sgnf $\times 10^4$	0.73	10.13	241.74	320.00	54.93	90.62	108.70	162.16
G24:	nevts	807	597	32	7	56	80	48	65
	efficiency (%)	100.00	73.98	3.97	0.87	6.94	9.91	5.95	8.05
	S/B (%)	0.00	0.00	2.67	7.00	0.14	0.31	0.53	0.93
	Sgnf $S/\sqrt{S+B}$	0.06	0.66	4.82	2.47	2.58	4.33	4.07	5.59
	Punzi sgnf $\times 10^4$	0.72	8.04	78.81	34.23	31.34	55.39	53.15	80.54
SO10A:	nevts	6817	3323	53	9	270	348	171	197
	efficiency (%)	100.00	48.75	0.78	0.13	3.96	5.10	2.51	2.89
	S/B (%)	0.00	0.00	4.42	9.00	0.65	1.33	1.88	2.81
	Sgnf $S/\sqrt{S+B}$	0.50	3.66	6.57	2.85	10.32	14.10	10.56	12.06
	Punzi sgnf $\times 10^4$	0.59	4.34	12.67	4.27	14.67	23.40	18.39	23.70
SO10D:	nevts	7564	3975	70	13	292	428	191	261
	efficiency (%)	100.00	52.55	0.93	0.17	3.86	5.66	2.53	3.45
	S/B (%)	0.00	0.00	5.83	13.00	0.71	1.64	2.10	3.73
	Sgnf $S/\sqrt{S+B}$	0.55	4.37	7.73	3.47	10.99	16.31	11.37	14.35
	Punzi sgnf $\times 10^4$	0.54	4.29	13.81	5.09	13.09	23.74	16.94	25.90
FP1:	nevts	2150	1329	42	10	117	162	93	111
	efficiency (%)	100.00	61.81	1.95	0.47	5.44	7.53	4.33	5.16
	S/B (%)	0.00	0.00	3.50	10.00	0.28	0.62	1.02	1.59
	Sgnf $S/\sqrt{S+B}$	0.16	1.46	5.72	3.02	5.08	7.88	6.86	8.25
	Punzi sgnf $\times 10^4$	0.53	4.93	28.49	13.47	18.03	30.89	28.36	37.88
FP2:	nevts	426	243	16	4	31	39	28	30
	efficiency (%)	100.00	57.04	3.76	0.94	7.28	9.15	6.57	7.04
	S/B (%)	0.00	0.00	1.33	4.00	0.07	0.15	0.31	0.43
	Sgnf $S/\sqrt{S+B}$	0.03	0.27	3.02	1.79	1.47	2.25	2.57	3.00
	Punzi sgnf $\times 10^4$	0.21	1.84	22.15	11.00	9.75	15.18	17.43	20.90
WnJ	nevts	115196	9432	1	0	2	7	2	6
	eff (%)	100.00	8.19	0.00	0.00	0.00	0.01	0.00	0.01
ZnJ	nevts	19624	725	0	0	0	0	0	0
	eff (%)	100.00	3.69	0.00	0.00	0.00	0.00	0.00	0.00
ttnJ	nevts	18559	3134	8	1	39	62	22	40
	eff (%)	100.00	16.89	0.04	0.01	0.21	0.33	0.12	0.22
QCD	nevts	185288380	807170	3	0	373	192	67	24
	eff (%)	100.00	0.44	0.00	0.00	0.00	0.00	0.00	0.00
PJ	nevts	1408307	1557	0	0	0	0	0	0
	eff (%)	100.00	0.11	0.00	0.00	0.00	0.00	0.00	0.00
All BG	nevts	186850066	822018	12	1	414	261	91	70
	eff (%)	100.00	0.44	0.00	0.00	0.00	0.00	0.00	0.00

of x to be accepted and y to be rejected, B is the intersection of x to be rejected and y to be rejected, C is the intersection of x to be accepted and y to be accepted while D is the intersection of x to be rejected and y to be accepted.

Here C is the eventually accepted signal rich region while A, B and D are the background rich regions to be rejected, with D having the lowest S/B ratio. Assuming that x and y are uncorrelated for the backgrounds, for a no signal case, where regions could be renamed as as A_0, B_0, C_0 and D_0, we would have $A_0/B_0 = C_0/D_0$. Including the signal obscures the equality, however due to the relatively high amount of background in A, B and D, one could approximate the relation to $A/B \approx C_0/D$. Therefore, the number of background events C_0 in the signal region C, which actually is the number of backgrounds remaining after all cuts, can be estimated to be $\sim (A/B)D$.

We choose the leading jet $|\eta|$ as the y variable, since it offers a distinct signal-background seperation besides being relatively uncorrelated with other variables, and examine it versus all variables that directly aim to eliminate SM backgrounds, namely $\not{E}_T$, jet multiplicity, $\not{E}_T/H_T$, R2, R_a1, $d\phi(j_2 - \not{E}_T)$ and $d\phi(j - \not{E}_T)_{min}$. We do not consider cuts used for eliminating detector effects or machine/cosmic backgrounds. We primarily apply the ABCD method on the selection including the b triggers requirement, but we also consider the case with no b triggers for the sake of investigating the effect of an increased statistics on background estimation as well as the case including b triggers plus the aplanarity requirements for the sake of investigating the effect of an increased S/B ratio on background estimation. We try to find the optimum variables to use for each of the six selection paths.

Table 7.14 shows the results of background estimation with $\mathcal{L} = 100$ pb^{-1} where for each path the numbers are displayed for the variable that gives the overall best estimation considering all signals. There S and B are the true signal and background while S_E and B_E are the estimated signal and background. We check the signal and background estimation efficiencies by looking at S_E/S and B_E/B as well as comparing $(S + B)/B$ with $(S + B)/B_E$. Furthermore we introduce the background estimation bias on significance defined as $\frac{B_E - B}{\sqrt{S+B}}$ which gives in sigmas the significance of the background estimation error. Then the signed ratio of background estimation bias on significance to signal significance

$$\frac{B_E - B}{\sqrt{S + B}} \Big/ \frac{S}{\sqrt{S + B}} = \frac{B_E - B}{S} \tag{7.11}$$

can be defined as a robust parameter to quantify the estimation quality. For example, in a case where B_E/B is relatively high, if S/B is much higher, an excess in background estimation will

Table 7.14: Background estimation results for different selection paths including b trigger requirement for $\mathcal{L} = 100$ pb^{-1} using variables that optimize the estimation for all signals.

	$S+B$	B	B_E	$\frac{B_E}{B}$	$\frac{S_E}{S}$	$\frac{S+B}{B}$	$\frac{S+B}{B_E}$	$\frac{S_E}{\sqrt{S+B}}$	$\frac{B_E-B}{\sqrt{S+B}}$	$\frac{B_E-B}{S}$
Path1	$\not{E}_T - j_1\|\eta\|$									
G21	14	11	3	0.30	3.35	1.30	4.26	0.87	-2.04	-2.35
G24	43	11	7	0.62	1.13	3.90	6.27	4.90	-0.64	-0.13
SO10A	65	11	21	1.91	0.81	5.80	3.04	6.65	1.26	0.19
SO10D	82	11	34	3.05	0.68	7.32	2.40	7.80	2.53	0.32
FP1	53	11	16	1.40	0.89	4.77	3.41	5.76	0.61	0.11
FP2	27	11	5	0.45	1.38	2.45	5.46	3.10	-1.17	-0.38
Path2	$\not{E}_T - j_1\|\eta\|$									
G21	3	1	1	0.38	1.41	2.50	6.59	1.10	-0.45	-0.41
G24	9	1	1	1.05	0.99	6.46	6.13	2.49	0.02	0.01
SO10A	11	1	4	3.25	0.68	7.97	2.45	2.86	0.92	0.32
SO10D	14	1	5	3.52	0.74	10.64	3.03	3.42	0.89	0.26
FP1	11	1	3	2.02	0.86	8.36	4.13	2.95	0.41	0.14
FP2	6	1	1	0.72	1.09	4.20	5.87	1.81	-0.16	-0.09
Path3	$\not{E}_T/HT - j_1\|\eta\|$									
G21	418	415	370	0.89	13.96	1.01	1.13	0.17	-2.18	-12.96
G24	471	415	385	0.93	1.53	1.14	1.22	2.59	-1.38	-0.53
SO10A	685	415	500	1.21	0.68	1.65	1.37	10.33	3.27	0.32
SO10D	706	415	522	1.26	0.63	1.70	1.35	10.97	4.02	0.37
FP1	532	415	424	1.02	0.92	1.28	1.25	5.08	0.41	0.08
FP4	446	415	377	0.91	2.19	1.08	1.18	1.49	-1.77	-1.19
Path4	$d\phi(j - \not{E}_T)_{min} - j_1\|\eta\|$									
G21	265	261	237	0.91	6.84	1.02	1.12	0.26	-1.51	-5.84
G24	341	261	258	0.99	1.04	1.30	1.32	4.31	-0.18	-0.04
SO10A	609	261	382	1.46	0.65	2.33	1.59	14.09	4.91	0.35
SO10D	690	261	409	1.57	0.66	2.64	1.69	16.31	5.63	0.34
FP1	423	261	299	1.14	0.77	1.62	1.42	7.88	1.82	0.23
FP2	300	261	248	0.95	1.34	1.15	1.21	2.25	-0.77	-0.34
Path5	Not possible									
Path6	$d\phi(j - \not{E}_T)_{min} - j_1\|\eta\|$									
G21	74	70	27	0.38	11.32	1.06	2.77	0.49	-5.02	-10.32
G24	135	70	36	0.52	1.52	1.93	3.72	5.61	-2.90	-0.52
SO10A	267	70	82	1.17	0.94	3.81	3.26	12.05	0.72	0.06
SO10D	331	70	97	1.38	0.90	4.73	3.42	14.35	1.47	0.10
FP1	181	70	53	0.76	1.15	2.58	3.40	8.22	-1.27	-0.15
FP2	100	70	31	0.44	2.29	1.43	3.22	3.02	-3.89	-1.29

not have a drastic effect on the signal discovery. Contrarily, in a case where the background is closely estimated, if the S/B is low, the estimated background could be in the range of statistical fluctuations of signal, hence making the discovery difficult. This ratio is especially useful in judging the estimation power of a variable when such cases are considered.

For an ideal background estimator variable on a path we would request for each signal to have a ratio less than 0.50, while in order to guarantee a 3 sigma discovery, signal significance should be 3 sigmas greater than the background estimation bias significance. We would naturally prefer background overestimation to underestimation - that is, a positive ratio - in order to prevent false signal discoveries. However if the signal significance is huge, one could allow for a ratio down to -0.25. The results in Table 7.14 nearly comply with this criteria except for the low cross section scenarios G21 and FP2, which always underestimate the background. The SO10s have acceptable ratios for all paths, which are occasionally better when using other variables, but the current selection was optimized regarding all signals, especially G24 and FP1.

In essence, best performing variables are the ones that eliminate the most BG and the least signal. In this sense, effectiveness of a variable on a benchmark depends most on the gluino mass (hence the cross section) and the $\tilde{\chi}_1^0$ mass (hence the $\not{E}_T$ amount). $\not{E}_T$ versus 1st jet $|\eta|$ performs best for the high $\not{E}_T$ benchmarks (G2s and SO10s) since $\not{E}_T$ is the most effective cut in this case. For the high cross section-low $\not{E}_T$ benchmarks, angular cut variables R2, R_a1, $d\phi(j_2 - \not{E}_T)$ and $d\phi(j - \not{E}_T)_{min}$ versus 1st jet $|\eta|$ give better estimates because in this case angular variables are the main actors in eliminating the huge QCD backgrounds since a high $\not{E}_T$ cut cannot be used.

Regarding the relation of paths and variables, we see that $\not{E}_T$ versus 1st jet $|\eta|$ works best for the high $\not{E}_T$ paths 1,2 and 6, since it is the best discriminator in their analysis flows. $\not{E}_T/H_T$ also gives good results. Then for the no or moderate $\not{E}_T$ paths 3,4 and 5, variables R2, R_a1, $d\phi(j_2 - \not{E}_T)$ or $d\phi(j - \not{E}_T)_{min}$ versus 1st jet $|\eta|$ perform a better estimation because here we mostly rely on these angular cuts while eliminating the QCD background with fake $\not{E}_T$. We note that despite its high final S/B ratios, no variable was able to make an overall acceptable estimation for path 5. On the other hand, the no-$\not{E}_T$ path 3 yields a remarkable background estimation despite the high background contamination remaning after final selection. Generally the best performing variables with 1st jet $|\eta|$ are seen to be $\not{E}_T$, $\not{E}_T/H_T$ and $d\phi(j - \not{E}_T)_{min}$.

One can further comment on the method's performance by comparing the estimation

errors $B_E - B$ with the statistical and systematic uncertainties calculated in the next section and presented in Table 7.16. For Path 1, background uncertainty is $\sim$ 5 events. Estimation error is greater than this for four signals, but since the background numbers are small, only significant difference is in SO10D and creates a false negative change in the signal. Also for path 2 the number of background events is small and the estimation errors become more unimportant. Path 3 has an uncertainty of 40-50, which is exceeded by the estimtion errors in two SO10s, leading to signal underestimation. For path 4 all estimations are within the uncertainties. Path 6 has a background uncertainty of 20. Estimation exceeds this in three cases, always doing an underestimate of background, which manifests itself as excess signal. However this is compensated by a high signal significance in the higher cross section scenarios as seen from the final $(B_E - B)/S$ result.

Table 7.15 then presents some alternative cases that act well when b triggers are neglected or both b triggers and aplanarity are required. Adding the aplanarity requirement is a possibility for path 1, which leads to better ratios for G24 and FP2. On the other hand, relaxing the b triggers improves the ratios remarkably well for path 2. Among the two alternatives considered for path 3, the no b trigger case with $d\phi(j - \not{E}_T)_{min}$ improves estimation with G24 and FP2, while the second possibility featuring R_a1 yields nearly exact estimation for the SO10s. Path 4 without b triggers presents the possibility to use $R2$. Moreover, relaxing the b triggers also opens up two possibilities for path 5, through $\not{E}_T$ and $d\phi(j_2 - \not{E}_T)$, although FP2 ratio is still below -1. Finally, if aplanarity cut is considered for path 6, $\not{E}_T$ gives much better estimation for G24 and FPs while keeping the SO10 ratios at 0.21.

To illustrate the estimation procedure in more detail, we plot in Figure 7.23 the 1st jet $|\eta|$ versus $d\phi\, j - \not{E}_T$ for SO10A and total background after a path 6 selection including the b triggers and mark the A, B, C, D regions. Furthermore, to prove the non-correlation of $d\phi(j - \not{E}_T)_{min}$ with 1st jet $|\eta|$, Figure 7.24 shows $d\phi(j - \not{E}_T)_{min}$ distributions for signals and backgrounds in different $|\eta|$ bins having $0 < |\eta| < 0.42$, $0.42 < |\eta| < 0.85$, $0.85 < |\eta| < 1.7$ and $1.7 < |\eta| < 3$ again for the same path. The non-correlation for the backgrounds means that the ratio $d\phi(j - \not{E}_T)_{min} > 0.3/d\phi(j - \not{E}_T)_{min} < 0.3$ should be constant for any value of $|\eta|$ for the backgrounds, which is equivalent to the statement $A_0/B_0 = C_0/D_0$. To see this, we plot in Figure 7.25 $d\phi(j-\not{E}_T)_{min} > 0.3/d\phi(j-\not{E}_T)_{min} < 0.3$ versus 1st jet $|\eta|$ for total background and total $S + B$ for each signal, where we consider $\mathcal{L} = 1$ fb^{-1} to reduce the statistical fluctuations. Total background is a constant within the errors, while adding the signals on top leads to higher ratios in the signal regions.

Table 7.15: Background estimation results using alternative variables for different selection paths given for $\mathcal{L} = 100\ \mathrm{pb}^{-1}$.

	$S+B$	B	B_E	$\frac{B_E}{B}$	$\frac{S_E}{S}$	$\frac{S+B}{B}$	$\frac{S+B}{B_E}$	$\frac{S_E}{\sqrt{S+B}}$	$\frac{B_E-B}{\sqrt{S+B}}$	$\frac{B_E-B}{S}$
Path1	alt 1:	$\not{E}_T - j_1\lvert\eta\rvert$, b triggers + aplanarity required								
G21	11	8	3	0.37	2.78	1.35	3.64	0.88	-1.57	-1.78
G24	37	8	6	0.73	1.08	4.40	6.01	4.72	-0.37	-0.08
SO10A	53	8	20	2.33	0.74	6.22	2.67	6.09	1.55	0.26
SO10D	66	8	28	3.32	0.66	7.86	2.37	7.11	2.41	0.34
FP1	45	8	17	1.95	0.78	5.34	2.73	5.46	1.20	0.22
FP2	23	8	5	0.61	1.22	2.75	4.47	3.07	-0.68	-0.22
Path2	alt 1:	$\not{E}_T - j_1\lvert\eta\rvert$, without b triggers								
G21	8	3	1	0.24	1.60	2.27	9.40	1.55	-0.92	-0.60
G24	22	3	3	1.03	0.99	6.51	6.32	3.97	0.02	0.01
SO10A	19	3	4	1.21	0.95	5.56	4.59	3.55	0.16	0.05
SO10D	25	3	5	1.45	0.93	7.35	5.06	4.30	0.31	0.07
FP1	26	3	4	1.33	0.95	7.74	5.80	4.45	0.22	0.05
FP2	11	3	1	0.43	1.26	3.14	7.24	2.22	-0.59	-0.26
Path3	alt 1:	$d\phi(j - \not{E}_T)_{min} - j_1\lvert\eta\rvert$, without b triggers								
G21	1962	1955	1923	0.98	5.48	1.00	1.02	0.16	-0.71	-4.48
G24	2079	1955	1971	1.01	0.87	1.06	1.05	2.72	0.36	0.13
SO10A	2369	1955	2139	1.09	0.56	1.21	1.11	8.52	3.78	0.44
SO10D	2390	1955	2147	1.10	0.56	1.22	1.11	8.91	3.93	0.44
FP1	2179	1955	2036	1.04	0.64	1.11	1.07	4.79	1.73	0.36
FP2	2004	1955	1946	1.00	1.18	1.03	1.03	1.11	-0.20	-0.18
Path3	alt 2:	$R_a 1 - j_1\lvert\eta\rvert$								
G21	418	415	276	0.66	41.44	1.01	1.52	0.17	-6.79	-40.44
G24	471	415	294	0.71	3.14	1.14	1.60	2.59	-5.54	-2.14
SO10A	685	415	417	1.01	0.99	1.65	1.64	10.33	0.10	0.01
SO10D	706	415	435	1.05	0.93	1.70	1.63	10.97	0.75	0.07
FP1	532	415	331	0.80	1.71	1.28	1.60	5.08	-3.61	-0.71
FP2	446	415	284	0.68	5.16	1.08	1.57	1.49	-6.19	-4.16
Path4	alt 1:	$R2 - j_1\lvert\eta\rvert$, without b triggers								
G21	1123	1114	1108	0.99	1.68	1.01	1.01	0.26	-0.17	-0.68
G24	1293	1114	1152	1.03	0.79	1.16	1.12	4.97	1.05	0.21
SO10A	1637	1114	1334	1.20	0.58	1.47	1.23	12.94	5.45	0.42
SO10D	1752	1114	1374	1.23	0.59	1.57	1.28	15.25	6.21	0.41
FP1	1409	1114	1209	1.09	0.68	1.26	1.17	7.86	2.53	0.32
FP2	1174	1114	1123	1.01	0.86	1.05	1.05	1.77	0.25	0.14
Path5	alt 1:	$\not{E}_T - j_1\lvert\eta\rvert$, without b triggers								
G21	452	445	359	0.81	13.53	1.02	1.26	0.33	-4.08	-12.53
G24	552	445	378	0.85	1.63	1.24	1.46	4.55	-2.87	-0.63
SO10A	710	445	464	1.04	0.93	1.59	1.53	9.94	0.71	0.07
SO10D	741	445	469	1.05	0.92	1.66	1.58	10.85	0.87	0.08
FP1	620	445	403	0.90	1.24	1.39	1.54	7.00	-1.71	-0.24
FP2	489	445	365	0.82	2.84	1.10	1.34	1.98	-3.66	-1.84
Path5	alt 2:	$d\phi(j_2 - \not{E}_T) - j_1\lvert\eta\rvert$, without b triggers								
G21	452	445	382	0.86	10.17	1.02	1.18	0.33	-2.99	-9.17
G24	552	445	422	0.95	1.22	1.24	1.31	4.55	-0.98	-0.22
SO10A	710	445	521	1.17	0.71	1.59	1.36	9.94	2.85	0.29
SO10D	741	445	526	1.18	0.73	1.66	1.41	10.85	2.96	0.27
FP1	621	445	487	1.09	0.76	1.39	1.27	7.04	1.67	0.24
FP2	489	445	397	0.89	2.10	1.10	1.23	1.98	-2.17	-1.10
Path6	alt 1:	$\not{E}_T - j_1\lvert\eta\rvert$, b triggers + aplanarity required								
G21	51	47	22	0.47	7.89	1.08	2.32	0.51	-3.55	-6.89
G24	104	47	33	0.69	1.26	2.18	3.16	5.52	-1.44	-0.26
SO10A	203	47	80	1.69	0.79	4.29	2.53	10.94	2.31	0.21
SO10D	257	47	92	1.93	0.79	5.43	2.81	13.09	2.76	0.21
FP1	139	47	48	1.02	0.99	2.94	2.88	7.79	0.09	0.01
FP2	74	47	26	0.55	1.80	1.56	2.84	3.10	-2.48	-0.80

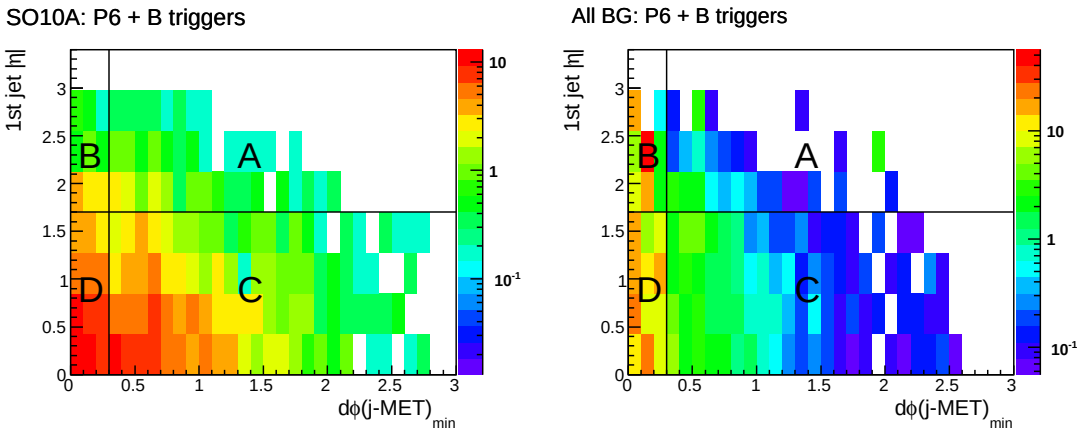

Figure 7.23: 1st jet $|\eta|$ vs $d\phi(j - \not{E}_T)_{min}$ for SO10A (left) and total background (right) for path 6 with b triggers, excluding the cuts on d$\phi(j - \not{E}_T)_{min}$ and 1st jet η. A, B, C, D regions are shown.

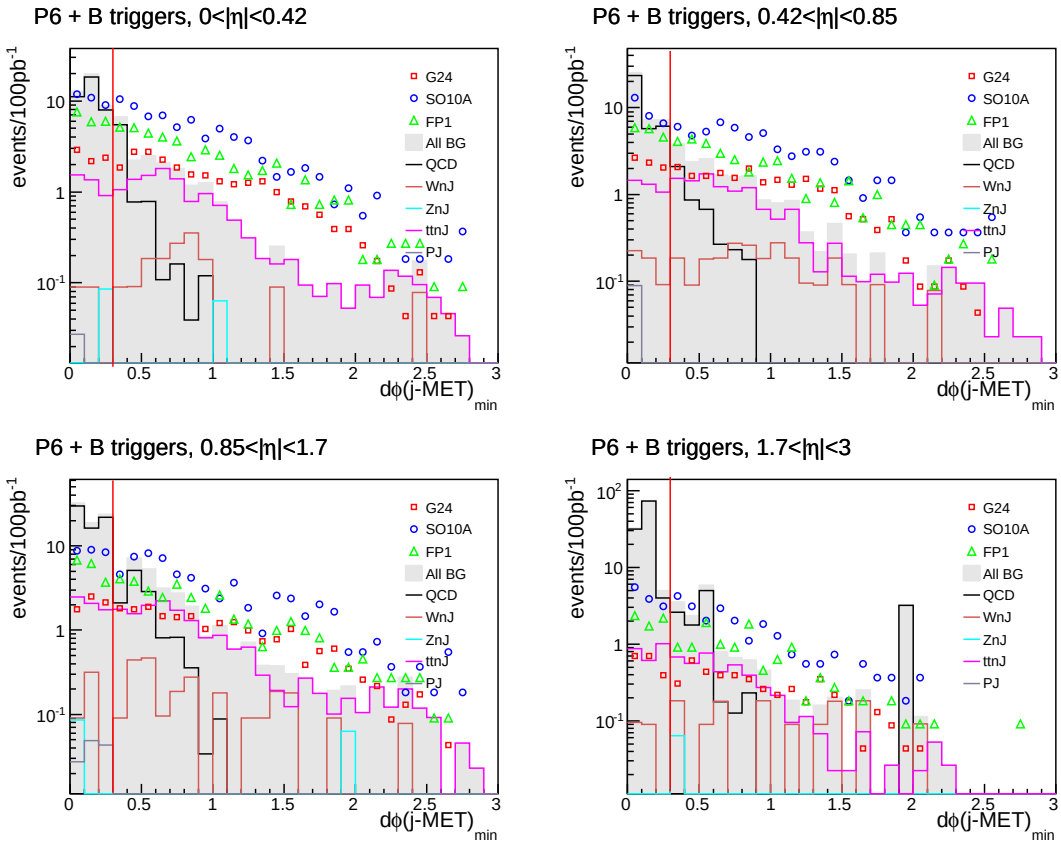

Figure 7.24: $d\phi(j - \not{E}_T)_{min}$ distribution in different 1st jet $|\eta|$ bins: $0 < |\eta| < 0.42$ (top left), $0.42 < |\eta| < 0.85$ (top right), $0.85 < |\eta| < 1.7$ (bottom left), $1.7 < |\eta| < 3$ (bottom right. Shown for path 5 + b triggers, excluding the cuts on d$\phi(j - \not{E}_T)_{min}$ and 1st jet η.

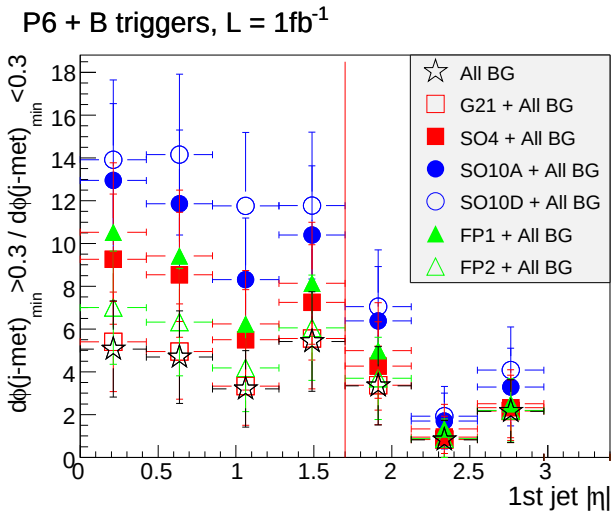

Figure 7.25: $(d\phi(j - \not{E}_T)_{min} > 0.3)/(d\phi(j - \not{E}_T)_{min} < 0.3)$ ratio versus 1st jet $|\eta|$ for true background and $S + B$ for all signals. Shown for path 6 + b triggers excluding the cuts on $d\phi(j - \not{E}_T)_{min}$ and 1st jet η, with $\mathcal{L} = 1$ fb^{-1}.

Finally Figure 7.26 shows distributions of $S + B$, true background and estimated background for all six signals. For G2s, $\not{E}_T$ was used with path 2 without b triggers, and the results are shown for $\mathcal{L} = 1$ fb^{-1}, though $\mathcal{L} = 100$ pb^{-1} would as well be sufficient for G24. For the SO10s, results for $d\phi(j - \not{E}_T)_{min}$ with b triggers along path 6 are shown while for FPs $\not{E}_T$ results for path 6 with b triggers and aplanarity can be seen. All cases present a good agreement between true and estimated backgrounds.

We note however that the low cross section benchmarks (like G2s and FP2) always give a background underestimation. In a more generic sense it was seen that the estimation variables which work best within presence of signals underestimate the background when they are exercised for the no signal case. To trace the reason, we decomposed the total background and studied the estimation of its individual components in the absence of a signal. We found that QCD is the best estimated background and $t\bar{t} + n$ jets is the worst estimated background. This is because $t\bar{t} + n$ jets is more signal-like and less uncorrelated. So $t\bar{t} + n$ jets-rich background rather acts like $S + B$ and the ABCD method estimates a lower background. Consequently no or moderate $\not{E}_T$ paths 3,4 and 5 perform a better estimation for no signal case since their backgrounds are QCD-dominated while high $\not{E}_T$ paths 1,2 and 6 lead to underestimation since their backgrounds are dominated by $t\bar{t} + n$ jets. In case a signal excess is observed, one needs to do complementarity checks using different paths or variales to study its true nature

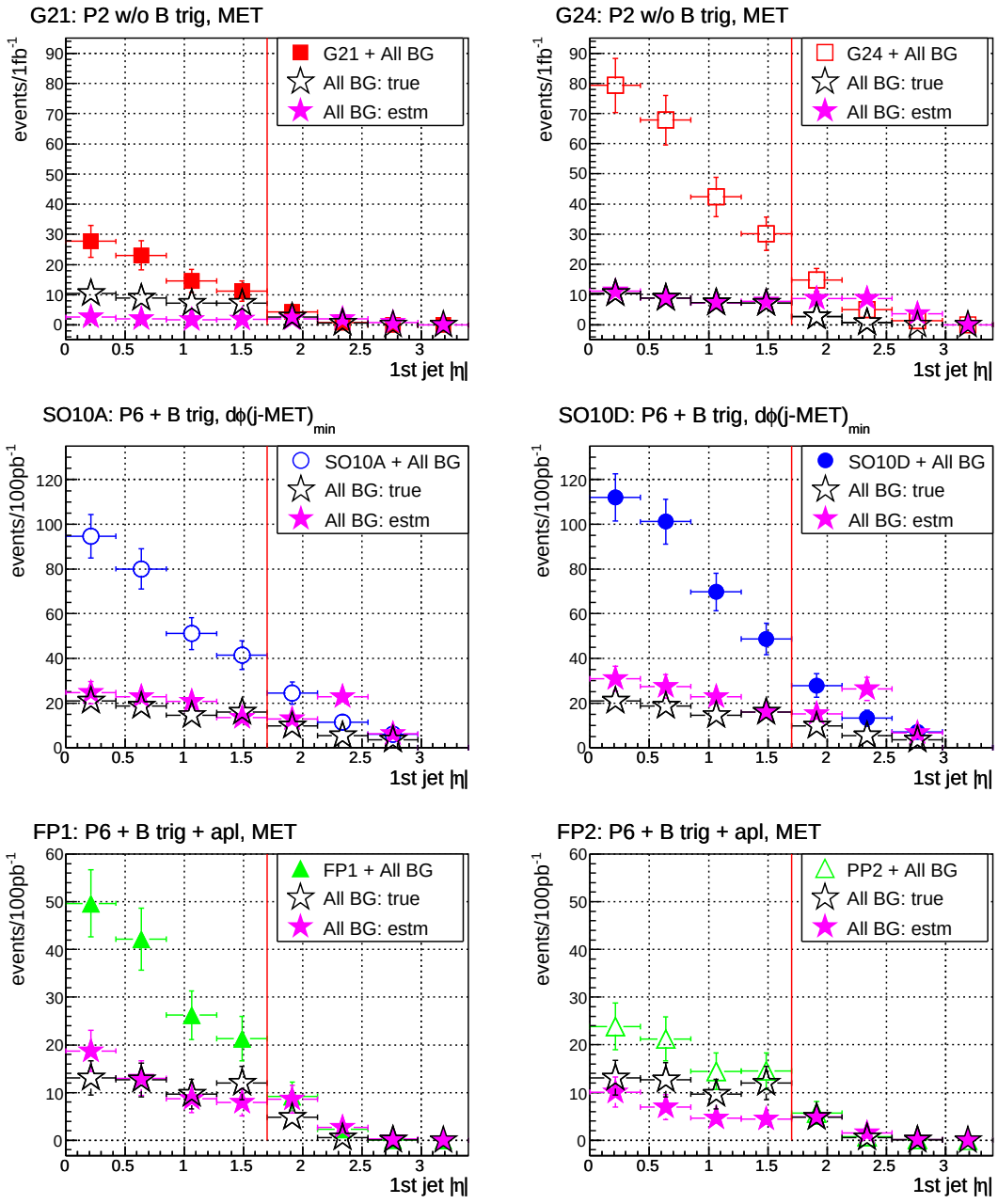

Figure 7.26: Distributions of $S + B$, true background and estimated background versus 1st jet $|\eta|$ for all six signal benchmarks. where estimation for G2s, SO10s and FPs are made using different variables and for different paths. For G2s $\not{E}_T$ was used on path 2 without b triggers, for SO10s $d\phi(j - \not{E}_T)_{min}$ was used on path 6 including b triggers and for FPs $\not{E}_T$ was used on path 6 including b triggers and aplanarity.

in order to avoid fake signal discovery. The $t\bar{t} + n$ jets background underestimation can be cross-checked using the low $\not{E}_T$ paths 3,4,5 and the angular variables, that are orthogonal in terms of background prediction (i.e. they give a more moderate background estimation in the presence of signal). This would provide a cross-validation of the excess.

The ABCD method is a simple and rudimentary technique for background estimation that can provide data-driven background estimated for each of the benchmarks. In the absence of collider data the current study on Monte Carlo is a first iteration and the technique can be developed already with the first LHC data at 10 TeV in the fall of 2009.

7.9 Effects of uncertainties

Finally we study the effects of statistical and systematic uncertainties on the discovery potential of the scenarios. We take the error on a Poisson distribution $\sqrt{N}$, as the statistical error where N is the number of events. For the systematics, we consider the contributions from two effects. First we study the variation caused by the effect of jet energy scale uncertainty (JES) where the jet 4-vector is scaled with the addition of an uncertainty, such that

$$(p^{\mu}_{jet})_{\text{scaled}} = (1 + \delta)(p^{\mu}_{jet})_{\text{measured}}. \tag{7.12}$$

Here we implement a JES uncertainty of ±5 and record the number of resulting signal and background events after −%5 and +%5 variation for all paths after final event selection including b triggers.

As a second source of systematics we take the variation of the $\not{E}_T$ tails due to the contributions from jet mismeasurements. As was studied earlier, normally a perfect detector response for jets with a certain p_T would result in a Gaussian distribution around the true value. However imperfections in the detector, such as those created by uninstrumented or poorly functioning regions will lead to non-Gaussian increases in the downward going tails, resulting in undermeasured jets. Furthermore, contributions from pile-up or underlying events which would coincide to the jet cones will create a similar non-Gaussian effect in the upward tails, hence resulting in overmeasured jets. Both undermeasurements and overmeasurements will directly effect the total missing energy, creating a contribution which will especially be visible at the $\not{E}_T$ tails.

We try to see the variation in $\not{E}_T$ tails through an exaggerated simulation of the under and overmeasurement effects. For each event we consider a simultaneous $-\%\delta$ undermeasurement

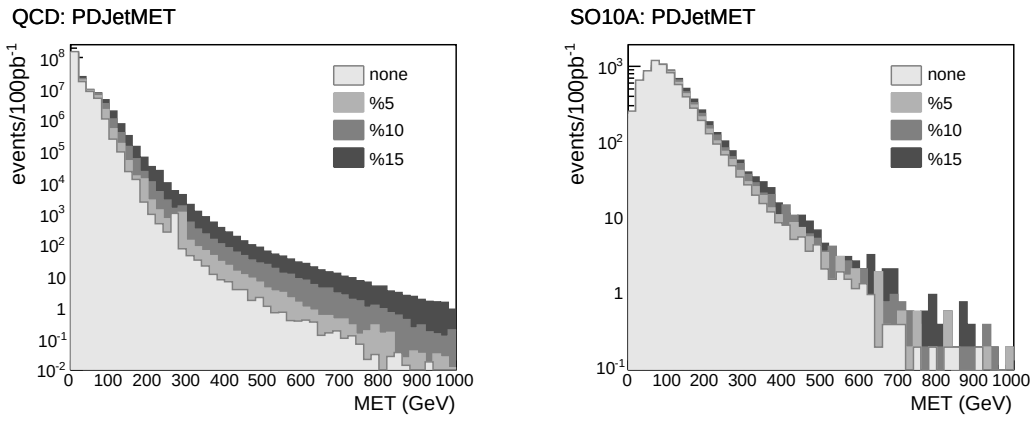

Figure 7.27: Effect of event-averaged jet over and undermeasurements on the $\not\!\!E_T$ tails calculated as described in the text for QCD (left) and SO10A(right). Results shown for $\delta = 5, 10, 15$.

on the 2nd jet [4] and a +%δ overmeasurement on the 1st jet. The implication is such that the p_T of the 1st jet is taken, and a random p_T value is selected from the upward half of a Gaussian with mean p_T^{j1} and width $|\delta p_T^{j1}|$ while simultaneously the p_T of the 2st jet is taken, and a random p_T value is selected from the downward half of a Gaussian with mean p_T^{j2} and width $|\delta p_T^{j2}|$, thus taking an average on the event basis. The resulting variations in the 1st and 2nd jet p_Ts are then summed up and added to the $\not\!\!E_T$ and the event selection is applied on this new set of modified objects.

Figure 7.27 shows the reflection of non-gaussian tails in jet mismeasurements to the $\not\!\!E_T$ tails for $\delta = 5, 10, 15$ for QCD (left) and SO10A (right). QCD tails are vastly effected due to the fact that QCD $\not\!\!E_T$ totally results from mismeasurements while on the other hand the impact on SO10 tails is mild since this scenario posesses true $\not\!\!E_T$. For the systematics we take into account the case with $\delta = 5$, since $\delta = 10$ and 15 would be unrealistically large for a controlled detector.

When finding the systematic uncertainty on the number of events, we treat the upward (+) and downward (-) uncertainties seperately and calculate them as

$$\Delta N^{+}_{tot} = \Delta N^{+}_{JES\,(+5)} \oplus \Delta N^{+}_{JES\,(-5)} \oplus \Delta N^{+}_{mettail(5)} \tag{7.13}$$

$$\Delta N^{-}_{tot} = \Delta N^{-}_{JES\,(+5)} \oplus \Delta N^{-}_{JES\,(-5)} \oplus \Delta N^{-}_{mettail(5)} \tag{7.14}$$

where

[4] Here undermeasurement effect is applied only if after the p_T decrease 2nd jet still stays as the 2nd jet

$$\Delta N_x^+ = N_x - N, \quad \text{for} \quad N_x > N$$
$$\Delta N_x^+ = 0, \quad \text{for} \quad N_x \leq N$$
$$\Delta N_x^- = N - N_x, \quad \text{for} \quad N_x < N$$
$$\Delta N_x^- = 0, \quad \text{for} \quad N_x \geq N.$$

Table 7.16 lists the resulting statistical and systematic uncertainties on signal and background events where the systematic uncertainty on total background is the sum in quadriture of the individual background components.

We next consider the impact of these errors on significance and find the significance error through a MC study as follows: For each try i, we calculate a number of signal and background events N_S^i and N_B^i by adding up N^i selected from a Poisson distribution plus a random systematic error selected from a asymmetric gaussian centered at 0 which has the asymmetric systematic errors as widths, such that

$$N^i = (\text{Poisson}(N))^i + (\text{Gaus}(0, N_{tot}^-, N_{tot}^+)^i. \tag{7.15}$$

For each i, a significance $N_S^i / \sqrt{N_S^i + N_B^i}$ is found. The significance then is given as the mean of all values from $i = 0, ..n$ and the error on significance is given by the RMS. In Figure 7.28 we show the significances with errors versus gluino mass for the six scenarios and the six paths, also showing the errors computed. We also perform fits to the function $x = a/y^b$. Highest $m_{\tilde{g}}$ reach for a 5σ significance is provided by path 6 and is ~550 GeV. Path 2 does not offer a 5σ significance for any $m_{\tilde{g}}$, but this can be improved for $\mathcal{L} = 1$ fb^{-1}.

We finally compute the integrated luminosity necessay to achieve 5σ, which is given as $\mathcal{L}(5\sigma) = 2500/sig(100 \text{ pb}^{-1})^2)$ along with the error on this luminosity which is found by propagation of errors to be $\Delta\mathcal{L}(5\sigma) = |-5000/sig(100 \text{ pb}^{-1})^3)|\Delta sig(100 \text{ pb}^{-1})$. Resulting luminosities are displayed in Figure 7.29 and a fit is performed this time to the function $y = ax^b$. The plots except path 1 and 2 do not show G21 due to its very low cross section which results in extreme uncertainties. On the other hand, SO10s show a remarkable behavior and require only 20-30 pb^{-1} except for path 2.

To conclude, we can say that gluinos with masses up to 1 TeV are accessible at the LHC with over 5σ significance for 50-100 fb^{-1} corresponding to a 3-5 year running with $\mathcal{L} = 2 \times 10^{33}$ cm^{-2}s^{-1}. High $\not{E}_T$ paths would be necessary to distinguish the cases with $m_{sq} > 700$ GeV while for $m_{\tilde{g}} < 700$ GeV all proposed paths serve well for a 5σ discovery with luminosities less then ~1 fb^{-1}, providing results within the first year.

Table 7.16: Statistical (first) and systematic (second) errors on signal and background events after cuts (including *b* triggers) for the six paths. Systematics consist of %5 JES uncertainty and %5 event averaged $\not\!\!E_T$ tail uncertainty.

	path1	path2	path3	path4	path5	path6
G21	$3^{+1.7+0.0}_{-1.7-0.0}$	$2^{+1.4+0.0}_{-1.4-0.0}$	$3^{+1.7+0.0}_{-1.7-0.0}$	$4^{+2.0+0.0}_{-2.0-0.0}$	$3^{+1.7+0.0}_{-1.7-0.0}$	$4^{+2.0+0.0}_{-2.0-0.0}$
G24	$32^{+5.7+4.1}_{-5.7-4.0}$	$7^{+2.6+2.2}_{-2.6-1.0}$	$56^{+7.5+3.0}_{-7.5-2.2}$	$80^{+8.9+3.0}_{-8.9-3.0}$	$48^{+6.9+4.0}_{-6.9-3.0}$	$65^{+8.1+4.5}_{-8.1-3.0}$
SO10A	$53^{+7.3+17.5}_{-7.3-11.0}$	$9^{+3.0+4.2}_{-3.0-1.0}$	$270^{+16.4+17.0}_{-16.4-22.8}$	$348^{+18.7+45.9}_{-18.7-42.0}$	$171^{+13.1+25.0}_{-13.1-26.0}$	$197^{+14.0+30.5}_{-14.0-23.0}$
SO10D	$70^{+8.4+20.1}_{-8.4-13.0}$	$13^{+3.6+3.6}_{-3.6-3.0}$	$292^{+17.1+16.0}_{-17.1-23.3}$	$428^{+20.7+53.5}_{-20.7-43.0}$	$191^{+13.8+26.2}_{-13.8-27.0}$	$261^{+16.2+37.1}_{-16.2-34.0}$
FP1	$42^{+6.5+6.7}_{-6.5-6.0}$	$10^{+3.2+2.2}_{-3.2-2.0}$	$117^{+10.8+6.0}_{-10.8-8.0}$	$162^{+12.7+10.4}_{-12.7-13.0}$	$93^{+9.6+9.5}_{-9.6-12.0}$	$111^{+10.5+10.3}_{-10.5-12.0}$
FP2	$16^{+4.0+2.2}_{-4.0-2.0}$	$4^{+2.0+2.2}_{-2.0-1.0}$	$31^{+5.6+1.0}_{-5.6-0.0}$	$39^{+6.2+1.0}_{-6.2-1.0}$	$28^{+5.3+2.0}_{-5.3-2.0}$	$30^{+5.5+2.2}_{-5.5-1.0}$
WnJ	$1^{+1.0+0.0}_{-1.0-1.0}$	$0^{+0.0+0.0}_{-0.0-0.0}$	$2^{+1.4+1.0}_{-1.4-0.0}$	$7^{+2.6+1.0}_{-2.6-1.0}$	$2^{+1.4+0.0}_{-1.4-1.0}$	$6^{+2.4+2.2}_{-2.4-1.0}$
ZnJ	$0^{+0.0+0.0}_{-0.0-0.0}$	$0^{+0.0+0.0}_{-0.0-0.0}$	$0^{+0.0+0.0}_{-0.0-0.0}$	$0^{+0.0+0.0}_{-0.0-0.0}$	$0^{+0.0+0.0}_{-0.0-0.0}$	$0^{+0.0+0.0}_{-0.0-0.0}$
ttnJ	$8^{+2.8+1.4}_{-2.8-2.0}$	$1^{+1.0+1.0}_{-1.0-0.0}$	$39^{+6.2+4.0}_{-6.2-3.0}$	$62^{+7.9+8.5}_{-7.9-10.0}$	$22^{+4.7+4.1}_{-4.7-4.0}$	$40^{+6.3+6.7}_{-6.3-7.0}$
QCD	$3^{+1.7+2.0}_{-1.7-1.0}$	$0^{+0.0+0.0}_{-0.0-0.0}$	$373^{+19.3+59.0}_{-19.3-27.5}$	$192^{+13.9+127.9}_{-13.9-52.0}$	$67^{+8.2+38.5}_{-8.2-26.0}$	$24^{+4.9+17.0}_{-4.9-8.0}$
PJ	$0^{+0.0+0.0}_{-0.0-0.0}$	$0^{+0.0+0.0}_{-0.0-0.0}$	$0^{+0.0+0.0}_{-0.0-0.0}$	$0^{+0.0+0.0}_{-0.0-0.0}$	$0^{+0.0+0.0}_{-0.0-0.0}$	$0^{+0.0+0.0}_{-0.0-0.0}$
Total BG	$12^{+3.5+2.4}_{-3.5-2.4}$	$1^{+1.0+1.0}_{-1.0-0.0}$	$414^{+20.3+59.1}_{-20.3-27.7}$	$261^{+16.2+128.2}_{-16.2-53.0}$	$91^{+9.5+38.7}_{-9.5-26.3}$	$70^{+8.4+18.4}_{-8.4-9.3}$

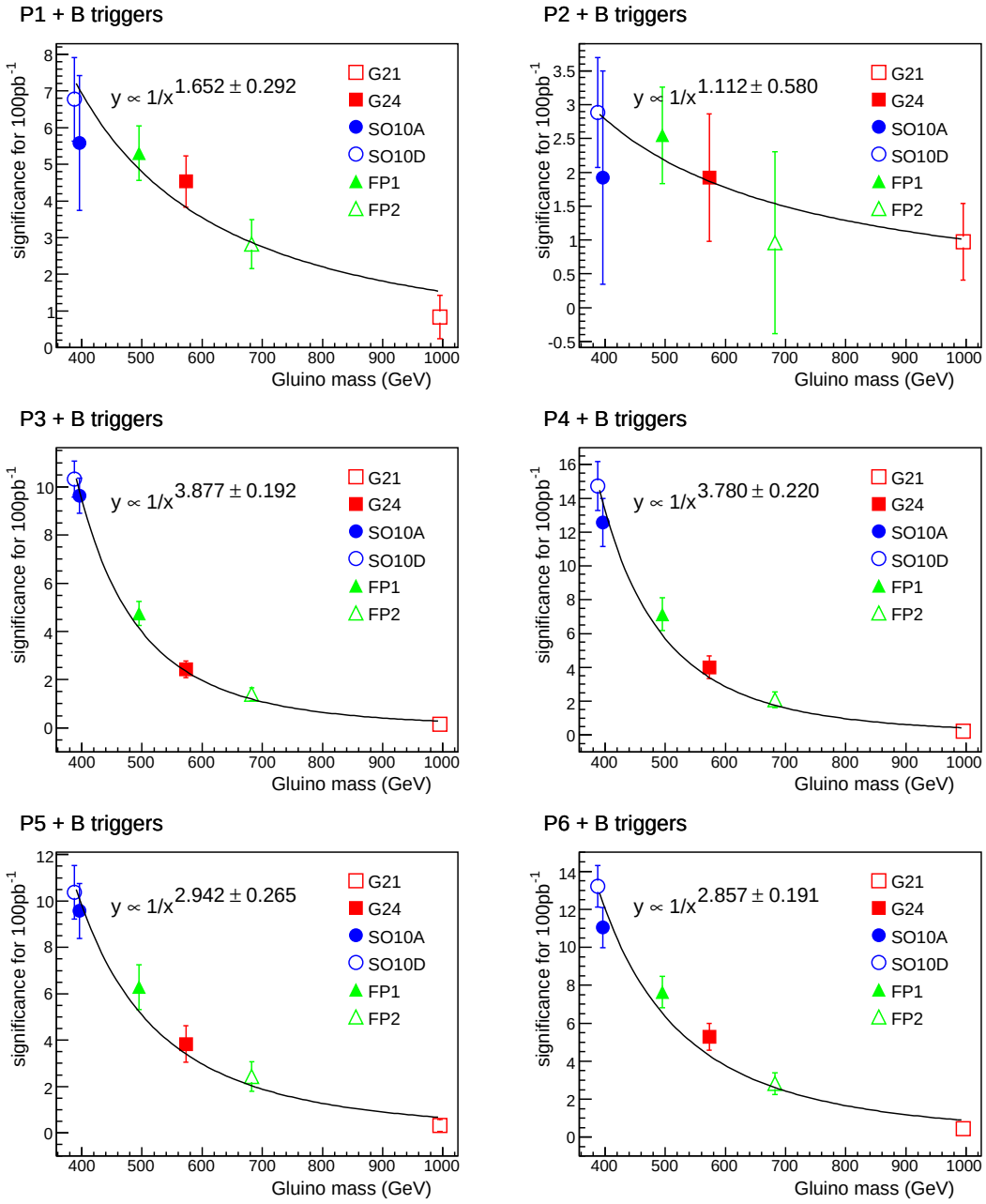

Figure 7.28: Signal signiicance $S/\sqrt{S+B}$ corresponding to an integrated luminosity of 100 pb^{-1} versus gluino mass, showing all the signals for all paths including significance errors whose calculation was described in the text. Also shown are the results for fits to the function $y = a/x^b$.

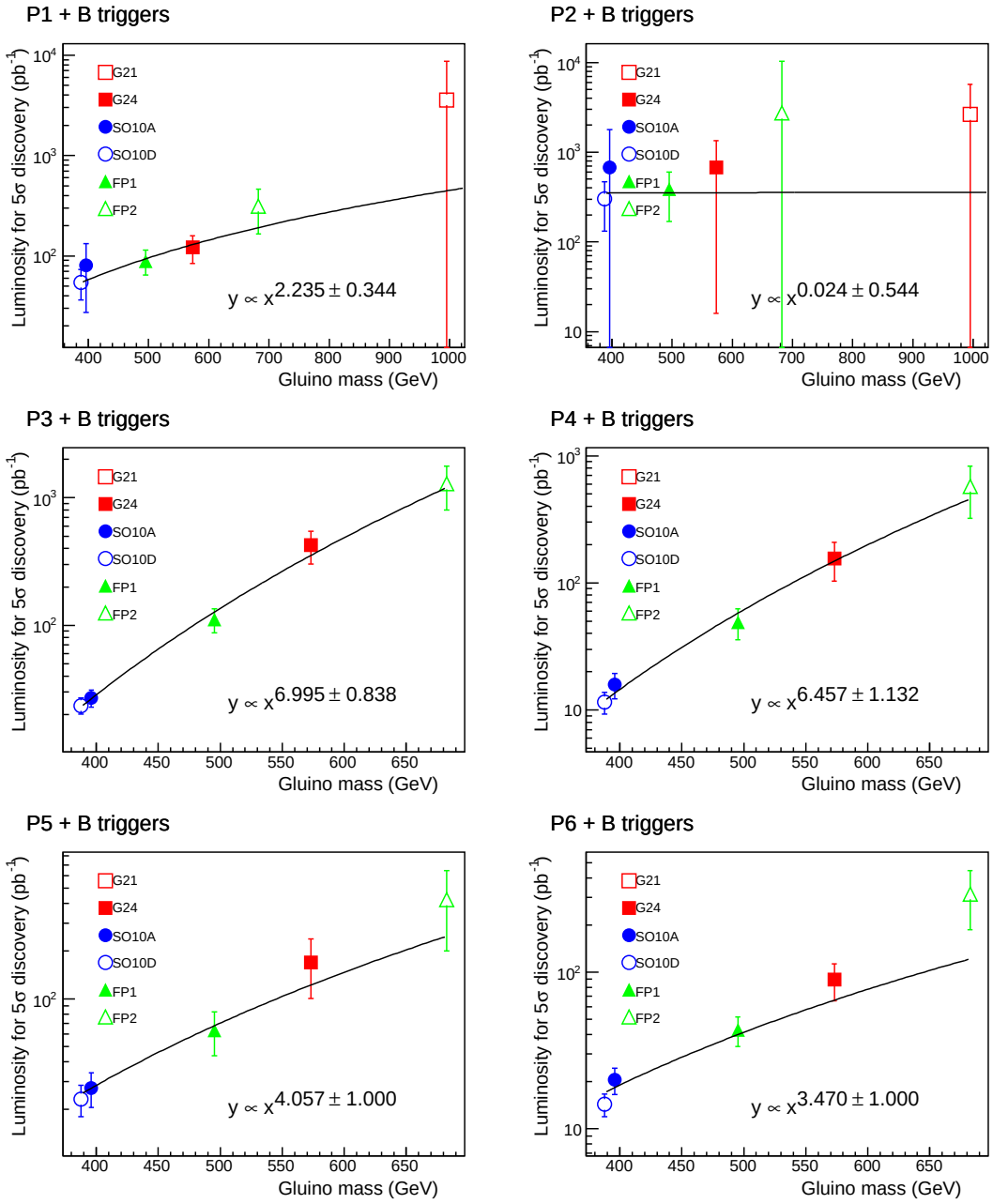

Figure 7.29: Integrated luminosity required for a 5σ signiicance versus gluino mass, showing signals for all paths including luminosity errors whose calculation was described in the text. G21 is not shown for low $\not\!\!E_T$ paths due to its extreme errors. Also shown are the results for fits to the function $y = ax^b$.

CHAPTER 8

CONCLUSIONS

The successful turn-on of the LHC (though followed by a technical delay...) has finally signaled the start for a new era of discovery. But the long time that took for experiment to lift the energy reach by 12 more TeVs has been sufficient for theorists to come up with more and more scenarios as candidates for observation. The divergent variety of candidates may seem frustrating, but still, one can take hints from deficits of the SM, requirements for a consistent phenomenology and guidence of the perception of an ultimate theory to converge on a special subset as favored solutions.

Here we conclude that supersymmetry with (very) heavy scalars and light-to-moderate gauginos is a viable scenario. Such a phenomenology is pointed out in consensus by (at least) three scenarios with different descent: the G_2-MSSM, a low energy limit of M theory with consistent real world predictions (which is a rare gift for a string-inspired model); the simple SO(10) SUSY GUTs, a robust unifier of matter fields, Higgsino fields as well as GUT scale Yukawa couplings; and the focus point mSUGRA, an alternative supplier of naturalness with considerable phenomenological virtues. Furthermore, the consensus is supported by the presence of a consistent dark matter candidates.

The G_2-MSSM phenomenology was already at hand, thanks to Kane, et.al. So we started with SO(10) SUSY GUTs, and to justify that they actually lead to such a mass hierarchy, we performed extensive Markov Chain Monte Carlo (MCMC) scans of the MSSM parameter space, looking for trademark Yukawa-unified and WMAP-compatible scenarios. We found that excellent Yukawa unification indeed occurs for multi-TeV scalars, light gauginos and a $\tilde{\chi}_1^{\pm}$ slightly above the current LEP2 limit, and these models are consistent with the Bagger *et al.* boundary conditions for $\mu > 0$ which we can re-state as $A_0^2 = 2m_{10}^2 = 4m_{16}^2$ and $A_0 < 0$. The MCMC also discovered a new class of solutions with $m_{16} \sim 3-4$ TeV, where neutralinos

annihilate through the light higgs (h) resonance. But these low values for m_{16} typically lead to Yukawa unification at the %5–10 level at best. The better unified points resulted in a neutralino relic density $10 - 10^4$ times the amount measured by WMAP. To reconcile these solutions we suggested that neutralinos are not the lightest sparticles, but they could instead decay to axinos.

Starting from there we proposed a candidate dark matter cocktail with tree ingredients: axion dark matter produced via vacuum mis-alignment at the QCD phase transition, non-thermally produced axinos from $\tilde{\chi}_1^0 \rightarrow \tilde{a}\gamma$ decay which are likely warm dark matter when $m_{\tilde{a}} \lesssim 1$ GeV, and thermally produced axinos which are likely cold dark matter unless $m_{\tilde{a}} \lesssim 100$ keV. Since present observations favor a Universe with cold dark matter, we considered cases with either dominant axion or dominant axino cold dark matter. For four scenarios defined by the choice of Peccei-Quinn symmetry breaking scale f_a/N and percentage axion, thermal axino and non-thermal axino abundances we calculated the thermal re-heat temperature T_R. We saw that all SO(10) scenarios easily give T_R below the limit imposed by the gravitino BBN problem. But the non-thermal leptogenesis preference of $T_R > 10^6$ proved to be more coercive. Solutions with $f_a \lesssim 2\times10^{11}$ GeV were found difficult to generate at high T_R since that case favors $m_{\tilde{a}} \lesssim 100$ keV and thus leads to warm axino dark matter. Increasing f_a to and beyond 4×10^{11} GeV allows finding consistent solutions with $m_{16} \gtrsim 10$ TeV. We further investigated the case with a tiny axion relic abundance due to accidental vacuum allignment plus dominant cold and warm axino dark matter contributions which also provided favored T_R solutions with $m_{\tilde{a}} \gtrsim 100$ keV in the $5 < m_{16} < 12$ TeV range. In the end we showed that excess $\tilde{\chi}_1^0$ relic density does not constitute a cosmological catastrophe for the SO(10) SUSY GUTs.

The focus point mSUGRA is generally considered a difficult scenario for the LHC. We questioned this by making a deep search in the mSUGRA parameter space using again the MCMC, aiming at focus point scenarios that have a low-to-moderate gluino mass. Especially varying A_0 led to many new and consistent regions. We were able to come up with two feasable types of solutions for the LHC which optimize $m_{\tilde{g}}$ and $m_{\tilde{\chi}_1^0}$ to achieve higher reach. First option features a low $m_{\tilde{g}} \sim 500$ GeV that enhances $\tilde{g}\tilde{g}$ production, but it has the disadvantage of a low $m_{\tilde{\chi}_1^0} \sim 60$ GeV which leads to less missing energy and makes signal discrimination difficult. Second option features heavier gluinos with $m_{\tilde{g}} \sim 650$ GeV that have lower $\tilde{g}\tilde{g}$ production cross sections, but also heavier neutralinos with $m_{\tilde{\chi}_1^0} \sim 80$ GeV which can generate more missing energy and thus make signal discrimination easier.

Equipped with all this, we aim for the LHC reach of supersymmetry with heavy scalars. The six benchmarks chosen from the three models with scalars sequestered from LHC physics have gluinos at the mass range 400-1000 GeV which dominantly decay to 3-body modes crowded with bottoms and tops. Then $\tilde{\chi}_2^0$s and $\tilde{\chi}_1^\pm$s, with masses $\sim$ 100 GeV also make 3-body decays (except in G21) to hadronic and leptonic states. One could either take the leptonic or hadronic paths. We took both.

The leptonic case was only investigated for the SO(10)s and with a toy detector simulation. It was shown that signal should be easily visible above the SM backgrounds in the ≥ 4 jets + ≥ 3 leptons channel, even without using the $\not{E}_T$ variable, for $\sim$1 fb^{-1} of integrated luminosity. Furthermore mass edges $m(l^+l^-)$, $m(b\bar{b})$ and $m(b\bar{b}l^+l^-)$ along with total cross section rates (which depend sensitively on the value of $m_{\tilde{g}}$) should allow for sparticle mass reconstruction of $m_{\tilde{g}}$, $m_{\tilde{\chi}_2^0}$ and $m_{\tilde{\chi}_1^0}$ to O(%10) accuracy for $\sim$ 100 fb^{-1} of integrated luminosity. The gluino pair production signal can be complemented by another signal in the clean trilepton channel from $\tilde{\chi}_1^\pm\tilde{\chi}_2^0 \rightarrow 3l + \not{E}_T$, which should also be visible for higher integrated luminosities around $\sim$5-10 fb^{-1}. The dilepton and trilepton channels can also be applied to the focus point searches, since light gaugino production and gaugino decays to leptons occur in similar rates. However focus points are further obscured by leptonic decays of the heavier gauginos, which are lighter and more accessible at the LHC. G2s are different in the sense that $\tilde{\chi}_1^0$s are degenerate with $\tilde{\chi}_1^\pm$s, and $\tilde{\chi}_2^0$ decays lead to states involving Ws or $\tilde{\chi}_1^\pm$s.

On the other side G2s, SO10s and FPs all offer an inviting feast of hadrons to which we eagerly joined through an all inclusive jets +$\not{E}_T$ analysis with the full simulation of the CMS detector.

Aiming for a simple and robust approach for 100 pb^{-1}, we made extensive use of triggers. We showed that triggers built upon jet and $\not{E}_T$ requirements, specially the subset based on the acoplanarity requirement reduced the backgrounds with ease, giving us a good head start. Next we designed six prototype all-hadronic selection paths with different jet multiplicities, $\not{E}_T$ and $\not{E}_T/H_T$ in order to create alternatives to serve a complementary search for a signal excess. Then we refined the paths, using the "indirect lepton veto" technique for leptonic background rejection plus a specialized set of angular cuts designed to distinguish $\not{E}_T$ mismeasurements for QCD rejection. We further applied supplementary cuts on 1st jet $|\eta|$ and event shapes. These selections already offered significant discovery, but there was still room for tuning. The richness in bs and ts offered a distinct opportunuty, and we took it by implementing b triggers which proved to be a more powerful tool than the yet ambigous

and analysis-dependent offline b tagging while cleaning the QCD, $W + n$ jets and $t\bar{t} + n$ jets remnants.

For a more realistic interpretation of results, we exercised data-driven background estimation via ABCD method and checked the effects of systematic uncertainties that arise from jet energy scale and variations in $\not{E}_T$ tails due to jet mismeasurements. In the end we showed that gluinos with masses up to 1 TeV are accessible at the LHC with over 5σ significance for 50-100 fb^{-1} corresponding to a 3-5 year running with $\mathcal{L} = 2 \times 10^{33} cm^{-2} s^{-1}$. Significance $S/\sqrt{S+B}$ was found to be inversely related to gluino mass as $1/(m_{\tilde{g}})^a$, which stood coherent with the behavior of $\tilde{g}\tilde{g}$ cross section. Consequently luminosity for 5σ discovery was seen to behave like $(m_{\tilde{g}})^b$. Cases with heavy gluinos where $m_{\tilde{g}} > 700$ GeV need the high $\not{E}_T$ selection paths to stand out more significantly, while for cases with $m_{\tilde{g}} < 700$ GeV all paths serve well in achieving a 5σ discovery with luminosities less then $\sim$1 fb^{-1}, providing results within the first year.

But this is just a humble beginning. Phenomenological motivation and experimental accessibility praise SUSY with heavy scalars as a possible scenario. Still, on the phenomenology side one must look into other models with similar predictions and map a more complete parameter space with a better defined set of signatures. On the experimental side, one must refine the selection to improve the gluino mass reach especially by taking into account b and top physics; enrich the scope of observables; combine and compare results from different paths coherently to achieve quantitive information on the discovery; and find a comprehensive way to combine full signal and background kinematics from different channels, paths and measurements to devise a way to distinguish the origins of supersymmetry with heavy scalars, in case it is discovered.

We hope LHC will soon be there to guide us.

REFERENCES

[1] S. L. Glashow, Nucl. Phys. **22** (1961) 579.

[2] S. Weinberg, Phys. Rev. Lett. **19** (1967) 1264.

[3] A. Salam, *Originally printed in *Svartholm: Elementary Particle Theory, Proceedings Of The Nobel Symposium Held 1968 At Lerum, Sweden*, Stockholm 1968, 367-377*

[4] http://lepewwg.web.cern.ch/LEPEWWG/

[5] P. Ball and R. Fleischer, Eur. Phys. J. C **48** (2006) 413 [arXiv:hep-ph/0604249].

[6] M. Maltoni, T. Schwetz, M. A. Tortola and J. W. F. Valle, New J. Phys. **6** (2004) 122 [arXiv:hep-ph/0405172].

[7] S. R. Coleman and J. Mandula, Phys. Rev. **159** (1967) 1251.

[8] Ya. B. Zeldovich, Uspekhi Fiz. Nauk **95**, 209 (1968).

[9] Yu. A. Golfand and E. P. Likhtman, JETP Lett. **13** (1971) 323 [Pisma Zh. Eksp. Teor. Fiz. **13** (1971) 452].

[10] A. Neveu and J. H. Schwarz, Nucl. Phys. B **31** (1971) 86.

[11] P. Ramond, Phys. Rev. D **3** (1971) 2415.

[12] J. Wess and B. Zumino, Phys. Lett. B **49** (1974) 52.

[13] J. Wess and B. Zumino, Nucl. Phys. B **70** (1974) 39.

[14] J. Wess and B. Zumino, Nucl. Phys. B **78** (1974) 1.

[15] S. Ferrara, J. Wess and B. Zumino, Phys. Lett. B **51** (1974) 239.

[16] S. Ferrara, J. Iliopoulos and B. Zumino, Nucl. Phys. B **77** (1974) 413.

[17] D. Z. Freedman, P. van Nieuwenhuizen and S. Ferrara, Phys. Rev. D **13** (1976) 3214.

[18] S. Deser and B. Zumino, Phys. Lett. B **62** (1976) 335.

[19] H. P. Nilles, Phys. Rept. **110** (1984) 1.

[20] H. E. Haber and G. L. Kane, Phys. Rept. **117** (1985) 75.

[21] H. Baer and X. Tata, *Cambridge, UK: Univ. Pr. (2006) 537 p*

[22] S. P. Martin, arXiv:hep-ph/9709356.

[23] D. I. Kazakov, arXiv:hep-ph/0012288.

[24] J. R. Ellis, arXiv:hep-ph/0203114.

[25] H. P. Nilles, Phys. Lett. B **115** (1982) 193; A. H. Chamseddine, R. L. Arnowitt and P. Nath, Phys. Rev. Lett. **49** (1982) 970; P. Nath, R. L. Arnowitt and A. H. Chamseddine, Nucl. Phys. B **227** (1983) 121; R. Barbieri, S. Ferrara and C. A. Savoy, Phys. Lett. B **119** (1982) 343; E. Cremmer, P. Fayet and L. Girardello, Phys. Lett. B **122** (1983) 41; L. E. Ibanez, Phys. Lett. B **118** (1982) 73; H. P. Nilles, M. Srednicki and D. Wyler, Phys. Lett. B **124** (1983) 337.

[26] M. Dine and A. E. Nelson, Phys. Rev. D **48** (1993) 1277 [arXiv:hep-ph/9303230]; M. Dine, A. E. Nelson and Y. Shirman, Phys. Rev. D **51** (1995) 1362 [arXiv:hep-ph/9408384]; M. Dine, A. E. Nelson, Y. Nir and Y. Shirman, Phys. Rev. D **53** (1996) 2658 [arXiv:hep-ph/9507378].

[27] Particle Data Group, http://pdg.lbl.gov/

[28] J. R. Ellis, J. S. Hagelin, D. V. Nanopoulos, K. A. Olive and M. Srednicki, Nucl. Phys. B **238** (1984) 453.

[29] G. Hinshaw *et al.* [WMAP Collaboration], arXiv:0803.0732 [astro-ph]; J. Dunkley *et al.* [WMAP Collaboration], arXiv:0803.0586 [astro-ph]; E. Komatsu *et al.* [WMAP Collaboration], arXiv:0803.0547 [astro-ph].

[30] J. Hamann, S. Hannestad, G. G. Raffelt and Y. Y. Y. Wong, JCAP **0708** (2007) 021 [arXiv:0705.0440 [astro-ph]].

[31] S. Sekmen, M. T. Zeyrek, S. Kraml and M. Spiropulu, CERN-CMS-IN-2008-002

[32] M. M. Nojiri *et al.*, arXiv:0802.3672 [hep-ph].

[33] B. C. Allanach, S. Kraml and W. Porod, JHEP **0303** (2003) 016 [arXiv:hep-ph/0302102].

[34] G. Belanger, S. Kraml and A. Pukhov, Phys. Rev. D **72** (2005) 015003 [arXiv:hep-ph/0502079].

[35] F. E. Paige, S. D. Protopopescu, H. Baer and X. Tata, arXiv:hep-ph/0312045.

[36] B. C. Allanach, Comput. Phys. Commun. **143** (2002) 305 [arXiv:hep-ph/0104145].

[37] W. Porod, Comput. Phys. Commun. **153** (2003) 275 [arXiv:hep-ph/0301101].

[38] A. Djouadi, J. L. Kneur and G. Moultaka, Comput. Phys. Commun. **176** (2007) 426 [arXiv:hep-ph/0211331].

[39] G. Belanger, F. Boudjema, A. Pukhov and A. Semenov, Comput. Phys. Commun. **176** (2007) 367 [arXiv:hep-ph/0607059].

[40] M. B. Green, J. H. Schwarz and E. Witten, "SUPERSTRING THEORY. VOL. 1: INTRODUCTION, VOL. 2: Loop Amplitudes, Anomalies and Phenomenology" *Cambridge, Uk: Univ. Pr. (1987) 469 P. (Cambridge Monographs On Mathematical Physics)*

[41] A. M. Polyakov, *CHUR, SWITZERLAND: HARWOOD (1987) 301 P. (CONTEMPORARY CONCEPTS IN PHYSICS, 3)*

[42] J. Polchinski, *Cambridge, UK: Univ. Pr. (1998) 531 p*

[43] E. Kiritsis, *Princeton, USA: Univ. Pr. (2007) 588 p*

[44] T. Mohaupt, Lect. Notes Phys. **631** (2003) 173 [arXiv:hep-th/0207249].

[45] S. Kachru, R. Kallosh, A. Linde and S. P. Trivedi, Phys. Rev. D **68** (2003) 046005 [arXiv:hep-th/0301240].

[46] K. Choi, A. Falkowski, H. P. Nilles, M. Olechowski and S. Pokorski, JHEP **0411** (2004) 076 [arXiv:hep-th/0411066].

[47] K. Choi, A. Falkowski, H. P. Nilles and M. Olechowski, Nucl. Phys. B **718** (2005) 113 [arXiv:hep-th/0503216].

[48] V. Balasubramanian, P. Berglund, J. P. Conlon and F. Quevedo, JHEP **0503** (2005) 007 [arXiv:hep-th/0502058].

[49] J. P. Conlon, F. Quevedo and K. Suruliz, JHEP **0508** (2005) 007 [arXiv:hep-th/0505076].

[50] B. Acharya, K. Bobkov, G. Kane, P. Kumar and D. Vaman, Phys. Rev. Lett. **97** (2006) 191601 [arXiv:hep-th/0606262].

[51] B. S. Acharya, K. Bobkov, G. L. Kane, P. Kumar and J. Shao, Phys. Rev. D **76** (2007) 126010 [arXiv:hep-th/0701034].

[52] G. L. Kane, P. Kumar and J. Shao, Phys. Rev. D **77** (2008) 116005 [arXiv:0709.4259 [hep-ph]].

[53] B. S. Acharya, K. Bobkov, G. L. Kane, J. Shao and P. Kumar, Phys. Rev. D **78** (2008) 065038 [arXiv:0801.0478 [hep-ph]].

[54] B. S. Acharya, K. Bobkov, G. L. Kane, P. Kumar, J. Shao and S. Watson, *in preperation*.

[55] H. Georgi, in *Proceedings of the American Institue of Physics*, edited by C. Carlson (1974); H. Fritzsch and P. Minkowski, Ann. Phys. **93**, 193 (1975); M. Gell-Mann, P. Ramond and R. Slansky, Rev. Mod. Phys. **50**, 721 (1978). For recent reviews, see R. Mohapatra, hep-ph/9911272 (1999) and S. Raby, in Rept. Prog. Phys. **67** (2004) 755. For additional perspective, see G. Altarelli and F. Feruglio, [arXiv:hep-ph/0405048].

[56] T. Blazek, R. Dermisek and S. Raby, Phys. Rev. D **65** (2002) 115004 [arXiv:hep-ph/0201081].

[57] D. Auto, H. Baer, C. Balazs, A. Belyaev, J. Ferrandis and X. Tata, JHEP **0306** (2003) 023 [arXiv:hep-ph/0302155].

[58] H. Baer and J. Ferrandis, Phys. Rev. Lett. **87** (2001) 211803 [arXiv:hep-ph/0106352].

[59] H. Baer, S. Kraml, S. Sekmen and H. Summy, JHEP **0803** (2008) 056 [arXiv:0801.1831 [hep-ph]].

[60] Private communications with A. Pukhov.

[61] B. Allanach *et al.*, arXiv:0801.0045 [hep-ph].

[62] A. A. Markov, *Extension of the limit theorems of probability theory to a sum of variables connected in a chain*, reprinted in Appendix B of: R. Howard, *Dynamic Probabilistic Systems, volume 1: Markov Chains*, John Wiley and Sons, 1971.

[63] N. Metropolis, A.W. Rosenbluth, M.N. Rosenbluth, A.H. Teller, and E. Teller, Journal of Chemical Physics, 21(6):1087-1092, 1953; W.K. Hastings, Biometrika, 57(1):97–109, 1970;
see also C.G. Lester, M.A. Parker, M.J. White, JHEP **0601** (2006) 080, [arXiv:hep-ph/0609295].

[64] J. Feng, C. Kolda and N. Polonsky, *Nucl. Phys.* **B 546** (1999) 3; J. Bagger, J. Feng and N. Polonsky, *Nucl. Phys.* **B 563** (1999) 3; J. Bagger, J. Feng, N. Polonsky and R. Zhang, *Phys. Lett.* **B 473** (2000) 264.

[65] H. Baer, S. Kraml, S. Sekmen and H. Summy, JHEP **0810** (2008) 079 [arXiv:0809.0710 [hep-ph]].

[66] P. G. Mercadante, J. K. Mizukoshi and X. Tata, Phys. Rev. D **72** (2005) 035009 [arXiv:hep-ph/0506142].

[67] H. Baer, C. h. Chen, F. Paige and X. Tata, Phys. Rev. D **53** (1996) 6241 [arXiv:hep-ph/9512383].

[68] H. Baer, M. Drees, F. Paige, P. Quintana and X. Tata, Phys. Rev. D **61** (2000) 095007 [arXiv:hep-ph/9906233].

[69] H. Baer, M. Haider, S. Kraml, S. Sekmen and H. Summy, accepted for publication in JCAP, arXiv:0812.2693 [hep-ph].

[70] R. D. Peccei and H. R. Quinn, Phys. Rev. Lett. **38** (1977) 1440.

[71] R. D. Peccei and H. R. Quinn, Phys. Rev. D **16** (1977) 1791.

[72] S. Weinberg, Phys. Rev. Lett. **40** (1978) 223.

[73] F. Wilczek, Phys. Rev. Lett. **40** (1978) 279.

[74] E. J. Chun, J. E. Kim and H. P. Nilles, Phys. Lett. B **287** (1992) 123 [arXiv:hep-ph/9205229].

[75] J. E. Kim, Phys. Rev. Lett. **143** (1979) 103; M. A. Shifman, A. Vainstein and V. I. Zakharov, *Nucl. Phys.* **B 166** (1980) 493.

[76] M. Dine, W. Fischler and M. Srednicki, *Phys. Lett.* **B 104** (1981) 199; A. R. Zhitnitsky, Sov. J. Nucl. Phys. **31** (1980) 260

[77] K. Jedamzik, M. Lemoine and G. Moultaka, JCAP **0607** (2006) 010 [arXiv:astro-ph/0508141].

[78] L. Covi, J. E. Kim and L. Roszkowski, Phys. Rev. Lett. **82** (1999) 4180 [arXiv:hep-ph/9905212].

[79] L. Covi, H. B. Kim, J. E. Kim and L. Roszkowski, JHEP **0105** (2001) 033 [arXiv:hep-ph/0101009].

[80] A. Brandenburg and F. D. Steffen, JCAP **0408** (2004) 008 [arXiv:hep-ph/0405158].

[81] K. Kohri, T. Moroi and A. Yotsuyanagi, Phys. Rev. D **73** (2006) 123511 [arXiv:hep-ph/0507245]; for an update see M. Kawasaki, K. Kohri, T. Moroi and A. Yotsuyanagi, arXiv:0804.3745 (2008)

[82] M. Fukugita and T. Yanagida, *Phys. Lett.* **B 174** (1986) 45; M. Luty, *Phys. Rev.* **D 45** (1992) 455; W. Buchmüller and M. Plumacher, *Phys. Lett.* **B 389** (1996) 73; and *Int. J. Mod. Phys.* **A 15** (2000) 5047; R. Barbieri, P. Creminelli, A. Strumia and N. Tetradis, *Nucl. Phys.* **B 575** (2000) 61; G. F. Giudice, A. Notari, M. Raidal, A. Riotto and A. Strumia, arXiv:hep-ph/0310123.

[83] G. Lazarides and Q. Shafi, *Phys. Lett.* **B 258** (1991) 305; K. Kumekawa, T. Moroi and T. Yanagida, *Prog. Theor. Phys.* **92** (1994) 437; T. Asaka, K. Hamaguchi, M. Kawasaki and T. Yanagida, *Phys. Lett.* **B 464** (1999) 12.

[84] Unpublished study in collaboration with S. Kraml.

[85] J. L. Feng, K. T. Matchev and T. Moroi, Phys. Rev. D **61** (2000) 075005 [arXiv:hep-ph/9909334].

[86] K. L. Chan, U. Chattopadhyay and P. Nath, Phys. Rev. D **58** (1998) 096004 [arXiv:hep-ph/9710473].

[87] J. L. Feng, K. T. Matchev and F. Wilczek, Phys. Lett. B **482** (2000) 388 [arXiv:hep-ph/0004043].

[88] J. L. Feng and K. T. Matchev, Phys. Rev. D **63** (2001) 095003 [arXiv:hep-ph/0011356].

[89] Unpublished study in collaboration with L. Pape and M. Spiropulu.

[90] Bruning, Olivier Sim (ed.) ; Collier, Paul (ed.) ; Lebrun, P (ed.) ; Myers, Stephen (ed.) ; Ostojic, Ranko (ed.) ; Poole, John (ed.) ; Proudlock, Paul (ed.), "LHC Design Report", CERN-2004-03, (2004) CERN

[91] http://lhc.web.cern.ch/lhc/

[92] The Compact Muon Solenoid Technical Proposal, CERN-LHCC 94-038, December 1994

[93] CMS Collaboration, "The Tracker Project Technical Design Report ", CERN/LHCC **98-006** (1998) and CMS TDR 5, Addendum CERN/LHCC **20/016**

[94] CMS Collaboration, "ECAL Technical Design Report ", CERN/LHCC **97-033** (1997)

[95] CMS Collaboration, "The Hadron Calorimeter Technical Design Report ", CERN/LHCC **97-031** (1997)

[96] CMS Collaboration, "The Magnet Project, Technical Design Report ", CERN/LHCC **97-10** (1997), CMS TDR 1 (1997)

[97] CMS Collaboration, "The Muon Project, Technical Design Report ", CERN/LHCC **97-32** (1997), CMS TDR 3 (1997)

[98] F. Gianotti, Phys. Rept. **403** (2004) 379.

[99] CMS Collaboration, "Level-1 Trigger Technical Design Report ", CERN/LHCC **2000-038** (2000)

[100] CMS Collaboration, "DAQ and High Level Trigger Technical Design Report ", CERN/LHCC **2002-026** (2002)

[101] S. Sekmen, M. Spiropulu and M. T. Zeyrek, CERN-CMS-AN-2008-108

[102] G. L. Bayatian *et al.* [CMS Collaboration], J. Phys. G **34** (2007) 995.

[103] S. Abdullin *et al.* [CMS Collaboration], J. Phys. G **28** (2002) 469 [arXiv:hep-ph/9806366].

[104] S. Karapostoli and P. Sphicas, , CERN-CMS-AN-2008-038

[105] V. Zhukov, W. de Boer, I. Gebauer, M. Niegel, C. Sander, M. Weber and K. Mazumdar, CERN-CMS-NOTE-2006-113

[106] A. Djouadi, M. M. Muhlleitner and M. Spira, Acta Phys. Polon. B **38** (2007) 635 [arXiv:hep-ph/0609292].

[107] T. Sjostrand, S. Mrenna and P. Skands, JHEP **0605** (2006) 026 [arXiv:hep-ph/0603175].

[108] P. Skands *et al.*, JHEP **0407** (2004) 036 [arXiv:hep-ph/0311123].

[109] J. E. Huth *et al.*, FNAL-C-90-249-E

[110] G. C. Blazey *et al.*, arXiv:hep-ex/0005012.

[111] S. Catani, Y. L. Dokshitzer, M. H. Seymour and B. R. Webber, Nucl. Phys. B **406** (1993) 187.

[112] G. P. Salam and G. Soyez, JHEP **0705** (2007) 086 [arXiv:0704.0292 [hep-ph]].

[113] https://twiki.cern.ch/twiki/bin/view/CMS/TSG_24_IX_07

[114] M. Spiropulu, PhD Thesis, UMI-99-88600

[115] A. A. Affolder *et al.* [CDF Collaboration], Phys. Rev. Lett. **88** (2002) 041801 [arXiv:hep-ex/0106001].

[116] M. Spiropulu and T. Yetkin, CERN-CMS-AN-2006-089

[117] J. Hartert, O. Buchmuller, R. J. Cavanaugh, V. Drollinger, and M. Spiropulu, CERN-CMS-AN-2005-048

[118] J. D. Bjorken and S. J. Brodsky, Phys. Rev. D **1** (1970) 1416.

[119] S. Brandt, C. Peyrou, R. Sosnowski and A. Wroblewski, Phys. Lett. **12** (1964) 57.

[120] G. C. Fox and S. Wolfram, Nucl. Phys. B **149** (1979) 413 [Erratum-ibid. B **157** (1979) 543].

[121] H. Flascher, J. Jones, T. Rommerskirchen, B. Sinclair and M. Stoye, CERN-CMS-AN-2008-071

APPENDIX A

PDJetMET TRIGGERS

After the L1 and HLT algorithms are applied, CMS data is split into primary datasets (PDs) for a more efficient manipulation. The analysis in Chapter 7 uses PDJetMET which is an OR of 19 trigger selection paths based on jet and $\not{E}_T$ thresholds. These triggers are defined for the CSA07 exercise and implemented in `CMSSW_1_6_X`, relevant for the conditions for a physics run at 14 TeV and $\mathcal{L} = 10^{32}$ cm^{-2}s^{-1} [113]. Tables A.1 and A.2 list the complete PDJetMET triggers.

Table A.1: Information on triggers that define PDJetMET - 1

HLT path	L1 path	L1 obj	L1 trsh	L1 prscl	HLT obj	HLT thrshld	HLT prscl	HLT rate
HLT1jet	L1_SingleJet150	1jet	150	1	1jet	200	1	9.3 ± 0.1
HLT2jet	L1_SingleJet150	1jet	150	1	2jets	150	1	10.6 ± 0.0
	L1_DoubleJet70	2jets	70	1				
HLT3jet	L1_SingleJet150	1jet	150	1	3jets	85	1	7.5 ± 0.1
	L1_DoubleJet70	2jets	70	1				
	L1_TripleJet50	3jets	50	1				
HLT4jet	L1_SingleJet150	1jet	150	1	4jets	60	1	3.9 ± 0.1
	L1_DoubleJet70	2jets	70	1				
	L1_TripleJet50	3jets	50	1				
	L1_QuadJet40	4jets	40	1				
HLT1MET	L1_ETM40	MET	40	1	MET	65	1	4.9 ± 0.7
HLT2jetAco	L1_SingleJet150	1jet	150	1	2jets	125	1	1.4 ± 0.0
	L1_DoubleJet70	2jets	70	1	jet-jet	$0.0 \leq d\phi \leq 2.1$		
HLT1jet1METAco	Ł1_SingleJet150	1jet	150	1	1jet	100	1	1.6 ± 0.0
					MET	60		
					Jet-MET	$0.0 \leq d\phi \leq 2.1$		
HLT1jet1MET	L1_SingleJet150	1jet	150	1	1jet	180	1	2.2 ± 0.1
					MET	60		
HLT2jet1MET	L1_SingleJet150	1jet	150	1	2jets	125	1	1.0 ± 0.1
					MET	60		
HLT3jet1MET	L1_SingleJet150	1jet	150	1	3jets	60	1	0.6 ± 0.0
					MET	60		

Table A.2: Information on triggers that define PDJetMET - 2

HLT path	L1 path	L1 obj	L1 trsh	L1 prscl	HLT obj	HLT thrshld	HLT prscl	HLT rate
HLT4jet1MET	L1_SingleJet150	1jet	150	1	4jets	35	1	1.2 ± 0.1
					MET	60		
HLT1MET1HT	L1_HTT300	HT	300	1	HT	350	1	4.4 ± 0.1
					MET	65		
HLT2jetvbfMET	L1_ETM40	MET	40	1	MET	60	1	0.2 ± 0.0
					2jets	40		
					2jets	$2.5 \leq \lvert d\eta \rvert$		
HLTS2jet1METNV	L1_SingleJet150	1jet	150	1	MET	60	1	2.0 ± 0.1
					jet1	80		
					jet2	20		
HLTS2jet1METAco	L1_SingleJet150	1jet	150	1	MET	60	1	1.0 ± 0.0
					2jets	60		
					2jets	$0.0 \leq d\phi \leq 2.89$		
CandHLTSjet1MET1Aco	L1_SingleJet150	1jet	150	1	MET	70	1	–
					1jet	60		
					Jet-MET	$0.0 \leq d\phi \leq 2.89$		
CandHLTSjet2MET1Aco	L1_SingleJet150	1jet	150	1	MET	70	1	–
					2jets	$0.377 \leq d\phi \leq 3.142$		
					2jets	50		
CandHLTS2jetAco	L1_SingleJet150	Jet	150	1	MET	70	1	–
					2Jets	40		
					jet-jet	$0 \leq d\phi \leq 2.76$		
CandHLTJetMET-RapidityGap	L1_IsoEG10_Jet20_ForJet10	1IsoEG	10	1	$\sum$jetE_T	< 20		
		1jet	20		for			
		Forw jet[1]	10		$3 \leq \lvert\eta\rvert_{jet} \leq 5$			

APPENDIX B

APLANARITY

Aplanarity is calculated from the sphericity matrix

$$S^{\alpha\beta} = \frac{\sum_i^n p_i^\alpha p_i^\beta}{\sum_i |p_i|^2} \tag{B.1}$$

where $\alpha, \beta = 1, 2, 3$ are the x, y, z coordinates and p_i are the 4-momenta vectors, with $i = 0, 1, 2...n$ running over the n selected objects in the event, which in our case are the IC5 jets with $p_T > 30$ GeV and $|\eta| < 3$. Diagonalizing $S^{\alpha\beta}$ gives the eigenvalues $\lambda_1 \geq \lambda_2 \geq \lambda_3$. Aplanarity is then defined as

$$A = \frac{3}{2}\lambda_3 \tag{B.2}$$

and it is a measure of the transverse momentum component out of the event plane, where a planar event has $A \approx 0$ and an isotropic event has $A \approx 1$.

Figure B.1 shows the aplanarity distribution for the no-$\not\!\!E_T$ path 6 and $\not\!\!E_T > 150$ path 3 after the final selection. Signal events display a more isotropic nature. We introduce an optional cut of $A > 0.01$. The final selection results with added aplanarity requirement are given in Table B.1 for no *b* triggers requirement and in Table B.2 also including the *b* triggers requirement.

Table B.1: Selection results for all paths for signal and backgrounds after the offline selection plus $A > 0.01$. The numbers of events represent 100 pb^{-1} of integrated luminosity.

Point		PDJM	HLT	path1	path2	path3	path4	path5	path6
G21:	nevts	25	23	6	4	7	8	6	8
	efficiency (%)	100.00	92.00	24.00	16.00	28.00	32.00	24.00	32.00
	S/B (%)	0.00	0.00	0.26	2.00	0.00	0.01	0.02	0.05
	Sgnf $S/\sqrt{S+B}$	0.00	0.03	1.11	1.63	0.18	0.28	0.31	0.61
	Punzi sgnf $\times 10^4$	0.73	10.13	381.20	549.03	70.60	107.50	116.48	223.07
G24:	nevts	807	597	65	15	116	161	100	130
	efficiency (%)	100.00	73.98	8.05	1.86	14.37	19.95	12.39	16.11
	S/B (%)	0.00	0.00	2.83	7.50	0.08	0.20	0.27	0.79
	Sgnf $S/\sqrt{S+B}$	0.06	0.66	6.93	3.64	2.93	5.20	4.64	7.57
	Punzi sgnf $\times 10^4$	0.72	8.04	126.21	62.92	35.76	66.12	59.33	110.79
SO10A:	nevts	6817	3323	69	12	385	461	243	243
	efficiency (%)	100.00	48.75	1.01	0.18	5.65	6.76	3.56	3.56
	S/B (%)	0.00	0.00	3.00	6.00	0.26	0.58	0.67	1.47
	Sgnf $S/\sqrt{S+B}$	0.50	3.66	7.19	3.21	8.97	12.99	9.85	12.03
	Punzi sgnf $\times 10^4$	0.59	4.34	13.01	4.89	11.52	18.38	14.00	20.11
SO10D:	nevts	7564	3975	94	16	398	555	267	316
	efficiency (%)	100.00	52.55	1.24	0.21	5.26	7.34	3.53	4.18
	S/B (%)	0.00	0.00	4.09	8.00	0.27	0.69	0.73	1.92
	Sgnf $S/\sqrt{S+B}$	0.55	4.37	8.69	3.77	9.24	15.08	10.62	14.41
	Punzi sgnf $\times 10^4$	0.54	4.29	14.62	5.38	9.83	18.26	12.69	21.57
FP1:	nevts	2150	1329	70	19	205	265	162	173
	efficiency (%)	100.00	61.81	3.26	0.88	9.53	12.33	7.53	8.05
	S/B (%)	0.00	0.00	3.04	9.50	0.14	0.33	0.44	1.05
	Sgnf $S/\sqrt{S+B}$	0.16	1.46	7.26	4.15	5.03	8.12	7.06	9.41
	Punzi sgnf $\times 10^4$	0.53	4.93	37.44	21.95	17.40	29.98	26.47	40.61
FP2:	nevts	426	243	23	7	47	56	42	42
	efficiency (%)	100.00	57.04	5.40	1.64	11.03	13.15	9.86	9.86
	S/B (%)	0.00	0.00	1.00	3.50	0.03	0.07	0.12	0.25
	Sgnf $S/\sqrt{S+B}$	0.03	0.27	3.39	2.33	1.21	1.92	2.08	2.92
	Punzi sgnf $\times 10^4$	0.21	1.84	25.11	16.51	8.15	12.93	14.01	20.12
WnJ	nevts	115196	9432	5	0	24	65	14	54
	eff (%)	100.00	8.19	0.00	0.00	0.02	0.06	0.01	0.05
ZnJ	nevts	19624	725	0	0	2	2	1	1
	eff (%)	100.00	3.69	0.00	0.00	0.01	0.01	0.01	0.01
ttnJ	nevts	18559	3134	13	2	77	104	41	59
	eff (%)	100.00	16.89	0.07	0.01	0.41	0.56	0.22	0.32
QCD	nevts	185288380	807170	5	0	1350	626	308	51
	eff (%)	100.00	0.44	0.00	0.00	0.00	0.00	0.00	0.00
PJ	nevts	1408307	1557	0	0	3	2	1	0
	eff (%)	100.00	0.11	0.00	0.00	0.00	0.00	0.00	0.00
Total BG	nevts	186850066	822018	23	2	1456	799	365	165
	eff (%)	100.00	0.44	0.00	0.00	0.00	0.00	0.00	0.00

Table B.2: Selection results including the b triggers requirement for all paths for signal and backgrounds after the offline selection plus $A > 0.01$. The numbers of events represent 100 pb^{-1} of integrated luminosity.

Point		PDJM	HLT	path1	path2	path3	path4	path5	path6
G21:	nevts	25	23	3	2	3	4	3	4
	efficiency (%)	100.00	92.00	12.00	8.00	12.00	16.00	12.00	16.00
	S/B (%)	0.00	0.00	0.38	2.00	0.01	0.02	0.04	0.08
	Sgnf $S/\sqrt{S+B}$	0.00	0.03	0.90	1.15	0.17	0.27	0.32	0.55
	Punzi sgnf $\times 10^4$	0.73	10.13	277.24	320.00	62.62	98.78	113.10	189.84
G24:	nevts	807	597	29	6	53	72	45	56
	efficiency (%)	100.00	73.98	3.59	0.74	6.57	8.92	5.58	6.94
	S/B (%)	0.00	0.00	3.62	6.00	0.17	0.33	0.54	1.17
	Sgnf $S/\sqrt{S+B}$	0.06	0.66	4.77	2.27	2.77	4.24	3.98	5.49
	Punzi sgnf $\times 10^4$	0.72	8.04	81.91	29.34	33.81	54.34	51.85	81.23
SO10A:	nevts	6817	3323	44	7	251	311	155	156
	efficiency (%)	100.00	48.75	0.65	0.10	3.68	4.56	2.27	2.29
	S/B (%)	0.00	0.00	5.50	7.00	0.80	1.44	1.87	3.25
	Sgnf $S/\sqrt{S+B}$	0.50	3.66	6.10	2.47	10.58	13.55	10.05	10.92
	Punzi sgnf $\times 10^4$	0.59	4.34	12.07	3.32	15.55	22.79	17.34	21.97
SO10D:	nevts	7564	3975	58	9	271	378	177	210
	efficiency (%)	100.00	52.55	0.77	0.12	3.58	5.00	2.34	2.78
	S/B (%)	0.00	0.00	7.25	9.00	0.87	1.75	2.13	4.38
	Sgnf $S/\sqrt{S+B}$	0.55	4.37	7.14	2.85	11.22	15.51	10.98	13.07
	Punzi sgnf $\times 10^4$	0.54	4.29	13.12	3.52	13.85	22.85	16.33	24.40
FP1:	nevts	2150	1329	37	8	110	146	87	92
	efficiency (%)	100.00	61.81	1.72	0.37	5.12	6.79	4.05	4.28
	S/B (%)	0.00	0.00	4.62	8.00	0.35	0.68	1.05	1.92
	Sgnf $S/\sqrt{S+B}$	0.16	1.46	5.52	2.67	5.35	7.67	6.67	7.78
	Punzi sgnf $\times 10^4$	0.53	4.93	28.78	10.77	19.33	30.35	27.61	36.75
FP2:	nevts	426	243	15	4	30	36	27	27
	efficiency (%)	100.00	57.04	3.52	0.94	7.04	8.45	6.34	6.34
	S/B (%)	0.00	0.00	1.88	4.00	0.10	0.17	0.33	0.56
	Sgnf $S/\sqrt{S+B}$	0.03	0.27	3.13	1.79	1.62	2.27	2.57	3.12
	Punzi sgnf $\times 10^4$	0.21	1.84	23.82	11.00	10.76	15.28	17.49	22.02
WnJ	nevts	115196	9432	0	0	2	5	1	4
	eff (%)	100.00	8.19	0.00	0.00	0.00	0.00	0.00	0.00
ZnJ	nevts	19624	725	0	0	0	0	0	0
	eff (%)	100.00	3.69	0.00	0.00	0.00	0.00	0.00	0.00
ttnJ	nevts	18559	3134	6	1	35	51	19	28
	eff (%)	100.00	16.89	0.03	0.01	0.19	0.27	0.10	0.15
QCD	nevts	185288380	807170	2	0	275	160	63	16
	eff (%)	100.00	0.44	0.00	0.00	0.00	0.00	0.00	0.00
PJ	nevts	1408307	1557	0	0	0	0	0	0
	eff (%)	100.00	0.11	0.00	0.00	0.00	0.00	0.00	0.00
ppmuX	nevts	2259840	73040	0	0	0	0	0	0
	eff (%)	100.00	3.23	0.00	0.00	0.00	0.00	0.00	0.00
Total BG	nevts	186850066	822018	8	1	312	216	83	48
	eff (%)	100.00	0.44	0.00	0.00	0.00	0.00	0.00	0.00

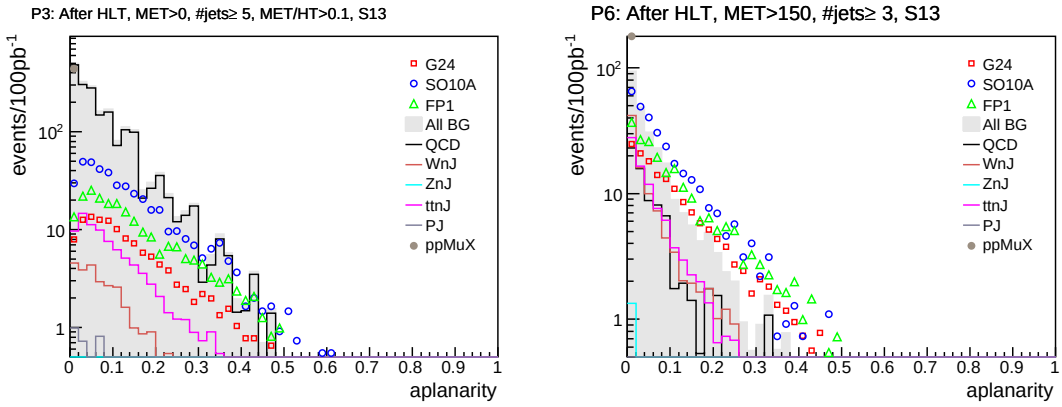

Figure B.1: Aplanarity distribution after the Fox-Wolfram cuts (step 13, the final cut). Shown for path 3 (left) and path 6 (right).

APPENDIX C

b TRIGGERS

Table C.1: Information on lifetime *b* triggers

HLT path	L1 seed	L2 obj	L2 thrshld	L2.5 cut	L3 cut	HLT prescale	HLT rate
HLTB1Jet		1jet	180	3.5	6.0	1	1.3 ± 0.0
HLTB2Jet	see	2jets	120	3.5	6.0	1	2.1 ± 0.0
HLTB3Jet	Table	3jets	70	3.5	6.0	1	1.7 ± 0.0
HLTB4Jet	C	4jets	40	3.5	6.0	1	1.8 ± 0.0
HLTBHT		HT	470	3.5	6.0	1	2.5 ± 0.0

Table C.2: Information on soft muon *b* triggers

HLT path	L1 seed	L2 obj	L2 thrshld	L2.5 cut $\Delta R(\mu - j)$	L3 cut $p_T^{rel}(\mu)$	HLT prescale	HLT rate
HLTB1JetMu	L1_Mu5_Jet15	1jet	20	0.5	–	20	4.0 ± 0.1
HLTB2JetMu	L1_Mu5_Jet15	2jets	120	0.5	0.7	1	0.5 ± 0.0
HLTB3JetMu	L1_Mu5_Jet15	3jets	70	0.5	0.7	1	0.3 ± 0.0
HLTB4JetMu	L1_Mu5_Jet15	4jets	40	0.5	0.7	1	0.4 ± 0.0
HLTBHTMu	L1_HTT300	HT	370	0.5	0.7	1	2.6 ± 0.2

Table C.3: Information on L1 seeds for *b* triggers

L1 path	L1 obj	L1 thrshld	L1 prescale	seed to B trigger:
L1_SingleJet150	1jet	150	1	all lifetime
L1_DoubleJet100	2jets	100	1	all lifetime
L1_TripleJet50	3jets	50	1	all lifetime
L1_QuadJet30	4jets	30	1	all lifetime
L1_HTT300	1jet	300	1	all lifetime and HLTBHTMu
L1_Mu5_Jet15	1jet 1μ	15 5	1	HLTB(1,2,3,4)Mu

CURRICULUM VITAE

Sezen Sekmen

Department of Physics, Middle East Technical University

06531, Ankara, Turkey

At CERN: B40, 2-A15

Personal information:

Date/place of Birth	*:* 9 April 1979, Bursa
Nationality	*:* Turkish (T.C.)
Phone	*:* +90 532 3545030 / +41 22 76 71563
e-mail	*:* Sezen.Sekmen@cern.ch

Major research interests:

Phenomenological/experimental high energy physics and implications for cosmology: Searches of BSM physics at the LHC with the CMS detector, collider signatures of supersymmetric dark matter and higher-dimensional miniature black holes

Education:

- **PhD:** (2003–2008), Middle East Technical University, Department of Physics, **Thesis:** *SUSY with Heavy Scalars at the LHC*
- **MSc:** (2001–2003), Middle East Technical University, Department of Physics
  Thesis: *Search for Higgs boson in the decays of higher-dimensional black holes at the LHC*
- **BS:** (1997–2001), Middle East Technical University, Department of Physics (Undergraduate Advanced Physics Program)

Language skills:

Turkish (native), English (fluent), German (beginner-intermediate)

Publications:

In refereed journals:

- H. Baer, M. Haider, S. Kraml, S. Sekmen, H. Summy, *Cosmological consequences of Yukawa-unified SUSY models with mixed axion/axino cold and warm dark matter*, accepted for publication in JCAP, [arXiv:0812.2693 [hep-ph]].
- H. Baer, S. Kraml, S. Sekmen, H. Summy, *Prospects for Yukawa Unified SO(10) SUSY GUTs at the CERN LHC*, JHEP **0810**, 079 (2008), [arXiv:0809.0710 [hep-ph]].
- H. Baer, S. Kraml, S. Sekmen, H. Summy, *Dark matter allowed scenarios for Yukawa-unified SO(10) SUSY GUTs*, JHEP **0803**, 056 (2008), [arXiv:0801.1831 [hep-ph]].
- S. Sekmen, M. T. Zeyrek, *Observing higher-dimensional black holes at the LHC*, Eur. Phys J. C Vol. 39 No.4 (2005) 503

CMS publications:

- S. Sekmen, M. Spiropulu, M. T. Zeyrek, *Search for SUSY with Heavy Scalars using the Inclusive Missing E_T+jets signature at $\sqrt{s}$ = 14 TeV at the CERN LHC*, CMS AN-2008/018.
- S. Sekmen, M. T. Zeyrek, S. Kraml, M. Spiropulu, *Comparison of SUSY Spectrum Codes: An Update*, CMS IN-2008/002.
- CMS Collaboration, *CMS Physics Technical Design Report, Volume II: Physics Performance*, CERN/LHCC/2006-021, J. Phys. G: Nucl. Part. Phys. 34 (2007) 995
- A. de Roeck, H. Gamsızkan, S. Sekmen, M.T. Zeyrek, *Higher-dimensional Black Holes at CMS*, CMS AN-2006/088 (2006)

Proceedings:

- S. Sekmen, *Search for WMAP-Compatible Simple SO(10) SUSY GUTs*, contribution to the proceedings of 43rd Rencontres de Moriond on Electrowek Interactions and Unified Theories, La Thuile, Italy, 1-8 Mar 2008. [arXiv:0805.2664 [hep-ph]]
- M. M. Nojiri, et.al., *Physics Beyond the Standard Model: Supersymmetry*, contribution to the proceedings of 5th Les Houches Workshop on Physics at TeV Colliders, Les Houches, France, 11-29 Jun 2007, [arXiv:0802.3672 [hep-ph]]

Other:

- *Future prospects of European Particle Physics*, S. Sekmen, E. Yazgan, M.T. Zeyrek input for CERN Council Strategy Group (2006)
- *Detector Outline Document for the Fourth Concept Detector ("4th") at the International Linear Collider* , Le Du et al. (2006)
- *Wisdom Generation in the Alps: A Student's Tale*, S. Sekmen, CERN Courier (November 2005)

Book:

- S. Sekmen, *Particle Physics: The Adventure of Discovering the Smallest*, (popular science book in Turkish), METU Developement Association Press, Science and Society Series (February 2007)

Talks and posters:

- *A black hole may end the quest: Tracing Higgs at the higher-dimensional black hole decays at the LHC* (seminar), Feza Gürsey Institute, Istanbul, Turkey (13 November 2003)
- *Tracing higher-dimensional black holes at the LHC*, The Four Seas Conference (Physique Sans Frontieres), Istanbul, Turkey (5-10 September 2004)
- *Black Holes on Earth* (poster), Turkish Physics Society 22nd Physics Congress, Bodrum, Turkey (14-17 September 2004)
- *Susy d'Arc at the ILC* (poster), CERN-JINR European School of High Energy Physics, Kitzbühel, Austria (21 August – 3 September 2005)
- *Introducing Susy d'Arc and its elegant actions*, International Workshop on Physics Beyond the Standard Model, Akyaka, Turkey (22-26 September 2005)
- *SUSY DM at the ILC* (poster), ICHEP 2006, Moscow, Russia (26 July – 2 August 2006)
- *SUSY and the LHC*, (seminar) Ankara HEP Seminars, Ankara University, (16 May 2006)
- *Which SUSY at the LHC?*, Ankara HEP Days (12−13 January 2007)

- *Black holes at the LHC* (CMS speaker), The Four Seas Conference (Physique Sans Frontieres), Iasi, Romania (29 May – 3 June 2007)
- *Black Holes and ADD Gravitons at the LHC* (CMS speaker), SUSY07, Karlsruhe, Germany (26 July – 1 August2007)
- *Yukawa Unification in SO(10) Models*, EuroGDR07 SUSY, Bruxelles, Belgium (12 – 14 November 2007)
- *Yukawa Unification in SO(10) SUSY GUTs*, 43rd Rencontres de Moriond, La Thuile, Italy (1 – 8 March 2008)
- *SO(10) SUSY GUs and their LHC signatures*, seminar, LPSC Grenoble, France (23 April 2008)
- Other local seminars (Ankara, 2002 – 2007) and various presentations at CMS physics meetings (CERN, 2006 – 2008)

Other meetings attended:

- *Cargese School of Physics and Cosmology, "Particle Physics and Cosmology: The Interface*, Cargese, France (03 – 16 August 2003)
- *CP and non-Standard Higgs Physics Workshop*, CERN (14 – 16 December 2005) (unofficial participation)
- *ISSMB '06: International Summer School on High Energy Physics*, Akyaka, Turkey (25 – 30 September 2006), assistant to the organizing committee
- *Hadron Collider Physics Summer School*, CERN (6 – 15 June 2007)
- *Les Houches, Physics at TeV Colliders Workshop*, Les Houches, France (11 – 20 June 2007)
- *CERN TH Institute on "LHC-Cosmology Interplay"*, CERN (25 June – 10 August 2007) (unofficial participation)
- *ISSMB '08: International Summer School on High Energy Physics*, Akyaka, Turkey (10 – 18 September 2008)
- Various CMS collaboration meetings and conferences at CERN (2004 – 2008)

Grants:

- Turkish Scientific and Technological Research Council (TUBITAK) grant 106T457 (TBAG-HD 190) (for visiting CERN: 2007)
- Turkish Atomic Energy Authority (TAEK) grant (for visiting CERN: 2007-2008)